NATIONAL AERONAUTICS AND SPACE ADMINISTRATION

The Deep Space Network
Progress Report 42-25

November and December 1974

JET PROPULSION LABORATORY
CALIFORNIA INSTITUTE OF TECHNOLOGY
PASADENA, CALIFORNIA

February 15, 1975

Preface

Beginning with Volume XX, the Deep Space Network Progress Report changed from the Technical Report 32- series to the Progress Report 42- series. The volume number continues the sequence of the preceding issues. Thus, Progress Report 42-20 is the twentieth volume of the Deep Space Network series, and is an uninterrupted follow-on to Technical Report 32-1526, Volume XIX.

This report presents DSN progress in flight project support, tracking and data acquisition (TDA) research and technology, network engineering, hardware and software implementation, and operations. Each issue presents material in some, but not all, of the following categories in the order indicated:

Description of the DSN

Mission Support
- Ongoing Planetary/Interplanetary Flight Projects
- Advanced Flight Projects

Radio Science
- Radio Science Support
- Special Projects

Supporting Research and Technology
- Tracking and Ground-Based Navigation
- Communications—Spacecraft/Ground
- Station Control and Operations Technology
- Network Control and Data Processing

Network Engineering and Implementation
- Network Control System
- Ground Communications
- Deep Space Stations

Operations
- Network Operations
- Network Control System Operations
- Ground Communications
- Deep Space Stations

Planning and Facilities
- TDA Planning
- Facility Engineering

In each issue, the part entitled "Description of the DSN" describes the functions and facilities of the DSN and may report the current configuration of one of the five DSN systems (Tracking, Telemetry, Command, Monitor and Control, and Test and Training).

The work described in this report series is either performed or managed by the Tracking and Data Acquisition organization of JPL for NASA.

Contents

DESCRIPTION OF THE DSN

MISSION SUPPORT

Ongoing Planetary/Interplanetary Flight Projects

SUPPORTING RESEARCH AND TECHNOLOGY

Tracking and Ground-Based Navigation

Communications–Spacecraft/Ground

Station Control and Operations Technology

NETWORK ENGINEERING AND IMPLEMENTATION

Ground Communications

OPERATIONS

Network Operations

DSN Functions and Facilities

N. A. Renzetti
Office of Tracking and Data Acquisition

The objectives, functions, and organization of the Deep Space Network are summarized. Deep space station, ground communication, and network operations control capabilities are described.

The Deep Space Network (DSN), established by the National Aeronautics and Space Administration (NASA) Office of Tracking and Data Acquisition (OTDA) under the system management and technical direction of the Jet Propulsion Laboratory (JPL), is designed for two-way communications with unmanned spacecraft traveling approximately 16,000 km (10,000 mi) from Earth to the farthest planets of our solar system. It has provided tracking and data acquisition support for the following NASA deep space exploration projects, for which JPL has been responsible for the project management, development of the spacecraft, and conduct of mission operations:

(1) Ranger.

(2) Surveyor.

(3) Mariner Venus 1962.

(4) Mariner Mars 1964.

(5) Mariner Venus 1967.

(6) Mariner Mars 1969.

(7) Mariner Mars 1971.

(8) Mariner Venus/Mercury 1973.

The DSN has also provided tracking and data acquisition support for the following projects:

(1) Lunar Orbiter, for which the Langley Research Center carried out the project management, spacecraft development, and mission operations functions.

(2) Pioneer, for which the Ames Research Center carried out the project management, spacecraft development, and mission operations functions.

(3) Apollo, for which the Lyndon B. Johnson Space Center was the project center and the Deep Space Network supplemented the Spaceflight Tracking and Data Network (STDN) which is managed by the Goddard Space Flight Center (GSFC).

(4) Helios, a joint United States/West Germany project.

(5) Viking, for which the Langley Research Center provides the project management and Lander spacecraft, and conducts mission operations, and for which JPL provides the Orbiter spacecraft.

The Deep Space Network is one of two NASA networks. The other, the Spaceflight Tracking and Data Network, is under the system management and technical direction of the Goddard Space Flight Center. Its function is to support manned and unmanned Earth-orbiting and lunar scientific and advanced technology satellites. Although the DSN was concerned with unmanned lunar spacecraft in its early years, its primary objective now and into the future is to continue its support of planetary and interplanetary flight projects.

A development objective has been to keep the network capability at the state of the art of telecommunications and data handling and to support as many flight projects as possible with a minimum of mission-dependent hardware and software. The DSN provides direct support to each flight project through that project's tracking and data systems. This management element is responsible for the design and operation of the hardware and software in the DSN which are required for the conduct of flight operations.

As of July 1972, NASA undertook a change in the interface between the network and the flight projects. Since January 1, 1964, the network, in addition to consisting of the Deep Space Stations and the Ground Communications Facility, had also included the Mission Control and Computing Facility and had provided the equipment in the mission support areas for the conduct of mission operations. The latter facilities were housed in a building at JPL known as the Space Flight Operations Facility (SFOF). The interface change was to accommodate a hardware interface between the network operations control functions and the mission control and computing functions. This resulted in the flight project's picking up the cognizance of the large general-purpose digital computers, which were used for network processing as well as mission data processing. It also assumed cognizance of all of the equipment in the flight operations facility for display and communications necessary for the conduct of mission operations. The network has already undertaken the development of hardware and computer software necessary to do its network operations control and monitor functions in separate computers. This activity became known as the Network Control System implementation. A characteristic of the new interface is that the network provides direct data flow to and from the stations via appropriate ground communications equipment to Mission Operations Centers, wherever they may be; namely, metric data, science and engineering telemetry, and such network monitor data as are useful to the flight project. It accepts command data from the flight project directly into the ground communications equipment for transmission to the station and thence to the spacecraft in a standardized format.

In carrying out its functions, the network activities can be divided into two general areas. The first includes those functions which are associated with the in-flight support and in tracking the spacecraft; its configuration can be characterized as follows:

(1) *DSN Tracking System.* Generates radio metric data; i.e., angles, one- and two-way doppler and range, and transmits raw data to mission control.

(2) *DSN Telemetry System.* Receives, decodes, records, and retransmits engineering and scientific data generated in the spacecraft to Mission Control.

(3) *DSN Command System.* Accepts coded signals from Mission Control via the Ground Communications Facility (GCF) and transmits them to the spacecraft in order to initiate spacecraft functions in flight.

The second category of activity supports testing, training, and network operations control functions and is configured as follows:

(1) *DSN Monitor and Control System.* Instruments, transmits, records, and displays those parameters of the DSN necessary to verify configuration and validate the network. Provides operational direction and configuration control of the network and primary interface with flight project mission control personnel.

(2) *DSN Test and Training System.* Generates and controls simulated data to support development, test, training, and fault isolation within the DSN. Participates in mission simulation with flight projects.

The capabilities needed to carry out the above functions have evolved in three technical areas:

(1) The Deep Space Stations that are distributed around Earth and which, prior to 1964, formed part of the Deep Space Instrumentation Facility. The technology involved in equipping these stations is strongly related to the state of the art of telecommunications and flight/ground design considerations and is almost completely multimission in character. Table 1 gives a description of the Deep Space Stations and the Deep Space Communications Complexes (DSCCs) they comprise.

(2) Ground communications. This technology supports the Earth-based point-to-point voice and data communications from the stations to the Network Operations Control Area at JPL, Pasadena, and to the Mission Operations Centers, wherever they may be. It is based largely on the capabilities of the common carriers throughout the world which are engineered into an integrated system by the Goddard Space Flight Center for support of all NASA programs. The term "Ground Communications Facility" is used for the sets of hardware and software needed to carry out the functions.

The Network Operations Control Center is the functional entity for centralized operational control of the network and interfaces with the users. It has two separable functional elements; namely, Network Operations Control and Network Data Processing.

The functions of the Network Operations Control Center are:

(1) Control and coordination of network support to meet commitments to network users.

(2) Utilization of the network data processing computing capability to generate all standards and limits required for network operations.

(3) Utilization of network data processing computing capability to analyze and validate the performance of all network systems.

The personnel who carry out the above functions are on the first floor of Building 230, wherein mission operations functions are carried out by certain flight projects. Network personnel are directed by an Operations Control Chief. The functions of the Network Data Processing are:

(1) Processing of data used by Network Operations Control for the control and analysis of the network.

(2) Display in Network Operations Control Area of data processed in Network Data Processing Area.

(3) Interface with communications circuits for input to and output from Network Data Processing Area.

(4) Data logging and production of the intermediate data records.

The personnel who carry out these functions are located in Building 202, which is approximately 200 m from Building 230. The equipment consists of minicomputers for real-time data system monitoring, two XDS Sigma 5's, display, magnetic tape recorders, and appropriate interface equipment with the ground data communications.

Table 1. Tracking and data acquisition stations of the DSN

DSCC	Location	DSS	DSS serial designation	Antenna		Year of initial operation
				Diameter, m (ft)	Type of mounting	
Goldstone	California	Pioneer	11	26(85)	Polar	1958
		Echo	12	26(85)	Polar	1962
		(Venus)[a]	13	26(85)	Az-El	1962
		Mars	14	64(210)	Az-El	1966
Tidbinbilla	Australia	Weemala	42	26(85)	Polar	1965
		Ballima	43	64(210)	Az-El	1973
—	Australia	Honeysuckle Creek	44	26(85)	X-Y	1973
Madrid	Spain	Robledo	61	26(85)	Polar	1965
		Cebreros	62	26(85)	Polar	1967
		Robledo	63	64(210)	Az-El	1973

[a]A maintenance facility. Besides the 26-m (85-ft) diam Az-El mounted antenna, DSS 13 has a 9-m (30-ft) diam Az-El mounted antenna that is used for interstation time correlation using lunar reflection techniques, for testing the design of new equipment, and for support of ground-based radio science.

DSN Automatic Test Equipment Subsystem

C. M . Smith
DSN Systems Engineering Office

The Automatic Test Equipment Subsystem (ATE) described in this article is being implemented to provide the capability to adequately test existing and future modules to existing and future test criteria. The initial ATE will be implemented at the Deep Space Network (DSN) Maintenance Center (DMC), providing digital test capability for a cross section of DSN modules. A final ATE providing complete network support will be implemented at the DMC and all Complex Maintenance Facilities. This article presents a description of the ATE design and implementation.

I. Introduction

For quite some time, there has been an unmistakable trend toward the use of medium- and large-scale integrated circuits, hybrids, thick films, and other types of miniaturized large-scale arrays. Present test criteria and practices have become inadequate to cope with the complexity and miniaturization—not only in degree, but also in kind.

The increasing pin and function density of new printed circuit modules (brought about largely because of large-scale integration) requires a greatly increased size of test pattern, along with increasing speed. The test problems, described herein, reveal the need for a general-purpose Automatic Test Equipment Subsystem (ATE).

II. Implementation

A computerized test subsystem in response to the objectives of the DSN must be capable of change to meet the dynamic requirements described above and must also be compatible with present economic and practical constraints. A four-phase implementation plan has been developed:

(1) Phase I provides the DSN Maintenance Center (DMC) with a single automated digital test station and an automated test program generator station.

(2) Phase II provides each Complex Maintenance Facility (CMF) with an automated digital test station.

(3) Phase III provides the DMC with an automated analog test station.

(4) Phase IV provides each CMF with an automated analog test station.

The DSN will generate the functional and detailed technical requirements. The actual development will be done by a contractor.

III. Functional Description

The Deep Space Network Automatic Test Equipment Subsystem is composed of hardware, software, and maintenance personnel to provide on-line test and repair of DSN modules. The subsystem assembly functions and data flow are shown in Fig. 1. The ATE is totally modular in nature, and performs the following three main functions:

(1) Dynamic testing.

(2) Diagnostic testing.

(3) Fault finding.

A. Key Characteristics

The key characteristics of the ATE are as follows:

(1) Because of the present availability of a wide variety of programmable peripheral devices, 90% of ATE hardware will be commercial off-the-shelf equipment.

(2) The test software will be test-oriented, English-like programming language.

(3) 95% of all peripherals are programmable.

(4) Subsystem permits on-line generation and editing of test programs.

(5) Hard-copies of test results in a variety of formats.

(6) Comprehensive evaluation of test results to obtain diagnostic information.

B. Hardware

Analysis of the existing peripheral devices indicated that many problems associated with automatic test systems control (sequencing, timing, and housekeeping) are due mainly to standardization of these devices not having been realized. Other problems associated with programmable peripheral devices were identified, and it soon became evident that the workings of these devices had to be carefully examined and specified.

The basic requirements developed for the DSN ATE hardware are:

(1) The peripheral devices shall be capable of operating under computer control, and have a 32-bit word (serial and parallel) handling capability.

(2) The hardware interface between peripheral device and computer input/output (I/O) bus shall contain control logic which covers virtually every possible combination of logic required for all types of testing.

(3) The data switching employed shall allow subsystem stimulus and measurement devices to be applied to any pin or combination of pins on the unit under test. It shall be possible to simultaneously apply all such stimulus and measurement devices (whether analog or digital, or any combination thereof) to the unit under test.

(4) Although there is a large number of minicomputers available, a tradeoff analysis will be performed by the vendor, and at this time he will be aware of the DSN current and future requirements. Some of the basic requirements are as follows:

(a) Test program entry shall be via cassette tape.

(b) Controlled transfers shall be provided to and from up to 60 peripheral devices and on expandable priority interrupt system.

(c) Word size: 16 bit; memory: 64K bytes; mass storage: 5M bytes.

(d) Indirect addressing with up to N levels of nesting.

(e) Instructions to permit control of memory protection or lockout.

(f) Direct addressing of entire memory.

(g) Hardware-assisted environment switching.

(h) Automatic traps for detection of error conditions.

(i) Buffered input and output for communication with external devices; once initiated, such I/O may continue without requiring further action by the computer.

C. Test Software

The programming language must be oriented toward the unit under test (UUT), rather than toward the test subsystem itself (with which the programmer never addresses a device in the test subsystem, but only describes the test to be performed on the UUT). With such a language, the user works only with a total

subsystem. He neither knows nor cares that he has a programmable pulse generator from one manufacturer and a pulse analyzer from another. Since the DSN ATE will utilize a UUT-oriented language, the user need not have a detailed knowledge of the test subsystem. (The user need know only his own UUT.)

Some of the test language characteristics are as follows:

(1) One-to-one correspondence between statements of the test language and test functions.

(2) Statement formats may be fixed field. However, ease of use is a prime requirement.

(3) The test operator shall have the capability, via the operator's console, to define or alter test functions and parameters.

IV. Summary

Advances in technology have brought about the need and, subsequently, the existence of several commercially available general-purpose automatic test systems. The DSN need to look beyond current test problems has been realized, resulting in the implementation of the Automatic Test Equipment Subsystem described in this report.

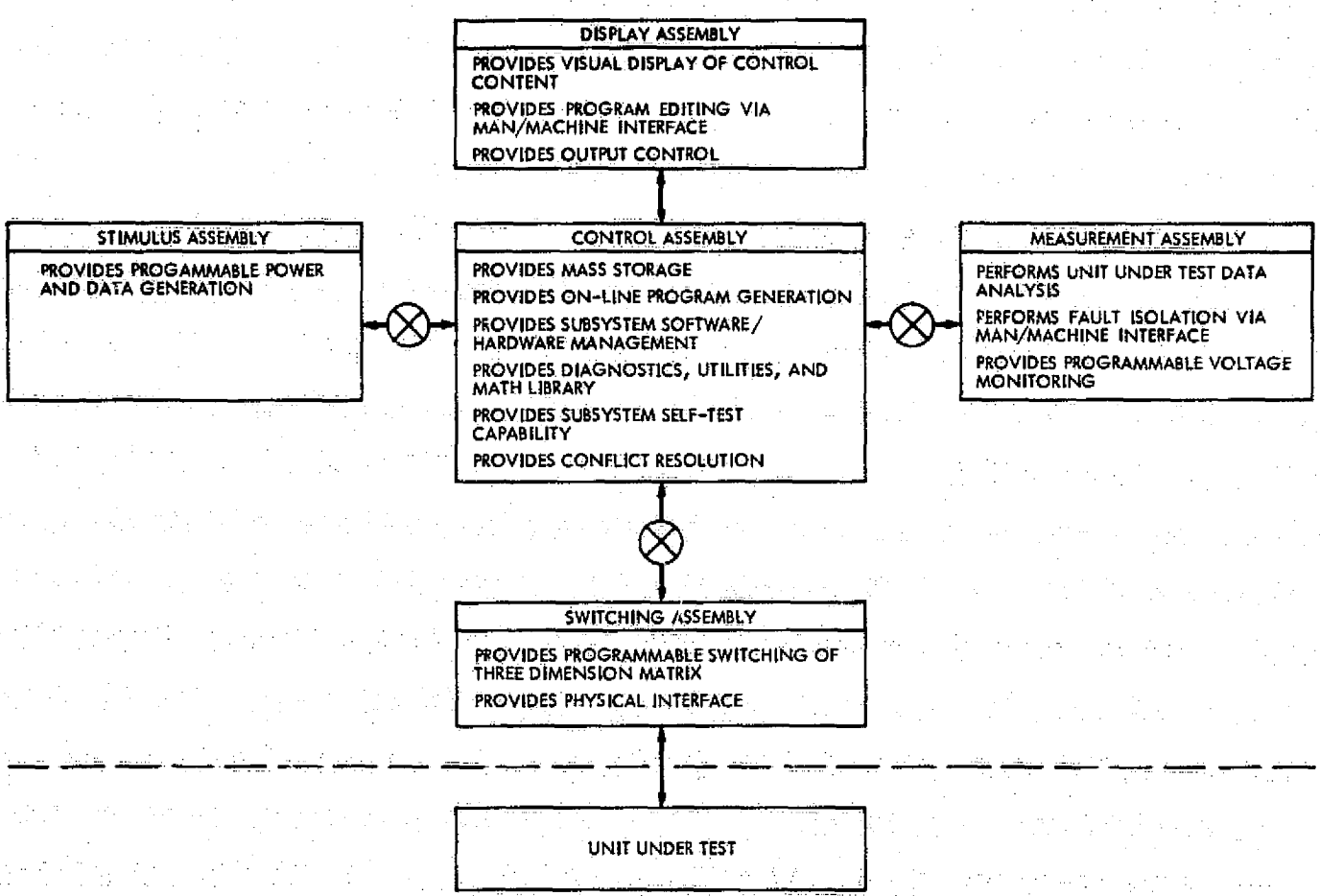

Fig. 1. Automatic Test Equipment Subsystem assembly functions and data flow

DSN Telemetry System—Network Control Telemetry Subsystem

E. C. Gatz and R. R. Wynn
DSN Systems Engineering Office

This article describes the real-time cathode ray tube displays which are now generated in the Network Operations Control Center. These displays are derived from received telemetry data and give a continuous update on the status of the DSN Telemetry System and the detailed parameters for any selected stream.

I. Introduction

A real-time monitoring capability has been implemented into the DSN Telemetry System to allow controllers and analysts to monitor the performance of telemetry receiving and processing equipment in the Deep Space Network. This real-time monitor is part of the Network Control Telemetry Subsystem and is implemented as part of the Network Control System Project.

The monitoring is performed by a MODCOMP II computer, located in the basement of Building 230 at JPL, Pasadena. This computer is connected via a Star Switch Controller to the Network Communications Processor. All telemetry high-speed data blocks are routed to the Telemetry Processor. The subsystem thus provides monitoring of all telemetry data sent from any Deep Space Station to the Mission Control Center via high-speed data lines. The MODCOMP II computer is equipped with 64K words of memory, two disk drives, two cathode ray tube (CRT)/keyboard terminals, and one keyboard character printer terminal. Additional CRT displays are slaved to the two CRT/keyboard units. The terminal and display equipment is located in the Network Operations Control Area for use by network controllers and analysts.

The processor can handle and display data from up to eight telemetry streams simultaneously. The presence of additional streams is indicated; the operator can select or delete the additional streams as desired. Two displays are generated: telemetry status and telemetry analysis. The content and format are described below. Data for these two formats are generated automatically and continuously. Either can be called up on any CRT device by the operator. The operator can make appropriate keyboard entries to control the displays. Each display is updated every 10 seconds.

II. Telemetry Status Display

The telemetry status display format is shown in Fig. 1. A line is devoted to each telemetry stream. Each stream is uniquely defined by the first five columns of the display:

DSS: Deep Space Station.

SC: Spacecraft number.

UDT: User data type number, identifies telemetry data and processor.

DDT: Data-dependent type number, identifies telemetry channel number and bit rate range.

GDD: Gross data descriptor, identifies data as real-time or playback from tape.

Up to eight lines are accommodated on the display. If more streams are present, the identifiers are displayed in turn on the tenth line with the indicator OTHERS. If the operator is interested in one of these, he can delete a currently displayed stream to make room for it.

For each stream displayed, the general status is displayed in the next three columns:

SYNC: Status of frame sync. This is the result of processing to assure the quality of the data stream by verifying the frame sync. This indicator has four states:

(1) Slash (/) indicates successful sync is achieved and maintained.

(2) Asterisk (*) indicates failure to sync.

(3) Blank indicates no data have yet been received.

(4) Zero (0) indicates that the frame sync algorithm is not active, either because it has been deleted by the operator or because data have stopped.

COUNT: This is the count of frames that have been received since sync was most recently acquired. When frame sync is lost, the count remains unchanged; when sync is reacquired, the count is restarted at zero. The size of the count, therefore, indicates to the operator the general stability and quality of the data stream.

ALARM: The alarm field has five possible values:

(1) Slash (/) indicates there are no time tag errors or data outages for the indicated stream

(2) TIME ERR indicates that the difference between the time tags on consecutive data blocks is not within 2% of the expected interval and cannot be explained by the block sequence numbers. The flag indicates a faulty time tag and is maintained for at least one display update (10 seconds).

(3) MISG DATA indicates that some data (at least one block) were missed. If the data are no longer being received for this stream, the alarm will persist. If, however, there is merely a gap, as indicated by block sequence numbers and time tags, the alarm will be removed when the data resume.

(4) DELETED indicates that the row has been deleted by operator input. This alarm persists until the row is released or reassigned by a subsequent operator input.

(5) OTHERS appears in row 10 only and indicates that one and possibly several streams of data are being received but not processed if the DSS through GDD fields are filled. If they are blank, no other streams are being received.

III. Telemetry Analysis Display

The telemetry analysis display format is shown in Fig. 2. This display contains data related to a single stream. Any of the streams on the status display can be selected. The data are derived or extracted from the high-speed data blocks. The fields are described as follows:

(1) DDD:HH:MM:SS (FMT): The time (GMT) the display was formatted.

(2) DDD:HH:MM:SS: (DATA): The time (GMT) of the block from which the data below are determined.

(3) DSS through GDD: The stream identifiers defined in the status display.

(4) FSIZE: The frame size in bits.

(5) TIME TAG ERROR: The time tag error count, i.e., the number of time tag errors that have occurred since the stream was assigned. This can be reset to zero by operator input.

(6) PN ERR: Pseudonoise (PN) frame sync errors allowed indicate the number of bit errors allowed for sync acquisition and maintenance.

(7) FR SYNC: Indicates the state of the frame sync process.

(a) Slash (/) indicates in sync.

(b) Asterisk (*) indicates out of sync.

(c) Zero indicates that the processor is not attempting to sync on the data (see the telemetry status format description).

(d) Blank indicates that not enough data have been received to make any sync determination.

(8) FR COUNT: The number of frames since sync was last acquired.

(9) RX: The receiver number and status (slash is in lock, asterisk is out of lock).

(10) SDA: The Subcarrier Demodulator Assembly (SDA) is similar to the receiver indication.

(11) SSA: The Symbol Synchronizer Assembly (SSA) fields may be a number and lock status, NA if not applicable or double asterisk (**) if an invalid number is received.

(12) BDA: The Block Decoder Assembly (BDA) is OFF, or ON with status (slash or asterisk for in or out of lock).

(13) DDA: The Data Decoder Assembly (DDA) is similar to the SSA.

(14) BIT SYNC: Bit sync is OFF or INT with lock status.

(15) TCP: The number of the Telemetry Command Processor (TCP) in use as 1, 2, or 3 or asterisk (*) if an invalid number is received.

(16) AGC and SNR: Both the Automatic Gain Control (ACG) and Signal-to-Noise Ratio (SNR) are extracted directly from the data block and displayed in decimal format. The AGC has a negative sign and the SNR can have either a positive or negative sign.

(17) BITRATE: The bit rate is deduced from the DDT and S/C.

Fields 18-20 relate to data extracted from the telemetry frame. The selection is made by operator input.

(18) DN LOC: The data number location (DN LOC) is the location in bits from the start of the sync code to the beginning of the extracted data.

(19) DN LGTH: The length in bits of the extracted data. Up to 33 bits may be selected.

(20) DN: The data number in octal representation of the extracted data.

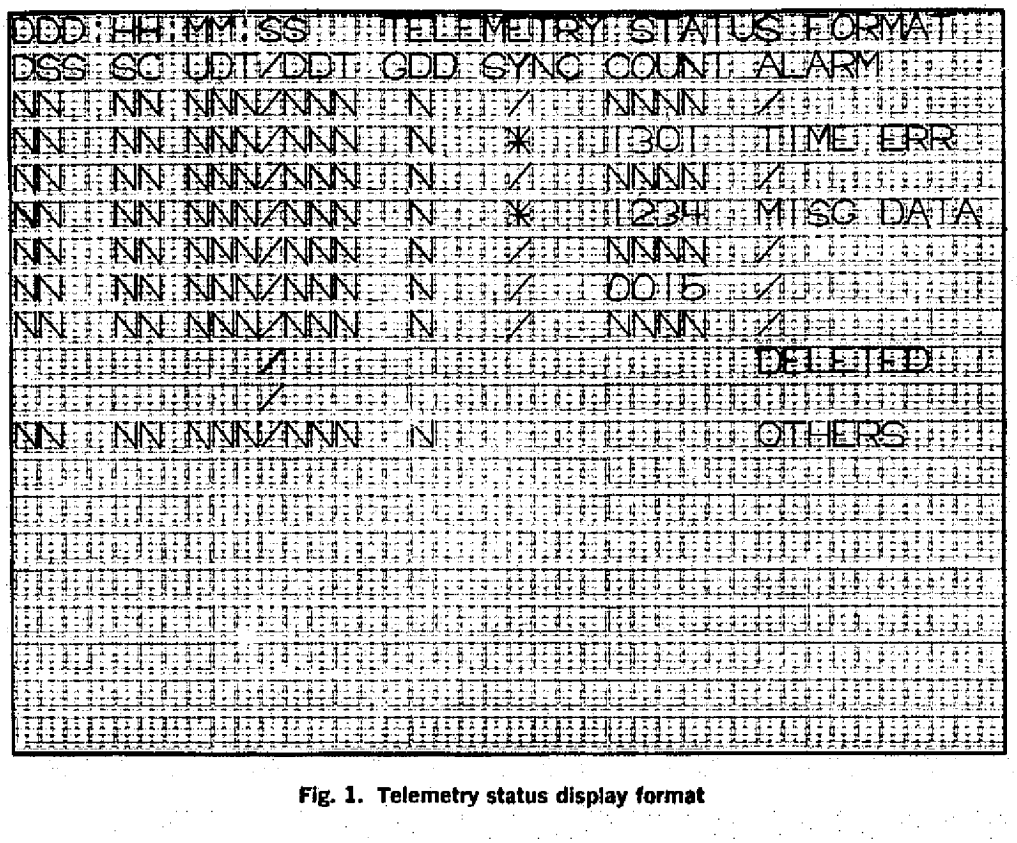

Fig. 1. Telemetry status display format

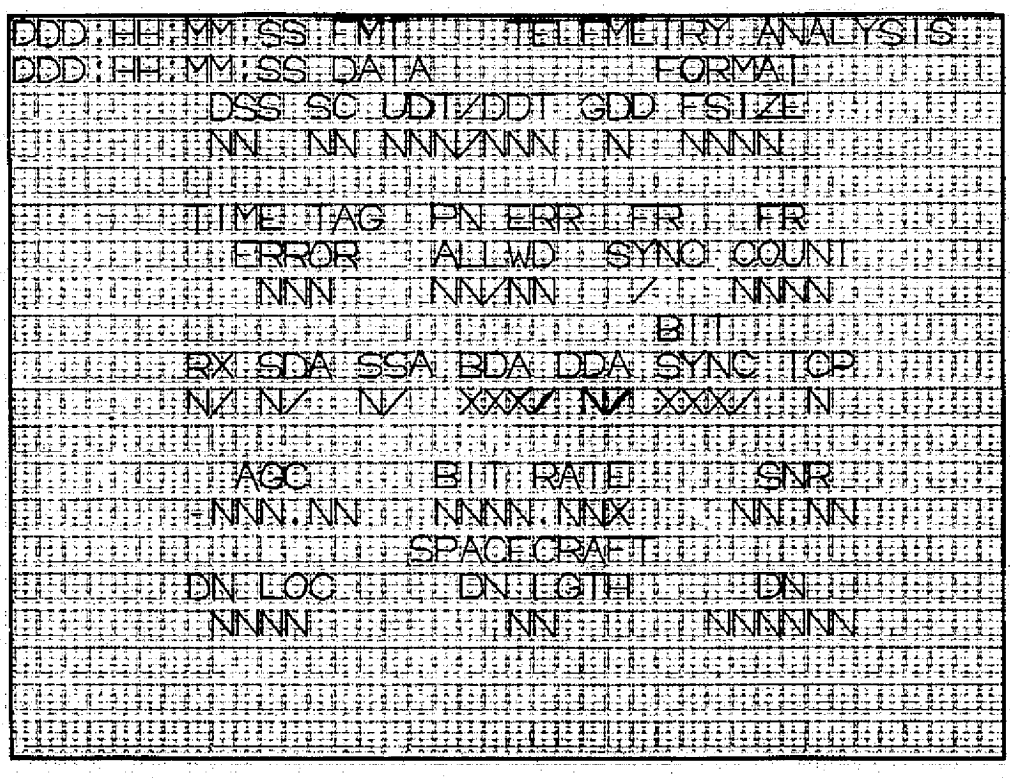

Fig. 2. Telemetry analysis display format

DSN Wideband Data Subsystem

C. K. Stein
DSN Systems Engineering

This article describes the Wideband Data Subsystem (WBS) of the Ground Communications Facility (GCF), which greatly increased the data yield and provided near-real-time video pictures during the Mariner 10 flyby of the planets Venus and Mercury.

I. Introduction

A. General

When Columbus discovered America, Queen Isabella had to await his return to learn where he had gone and what he had found. Even though our spaceships travel far greater distances than did Columbus' ships, we can almost instantaneously obtain the kind of information from them that Isabella had to wait months for. The current state of the art of deep space exploration does not provide for the return of an exploratory vehicle; therefore, we must depend upon communication with it to obtain its scientific and engineering data.

The purpose of this article is to review the Deep Space Network (DSN) Wideband Data Subsystem (WBS) of the Ground Communication Facility (GCF) that enabled us to greatly increase the data yield and provide near-real-time video (TV) pictures during the Mariner 10 flyby of the planets Venus and Mercury. Although much information was gained by the video pictures from the cloud-shrouded Venus, the spectacular video mapping of the planet Mercury was made possible by the increased data rate. TV pictures of the Mercury encounter were displayed on a large screen in near-real-time at both JPL and NASA Headquarters in Washington, D. C.

B. Deep Space Network Description

To discuss the wideband data link we must first understand how it fits into the total picture of tracking and data acquisition. The tracking and data acquisition system for communicating with spacecraft beyond the moon (Earth to the moon is referred to as near-space) is the DSN. The DSN communicates with spacecraft from Deep Space Station (DSS) locations on Earth approximately 120 deg apart in longitude, two in north and one in south latitudes. These complexes are located near Madrid, Spain, Canberra, Australia, and Goldstone, California. The general DSN configuration is shown in Fig. 1.

The Network presently consists of one 64-meter antenna subnet and two 26-meter antenna subnets. Each subnet includes three antennas, one at each location. These installations are known as Deep Space Stations. The spacecraft data are transmitted and received via the antennas at the DSSs and processed and sent via

telecommunication systems to JPL in Pasadena for processing and dissemination as specified by the mission plans. The facilities at JPL provide necessary data to the DSSs for tracking and commanding the spacecraft by the reverse procedure.

C. Ground Communications Facility

Communications between JPL and the DSSs is accomplished through the GCF. The 1973–1974 routing of the interconnecting GCF network is shown in Fig. 2. The total communications system consists of combinations of series and parallel routings using communication satellites, microwaves, landlines, underwater (submarine) cables and radio for redundancy and reliability. NASA Communications (NASCOM) leases the long-line links and data sets and provides switching at Goddard Space Flight Center (GSFC) Greenbelt, Maryland, and other locations as noted in Fig. 2.

II. Wideband Data Subsystem

A. General

The Wideband Data Subsystem is primarily implemented in the 64-meter (210-ft) antenna subnet. Figure 3 is a simplified block diagram of this subsystem. It includes lines to the Compatibility Test Area at JPL (CTA 21) and the Spacecraft Compatibility/Monitor Station at Merritt Island (STDN MIL). These were included on the block diagram because of their use in testing the WBS with the spacecraft and will not be discussed further. NASCOM GSFC is the NASA switching center at the Goddard Space Flight Center in Greenbelt, Maryland, and FDX indicates full duplex system (also denoted by double-arrowed lines).

The key design characteristics of the DSN GCF Wideband Subsystem are:

(1) Permanent terminal equipment with circuits activated only when wideband data rates are needed, thus reducing lease costs.

(2) Transmission rates of 28.5 and 50 kilobits per second (kbps) with bit error rates of 5×10^{-5} or better.

(3) Standard 1200/2400-bit block format with better than 97% of all blocks delivered error-free in real time.

(4) Transmission error detection for all DSS circuits but no error correction.

(5) Rapid semi-automatic recall.

(6) Full demultiplexing at DSS and Central Communications Terminal to provide only requested data to each user.

(7) Provision of subsystem real-time status to GCF Monitor and Control Subsystem (manual during Mariner Venus/Mercury 1973).

(8) Project remote terminal equipment not supplied by GCF.

(9) Nonstandard (open) formats may be used on project circuits, but such circuits are not automatically monitored nor will errors be detected by GCF.

(10) 33-bit error polynomial provides positive error detection.

(11) Block synchronous data transmission.

(12) Receive timing provided continuously.

Although it is used primarily for the 64-meter subnet, the WBS can support one 26-meter antenna station at Australia and one 26-meter antenna station at Spain because of a design commonality. Permanent wideband terminal equipment is installed at Australia and Spain, but the circuits are activated only when required to support a mission and its associated testing. There is permanent wideband interconnection from JPL to Goldstone via a leased microwave link. This basic capability operates at 28.5 kbps. It will be upgraded to 50 kbps to support the Viking program in the 1976–1977 era. Redundant 230-kbps microwave super group circuits were installed to DSS 14 only to accommodate the Mariner 10 Venus and Mercury encounters, enabling the spacecraft to transmit data at 117.6 kbps during the critical encounter time periods. A TV circuit was leased to transmit the near-real-time video picture of the Mercury encounter from JPL, Pasadena, to NASA Headquarters in Washington, D.C.

Additionally, two 230-kbps super group wideband circuits will be permanently activated from the JPL Central Communication Terminal to the Network Operations Control Center. Currently, 50-kbps wideband circuits are being used.

As a result of the expansion of the WBS a coded multiplexer/demultiplexer (CMD) assembly is used to accomplish the equivalent functions of a block detection decoder and block demultiplexer. This device is smaller and less costly than the previously used individual units (4) and can operate at the rate of 250 kbps and higher, accommodating block lengths of 1200, 2400 and 4800 bits.

Figure 4 provides a more detailed diagram of the Wideband Subsystem being used during the Mariner 10

mission. Redundant lines and/or switches are provided as required to assure that the data can be received in real time.

B. 28.5-kbps Wideband Capability

The basic wideband data capability for the operation of the Deep Space Network during MVM'73 is 28.5 kbps. All equipment is permanently installed in the network. The Goldstone–JPL microwave link and the hard-wired circuits to the Compatibility Test Area (CTA 21) at JPL are permanently maintained. The circuits between the overseas stations and JPL are activated as required a sufficient time prior to the mission for the support of testing and are maintained throughout the mission. The WBS utilizes the present standard DSN 1200 bit-blocked data while the Mariner 10 project support data transmissions utilize a non-blocked word-formatted data transmission mode. For wideband terminal equipment configurations refer to Figs. 5–7.

C. 50-kbps Wideband Capability

The 50-kbps wideband data rate is a requirement for future deep space missions. Initially, it is planned for support of the Viking program during orbit and lander operations in 1976 and for the Mariner Jupiter/Saturn mission commencing in 1977 at the overseas stations only, since Goldstone GCF super group will be operating at 230 kbps for Mariner Jupiter/Saturn.

During 1971, a lengthy wideband data test was conducted between JPL and the NASCOM Madrid Switching Center in Spain. The purpose of this test was to determine if the error rates of a circuit are generally comparable to those which were expected for the 28.5-kbps circuits planned for Mariner 10 support and to determine the statistical distribution of the errors. The test was successful and the data satisfied both purposes.

The configuration of the circuit used during this test is shown in Fig. 8. A circuit (GW-58619) was provided by NASCOM and consisted of 303 C data sets operating at 50 kbps. The routing of this American Telephone and Telegraph circuit was not known nor were the facilities from which it was derived. The 303 C data set required substantially all of the 48-kHz passband; hence a group bandwidth was used. The routing overseas was via communication satellite as shown in Fig. 8.

Test data consisted of 2047-bit pseudorandom bit pattern generated by Fredrich Electronic Company Model 600 test sets. At each receive location the pseudorandom pattern was also synchronized and compared against the test sets. The tests indicated that the bit error rate may be expected to be 6×10^{-5} or better measured on a long-term basis.

D. 230-kbps Wideband Subsystem, Mariner 10

The GCF 230-kbps wideband capability during the Mariner 10 project consists of one full duplex super group transmission path from DSS 14 (64-meter station at Goldstone) to the JPL Central Communication Terminal (CCT), then to the project computer interface. This wideband channel supported the real-time transmission of the Mariner 10, 117.6-kbps, high-rate telemetry data. The telemetry data were transmitted in a non-blocked, word-formatted mode and no specific GCF monitoring was provided. The GCF wideband super group capability was provided over existing 8-MHz radio channels of the DSS to the complex switching center (GCF 10), then via a 230-kHz super group wideband channel between Goldstone and JPL over Western Union leased microwave equipment. This capability was provided from July 1973 through April 1974 for the Venus and Mercury encounters and during August and September 1974 for the second Mercury encounter. Figures 9–11 illustrate this configuration from the incoming kbps signal through:

(1) Project symbol synchronizer assembly (SSA) word formatter switch.

(2) Project word formatter/deformatter.

(3) Wideband digital patch panel.

(4) General Electric TDM-522 data set MODEM (digital-to-analog converter and data regenerator).

(5) Wideband audio patch panels at DSS.

(6) Wideband analog patch panel (Goldstone Comm Terminal).

(7) General Electric TDM-501 data set.

(8) General Electric TDM-520 data MODEM.

(9) Western Union leased full duplex microwave between Goldstone and JPL.

(10) General Electric TDM-520 data MODEM.

(11) General Electric TDM-501 data set.

(12) DC patch panel.

(13) Patch panels and cables.

(14) Project word formatter/deformatter.

The GCF 230-kbps system experienced almost no technical or installation problems and performance exceeded all expectations. The bit error rate was equal to 1×10^{-5} or better for a 99% throughput during the Venus and Mercury encounters.

E. Network Operations Control Center Wideband Data Link

The Network Operations Control Center (NOCC) is being implemented in three stages. All configurations include a wideband data link from the JPL Central Communications Terminal (CCT) to the data processing equipment in the Network Data Processing Area. These locations are in different buildings approximately 600 meters apart. Figure 12 is a block diagram of the 50-kbps wideband system presently in operation. The system will be upgraded to a 230-kbps super group during the 1975–1976 time period.

The NOCC receives data by tying into the prime line between the DSSs and the project processing equipment. Two PDP-8 computers are located in the Network Data Processing Terminal adjacent to the GCF Communications Terminal at JPL. One of the PDP-8's is prime. Inbound data undergo serial-to-byte transformation in an external receive communications buffer. High-speed and wideband data are routed to the receive communications buffer and then buffered in the PDP-8 to await multiplexing onto the 50-kbps wideband circuit. Filler blocks are rejected rather than multiplexed. After multiplexing, the high-speed and/or wideband blocks are placed in a second buffer to be clocked out to the wideband data line to the Network Data Processing Area (NDPA). External to the PDP-8, byte-to-serial conversion occurs and, as required by the wideband data lines, a voltage-to-current conversion occurs. Multiple high-speed data lines are thus buffered onto a synchronous circuit. To accommodate this operation, the PDP-8 generates a control message for the NDPA computer (Xerox Sigma-5) which precedes each high-speed block multiplexed onto the wideband line. Outbound data are routed essentially the reverse of inbound.

The detailed block diagrams of both the Block I NDPT configuration and the Block I NDPA configuration are shown in Figs. 13 and 14, respectively. The PDP-8 and the Sigma-5 are interconnected by General Electric 401 data sets at either end of the wideband data lines.

III. Conclusions

The GCF Wideband Data Subsystem used in the Deep Space Network is unique in that it is wholly dedicated to transmitting data received by a ground antenna from a spacecraft and providing these data to the processing computers at JPL in real-time with very high reliability. Terminals are provided as permanent installations and lines to overseas stations are leased when required to support specific missions. A variety of data sets, modems, converters, switches, switching centers, test equipment, jack panels and ancillary equipment are provided. A follow-up paper would be useful to describe this equipment in detail, including inputs, outputs, functions and theory of operations; however, these details are not a part of this report.

Even though the Wideband Data Subsystem is unique in that it is fully committed to the DSN, it is similar to commercial systems in that the blocks are formatted and addressed so that each block or series of blocks has an originating location and destination. The theory is compatible with the commercial packet packaging concept if one considers that data can be directed to various locations.

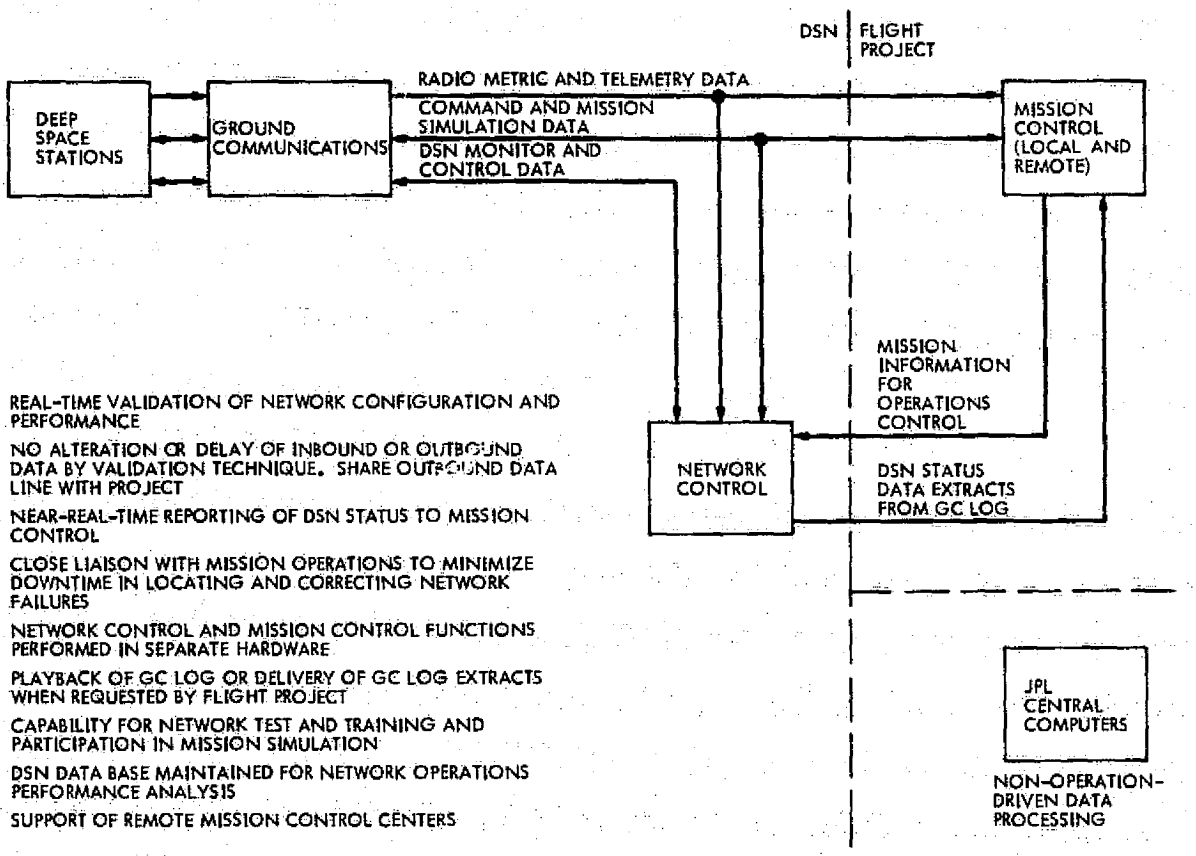

Fig. 1. General configuration of the Deep Space Network

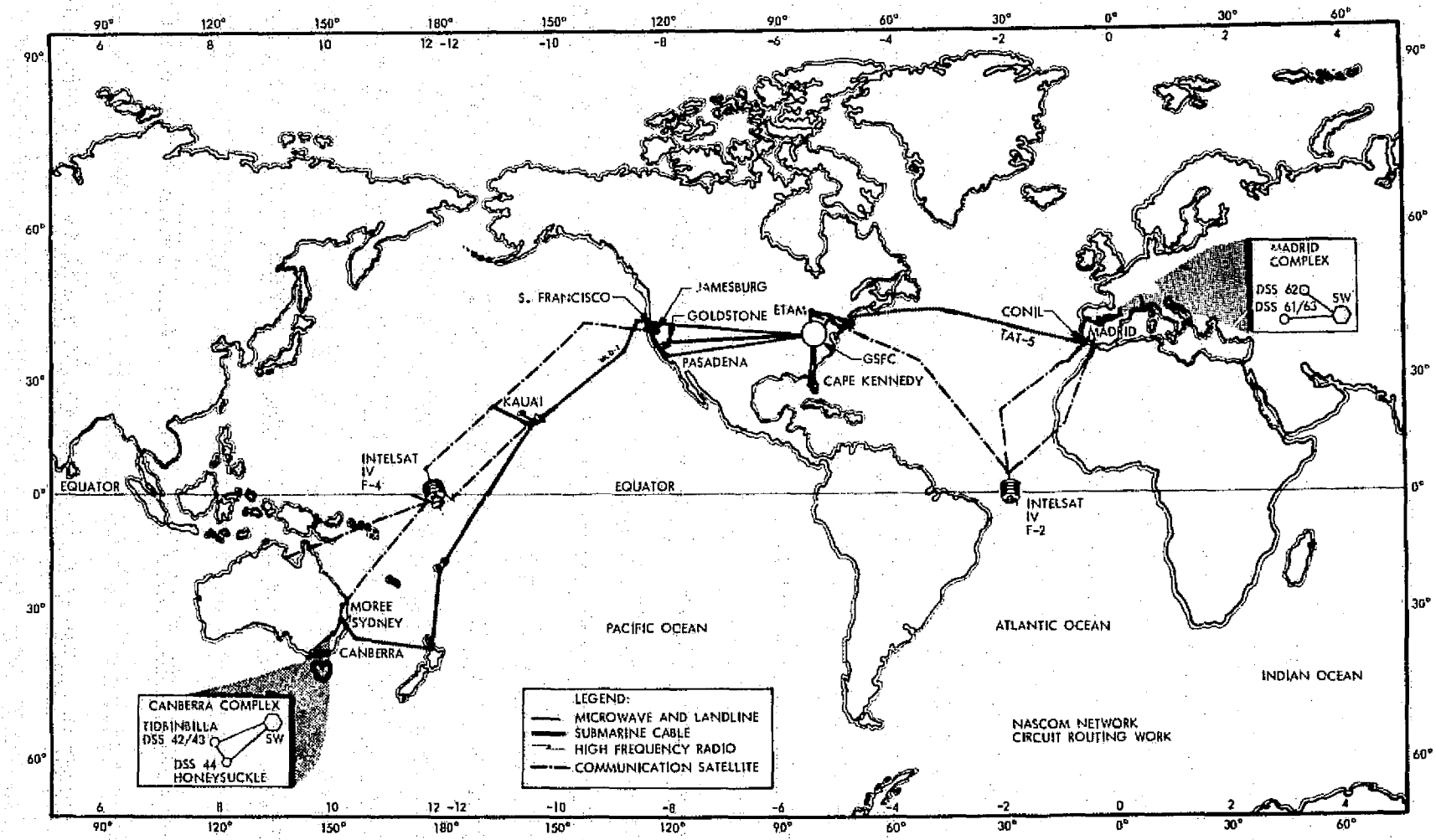

Fig. 2. NASCOM network circuit routing chart

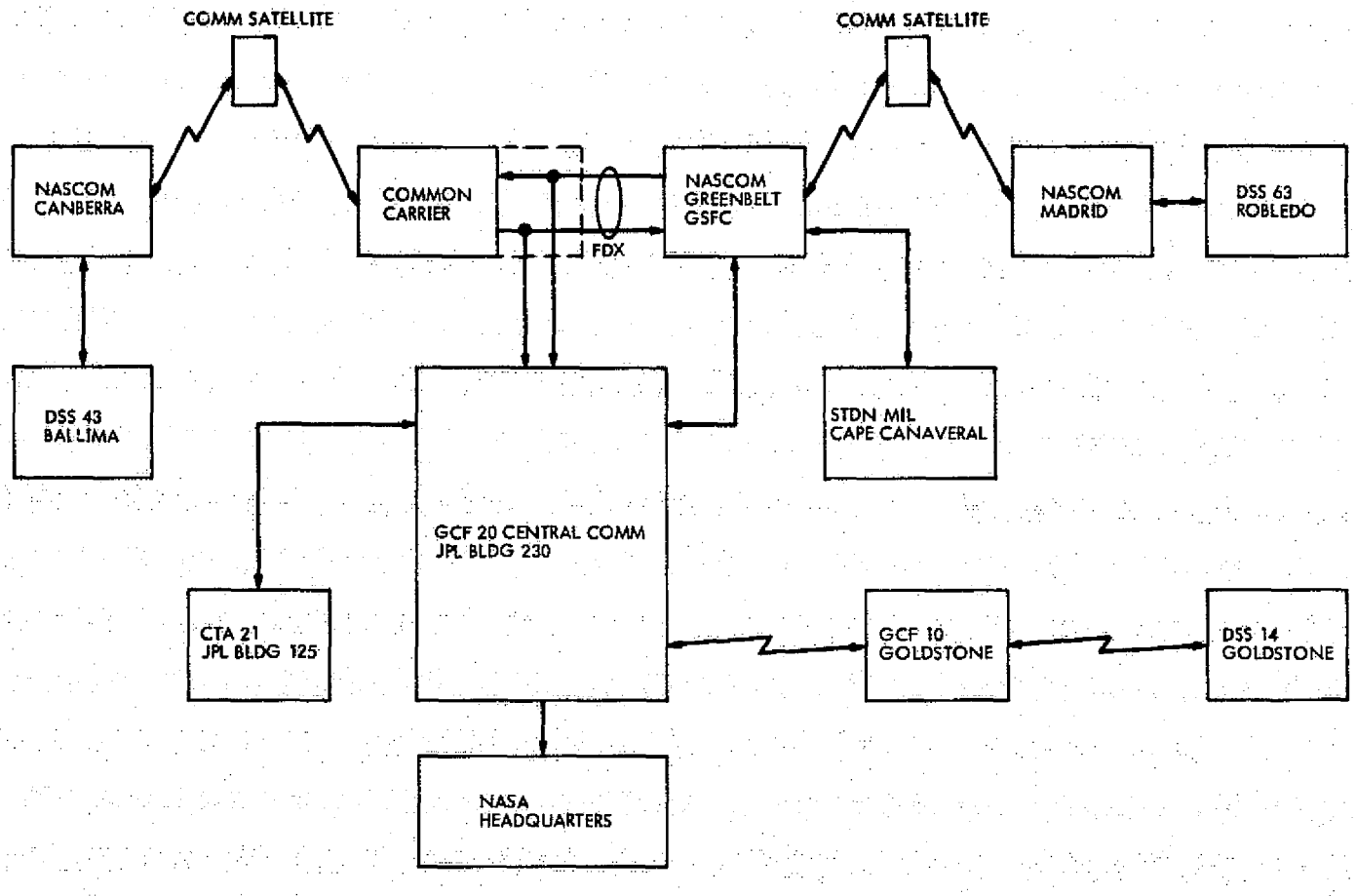

Fig. 3. Wideband Data Subsystem block diagram

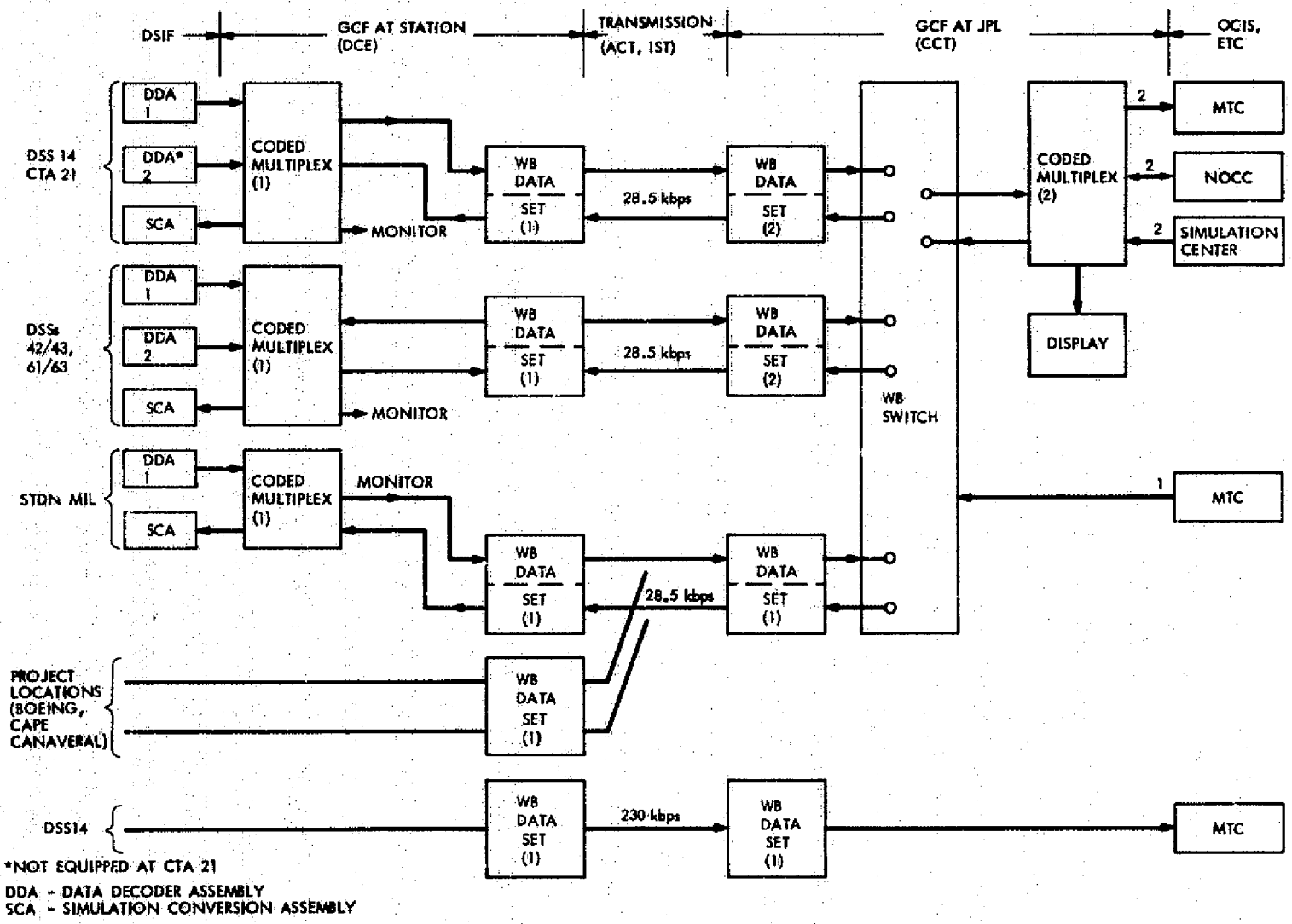

Fig. 4. GCF 1973–1974 wideband data capability

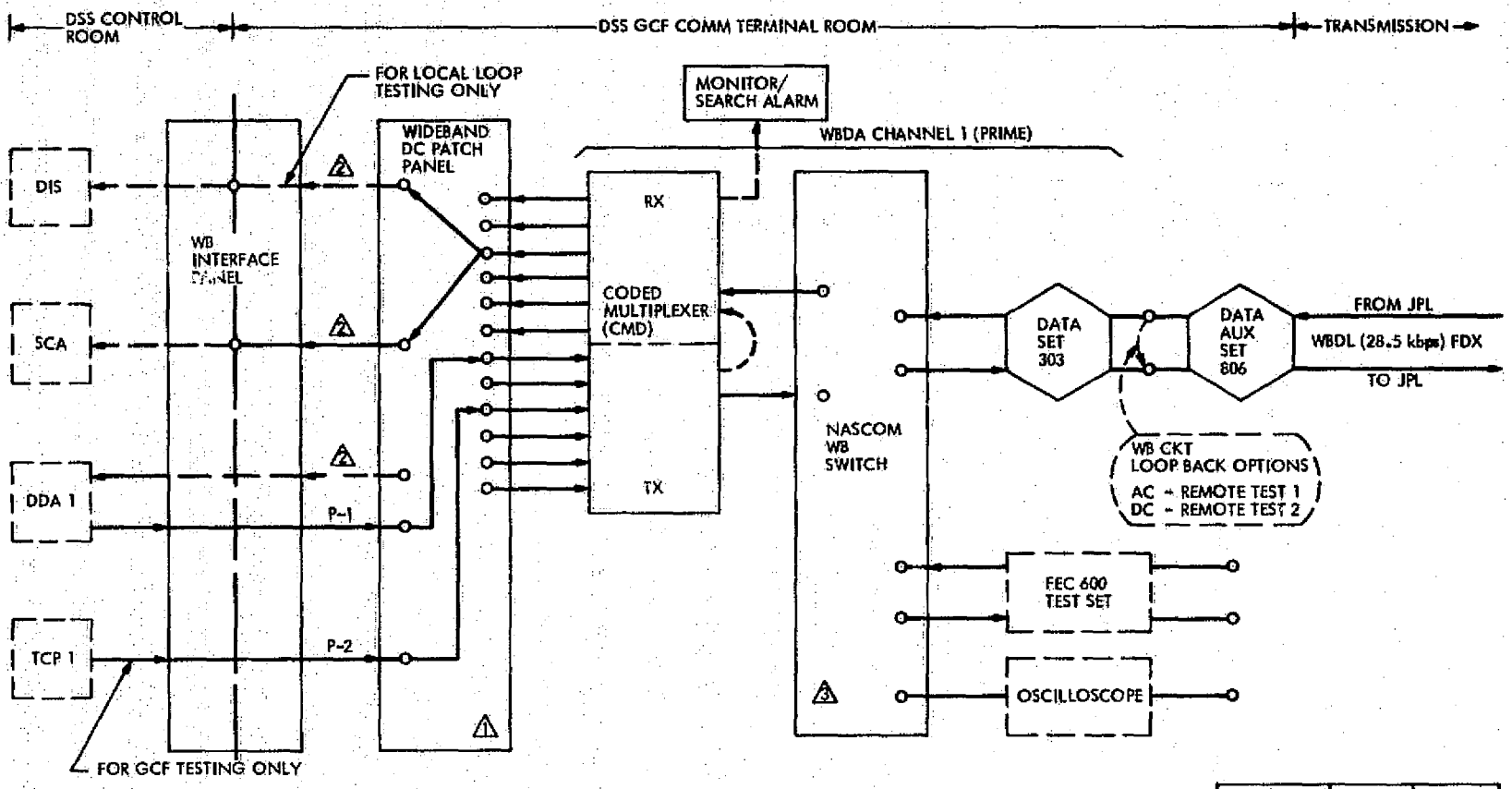

NOTES:

1. STDN MIL AND CTA 21 NOT CONFIGURED WITH CODED MULTIPLEXER SWITCH AND BACKUP WIDEBAND CHANNEL, AND HAVE ONLY ONE DDA WB INTERFACE
2. DIS AND DDA COMPUTER RECEIVE INTERFACES AT DSSs USED IN TEST SUPPORT AND DATA VALIDATION ONLY
3. CTA 21 NOT CONFIGURED WITH NASCOM WB SWITCH

WB EQUIP	DSS 71	CTA 21
DATA SETS (303)	1	1
NASCOM WB SW	1	0
CMDs	1	1

Fig. 5. STDN MIL and CTA 21 GCF (28.5 kbps) Wideband Data Subsystem assembly configuration

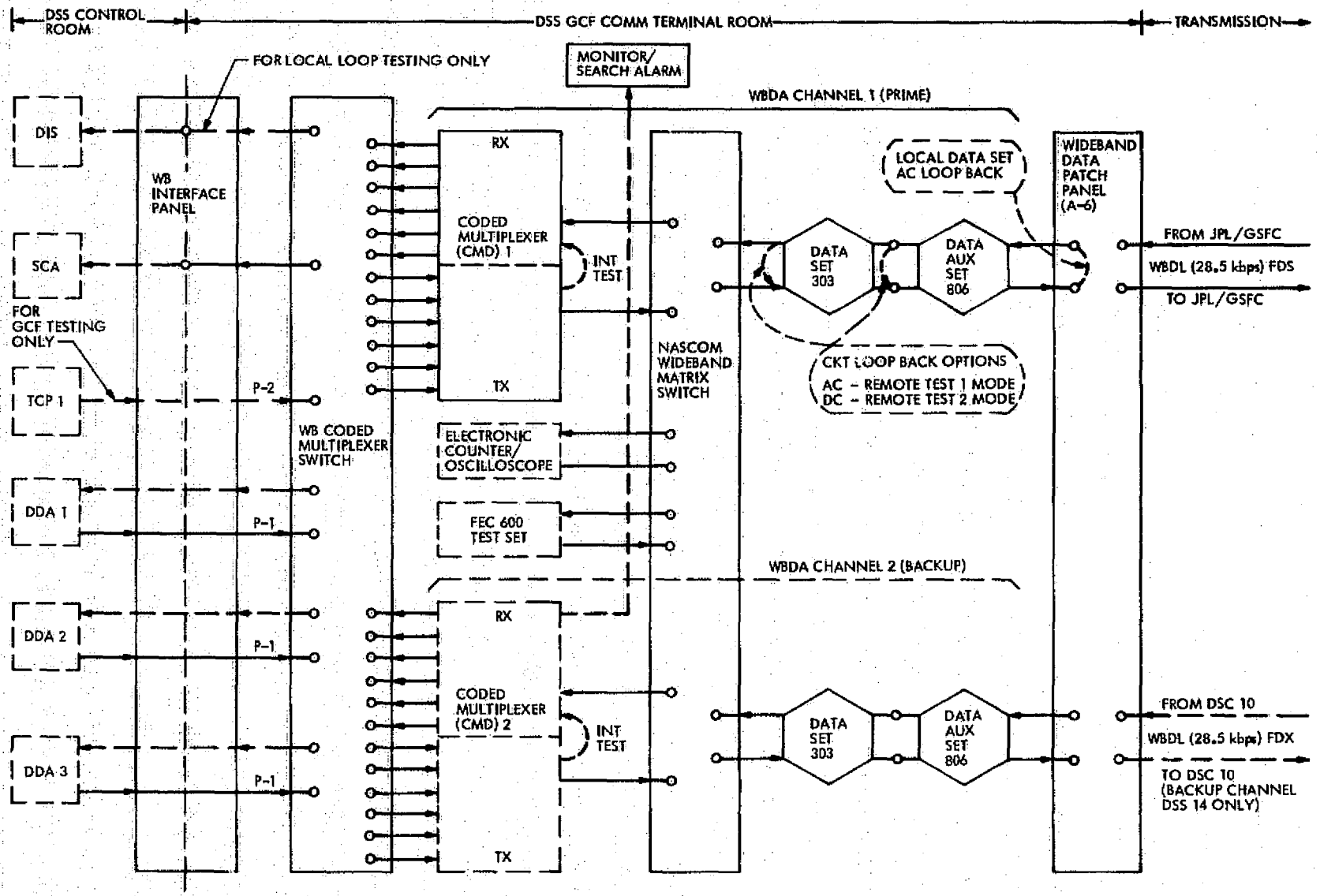

Fig. 6. Deep Space Stations 14/43/63 GCF (28.5 kbps) Wideband Data Subsystem assembly configuration

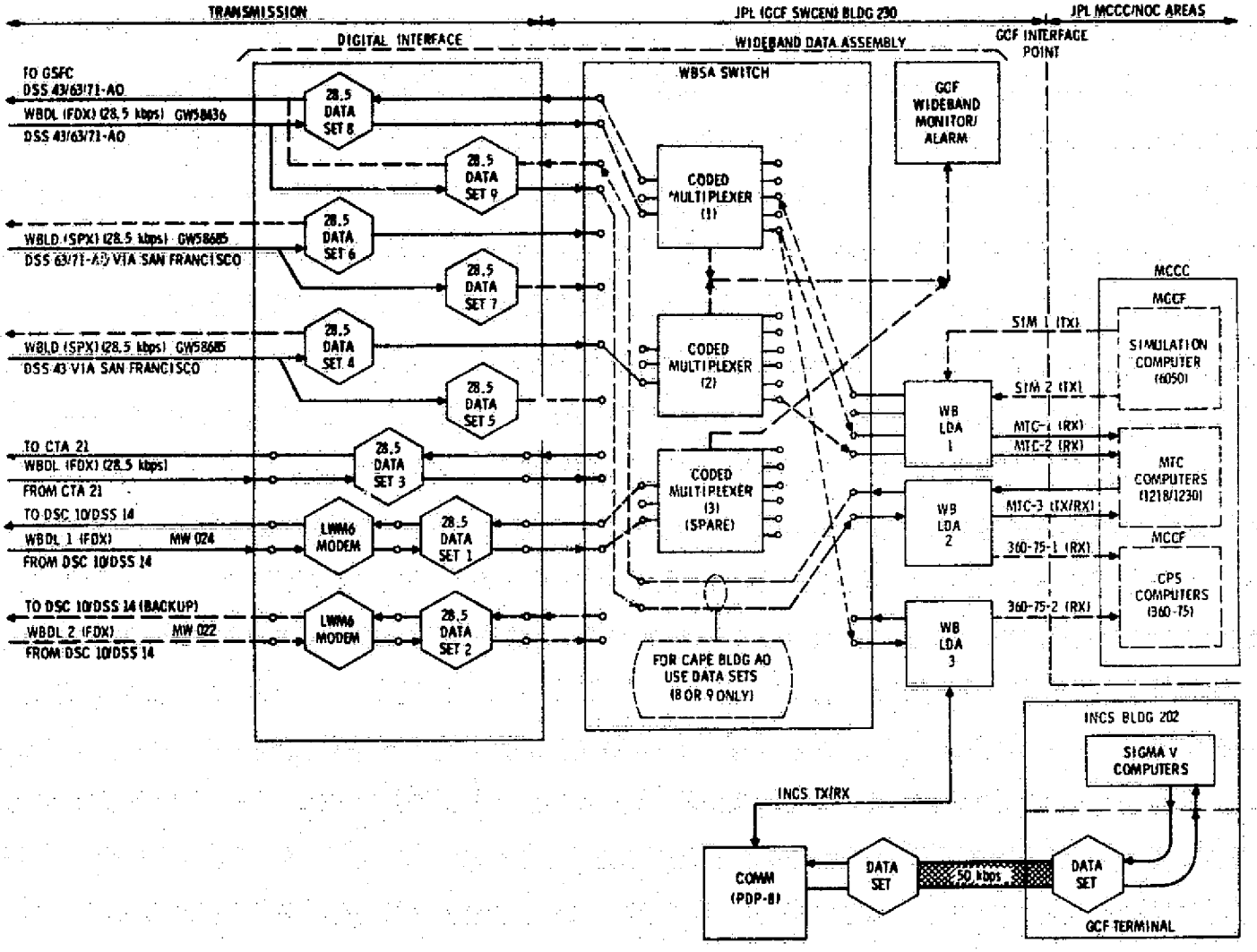

Fig. 7. JPL (GCF SWCEN) (28.5 kbps) Wideband Data Subsystem assembly, MVM'73 configuration

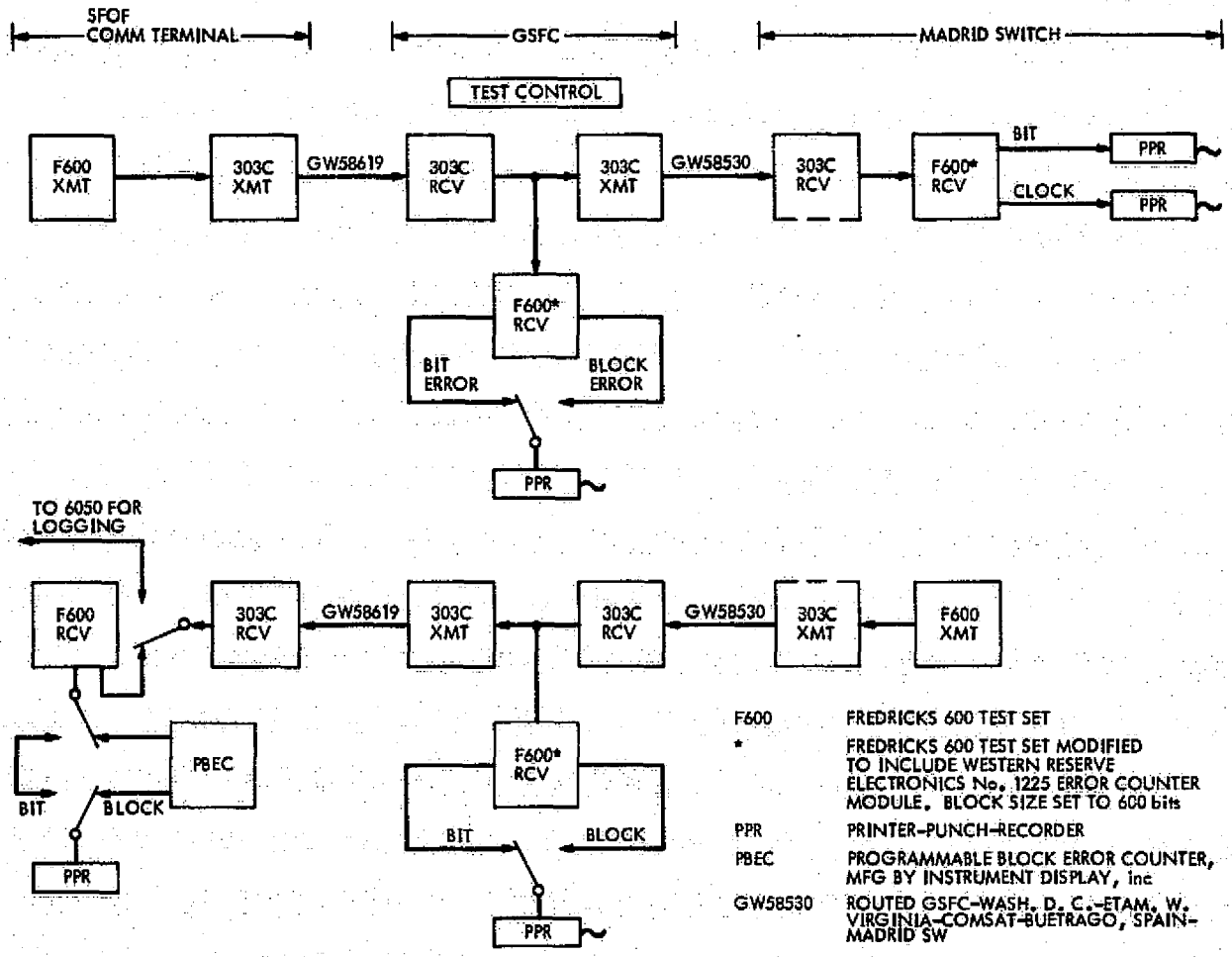

Fig. 8. Wideband Data Subsystem 50-kbps test configuration, June 1971

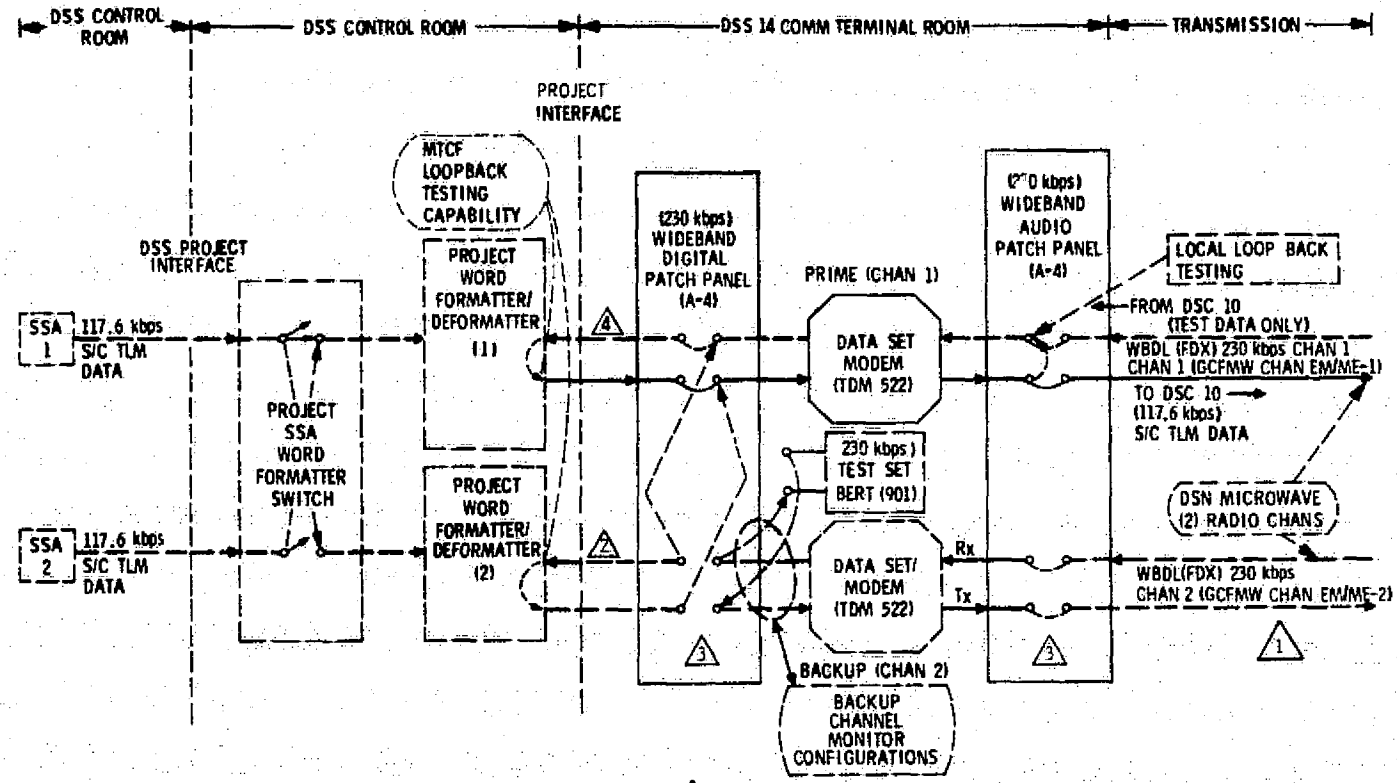

Fig. 9. DSS 14 GCF (230 kbps) Wideband Data Subsystem assembly configuration

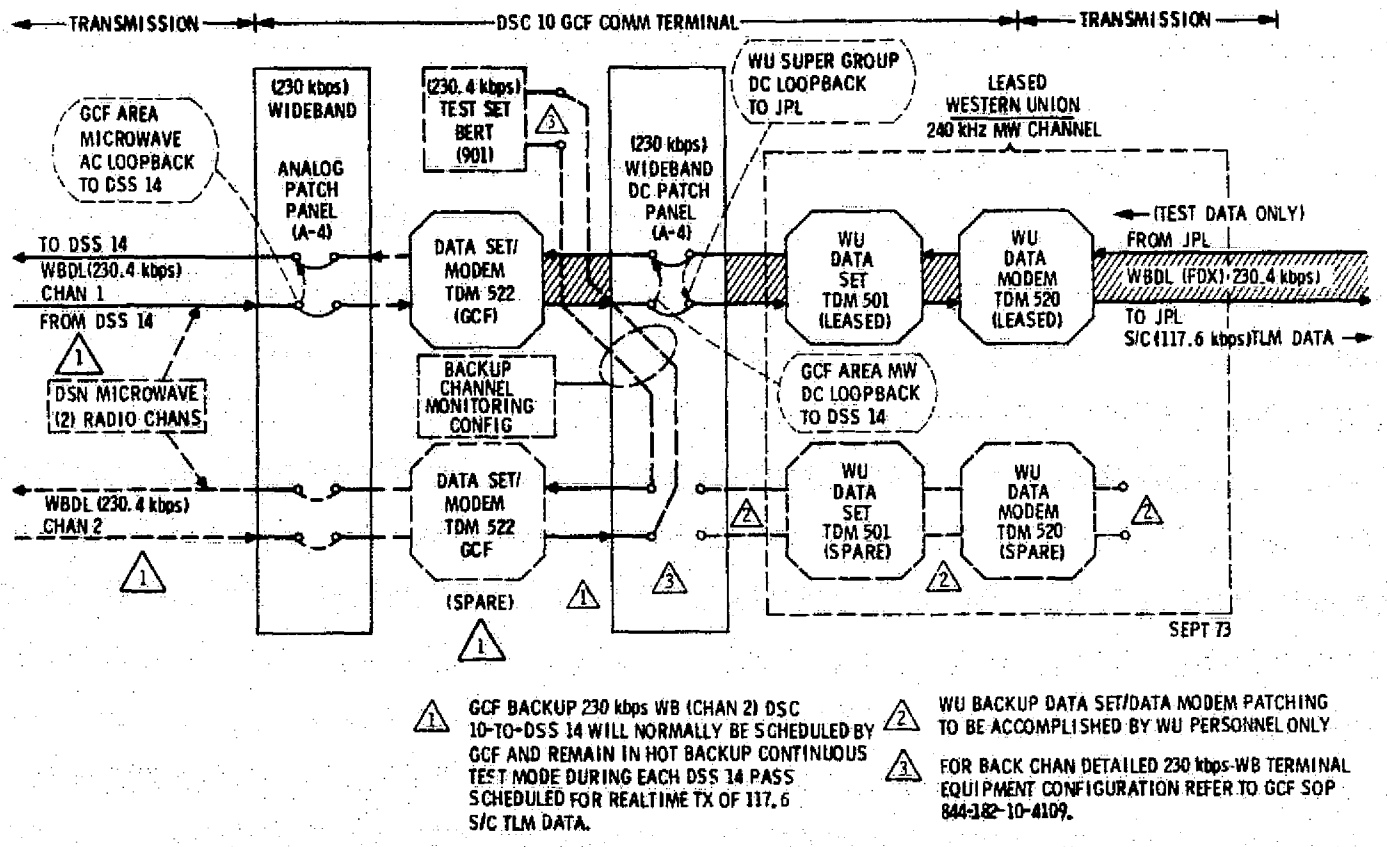

1. GCF BACKUP 230 kbps WB (CHAN 2) DSC 10-TO-DSS 14 WILL NORMALLY BE SCHEDULED BY GCF AND REMAIN IN HOT BACKUP CONTINUOUS TEST MODE DURING EACH DSS 14 PASS SCHEDULED FOR REALTIME TX OF 117.6 S/C TLM DATA.
2. WU BACKUP DATA SET/DATA MODEM PATCHING TO BE ACCOMPLISHED BY WU PERSONNEL ONLY
3. FOR BACK CHAN DETAILED 230 kbps-WB TERMINAL EQUIPMENT CONFIGURATION REFER TO GCF SOP 844-182-10-4109.

Fig. 10. DSS 10 communications terminal GCF (230 kbps) Wideband Data Subsystem assembly configuration

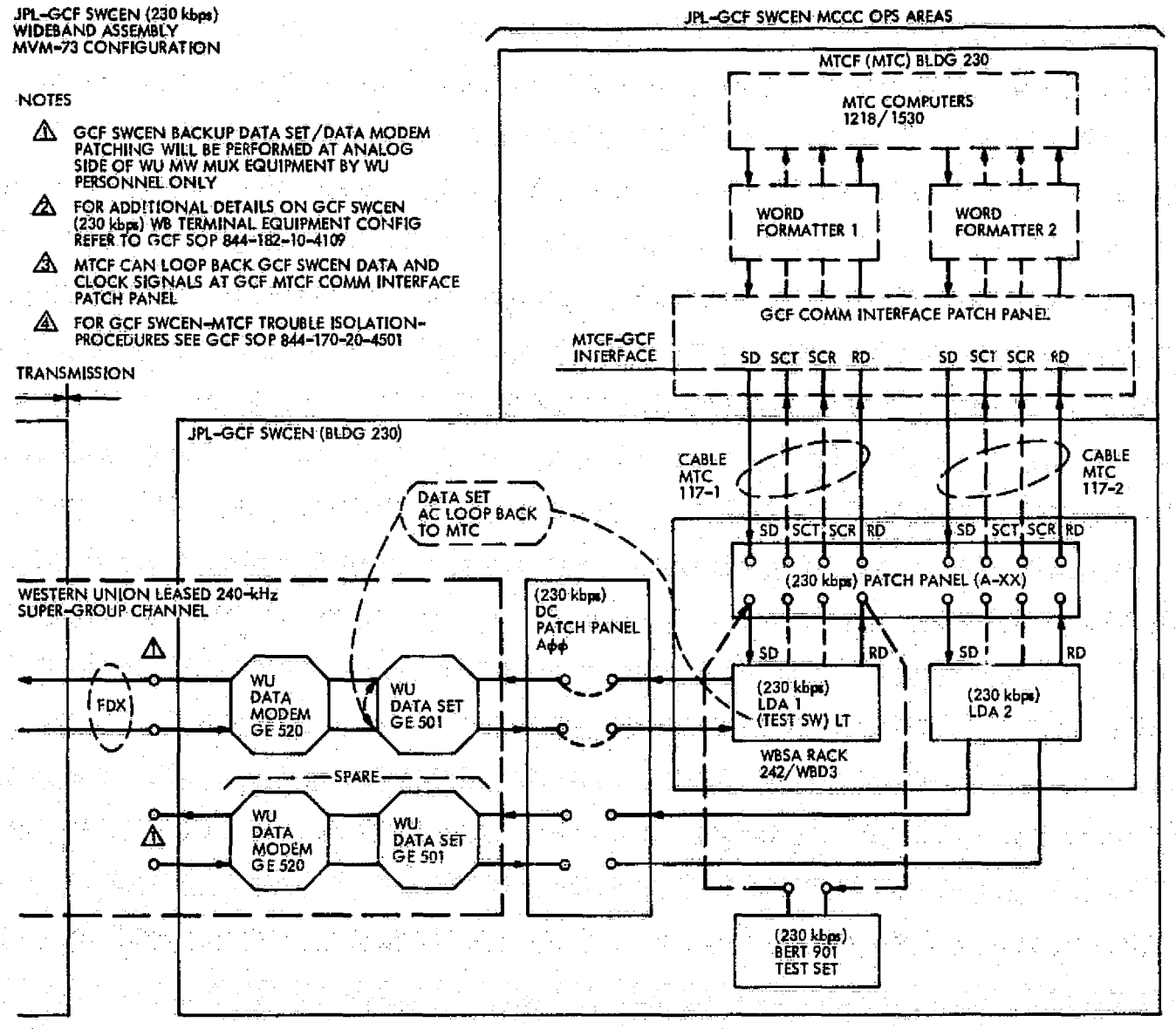

Fig. 11. JPL (GCF SWCEN) (230 kbps) Wideband Data Subsystem assembly configuration

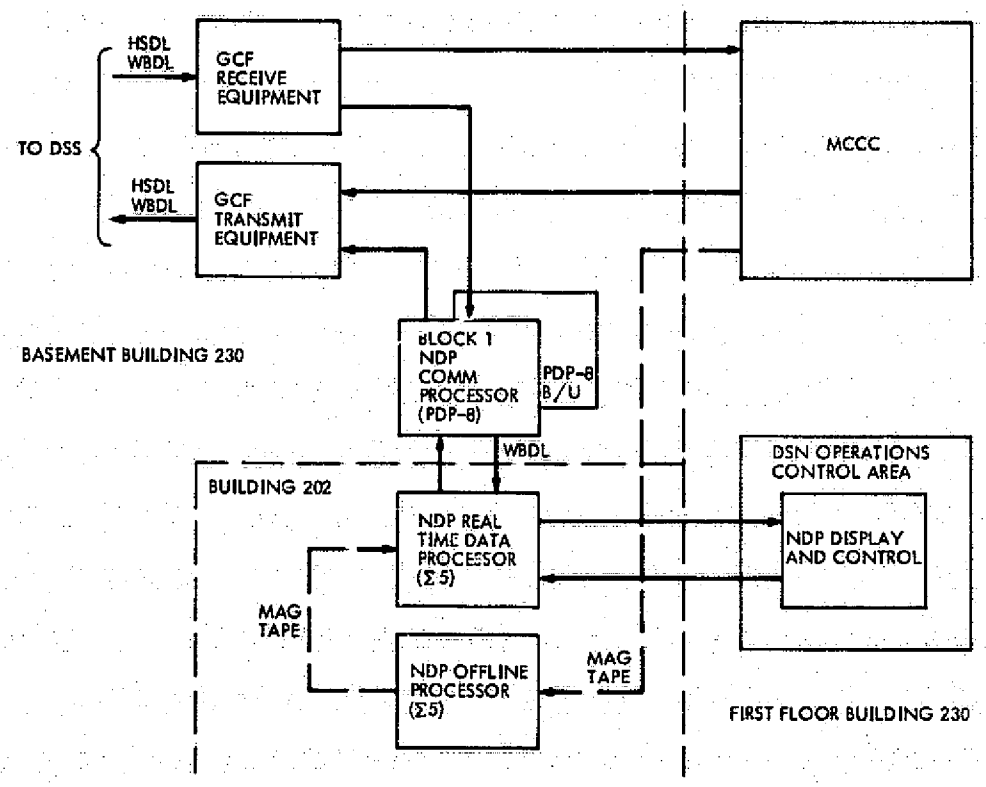

Fig. 12. Block I NDP configuration

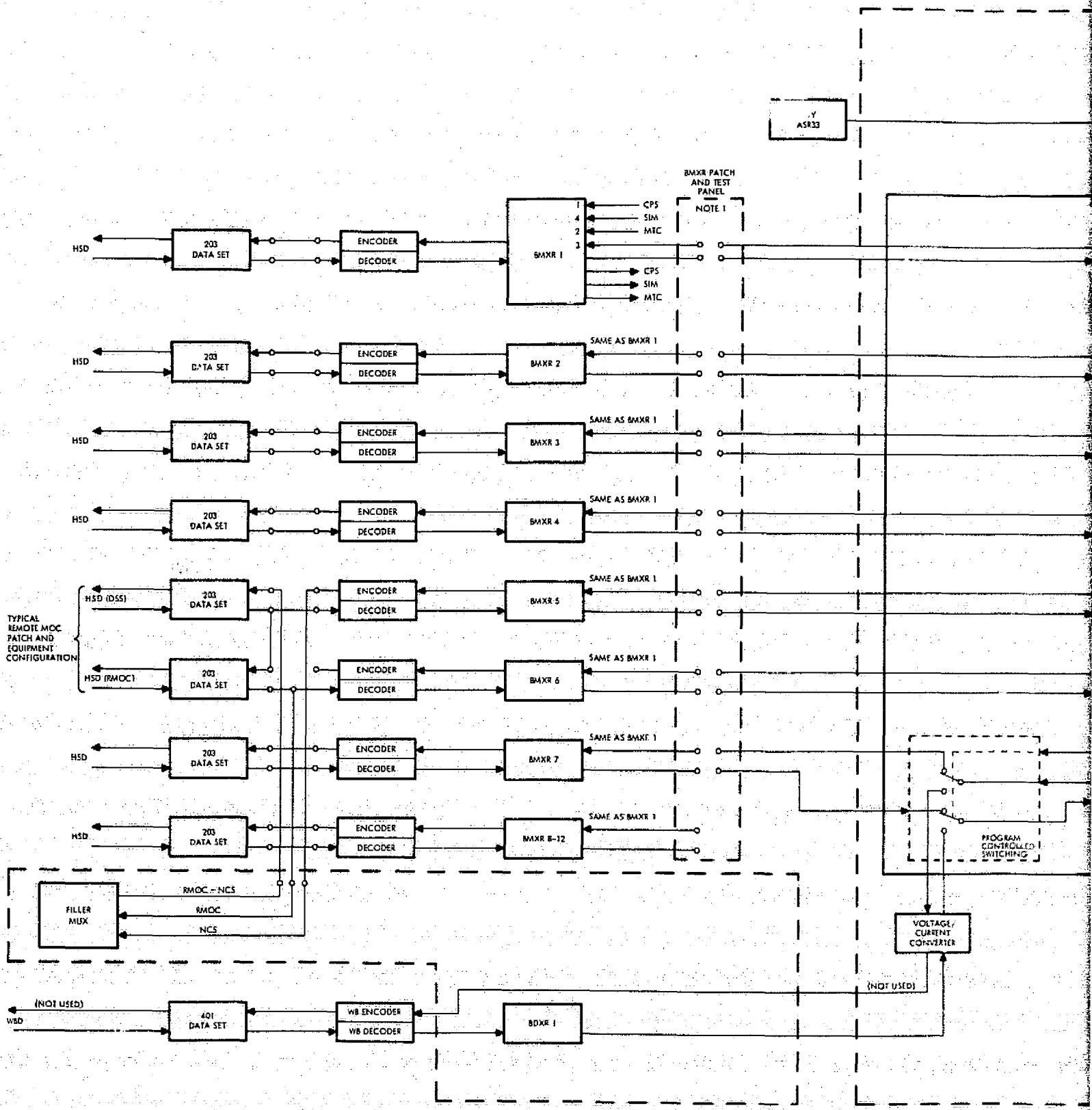

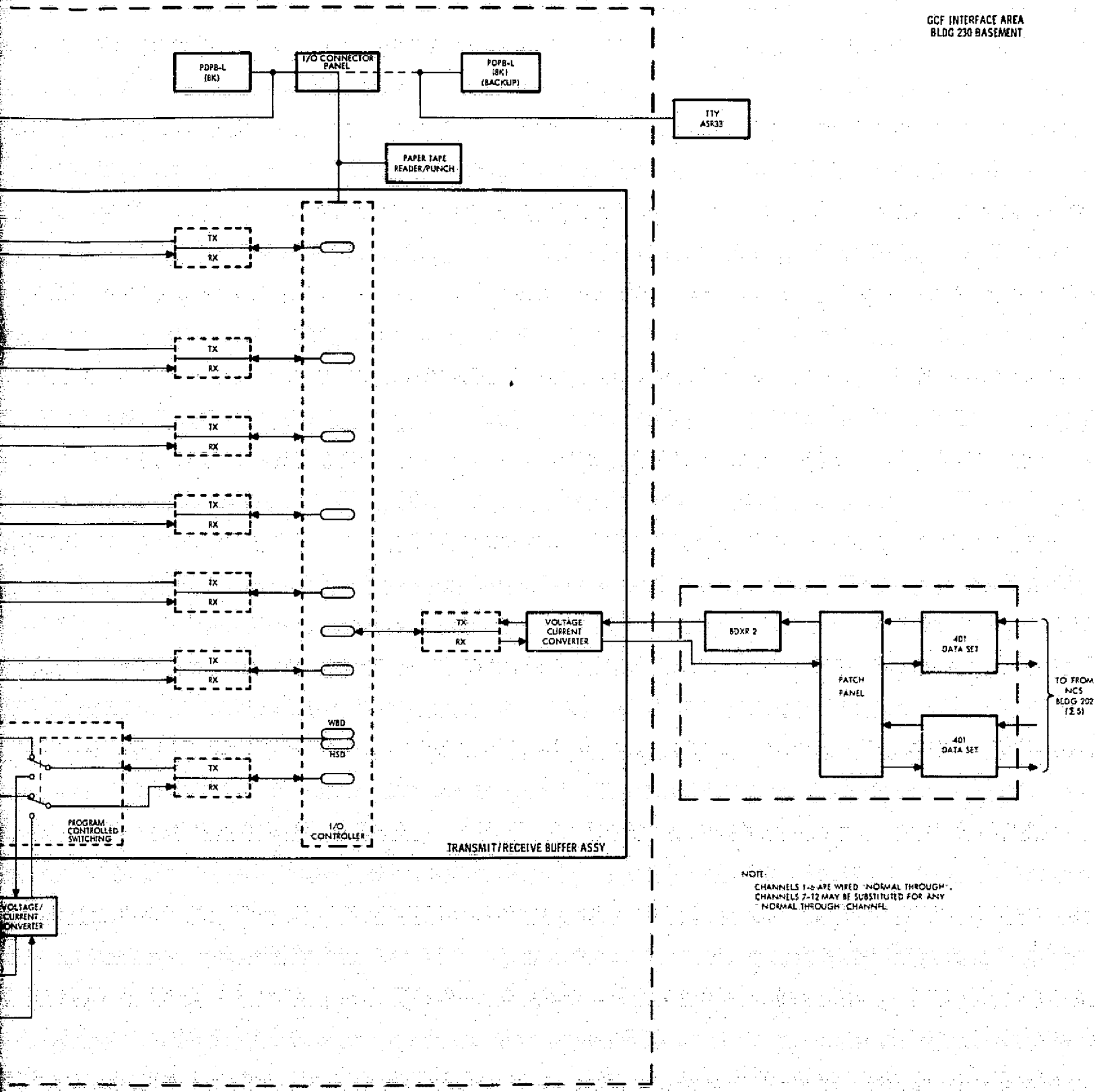

Fig. 13. Block I NDPT configuration

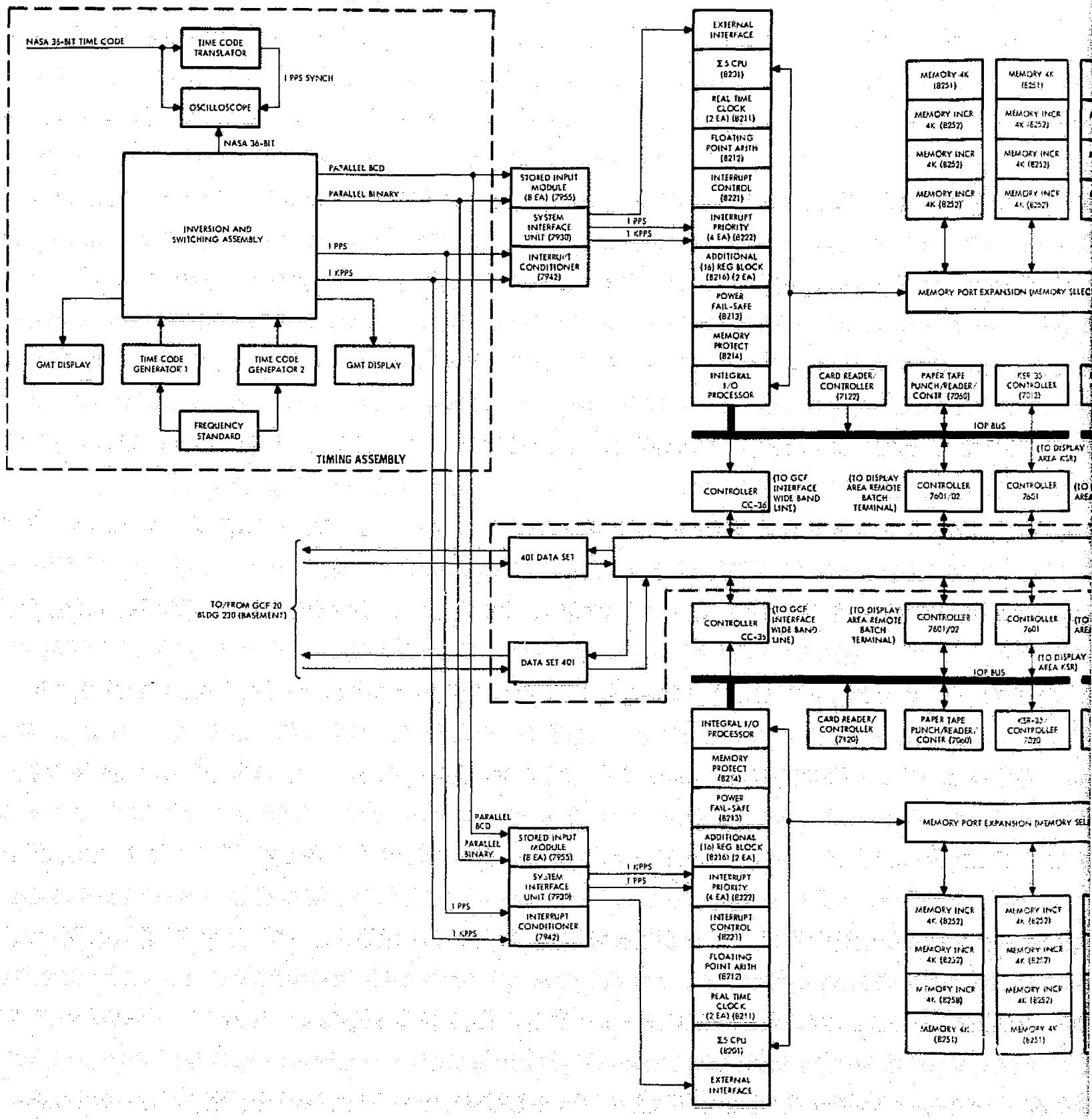

Fig. 14. Block I NDPA block diagram

FOLDOUT FRAME 2

ORIGINAL PAGE IS OF POOR QUALITY

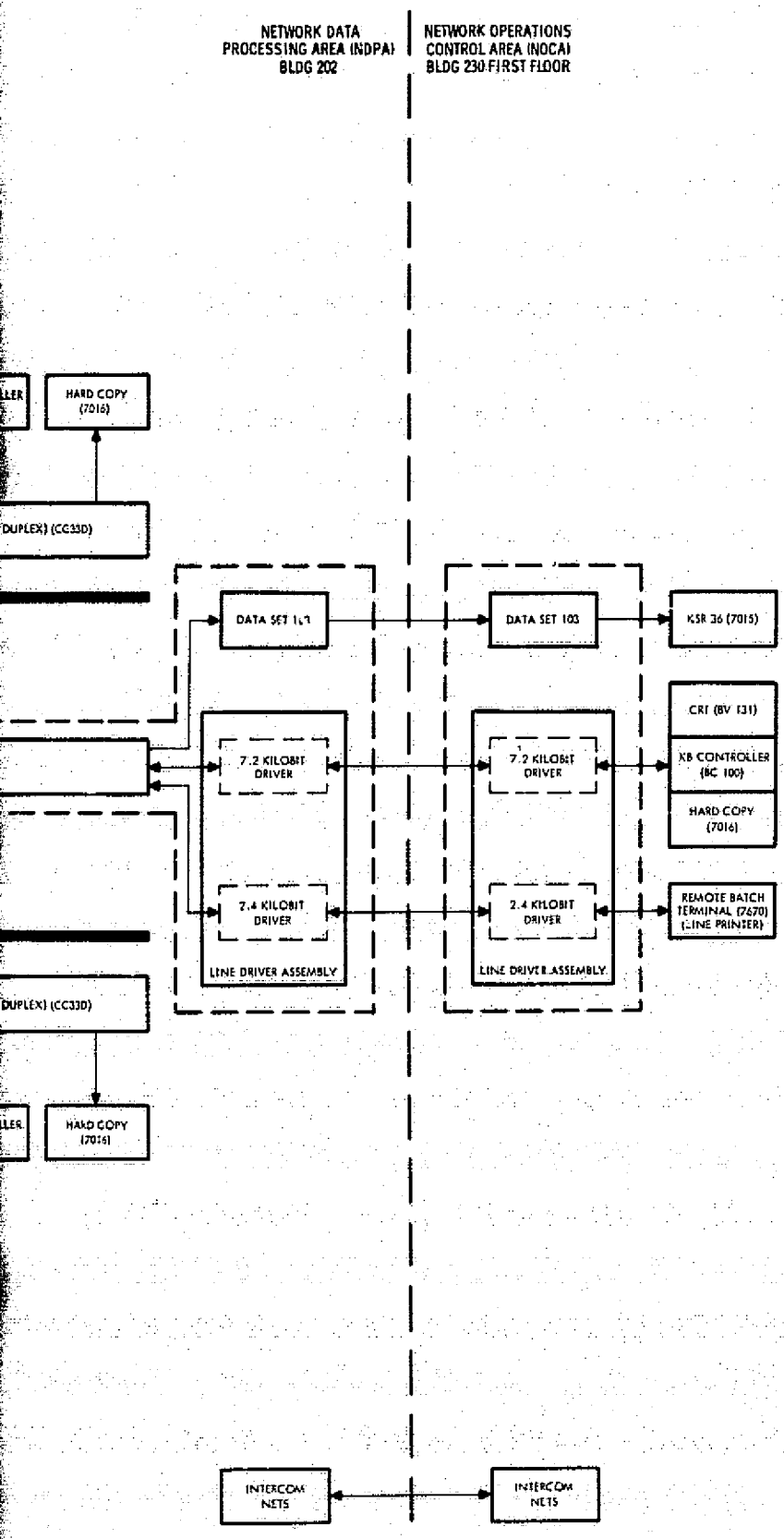
NETWORK DATA PROCESSING AREA (NDPA) BLDG 202
NETWORK OPERATIONS CONTROL AREA (NOCA) BLDG 230 FIRST FLOOR
HARD COPY (7016)
DUPLEX) (CC33D)
DATA SET 103
KSR 36 (7015)
CRT (BV 131)
XB CONTROLLER (BC 100)
HARD COPY (7016)
7.2 KILOBIT DRIVER
7.2 KILOBIT DRIVER
2.4 KILOBIT DRIVER
2.4 KILOBIT DRIVER
REMOTE BATCH TERMINAL (7670) (LINE PRINTER)
LINE DRIVER ASSEMBLY
LINE DRIVER ASSEMBLY
DUPLEX) (CC33D)
HARD COPY (7016)
INTERCOM NETS
INTERCOM NETS

FOLDOUT

Mariner 10 Mission Support

E. K. Davis
DSN Systems Engineering Office

This report covers the period from April 15, 1974 through October 15, 1974. April 15, 1974 marked the end of the Mariner Venus/Mercury 1973 Project and the beginning of the Mariner 10 Extended Mission Project. The Extended Mission Project was formally approved to include a Sun-side second encounter of Mercury and an understanding that every reasonable effort would be made to preserve the possibility of achieving a dark-side third encounter of Mercury in March 1975. In addition to the Mercury second encounter (Mercury II), DSN support during this report period included other major events, such as superior conjunction and two trajectory correction maneuvers. This article also summarizes the special antenna arraying experiment that the DSN conducted to enhance the video data quality at Mercury II.

I. Planning Activities

Only after completion of the primary mission in early April 1974 was any significant Project or DSN attention given to extended mission planning. This late start, combined with the number of required critical events and the occurrence of additional spacecraft problems, placed a heavy load on DSN planners during the short six-month interval between Mercury first and second encounters. Detailed planning was, however, satisfactorily accomplished in advance of each major event, which included the following: (1) trajectory correction maneuver (TCM) 4, (2) cruise support, (3) superior conjunction radio science, (4) TCM 5, and (5) Mercury second encounter.

A. Documentation

During April 1974, the Mariner 10 Extended Mission Project Support Instrumentation Requirements Document (SIRD) was prepared and approved by JPL. In response to this SIRD, the NASA Support Plan (NSP) was prepared and approved by JPL in June 1974. These documents covered requirements and commitments only through Mercury second encounter. Updates of these documents

will be required for activities beyond October 15, 1975. The Network Operations Plan for Mariner Venus/Mercury 1973 was revised to incorporate new configurations and capabilities described in this article.

B. TCM 4

First priority was given to supporting the Project in planning for TCM 4. The primary concern in the DSN was in arranging for required 64-meter DSS support once the date and time of TCM 4 were fixed. The Project had many factors to consider: spacecraft constraints, science return, encounter aim point, and third Mercury encounter, before finalizing the TCM design. On April 26, 1974, the DSN supported a special spacecraft gyro test conducted to determine if the roll axis oscillation would occur with the solar panels and the scan platform set in the planned maneuver configuration. No oscillations resulted. Also, spacecraft propulsion subsystem thermal constraints precluded one engine burn of the required duration; therefore, the maneuver was planned to be conducted in two parts. It was pointed out that real-time telemetry data would not be possible during the TCM unless the spacecraft high-gain antenna was adjusted to point at Earth. However, the Project opted to give up these data in order to maintain the high-gain antenna in the April 26, 1974 test configuration during the actual TCM. These data would be recorded on the spacecraft recorder for post-TCM playback.

C. Cruise Support Plan

The Mariner Venus/Mercury 1973 primary mission had enjoyed essentially continuous tracking coverage from November 3, 1973 through April 15, 1974, via a combination of the 26- and 64-meter deep space stations. This level of support could not be continued throughout the extended mission due to the higher priorities of other flight projects and DSN implementation requirements. Basically, the plan was for Mariner 10 to receive approximately two-thirds continuous coverage by a combination of full or partial passes each day. The daily coverage gap would normally occur over the Australian longitude since each of these stations was planned to be down for upgrade and repair, in a serial manner, throughout the extended mission. Therefore, it was plannned that the Mariner 10 spacecraft would record non-imaging science data during coverage gaps and then play back these data via a 7.35-kbps dump during the next scheduled 64-meter pass.

During the very first such coverage gap on April 16, 1974, analog-to-digital converter number two in the spacecraft flight data subsystem apparently failed, causing a loss of 50 of the 134 analog engineering measurements. This spacecraft failure, unlike some others, had no direct effect on the DSN. It did, however, raise some concerns regarding continuation of the partial coverage plan, but circumstances dictated a continuation in this mode. Unfortunately, the spacecraft was not long in putting an end to the record-playback plan.

On August 14, 1974, the spacecraft recorder was to serve as the data source for a ground telemetry test; however, no tape start occurred. It appeared that the recorder tape was stuck in the parking window and could not be freed. Trouble shooting continued through August 19. Some tape movement was achieved, but it then apparently became permanently jammed. The recorder was declared inoperable and tuned off on August 21, 1974. This, of course, meant complete loss of data during DSN coverage gaps. Of more concern, however, was the increased potential for loss of critical event data even while tracking due to inadequate telecommunications link performance (e.g., during TCMs) or failures at the deep space stations. As a result of this loss, the DSN gave added attention to redundant configurations and backup recordings to assure recovery of data on Earth.

D. Superior Conjunction Support Plans

Mariner 10 superior conjunction activities occurred during the period May 24–June 21, 1974. Recovery of dual-frequency S/X-band doppler, range, and open-loop receiver data types was required. In addition, it was desired that calibration tracks be provided beyond the stated interval. Since Mariner 10 provided the first opportunity for spacecraft dual-frequency analysis of solar corona and gravity effects, the DSN gave considerable emphasis to arranging proper support at DSS 14. Originally, DSS 14's Block IV S/X-band receiver was scheduled for removal and rework in preparation for Viking test support in mid-June 1974 following superior conjunction on June 6, 1974. The expanded observation period required negotiation of the removal date and was subsequently set for July 1, 1974. Support of the special Block IV receiver trouble-shooting team was planned to continue in effect until July 1, 1974.

E. TCM 5

In parallel with superior conjunction activities, the DSN assisted the Project in planning support for TCM 5. The TCM was planned to occur on July 2, 1974 over DSS 14, preceded by a gyro roll test on June 24, 1974. To avoid possible impact on DSS 14's support of the TCM, removal of the Block IV receiver was negotiated to occur on July 5 rather than July 1, 1974 as previously planned.

F. Mercury Second Encounter Support Planning

Following the Project's decision in May 1974 regarding the second encounter aim point, detailed encounter support plans were able to rapidly progress. Initially, the second encounter differed in two significant ways from the first encounter: (1) the second encounter would be a Sun-side pass having no solar or Earth occultations with emphasis on additional TV coverage of Mercury; and (2) the Earth–spacecraft distance would be greater than that at first encounter, resulting in a 1-dB lower signal level in the telecommunications link.

The aim-point difference in fact made second encounter planning easier for the DSN than that for first encounter since there were no occurrences of radio science occultation and rapid signal reacquisition requirements. The spacecraft could be continuously tracked near the planet in a listen-only mode. However, the lower signal level due to the increased distance posed some critical questions and support considerations. Would real-time 117-kbps video still be possible at Mercury II? Or would the reduced rate of 22 kbps be necessary to stay above the maximum allowable bit error rate of one in thirty? Could some improvement in the DSN deep space stations be implemented to regain the "lost" dB?

Telecommunications link analyses indicated that the bit error rate would be, at best, one in twenty and somewhat worse during much of the encounter pass at the 117-kbps rate. It appeared as if TV experimenters had a choice between a large number of TV frames of poor quality or a small number of high quality.

In June 1974, engineers of the DSN Communications Systems Research Section proposed that DSS antenna-arraying and signal-combining techniques might be employed to gain 0.6 to 0.7 dB. The feasibility of this approach was pursued in a number of meetings, and the decision was made to implement an arrayed antenna capability for Mercury second encounter. It was understood that data via this source would be provided on an engineering experiment basis in parallel with the standard configuration at DSS 14. The implementation of this capability is further discussed in Section III of this report.

Tests were planned which would evaluate the array performance using actual spacecraft data during far-encounter TV sequences. The Project would decide between the standard configuration and the array on the basis of these tests. Theoretically, the arraying gain was expected to produce a bit error rate of between one in thirty and one in fifty over most of the Goldstone near-encounter passes. If achievable, this would exceed minimum requirements and provide picture quality nearly equal to that of the first encounter. This would represent a significant increase in TV science data return; consequently, priority attention was given to the experiment.

The subsequent failure of the spacecraft tape recorder in August 1974 added a significant third difference to Mercury II. There would be no preservation of high-quality TV frames on board for later playback; only what was recorded on the ground in real time would be available to experimenters. The optional record–playback mode was no longer available, and this added more importance to the arraying implementation.

DSS 43 support was also employed as a part of the second encounter TV data acquisition plan. To provide for reasonable data quality, the low-noise ultra cone was retained at DSS 43 through second encounter.

II. Program Control

The DSN continued to provide monthly inputs to the Project Management Report throughout this period. With the decision to implement the antenna arraying capability, the DSN held weekly status meetings to review progress. These meetings continued until encounter. A DSN encounter readiness review was conducted on September 6, 1974, and all action items were closed prior to encounter.

III. Implementation Activities

Very little implementation activity was anticipated between Mercury first and second encounters. However, this proved to be a busy period, primarily as a result of antenna arraying and the possibility of real-time 117-kbps video data.

To provide tracking coverage flexibility in the Spain longitude, DSS 61 was, for the first time, configured and checked for Mariner 10 support. This also gave access to DSS 61's 20-kW transmitter for commanding during spacecraft loss-of-Canopus emergencies.

The 230-kbps super group communications service between DSS 14 and JPL was reinstalled and checked for encounter support. The service had been removed in the belief that real-time 117 kbps would not be possible during the second encounter. The 28.5-kbps wideband communications service to the overseas 64-meter stations was reactivated after being down in cruise for cost avoidance reasons. The DSS 14-to-JPL 28.5-kbps circuit

had been converted to 50 kbps in preparation for Viking test support.

Improvements were made in DSS 14's backup antenna cone-maser performance by relocation of the maser nearer the feed horn in the cone. This provided an acceptable backup to DSS 14's standard cone-maser in the event of failure. Special configurations were implemented at DSSs 14 and 43 for analog recording of integral values of video data bits at the symbol synchronizer assembly output for possible post-encounter processing and enhancement.

The proposed antenna array and signal combining experiment was successfully implemented at Goldstone and tested for encounter support. Tests with the spacecraft demonstrated achievement of the expected 0.6–0.7-dB improvement, and the decision was made to use this configuration for real-time handling of encounter data. The key characteristics of the array experiment are given in Table 1 and Fig. 1. It should be noted that DSS 13, which is not normally a flight support station, was employed as one of the arrayed stations to take advantage of its lower system temperature.

Table 1. Goldstone antenna arraying experiment key characteristics and comments

Three-station array, two 26-meter and one 64-meter, DSSs 12, 13, and 14, all listen-only.
DSS 12 and 13 receiver baseband output microwaved to DSS 14 for arraying experiment.
DSS 14 receiver 1 output to DSS 14 string alpha for normal 117-kbps processing recording.
DSS 14 receiver 2 baseband output microwaved to Goldstone area comm terminal and looped back to DSS 14 via microwave to induce signal delay nearly equivalent to DSSs 12 and 13.
Signal combiner device located in DSS 14 at microwave interface. Receives parallel input from microwave of DSS 12, 13 and 14 baseband signal.
Signal combiner correlated and phased signals providing a combined output to the DSS 14 SDA-string beta for processing, real-time transmission to JPL, and recording.
DSS 14 string alpha did a little better than expected on the non-arrayed data.
DSS 14 string beta performed a little worse than expected on the arrayed data.
String beta appeared to be about ½ dB down from alpha. Arraying was hard-wired into beta; a switch would have been ideal but no time to implement. Even so, arraying gave 0.3 to 0.4 dB better performance. Had arraying been on alpha, the expected 0.8-dB gain would have been realized or exceeded.
Signal combiner worked well, no difficulties.
Promised and delivered pictures at BER of ≤ 3 in 100 for 2½ hours near encounter.
Low-rate data (2450 bps) microwaved from DSS 14 to DSS 12 for processing and transmission to JPL.

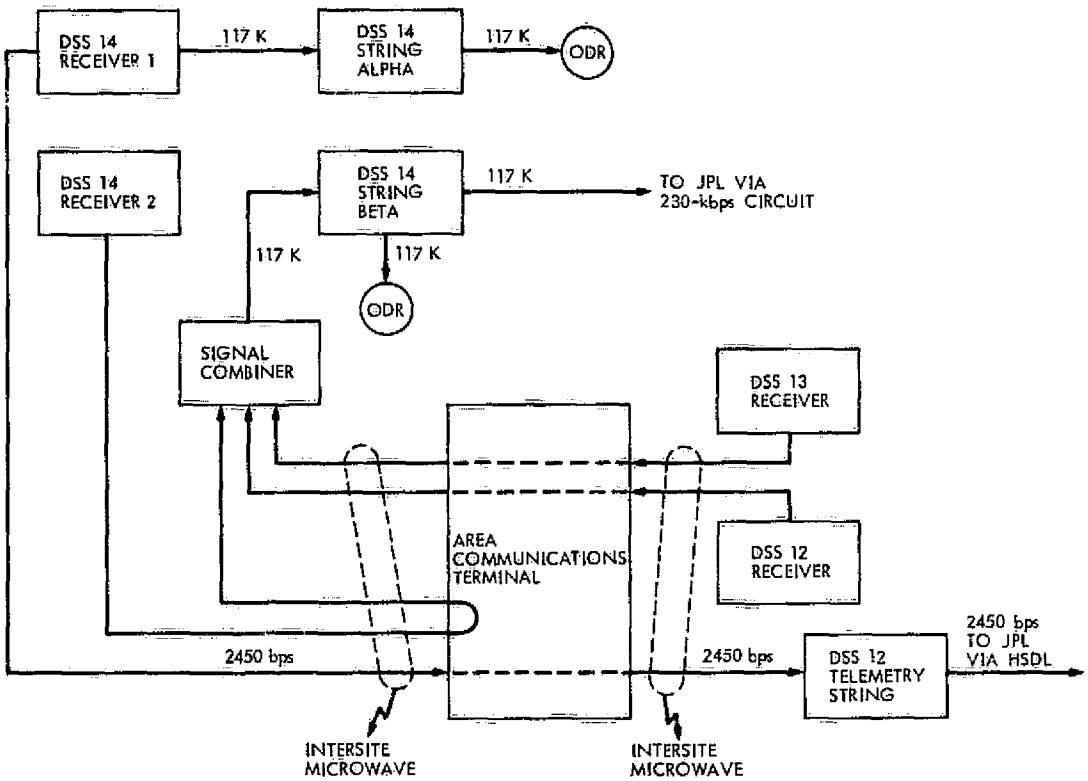

Fig. 1. Goldstone antenna array experiment configuration for Mariner 10

Viking Mission Support

D. J. Mudgway
DSN Systems Engineering Section

The previous article in this series described the results of the radio-frequency Compatibility Test Program for Viking test models of the Orbiter and Lander conducted at the Compatibility Test Area in August and September 1974. This article covers the initial phases of the network implementation for the Viking Project with particular emphasis on significant organizational changes that were found necessary to bridge a hitherto unforeseen gap between the higher level subsystem schedules and the lower level engineering modification schedules.

I. DSN Schedule Management

The DSN approach to schedule management for the Viking reconfiguration activities in the Deep Space Network has been described in Ref. 1. Starting from this basis, a family of schedules was developed starting with the Tracking and Data System (TDS) Level 3 Schedule and proceeding down through Levels 4 and 5 to individual deep space station implementation and test periods.

At Level 3, only major milestones representing TDS interaction with other systems of the Viking Project were identified. This schedule also included activities for the preparation of near-Earth support. The Level 3 schedule is updated monthly and published by the Viking Project Office, along with similar schedules for the other systems of the Project in Viking Project Working Schedules and Reports, Vol. II. A typical page from this document is shown in Fig. 1.

The next set of schedules shows activity necessary at each Deep Space Station (DSS) to meet the key milestones in Level 3. This, too, is updated monthly, in accordance with progress at each DSS and reported to the Viking Project Office for publication in the same document as the Level 3 schedules. A typical sheet for DSSs 11 and 14 for November 1974 is shown in Fig. 2.

At this point, it becomes necessary to identify implementation and test activity at the DSS subsystem level. For this purpose, a series of Level 5 schedules was developed. At Level 5, the required readiness dates for all DSS subsystems are shown together with the ensuing testing and training activities.

As in all the other schedules, the key dates needed to meet the committed Viking Project readiness dates are carried forward. These schedules are internal DSN documents and are distributed to the Project for information and to the DSSs and the implementation, test, and operations organizations as a basis for their own sub-tier planning.

The published document is called the DSN Viking Implementation Schedule and a typical page for November 1974 is shown in Fig. 3. This document is updated monthly from the data provided by the DSN Implementation Schedule (IMPSKED).

II. Engineering Change Management

In October 1974, DSS 14 was out of service for approximately one month in order to reconfigure for the approaching Helios A launch, Pioneer 11 Jupiter encounter, and to include a substantial number of the engineering changes necessary to meet the Viking configuration published in Ref. 2.

At the conclusion of this work, it was intended to start Viking System Performance Testing in accordance with the foregoing schedules and plans. After several futile attempts to accomplish this work it became apparent that there was an urgent need for better visibility and control of the multitude of Engineering Change Orders (ECOs) which are needed to supplement the implementation of the subsystems before full system performance testing can be commenced.

Further investigation soon revealed that the ECOs needed for the other stations in the network were not clearly understood, and in many cases, were not scheduled properly to mesh with the subsystem need dates reflected in the Level 5 schedules. This implied a serious risk to the DSN's ability to meet the committed Project need dates.

III. Corrective Action

At this point (November 1974), upper management attention was drawn to these potential difficulties, created to a large extent by the magnitude of the job involved, overloading of contributing organizations and preoccupation with preceding in-flight project problems, and the number of different organizational boundaries involved. A prompt response resulted in the establishment of a three-man task team charged to:

(1) Identify all the ECOs involved

(2) Select those essential to the Viking configuration

(3) Classify the essential ECOs according to categories of readiness

(4) Take all action necessary to expedite any of these latter ECOs which might delay the readiness dates

(5) Establish a frequent and regular reporting and management system at the ECO level.

The way in which the team was to work is shown in Table 1.

Division 33 was to compile the list of essential ECOs in order to permit the DSS directors to estimate subsystem readiness dates. Combined with operation data for the Mission Configuration Tests and the Operational Verification Tests, the DSN could estimate the chances of meeting the Viking need dates by comparison with the data originally provided by the Viking Project.

Where these dates could not be met, it became necessary to further reduce the test time (Organization 420), expedite the ECOs (Division 33), or renegotiate the Project need dates (Viking Project Office). As this work proceeded, all three approaches became necessary. The outcome of several iterations of this process had resulted in the DSN readiness summary shown in Fig. 4.

Further iterations were in progress to improve the schedule deviations to allow for contingencies which may arise in progress. Plans have been made for a computer-based ECO status reporting system using the following data sources as input:

(1) Data from the Engineering Division regarding engineering change kit deliveries to the cognizant operations engineers

(2) Data from the cognizant operations engineers regarding shipping and delivery of the modification kits to the stations

(3) Data from the station directors regarding implementation at the sites

It is planned to have this status reporting system in operation by mid-January 1975, and it will be described in the next report in this series.

References

1. Mudgway, D. J., "Viking Mission Support," in *The Deep Space Network*, Technical Report 32-1526, Vol. XIII, p. 29, Jet Propulsion Laboratory, Pasadena, Calif., Feb. 15, 1973.

2. *DSN Preparation Plan, Rev. A*, Doc. 614-20, Nov. 15, 1973 (JPL internal document).

Table 1. DSN Readiness summary

DSS	Readiness category	Start date	Total hours	Ready date	Project need date	Schedule deviation (12/3/74)
14	A/B	11/15/74	499	2/24/75	2/10/75	− 2 W[a]
	C	11/15/74	92	2/15/75	6/9/75	+ 11 W
	F	2/1/75	615	10/15/75	11/3/75	+ 2 W
43	C	2/1/75	237	4/1/75	4/7/75	+ 1 W
	D	4/1/75	198	7/1/75	8/1/75	+ 4 W
	F	12/1/74	775	11/5/75	1/5/76	+ 8 W
63	C	2/1/75	237	4/1/75	4/28/75	+ 4 W
	D	4/1/75	198	7/1/75	8/1/75	+ 4 W
	F	1/15/75	775	10/1/75	1/5/76	+ 12 W
11	A/B/C/F	1/15/75	167	2/21/75	2/24/75	0 W
42	C/F	2/1/75	177	3/7/75	4/7/75	+ 4 W
61	C/F	2/1/75	177	3/7/75	4/28/75	+ 7 W

[a]Ready date exceeds need date.

Maximum mission configuration test (MCT) rate is 10 hours per test, 2 tests per week.

Maximum operational verification test (OVT) rate is 6 hours per test, 2 tests per week for two weeks, prior to need date. Remaining OVTs are in parallel with system integration tests.

Station hours for ECO's which are not subject to MCTs or OVTs are not included in these estimates.

Categories of readiness:

A Support planetary verification tests (telemetry and command)

B Support planetary verification tests (tracking and monitoring)

C Support launch phase system integration tests

D Block IV receiver committed at DSSs 43 and 63

F Support planetary phase system integration tests

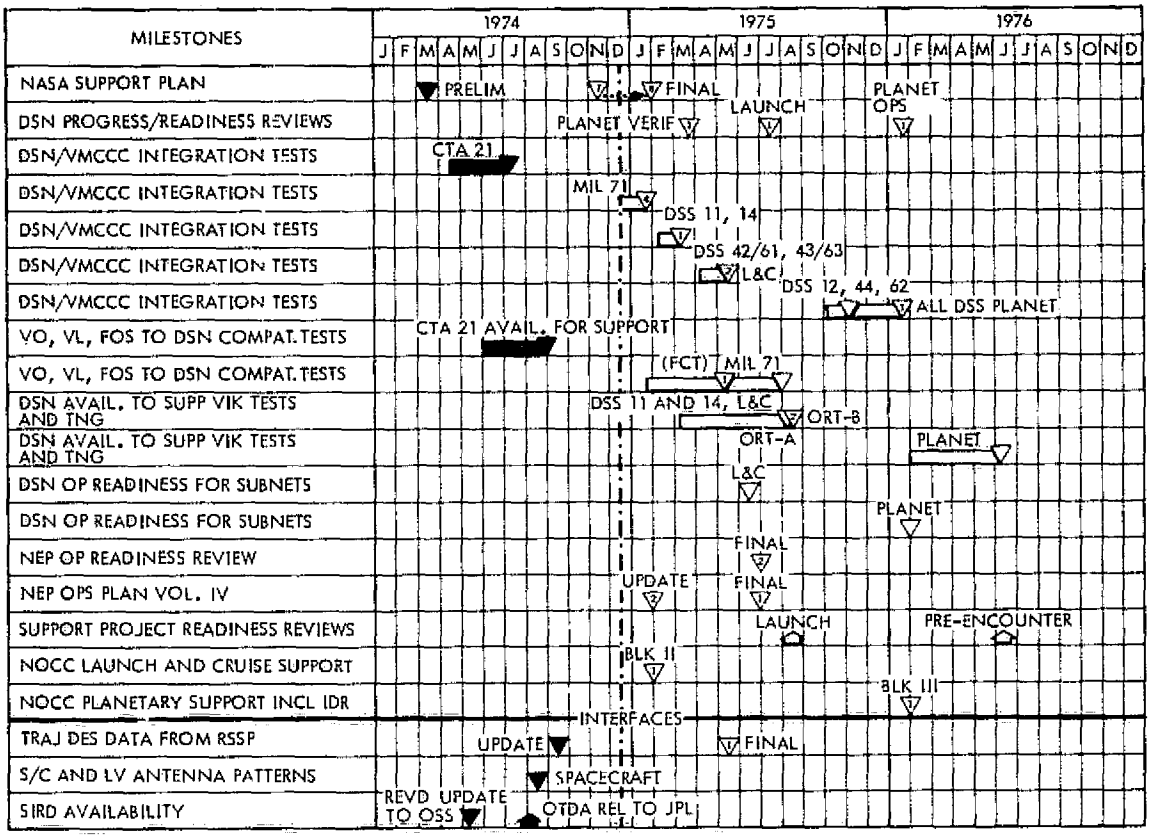

RSSP - RANGE SAFETY SUPPORT PACKAGE

Fig. 1. Extract from TDS schedule, Level 3 for November 1974

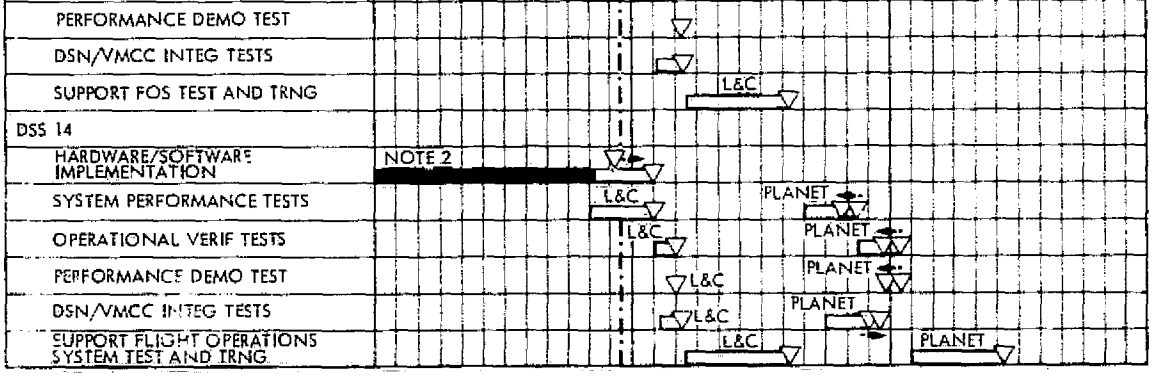

Fig. 2. Extract from DSSs 11 and 14, Level 4 schedule for November 1974

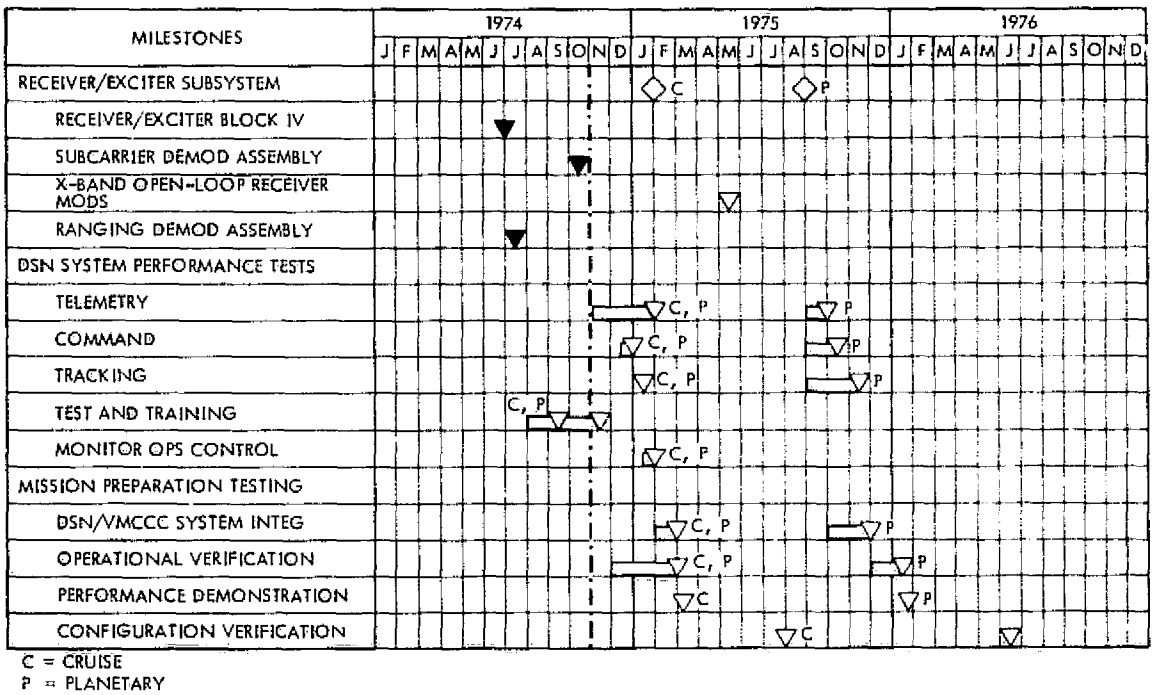

Fig. 3. Extract for DSS 14 milestone schedule for November 1974

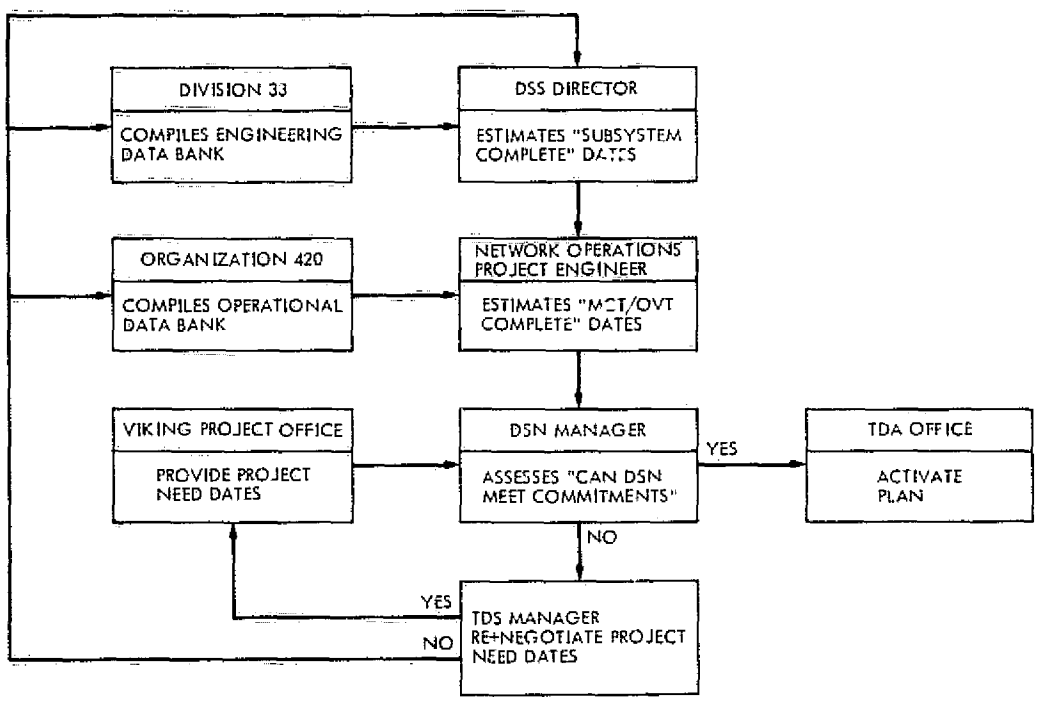

Fig. 4. DSN/Viking readiness plan

Helios Mission Support

P. S. Goodwin
DSN Systems Engineering Office

The first of two Helios spacecraft, built by West Germany, was successfully launched from Cape Kennedy on December 10, 1974 and is now enroute to an unprecedented 0.31-astronomical unit (AU) perihelion in mid-March 1975. This article describes the DSN support starting with the prelaunch activities and carrying through the first three critical days of the mission.

I. Introduction

The previous article (Ref. 1) discussed the results of the Helios prototype model spacecraft compatibility testing that was conducted at Cape Canaveral, Florida, utilizing the Spaceflight Tracking and Data Network (STDN) (MIL-71) facility. This article covers the compatibility testing of the flight spacecraft (F-1) and its subsequent launch on December 10, 1974 from Cape Canaveral, the initial DSN acquisition of the flight spacecraft over Australia, and the DSN support during the Step I and II maneuvers that occurred during the first three days of the mission.

II. Prelaunch Activities

A. Flight Model (F-1) Compatibility Testing

The Helios-A flight model spacecraft (F-1) arrived at Cape Canaveral on September 22, 1974 and was transported to Hangar AO, where it was assembled for testing of its compatibility with the DSN. Compatibility tests using the STDN (MIL-71) facility commenced on October 25, 1974 and continued for 68 hours. With only one minor exception, these tests showed that the F-1 model spacecraft either duplicated or exceeded the performance characteristics demonstrated by the prototype model spacecraft during the latter's compatibility tests in July/August 1974 (Ref. 1). The minor exception was that the F-1 spacecraft transponder has a range code polarity inverted from that measured with the prototype model spacecraft—however, this difference is not significant since the DSN Tracking System is capable of supporting either a normal or an inverted range code. The Helios flight model compatibility tests also demonstrated that the DSN's corrective steps to overcome the difficulties detected during the prototype compatibility tests at Cape Canaveral were successful. The overall success of the Helios flight model spacecraft/DSN compatibility test effort gave reassurance that Helios-A could achieve its December launch opportunity.

B. Initial Acquisition Backup by DSS 44

With Pioneer 11 Jupiter encounter operations occurring very close to the contemplated December 8, 1974 launch

of Helios-A, the DSN became concerned about providing redundancy within Australia to perform the initial acquisition of the Helios spacecraft. Prior planning had assumed that the Australian 64-meter station (DSS 43) could be employed in case of an emergency to provide backup support to DSS 42 during the initial acquisition. However, Pioneer Jupiter encounter requirements dictated that DSS 43 be exclusively devoted to the Pioneer Project—hence, there would be no backup to DSS 42. While no backup Australian station had been committed to the Helios Project, the DSN realized the importance of an early initial acquisition in order to perform the Step I maneuver and, therefore, took steps to see whether or not the scheduled conversion of the STDN Honeysuckle Creek facility to a DSN station (DSS 44) could be accelerated sufficiently to provide an "engineering level" support during the first pass over Australia. A teletype message presenting this proposal was sent to the Honeysuckle Creek facility on November 4, 1974. The station responded that they would give it their best effort and appreciated the DSN's offer of assistance. While a considerable amount of the necessary equipment was already located on site at Honeysuckle Creek, much remained to be done to implement the hardware and to debug the special computer software programs which were dictated by the Honeysuckle X-Y antenna mount. In addition, it was desirable to arrange for the loan of an STDN acquisition aid antenna from the Goddard Space Flight Center and to remount this antenna on the quadripod of the X-Y antenna. Completion of the implementation, plus at least a minimum amount of operator training, was desired prior to the Helios Operational Readiness Test (ORT) scheduled for December 5, 1974. All of this was very successfully accomplished—which is certainly a tribute to the personnel at DSS 44. While many of these station personnel had prior tracking experience during the Apollo Program, few, if any, had prior experience with the DSN or its procedures. Therefore, their efforts are doubly appreciated.

C. Helios Operational Readiness Test

The Helios-A Operational Readiness Test (ORT) was conducted on December 5, 1974 with the DSN configured as it would be on launch day—including all backup DSSs. This was the first (and only) exercise of the newly implemented DSS 44 in a Helios Project test. (Prior training had been on a *DSN internal* basis.) During the ORT, simulated failures at DSS 42 (Tidbinbilla, the Australian prime station) were exercised with DSS 44 assuming responsibility for the "failed" function at DSS 42. This included a simulated 100% failure at DSS 42. DSS 44 performed well under all simulated conditions. The ORT also simulated the Step I maneuver and science turn-on sequence over Australia, the near-Earth science return over Madrid, and a Step II maneuver sequence over Goldstone using DSS 12 as the prime facility and DSS 11 in a hot backup capacity. All DSN facilities performed well during the ORT. This fact, plus a favorable Mission Readiness Review held at Cape Canaveral on December 6, culminated in the Project Managers' decision to attempt a launch of Helios-A on December 8, 1974.

III. Launch Activity

A. December 8, 1974 Countdown

Preparations were commenced to launch Helios-A on December 8, 1974 with the opening of a 42-minute daily launch window at 07:16 GMT. During the minus count, all supporting DSN facilities began their pre-track calibration sequences. Besides STDN (MIL-71), DSSs 42 and 44 in Australia, DSS 62 in Madrid, and DSSs 11 and 12 at Goldstone were involved in this first-pass countdown procedure. At T - 10 minutes in the countdown sequence, which was at the point of a built-in hold, a launch vehicle telemetry readout from the Centaur liquid hydrogen engine caused some concern. The T - 10-minute hold extended into the opening of the launch window, but the Centaur telemetry problem was not resolved. The hold continued until approximately 20 minutes prior to the 07:58 GMT close of the daily window on December 8, at which time it was decided by the Project Managers to "scrub" the launch attempt for that day. Shortly thereafter, the Project Managers made a decision to reschedule the next launch attempt for December 10, 1974 in order to avoid unfavorable weather forecast for December 9, as well as to provide time to thoroughly diagnose the problem within the Centaur stage of the launch vehicle.

B. December 10, 1974 Launch of Helios-A

The launch countdown of Helios-A resumed on December 10, 1974 towards a targeted opening of the 42-minute daily window at 07:11 GMT. Again, the DSN stations at all three longitudes participated in the minus count by performing their pre-pass calibrations and dataflow tests. This time the launch vehicle proceeded through the T - 10-minute built-in hold and continued satisfactorily right up to the opening of daily launch window. Helios-A lifted off the pad at Cape Canaveral at 07:11:01.5 (hours:minutes:seconds) GMT with all subsequent launch vehicle events occurring on schedule. Early radar tracking from the Eastern Test Range Radar Stations indicated that the trajectory was entirely nominal. This fact, plus confirmation from the down-range telemetry stations that the

Helios spacecraft transmitter signal was "on the air" gave confidence that a nominal initial acquisition procedure could be employed by the Australian DSSs upon spacecraft rise.

C. DSN Initial Acquisition

Following a perfect launch trajectory, Helios-A spacecraft was acquired by the Australian DSSs at 07:57:33 GMT with DSS 42 providing the prime source of data and DSS 44 acting as a hot, redundant backup. During this time, the spacecraft's attitude was such that its signal as received by the Australian DSSs was being transmitted by the dipole (top) element of the omni-directional antenna (see Fig. 2, Ref. 2). However, as the spacecraft gained altitude during its trajectory over Australia, the aspect angle changed such that the DSS reception would be via the (bottom) circularly polarized horn element of the omni-directional antenna system. The spacecraft radiation pattern boundary between the top dipole antenna and the bottom circular horn antenna element of the omni-antenna system created an interference region. This was of concern to both the Project and the DSN with respect to whether successful telemetry reception could be achieved during the transition. However, during flight, the signal degradation caused by this interference region proved to be less than had been feared. Once the spacecraft's trajectory had carried the aspect angle past the interference region, commands were sent by DSS 42 to initiate the Step I maneuver sequence.

IV. Early Mission Support

A. Step I Maneuver

The Step I maneuver orients the spacecraft such that its solar panels are uniformly illuminated by the Sun, but with the spacecraft's spin axis still lying essentially in the plane of the ecliptic, i.e., the plane of its injection. This maneuver is required for both electrical power and thermal control.

At the completion of the Step I maneuver, the spacecraft was still rotating at its 92.8-rev/min velocity imparted during its spin-up prior to injection. The next sequence was to deploy the magnetometer booms (Fig. 2, Ref. 2)—a process that caused the spacecraft's rotational rate to decrease to less than 55 rev/min. Following the magnetometer boom deployment, the radiowave experiment antenna booms (located at 90 degrees to the magnetometer booms) were also commanded deployed. Early telemetry analysis indicated that one of the antenna booms did not deploy fully; however, the Helios Project decided to defer investigation of this possibility until the spacecraft had achieved its cruise phase configuration. With boom and antenna deployment completed, and the spacecraft still lying in the plane of the ecliptic, the next mission sequence over Australia was to initiate selected on-board science experiments in order to measure the solar wind bow wave that surrounds Earth. This was also successfully accomplished over Australia.

B. Near-Earth Science Return

Following science instrument activation, DSS 42/44 in Australia and DSS 62 in Madrid, Spain, processed the cislunar science telemetry desired by the Project. DSS 62 performed very well during this first pass over Madrid, during which the Helios Project began preparations for the Step II maneuver following the subsequent Goldstone rise.

C. Step II Maneuver Sequences

Following Helios-A spacecraft first rise at Goldstone, the spacecraft telemetry format was changed from science to engineering data in preparation for the Step II maneuver. At this time, the spacecraft was well past lunar distance so the near-Earth science had been accomplished. The first series of Step II maneuver commands caused the spacecraft to yaw within the plane of the ecliptic to calibrate the thrust of the cold gas attitude control nozzles. After this was accomplished, commands were sent to pitch the spacecraft such that the antenna mast began to move towards the North Pole of the ecliptic. During the early portion of the Step II maneuver pitch commands, the spacecraft attitude was such that DSS reception was via the off-axis horn antenna out of the bottom of the spacecraft. As the pitch angle increased, so did the spin modulation on the doppler frequency increase—thereby giving an indication of spacecraft attitude in the tracking data. The spin modulation doppler signal was usable up to the point where the interference region was being traversed. To traverse the interference region (a feat requiring numerous commands), the Helios Project, in cooperation with the DSN, requested horizontal (ecliptic-plane) polarization at DSS 12 and vertical (perpendicular) polarization at DSS 11, with both stations supplying spacecraft telemetry via high-speed data lines to the Mission Control and Computing Center in Pasadena. This technique enabled DSS 12 to communicate with the spacecraft via the horn antenna while DSS 11 was communicating via the spacecraft's omni-dipole antenna. The point of equal signal strength reception between DSS 11 and DSS 12 represented emergence from the interference region. Since the degradation of the signal was not as severe as had been feared, the interference region was traversed with a telemetry margin of +10 dB at a 128-

bit/s engineering data rate. Following emergence from the interference region, DSS 12 was switched to vertical polarization, and the spacecraft downlink was switched from the omni-antenna system to the medium-gain antenna system so the Goldstone DSS's received signal strength (AGC) readings would indicate the commanded traverse of the side lobe pattern of the spacecraft's medium-gain antenna (Fig. 2, Ref. 2) and also indicate when the peak of the main lobe of this antenna had been located. By the end of the first Goldstone pass, the spacecraft attitude was such that the medium-gain antenna pattern was very close to its peak value—indicating a nearly 90-degree orientation of the spacecraft with respect to the plane of the ecliptic. By this time the Helios Project's prime Mission Operations Support Team had been up nearly 24 hours (since many had participated in the prelaunch activities), so the reactivation of the on-board science instruments was deferred to the second Goldstone pass. Further Step II maneuver orientations were consequently deferred to the third Goldstone pass, during which time the exact center of the main lobe of the spacecraft medium-gain antenna was accurately measured and the spacecraft's attitude accordingly determined. Prior to this, during second-pass activity, the spacecraft spin rate was increased to nearly 60 rev/min—though not exactly 60 rev/min per the experimenters' real-time request. With both the spacecraft's spin rate and attitude in the cruise mode, the last engineering sequence of this series was to position the spacecraft's high-gain antenna (Fig. 2, Ref. 2) such that it was directed towards Earth. This was accomplished by commanding various phase adjustments to the despin velocity until the main lobe of the high-gain antenna had been determined through DSS receiver signal strength measurements. This completed the intense post-launch Helios activity, and the mission settled down to its primary objective of achieving science return enroute to its perihelion passage of the Sun.

V. Conclusions

With the successful launch and orientation of the spacecraft, Helios-A has now been officially renamed Helios-1. This feat was the culmination of approximately 10 years of effort on the part of both NASA and the Federal Republic of (West) Germany. The DSN is pleased to be a part of this effort.

Helios-1 is now on a trajectory that will carry it to a 0.31-astronomical unit (AU) perihelion in mid-March 1975. Its orbital period is 190 days, and its inclination to the plane of the ecliptic is 0.016 degrees. Since Helios does not have course correction capability, achievement of the above targeted orbital parameters was accomplished by the Titan–Centaur–TE-364-4 launch vehicle using the Centaur guidance system.

Future DSN support of Helios-1 will continue to provide continuous coverage throughout the primary mission, with special emphasis on the first perihelion passage and subsequent solar occultation. Following that, the DSN will provide scheduled support through the lifetime of Helios-1. In addition, both Project and DSN activities are now starting preparations to launch Helios-B in approximately one year.

References

1. Goodwin, P. S., "Helios Mission Support," in *The Deep Space Network Progress Report 42-23*, pp. 19–21, Jet Propulsion Laboratory, Pasadena, Calif., Oct. 15, 1974.

2. Goodwin, P. S., "Helios Mission Support," in *The Deep Space Network Progress Report*, Technical Report 32-1526, Vol. II, p. 22, Jet Propulsion Laboratory, Pasadena, Calif., Apr. 15, 1971.

DSN–MVM'73 S/X Dual-Frequency Doppler Demonstration During Superior Conjunction

K. W. Yip, F. B. Winn, and S. J. Reinbold
Tracking and Orbit Determination Section

During the Mariner Venus/Mercury 1973 (MVM'73) mission, the S/X dual-frequency doppler calibrations (for plasma and ionospheric charged-particle dynamics) have been demonstrated to improve post-flight radio metric doppler reductions: the error of one Mercury I encounter position estimate was reduced by 500 km (~ 80%). This demonstration used tracking data acquired from March 16–29, 1974. The Sun–Earth–probe angle (SEP) was greater than 30 deg during this time.

As the SEP decreases, S/X calibrations indicate dramatic increases in plasma dynamics. Simultaneously, the noises of the S and X dopplers and the S/X calibrations increase by 2 orders of magnitude as the SEP decreases from 30 to 3 deg. When these calibrations are used to support Mariner 10 navigation, unreasonable results are obtained. The calibrations, their noise characteristics, and their impact on Mariner 10 navigation are herein outlined.

One possible cause for this behavior is that multi-pathing of radio signals to Mariner 10 produces phase scintillations of the S-band uplink transmission in excess of $\pi/2$ rad/s (3.5 cm of integrated phase change per second). This probably exceeds the linear performance region of the second-order phase-locked loops.

I. Introduction

The successful demonstration of the S/X dual doppler experiment for the pre-Mercury I phase of MVM'73 has been reported in Ref. 1. This article reports on the status of the demonstration around the superior conjunction period from May 27 through June 9, 1974.

A study of the superior conjunction S/X dispersive doppler reveals that those data are excessively noisy

(approximately 0.5 Hz). Moreover, when the derived charged-particle information was applied in the orbit determination (OD) process, the resultant statistics were seriously degraded and the second Mercury B plane solution was moved by an unreasonably large amount from the uncalibrated solution, which was in fair agreement with the best pre-trajectory correction maneuver 5 (TCM5-July 2) estimates.

In the following paragraphs, the characteristics of the S/X calibrations will be investigated and the data noise will be discussed. The orbit determination results for this data arc will be briefly presented, and, finally, a report will be made on the status of the investigation into the origin of the noise.

II. Noise Characteristics of the S/X Dispersive Doppler Calibrations

To put the entire S/X dual doppler demonstration (up through June 9) in perspective, let us begin with a study of the noise characteristics of the pre-Mercury I S/X charged-particle calibrations. Figure 1 shows the noise characteristics for the March 24, 1974 pass. This is one of the passes from the successful pre-Mercury I charged-particle demonstration. Application of S/X calibrations to this 9-day arc improved the quality of the doppler fit by reducing the sum of the squares of the doppler residuals by over 70%. Also, errors were diminished by 80% for one Mercury I encounter plane position estimate, based on a data set for which calibrations exist.

Figure 1 displays the S/X dispersive doppler calibrations (*) and the mean and one-sigma values as obtained from a 20-point running average through the calibrations. Note that the vertical scale is in millihertz, and, as indicated, the noise of the S/X calibration is about 2 mHz on this day. This is typical of the noise characteristics for the pre-Mercury I S/X dual-frequency doppler.

Figure 2a shows the noise characteristics for a typical day in the superior conjunction phase of the MVM'73 mission. Note, however, that the vertical scale is in hertz and the noise characteristics for this day are, therefore, at least two orders of magnitude larger than those on the pre-Mercury I days. It is also evident that the amplitude of the S/X doppler noise is not stationary. Figure 2b shows the March 24 pass plotted on the one-hertz scale.

Figure 3 displays the noise characteristics of the S/X dispersive doppler charged-particle calibrations for a few days between March 24 and June 7, 1974. Note that the scatter increases as the SEP angle decreases (Fig. 4).

III. Demonstration That the Superior Conjunction S/X Doppler Calibration Is No Reflection on Charged Particles

Figures 5, 6, and 7 display the unedited S- and X-band doppler residuals after the removal of the effects of the spacecraft trajectory and Earth's troposphere. Figure 8 shows the ratio of the noise of the X-band to that of the S-band residuals. Again these ratios have been obtained by 20-point running averages. For significant fractions of these passes, these ratios of the rms noises are larger than four. This is an important observation. The S/X experiment, as configured for Mariner 10, has only an S-band uplink capability. The X-band downlink retransmitted by the spacecraft is obtained by multiplying the S-band uplink by 880/221 (approximately a factor of 4). The charged-particle effect on the X-band is approximately 1/16 that of the S-band. Consequently, even if there is no charged-particle effect on the S-band downlink signal, the ratios as computed should be *at most four*. In other words, considering only plasma-induced noise, the relative rms noise of the X- and S-band dopplers transmitted from the spacecraft is 4 to 1, and, if the downlink S-band doppler is further scintillated by plasma dynamics, the ratio decreases. Thus, it is obvious that the high frequency variations of the dopplers are not due to charged-particle content fluctuations.

The following analysis again confirms that the "charged-particle" calibrations derived from the superior conjunction S/X dispersive doppler data do not accurately reflect the line-of-sight charged-particle dynamics. Figures 9, 10, and 11 show the S-band tracking doppler residuals before and after the application of the calibrations. The S-band residuals are of the order of 100 mHz, except for the June 7 pass when they are as large as 200 mHz. However, without exception, they become significantly larger after calibrations. This demonstrates that the S/X calibrations of the superior conjunction phase quality cannot remove the charged-particle effect. In fact, noise has been added to the doppler residuals—a noise which is not stationary.

IV. Orbit Determination Results

Since the calibrations derived from the S/X dispersive doppler data do not accurately reflect the line-of-sight charged-particle effects, when they are applied to the orbit determination process, unreasonable results are obtained. Figure 12 shows the OD results for the "state only" solution with and without calibrations. Whereas the uncalibrated B-plane solution is fairly close to the pre-TCM5 current best estimate ($\mathbf{B}\cdot\mathbf{R} \cong 24{,}000$ km, $\mathbf{B}\cdot\mathbf{T} \cong -24{,}050$ km), the calibrated estimate is displaced from the

B·R values by approximately 10,000 km. The sum of squares of the after-the-fit doppler residuals is increased by almost a factor of 20 when calibrations are applied. As illustrated in Figs. 9, 10, and 11, the calibrations have degraded the S-band residuals by imparting to them the large noise signatures that are in the S/X dispersive doppler data.

V. Status on the Investigation of Possible Noise Origins

The rms noise of S-band doppler increases dramatically as the SEP angle of the probe decreases (Fig. 13) below 10 deg. Similar behavior was observed in the Mariner 10 (Fig. 13), Mariner 9 (Fig. 13), Mariners 6 and 7 (Ref. 2), and in the Pioneer 10 and 11 (Fig. 13) S-band doppler data.

D. O. Muhleman (Ref. 3) computed the rms phase jitter of S-band frequency transmissions from plasma amplitude scintillation observations and scintillation theory. The curve containing the shaded area (Fig. 13) is the theoretical rms noise as a function of SEP angle computed by Muhleman.

The S-band doppler rms observed is 5- to 6-fold greater than the rms predicted if the SEP angle region of ±3 deg is excluded from consideration. It is an order of magnitude greater than that predicted in the ±3-deg zone.

One possible explanation for this is suggested from the knowledge that spacecraft radio tracking systems employ "second-order phase-locked loops" (Ref. 4). Such loops require less than $\pi/2$-rad phase jitter in the pass bands (Ref. 3) if they are to remain in "uninterrupted" phase lock. That is, the signal received by such a system must have coherence for time scales on the order of a second. $\pi/2$ rad of phase shift at S-band frequencies amounts to approximately 3.5 cm. A change in the total electron content along the ray path of 5×10^{15} electrons/m^2 is required. Variations of electron content far larger than these have been observed (Ref. 5). It is reasonable to assume that electron content dynamics larger than 5×10^{15} electrons/m^2/s were encountered by the Mariner 10 radio metric doppler. When such dynamics are encountered by a radio signal at S-band frequencies, the domain of linear performance of the radio tracking system may be exceeded. Note further that the doppler noise shown in Fig. 13 is roughly consistent with the 3.5-cm short-term instability.

The X-band transmission leaving the spacecraft is obtained by multiplying the spacecraft-received S-band by 880/221. Since this is an exact process, this X-band transmission has approximately 4 times the phase jitter of the S-band transmission. If the spacecraft-tracked S-band doppler contains cycle slips, then the spacecraft-transmitted X-band doppler may exceed the linear performance domain of ground receivers.

How a "linear receiving system" responds to such S- or X-band signals with such spectral characteristics may be shown:

(1) Theoretically by studying the "mathematical model of second-order loops" and how they respond to real and simulated data of the type encountered during the Mariner 10 superior conjunction.

(2) Empirically by passing wide-band doppler through the DSS 14 Block 4 receiver.

VI. Conclusion

Our experience with the S/X dual-frequency doppler demonstration for the pre-Mercury I phase was very promising. For the superior conjunction period of the mission, during which the charged-particle activities are very high, the X-band downlink only configuration is incapable of providing meaningful charged-particle calibrations.

References

1. Winn, F. B., Yip, K. W., and Reinbold, S. J., "DSN–MVM'73 S/X Dual-Frequency Doppler Demonstration," in *The Deep Space Network Progress Report 42-22*, pp. 28–50, Jet Propulsion Laboratory, Pasadena, Calif., Aug. 15, 1974.

2. Esposito, P. B., *Helios-Investigation of the Solar Corona and Relativistic Time Delays During Superior Conjunction*, TM 391-478, Aug. 22, 1973 (JPL internal document).

3. *Proceedings of the Conference on Experimental Tests of Gravitation Theories*, California Institute of Technology, Pasadena, Calif., Nov. 1970.

4. *Telecommunication System Design Techniques Handbook*, Technical Memorandum 33-571, Jet Propulsion Laboratory, Pasadena, Calif., July 15, 1972.

5. Brandt, J. C., *Introduction to the Solar Wind*, pp. 133–134, W. H. Freeman and Co., 1970.

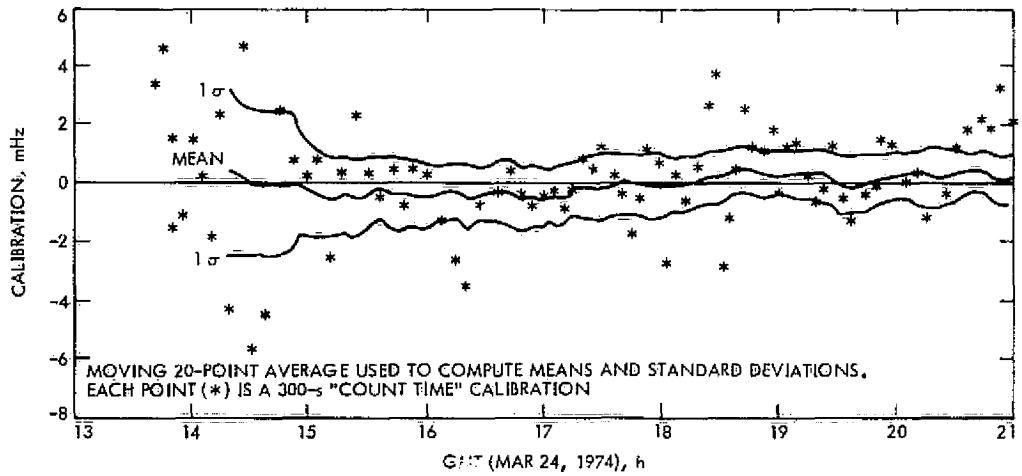

Fig. 1. Typical S/X dual doppler, charged-particle calibrations, and associated noise characteristics for the pre-Mercury I phase

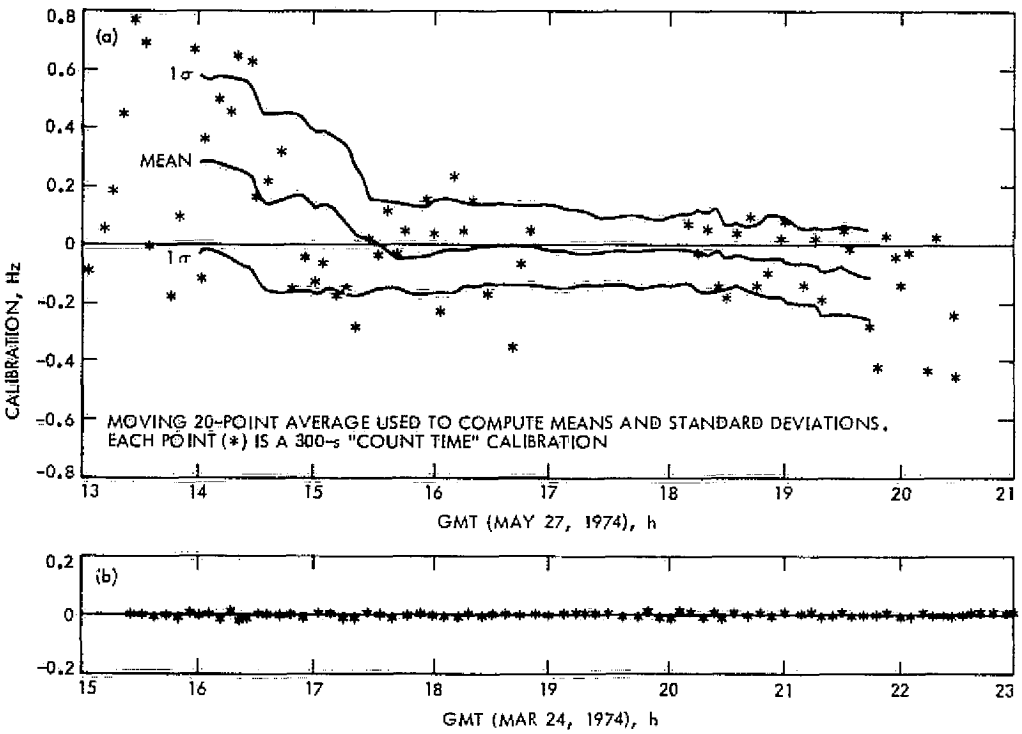

Fig. 2. Comparison of S/X dual doppler, charged-particle calibrations, and associated noise characteristics for the pre-Mercury I phase and superior conjunction phase

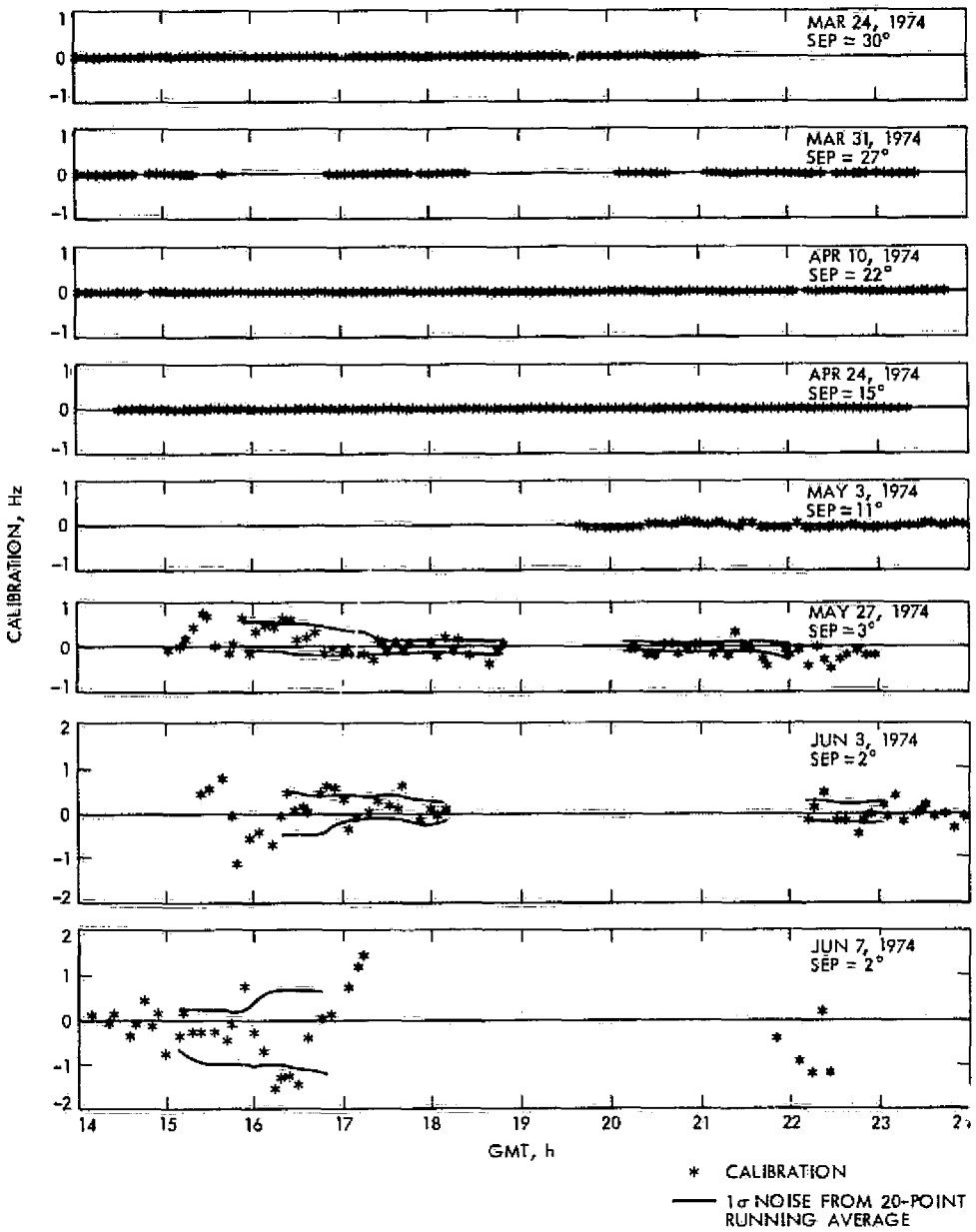

Fig. 3. Noise characteristics of S/X dual doppler charged-particle calibrations

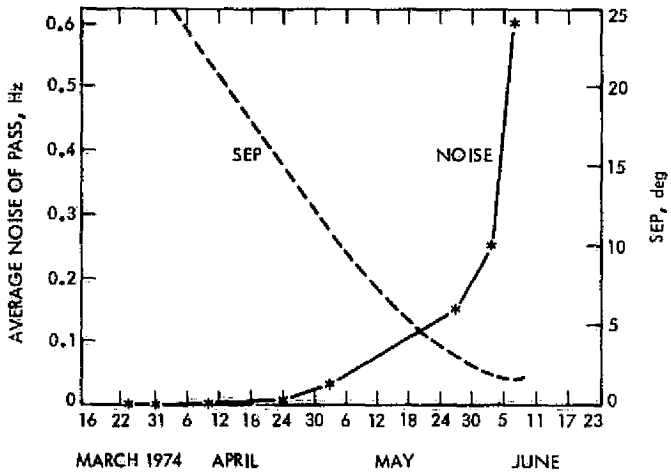

Fig. 4. Noise in S/X doppler calibrations vs SEP angle

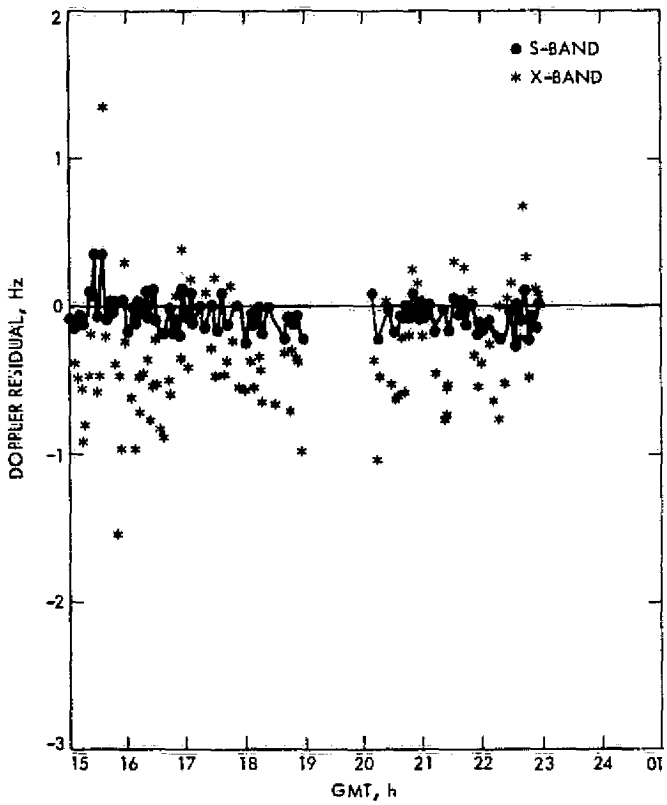

Fig. 5. S- and X-band doppler residuals for May 27, 1974

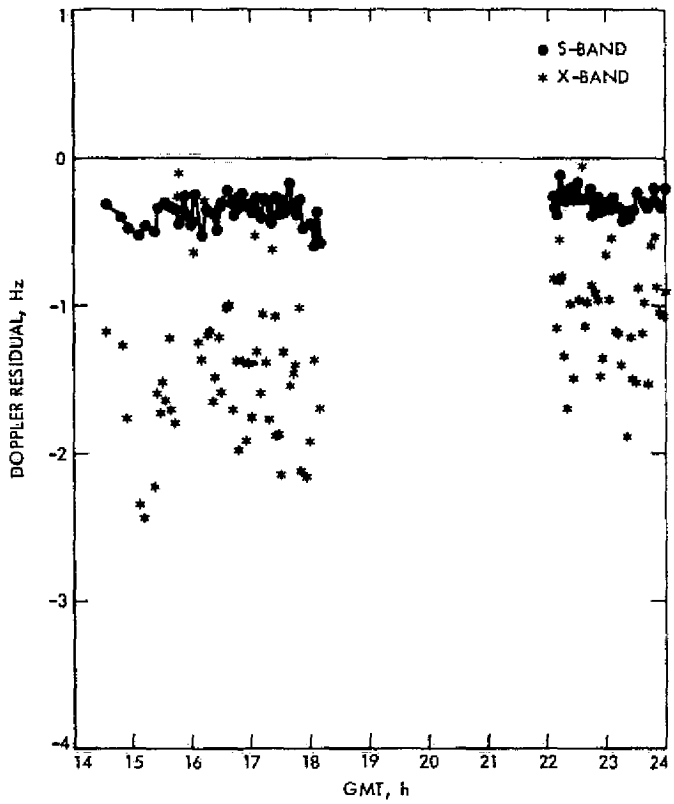

Fig. 6. S- and X-band doppler residuals for June 3, 1974

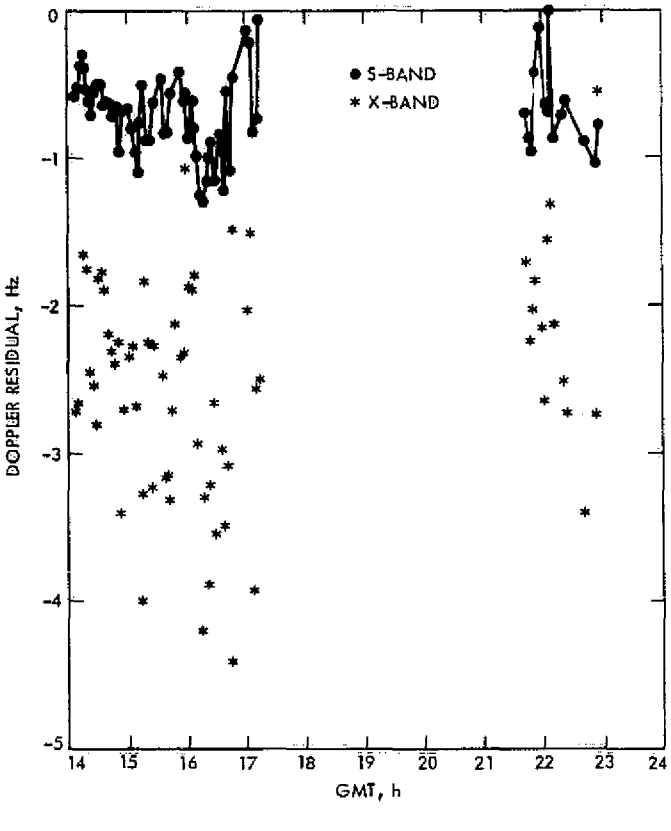

Fig. 7. S- and X-band doppler residuals for June 7, 1974

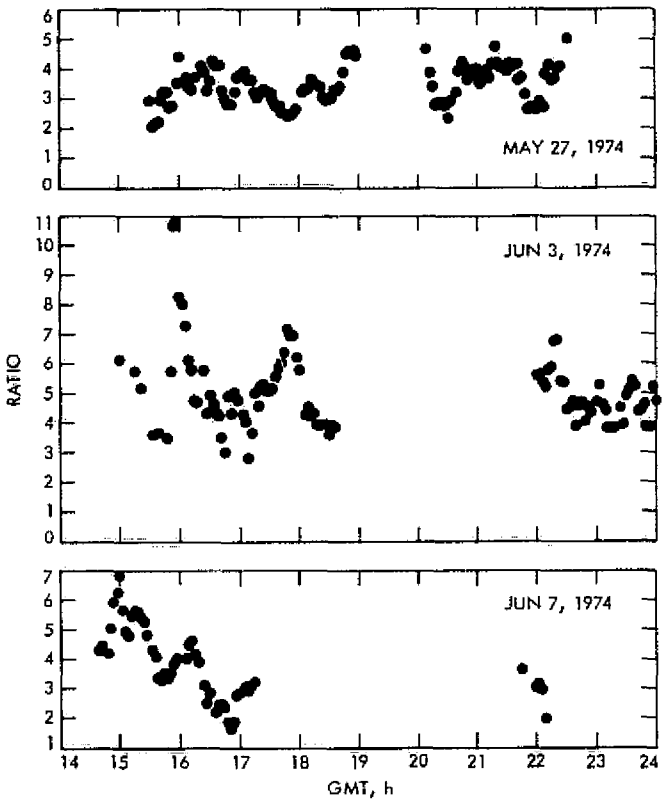

Fig. 8. Ratio of X-band to S-band doppler residual noise

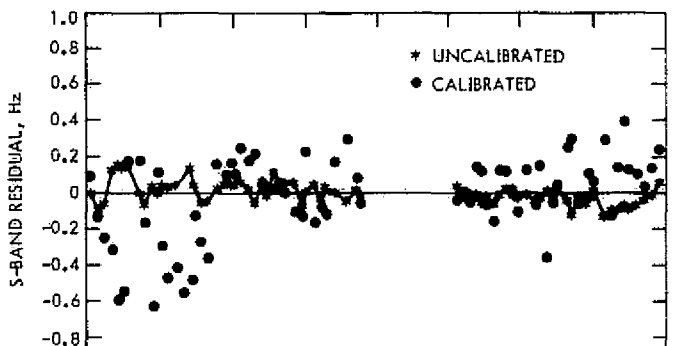

Fig. 9. Calibrated and uncalibrated S-band tracking doppler residuals (after the fit) for May 27,1974

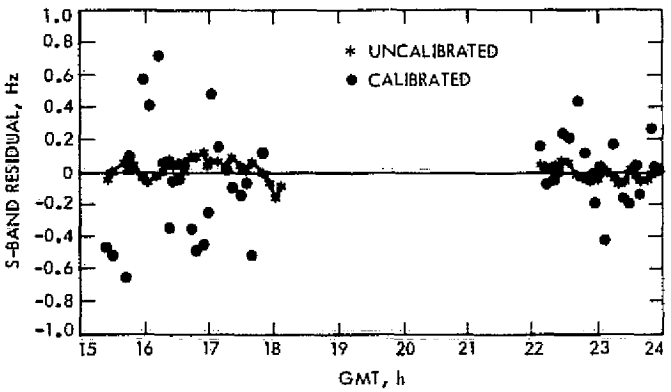

Fig. 10. Calibrated and uncalibrated S-band tracking doppler residuals (after the fit) for June 3, 1974

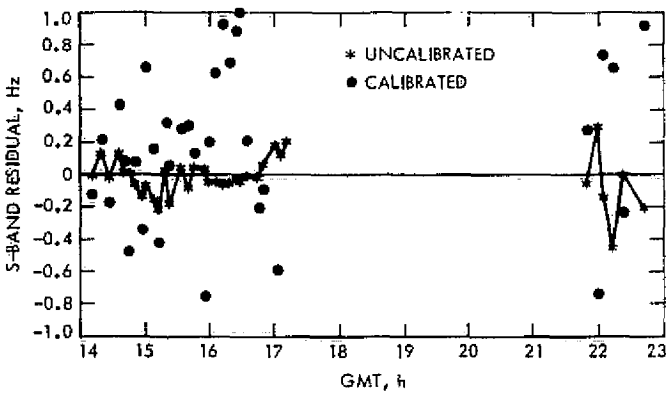

Fig. 11. Calibrated and uncalibrated S-band tracking doppler residuals (after the fit) for June 7, 1974

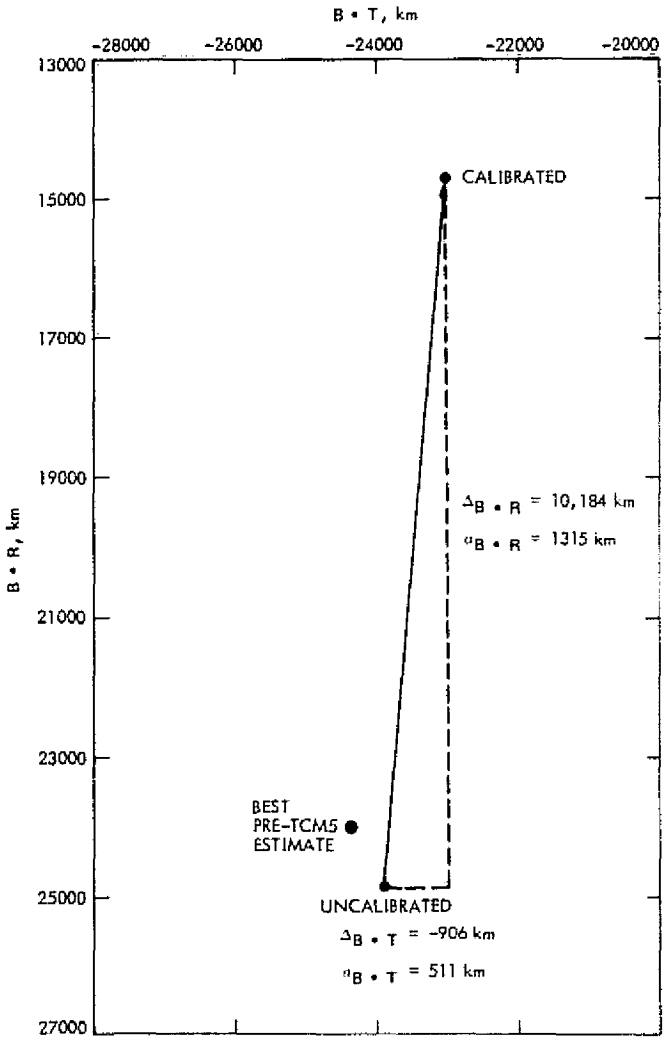

Fig. 12. Pre-TCM5 MVM'73 Mercury II encounter plane coordinate estimates: impact of superior conjunction S/X calibrations

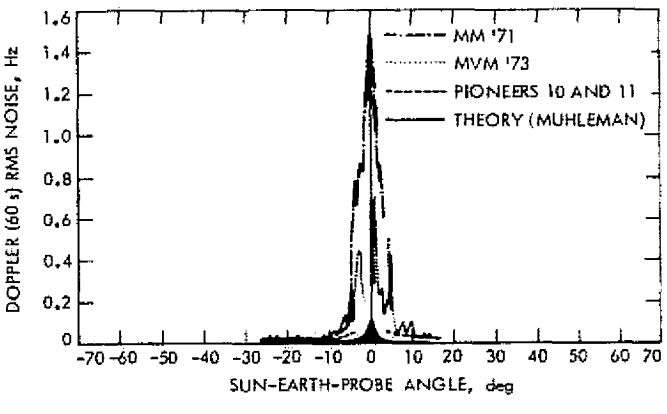

Fig. 13. Rms noise of S-band doppler vs SEP angle

Non-ionizing Radiation Hazards With the High-Power X-Band Transmitter

R. B. Kolbly
R. F. Systems Development Section

This article describes the results of a survey made to determine if any personnel hazard due to non-ionizing (microwave) radiation would be present when operating the 400-kW X-band transmitter at the Mars (DSS 14) station. This survey showed no significant hazards due to non-ionizing radiation.

I. Introduction

Traditionally, any time a DSN station is reconfigured in such a manner as to change its power output, operating frequency, or microwave configuration that in turn may alter its radiation pattern, a survey is conducted to determine if any personnel hazards are present. The Developmental Support Group, Section 335, has, in general, been responsible for these measurements.

Although the normally accepted level of non-ionizing radiation for safety is 10 mW/cm^2 (Ref. 1), there is some argument in favor of a lower power density standard for normal working conditions. JPL has used a power density of 1.0 mW/cm^2 as a working limit for personnel safety (Ref. 2).

In preparation for the MJS'77 mission, a 400-kW X-band (8495 MHz) CW radar has been installed on the DSS 14 64-m antenna. This radar is to determine the structure of the rings of Saturn in preparation for spacecraft encounter. This high-power radar installation represents a significant extension of the capabilities of DSS 14, and previous experience with high-power X-band operation of the DSS 13 100-kW X-band transmitter on the 9-m antenna has indicated a possibility of hazardous radiation levels (Ref. 3).

II. Procedure

Since this survey was conducted for the sole purpose of determining if any personnel hazards exist due to non-ionizing radiation, an isotropic survey probe was used. Although other techniques, such as a power meter and standard gain horn, are more sensitive than the isotropic probes, the standard gain horn tended to give readings 6 to 10 dB lower. This is because the stray radiation from an antenna does not, in general, present a plane wavefront to the signal gain horn. The isotropic probe has a much smaller aperture so the phase error across the measurement aperture is not significant.

The Narda Model 8315 power density meter and the Narda Model 8321 isotropic probe were used to conduct this survey. The minimum detectable signal with these instruments is approximately 0.1 mW/cm^2, giving a safety factor of 10 over the minimum hazard level. The Narda instruments have a history of reliability, and their usage is approved by the JPL Safety Office. In addition, two instruments were used in some instances as a cross-check. A catastrophic failure of one instrument (not due to a fault within the instrument) prevented complete redundancy throughout this survey.

This survey was conducted in two parts. The first part was with the antenna in the stowed (zenith) position, and a survey of work locations, both on the antenna and at the station in general, was made. Also, normally used access routes (ladders, stairways, sidewalks, etc.) were searched for possible hazards. The second part of this survey was conducted with the antenna in several positions representing beginning, mid-point, and end of a Saturn track (planet rise, meridian crossing, and set). During the second part of this survey, no checks were made of the antenna structure itself.

III. Results

The results of the first part of the survey with the antenna in its stowed (zenith) position are shown in Table 1. The areas in excess of 1.0 mW/cm^2 are confined to the Module III area of the cone. This is the area immediately below the feed cones and is primarily used for receiver equipment. These "hot spots" are associated in all cases with hatches and doorways. All areas below the surface of the antenna were "cold," and no hazardous spots were detected.

Table 2 gives the observed data of that portion of the survey with the antenna in typical Saturn tracking positions. The significant feature is the lack of stray microwave radiation. At the conclusion of this test, the antenna was raised to zenith with the probe held in one spot to determine if spill-over or hyperboloid/quadripod scatter could cause a radiation hazard. No significant signals were detected during this test.

IV. Conclusions

Based on the data in Tables 1 and 2, the operation of an X-band 400-kW transmitter on the DSS 14 64-m antenna will not result in any hazard to personnel if personnel are restricted to areas below the antenna surface during high-power operations. By more effectively sealing the hatches and doors in the Module III area, it would be possible to allow personnel to work in the Module II and III areas without hazard during high-power X-band radiation.

References

1. *Safety Level of Electromagnetic Radiation with Respect to Personnel*, USAS C95.1-1966, United States of America Standards Institute, 1966.
2. *Radiation Precautions in the Deep Space Instrumentation Facilities*, EPD-108, Aug. 1, 1962 (JPL internal document).
3. Kolbly, R. B., *Non-Ionizing Radiation Hazard Survey at Venus 9 Meter Antenna*, IOM 335C-71-060, Oct. 15, 1971 (JPL internal document).

Table 1. DSS 14 radiation survey (antenna at zenith)

Location	Transmitter power, kW	Measured value, mW/cm²	Expected value at 500 kW, mW/cm²
Module III area			
Right access door	100	0.1	0.3
Left access door	100	0.3	0.9
XKR cone access hatch	200	2.0	3.0
SMT cone access hatch	150	0.8	1.6
Room area in general	150	<0.1	0.1
RF connector at TWT	150	1.5	1.5[a]
Hatch near harmonic filter (unused)	200	5.0	7.5
Central hub area (overhead)	300	0.7	0.7
Module II area			
Transmitter bay doors	300	0.2	0.2
Room work areas (overall)	300	<0.1	<0.1
Hub area			
Surface access door	300	0.1	0.1
Ladder area	180	<0.1	<0.1
Lower hub area	300	<0.1	<0.1
Elevation axis catwalk	300	<0.1	<0.1
Elevation bearing platform	300	<0.1	<0.1
Stairway above elevation bearing	300	<0.1	<0.1
Elevation drive platform	300	<0.1	<0.1
Lower elevation drive platform	300	<0.1	<0.1
Filter house area	300	<0.1	<0.1
Azimuth platform	300	<0.1	<0.1
Maser compressor area	300	<0.1	<0.1
Stairway to ground	300	<0.1	<0.1
Walkway to control building	300	<0.1	<0.1
Control room	300	<0.1	<0.1
Butler building general area	300	<0.1	<0.1
Generator building (G-81)	300	<0.1	<0.1

[a]Not a function of transmitter power.

Table 2. DSS 14 radiation survey (tracking positions)[a]

Location	Saturn rise (Az = 84.0°, El = 10.8°), mW/cm²	Saturn meridian crossing (Az = 180.0°, El = 76.0°), mW/cm²	Saturn set (Az = 282.0°, El = 10.8°), mW/cm²
DSS 14 control room	<0.1	<0.1	<0.1
Walkway to 64-m antenna	<0.1	<0.1	<0.1
64-m antenna chain perimeter	<0.1	<0.1	<0.1
Directly below disk lip	0.10	<0.1	0.12
Steps to heat exchanger	0.15	<0.1	<0.1
30 m (100 ft) on dish axis	<0.1	<0.1	<0.1
15 m (50 ft) east of G-83 heat exchanger	0.12	<0.1	<0.1
Building G-82	<0.1	<0.1	<0.1
MG Set and G-82 area	<0.1	<0.1	<0.1
West wind tower	<0.1	<0.1	<0.1
G-81 (power house)	<0.1	<0.1	<0.1
SSE Butler building	<0.1	<0.1	<0.1
Front of control building	<0.1	<0.1	<0.1
Road to guard station	<0.1	<0.1	<0.1
Guard station	<0.1	<0.1	<0.1
Road to rear of control room	<0.1	<0.1	<0.1
West survey marker plate antenna plunge test (Az = 282.0°, 10.8° < El < 87°): <0.1 mW/cm² (weak signal ~0.1 mW/cm² as hyperboloid went out of view ~22° elevation)			

[a] $P_{T\,Radiation}$ = 300 kW.

Noisy Reference Effects on Multiple-Antenna Reception

J. W. Layland
Communications Systems Research Section

Multiple-Antenna Reception (MAR) is a technique for coherently adding the spacecraft signals received at two or more antennas in order to achieve an improvement in down-link telemetry performance. The feasibility was recently demonstrated at the second Mercury Encounter of Mariner 10. The data rate for this demonstration was a lusty 117 kbps uncoded. At this data rate, the received carrier signal is strong enough at each of the receiving sites that there is negligible loss due to noise in the carrier–tracking loops. The MAR technique could also be used to enhance the data return from the outer planet Pioneer and Mariner probes, in which case the data rates are, or can become, low enough that the effects of the noisy carrier references cannot be ignored. In the work which follows, previously developed tools for analyzing the effects of noisy carrier reference losses in the standard Deep Space Network configuration are applied to the MAR technique.

Multiple-Antenna Reception (MAR) is a technique for coherently adding the spacecraft signals received at two or more antennas in order to achieve an improvement in down-link telemetry performance. The feasibility was recently demonstrated by Wilck, et al. (Ref. 1) at the second Mercury Encounter of Mariner 10. The data rate for this demonstration was a lusty 117 kbps uncoded. At this data rate, the received carrier signal is strong enough at each of the receiving sites that there is negligible loss due to noise in the carrier–tracking loops. The MAR technique could also be used to enhance the data return from the outer planet Pioneer and Mariner probes, in which case the data rates are, or can become, low enough that the effects of the noisy carrier references cannot be ignored. In the work which follows, previously developed tools for analyzing the effects of noisy carrier reference losses in the standard Deep Space Network configuration are applied to the MAR technique.

Figure 1 is a block diagram of the MAR technique. The spacecraft signal plus Additive White Gaussian Noise is received at each of two or more receiving systems. The additive noise can be assumed to be independent at each of the receiving sites. The received carrier is phase-and-frequency tracked at each of the receiving sites, and the resulting reconstructed carrier reference is used to demodulate the telemetry sidebands from the received signal. The resulting baseband telemetry signals

are combined in a weighted average depending upon their relative average SNRs; and the telemetry data stream is then detected/decoded from this combined baseband telemetry signal. The signals from each antenna are aligned in time and add coherently. The independent additive noises from each receiver add incoherently, or in mean square. The carrier phase reference noises at each antenna/receiver are also independent. We cannot, however, conveniently add these phase noises in their effect upon the detection error rate. For single-antenna reception, the effects of the carrier reference errors are included by computing the error probability as conditioned upon some value of carrier reference efficiency (losses), and then averaging over the distribution of that efficiency. Specifically, if we let η be the coherent demodulator efficiency, and $p(\eta)$ its distribution,

$$P_e = \int_0^1 \Pr\{\text{Error}|\text{SNR}, \eta\}\, p(\eta)\, d\eta \qquad (1)$$

The form of this probability integral has been previously computed for both uncoded and convolutionally encoded–sequentially decoded telemetry (Refs. 2 and 3). This procedure can be readily utilized for the MAR situation by replacing η in Eq. (1) with the weighted average of the detection efficiencies of the individual receivers, and averaging over the distribution of the individual efficiencies. For two antennas,

$$P_e' = \int_0^1 \int \Pr\{\text{Error}|\text{SNR}^c, g_1\eta_1 + g_2\eta_2\}\, P(\eta_1)\, P(\eta_2)\, d\eta_1 d\eta_2 \qquad (2)$$

SNR^c is the combined effective SNR; η_1, η_2 are the two instantaneous efficiencies; and g_1, g_2 are the combining weights for the two receiving systems ($g_1 + g_2 = 1$).

Figures 2a through 2c show the computed bit error probability for the MAR operation of two identical receiving antennas in comparison with the performance of a single antenna/receiver for data rates of 8, 128, and 2048 bps. The data are shown as a function of down-link modulation index for several values of the total power-to-noise spectral-density ratio. The performance shows the expected 3 dB advantage of the MAR at low modulation indices where it is determined largely by the combined SNR without consideration of the carrier reference detection efficiency. As is evidenced by Fig. 2, at extremely high modulation indices where the carrier reference efficiency is a dominant factor, there is almost no improvement in the MAR performance as compared to the individual antenna/receiver's performance. At reasonable modulation indices, the degradation due to carrier detection efficiency for uncoded telemetry from the potential 3 dB improvement of MAR is less than 0.1 dB for 2048 bps (or higher), about 0.3 dB for 128 bps, and almost 1 dB for 8 bps.

The same set of calculations has been performed for the sequential decoding deletion probability using a medium rate model (Ref. 3). The results appear as shown in Figs. 3a through 3c. At reasonable modulation indices, the degradation due to carrier detection efficiency from the potential 3 dB improvement of MAR is again less than 0.1 dB at 2048 bps, about 0.3 dB at 128 bps, and almost 1 dB at 8 bps.

References

1. Wilck, H. et al., "A Signal Combiner for Antenna Arraying," in this issue.
2. Layland, J. W., "A Note on Noisy Reference Detection," in *The Deep Space Network Progress Report*, Technical Report 32-1526, Vol. XVII, pp. 83–88, Jet Propulsion Laboratory, Pasadena, Calif., Oct. 15, 1973.
3. Layland, J. W., "A Sequential Decoding Medium Rate Performance Model," in *The Deep Space Network Progress Report*, Technical Report 32-1526, Vol. XVIII, pp. 29–33, Jet Propulsion Laboratory, Pasadena, Calif., Dec. 15, 1973.

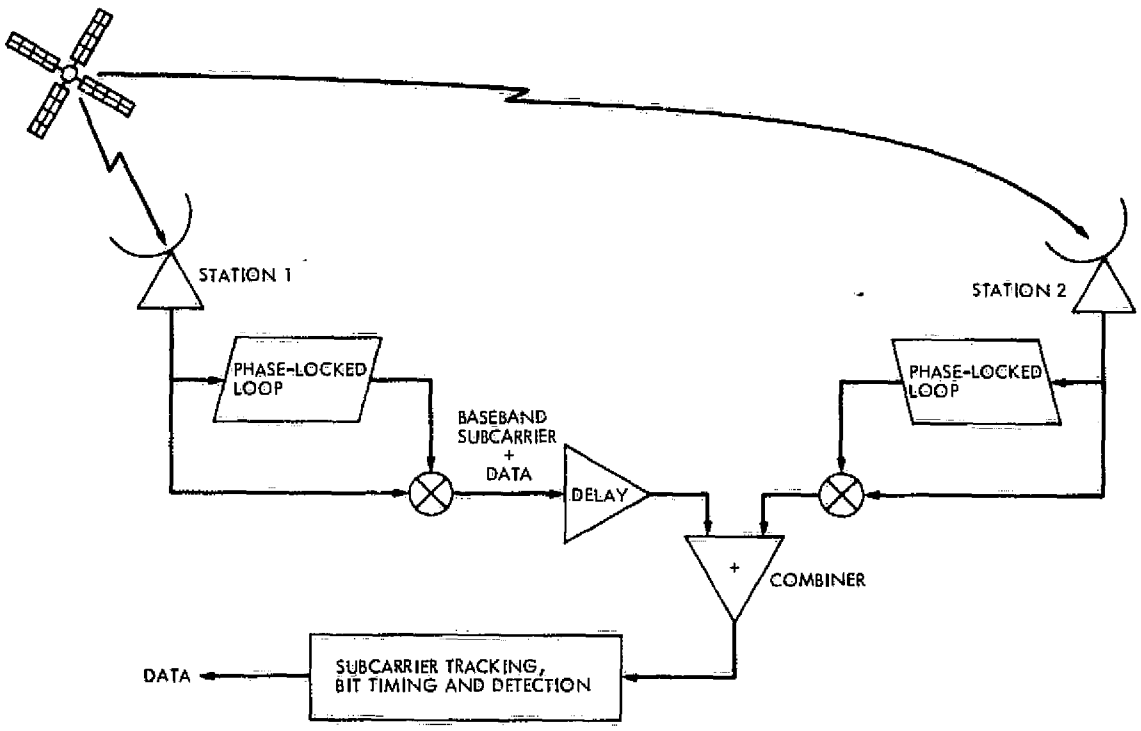

Fig. 1. Block diagram of MAR configuration

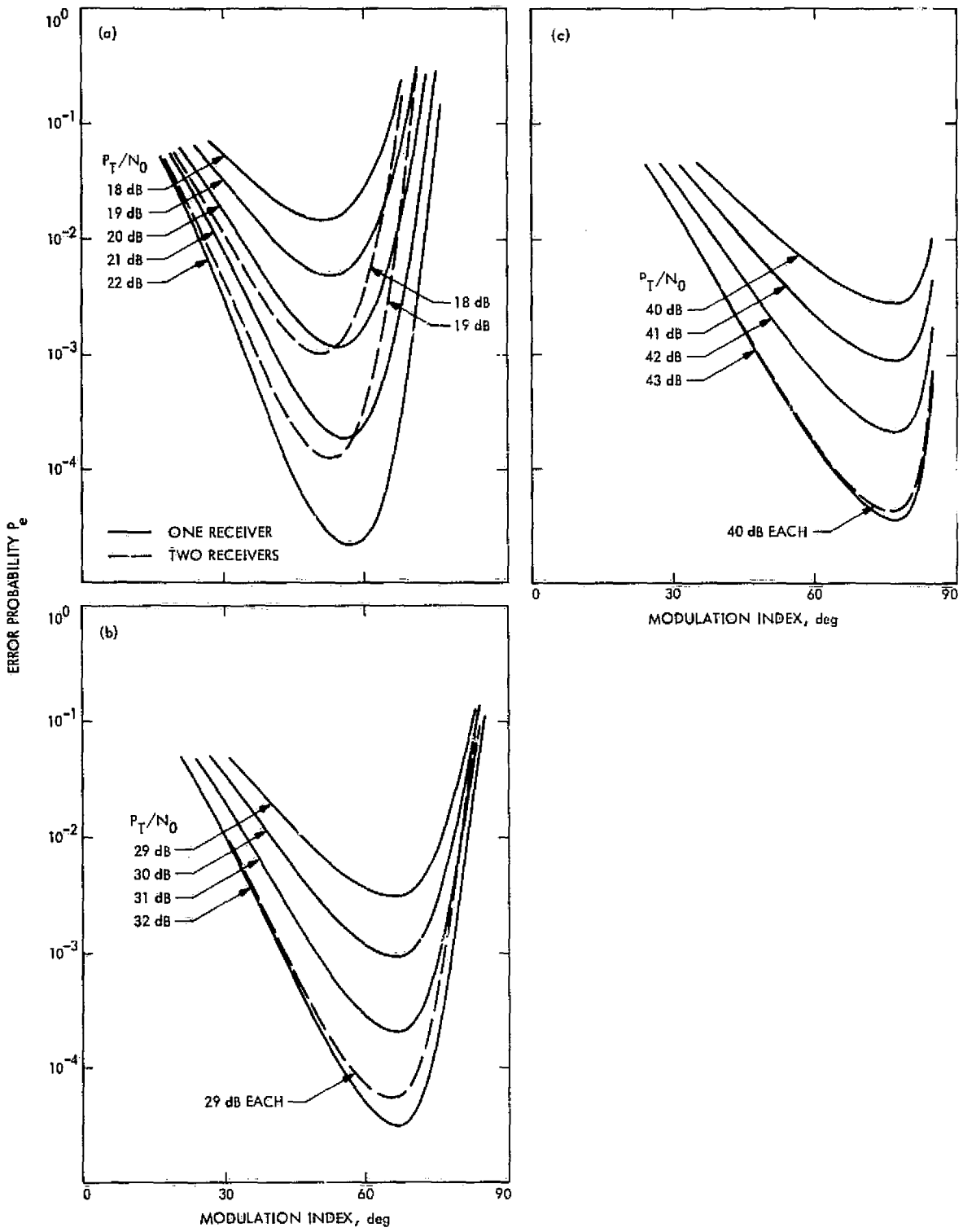

Fig. 2. Uncoded MAR performance estimate; (a) 8 bps, (b) 128 bps, (c) 2048 bps

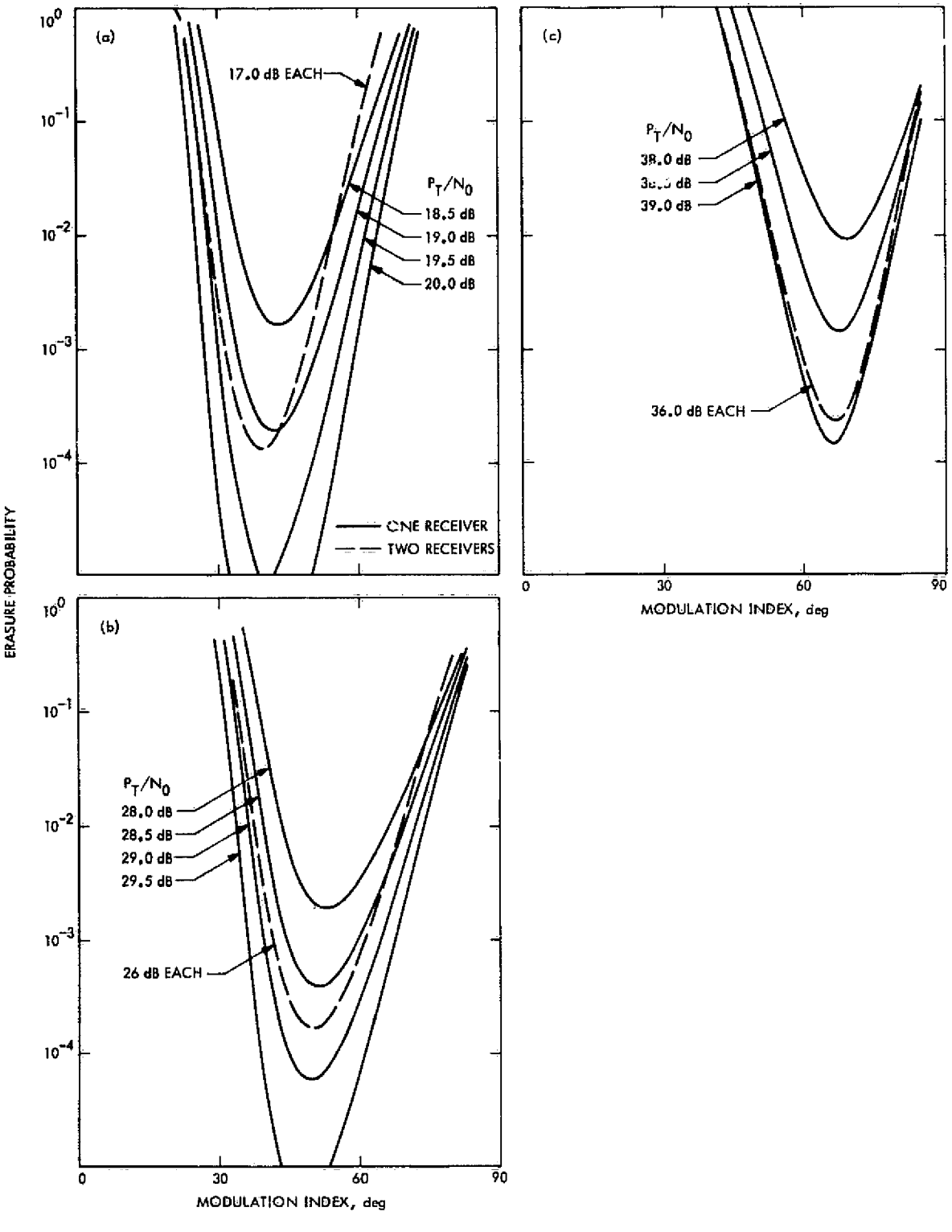

Fig. 3. Sequential decoding MAR performance estimate; (a) 8 bps, (b) 128 bps, (c) 2048 bps

Low Noise Receivers: Microwave Maser Development

R. C. Clauss
Communications Elements Research Section

A well-matched dielectrically loaded waveguide, for operation between 18 and 26.5 GHz, has been built and is being used to test the characteristics of ruby for wide-bandwidth maser applications. The unit serves a dual purpose. The initial plan was to investigate and optimize pumping techniques at 19 and 24 GHz for future use with wide-bandwidth X-band masers. Results show that an order of magnitude improvement in pumping efficiency is possible. A second use for the dielectrically loaded waveguide was found during the initial tests. The unit has excellent amplifying capability in the 18- to 26.5-GHz range when used as a reflection-type amplifier. Gains of 7.5 dB (at 4.4 kelvins) and 16 dB (at 1.9 kelvins) were measured with instantaneous bandwidth exceeding 250 MHz.

I. Introduction

A ruby-filled waveguide section has been built and is being used to investigate wide-bandwidth maser techniques. The device is used to measure pump power absorption characteristics of ruby at 19 and 24 GHz; these frequencies will be used to pump a wide-bandwidth X-band maser. The ruby-filled waveguide is well matched and has low loss across the entire 18- to 26.5-GHz range. Excellent gain and bandwidth have been achieved at 24 GHz by using the device as a reflection-type amplifier.

II. Waveguide and Matching Section

A 0.178-cm-high, 0.356-cm-wide, 4.54-cm-long waveguide, loaded with ruby, is matched to a standard WR 42 (18- to 26.5-GHz) waveguide. The matching section is a 7.62-cm-long waveguide taper partially filled with ruby. The dielectric constant (ϵ) of ruby is approximately 9. The waveguide and matching section are machined copper parts, consisting of a body and covers, which are bolted together. The body, top cover, and ruby dielectric are shown in Fig. 1. Figure 2, a cutaway

drawing, shows two views which illustrate the waveguide and matching taper details. The copper waveguide matching section tapers towards the dielectric in two directions. The dielectric is tapered in only one direction, leaving a flat (0.365-cm-wide) surface with intimate contact to a flat copper surface along the entire length of the dielectric piece. No other surface of the dielectric piece needs to contact the copper waveguide. A gap of 0.003 cm between the dielectric and the copper waveguide is used so that parts may be machined and assembled with ease, and problems caused by differential thermal expansion between the dielectric and the copper waveguide are avoided. The gap across the 0.178-cm dimension affects the electric field, raising the low cutoff frequency of the loaded waveguide (about 14 GHz) about 3%. The gap does not degrade the match of the device in the 18- to 26.5-GHz range. An absorber was used at the end of the dielectric waveguide for measurement purposes; a VSWR of less than 1.2 to 1 was achieved across the 18- to 26.5-GHz range. The one-way transmission loss of the ruby-filled waveguide and matching section at room temperature is 0.6 dB. At temperatures below 20 kelvins, the one-way loss is estimated to be 0.2 dB.

III. Pump Power Considerations

X-band traveling-wave masers now in use require pump sources which produce more than 100 mW of power at both 19 and 24 GHz (Ref. 1). Refrigeration capacity measurements show that 50 to 100 mW of the applied pump power result in a heat load which is delivered from the maser to the 4.5-kelvin refrigeration station. Attempts to measure the absorption of pump power caused by the paramagnetic resonance of the maser material at the pump frequencies by thermal capacity measurements gave no detectable results. The resolution of the refrigeration capacity measurement system was about 5 mW. The conclusion, that more than 95% of applied pump power is wasted in the existing maser systems, is reinforced by test results using the ruby-filled waveguide. Application of a 5-mW test signal to the ruby-filled waveguide eliminates detectable signal absorption due to paramagnetic resonance at 19 and 24 GHz; this indicates that complete saturation of the pump transitions is possible at the 5-mW power level.

Masers with wide instantaneous bandwidth have the requirement that pump energy must also be distributed across a wide bandwidth. To achieve a 100-MHz bandwidth at X-band, the K-band pump sources must distribute energy across a 300-MHz range. Improvements in pumping efficiency will reduce pump power requirements, simplify construction and reduce the cost of pumping systems, and reduce heat loads caused by pump power at the 4.5-kelvin refrigerator station.

IV. Gain and Bandwidth Near 24 GHz

The ruby-filled waveguide was tested as an amplifier near 24 GHz. A block diagram of the amplifier system is shown in Fig. 3; a pump source (Siemens RWO 60 backward wave oscillator), a pump power coupling device, and a 33-GHz cutoff low-pass filter were added to the system, which had been assembled for previous pump transition saturation tests. Magnetic shims were added to the ruby-filled waveguide body to broaden the maser-material linewidth. Figure 4 shows gain between 7 and 7.7 dB across a 285-MHz bandwidth centered at 24.6 GHz. This performance was achieved at a refrigerator temperature of 4.4 kelvins. Figure 5 shows gain between 15 and 17 dB across a 250-MHz bandwidth centered at 24.4 GHz; a 1.9-kelvin refrigerator temperature was used to achieve this performance. Between 5 and 10 mW of pump energy was applied to the ruby in the above tests. Saturation of the pump level was almost complete; a 3-dB increase in pump power would cause only a 1-dB increase in gain. The pump energy supplied by the RWO 60 was distributed across a 500-MHz bandwidth near 52 GHz by frequency modulation at a 20-kHz rate.

The ruby-filled waveguide, combined with a circulator and a pump source, forms a simple maser amplifier stage which can be electronically tuned across the entire 18- to 26.5-GHz range. Combination of several stages can be used to achieve high gain with wide instantaneous bandwidth.

Reference

1. Clauss, R. C., and Quinn, R. B., "Low Noise Receivers: Microwave Maser Development," in *The Deep Space Network Progress Report*, Technical Report 32-1526, Vol. IX, pp. 128–136, Jet Propulsion Laboratory, Pasadena, Calif., June 15, 1972.

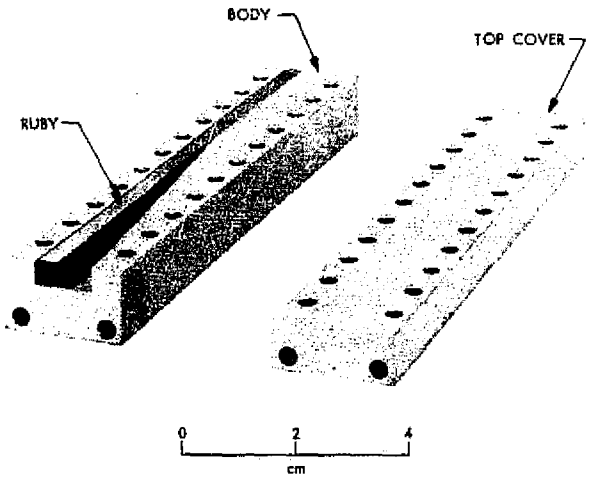

Fig. 1. Ruby-filled waveguide and matching section (covers removed)

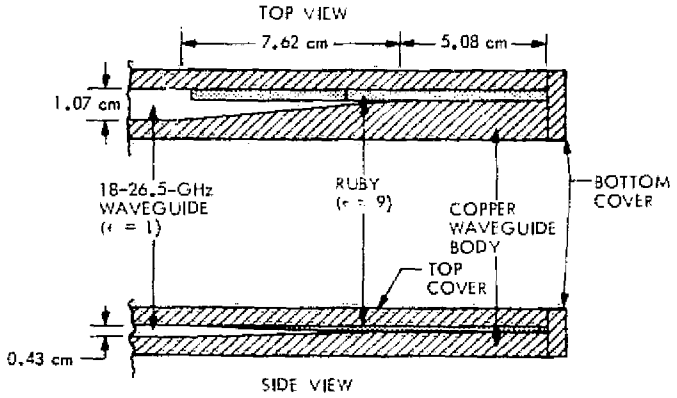

Fig. 2. Cutaway drawing of ruby-filled waveguide and matching section

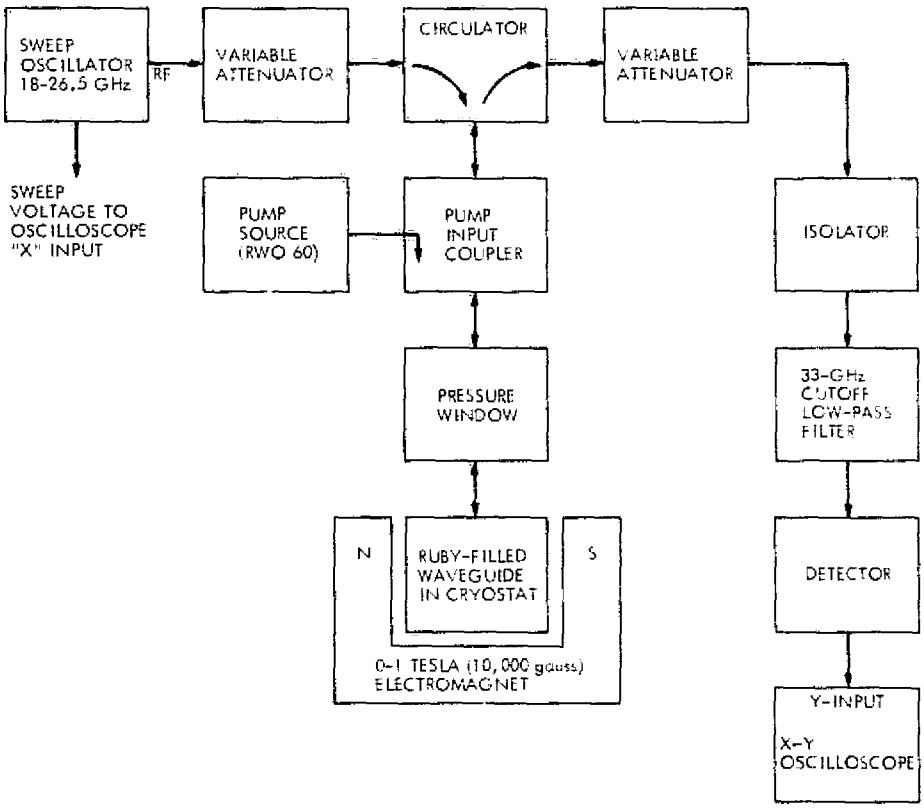

Fig. 3. 24-GHz maser amplifier system

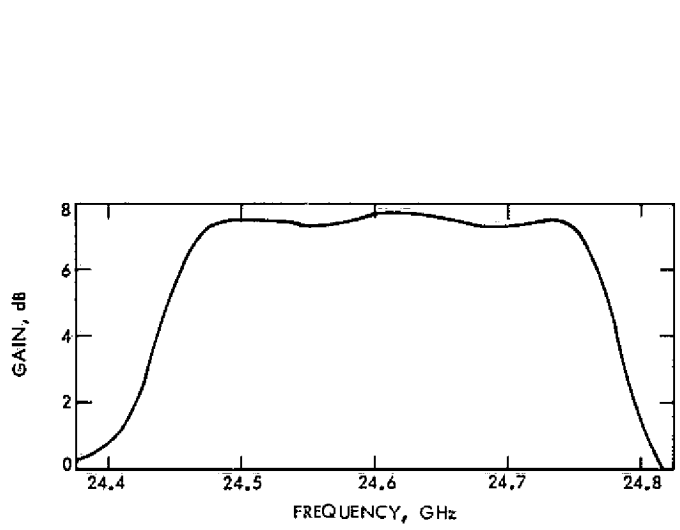

Fig. 4. Maser gain and bandwidth: refrigerator at 4.4 kelvins

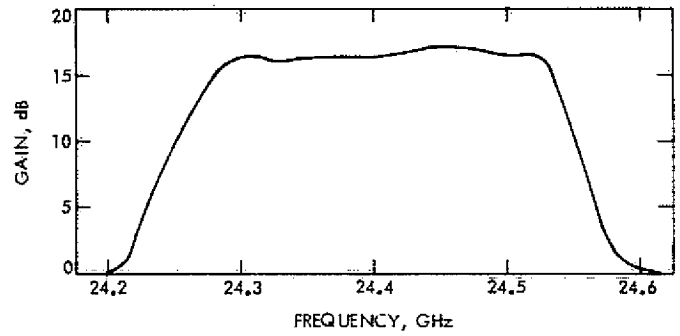

Fig. 5. Maser gain and bandwidth: refrigerator at 1.9 kelvins

S/X Band Experiment: A Study of the Effects of Multipath on Two-Way Range

T. Y. Otoshi
Communications Elements Research Section

Equations are presented for determining two-way range errors caused by multipath. The analysis of two-way range error is more complex than that for one-way range due to the fact that the uplink and downlink range errors oscillate at different rates when the leakage path length is varied. A limited amount of two-way range data was obtained with the Mu-1 ranging machine, Mariner Venus/Mercury 1973 Radio Frequency Subsystem, and Block 3 receiver. The agreement between theoretical and experimental values was typically better than 2 ns.

I. Introduction

In this article, the term "one-way" range will be used to refer to either uplink or downlink range while the term "two-way" range will be used to refer to the sum of the uplink and downlink ranges. For the S/X band experiment the uplink frequency transmitted to the spacecraft transponder was 2113 MHz, while coherent S/X band downlink frequencies transmitted back to the ground station were 2295 and 8415 MHz. In a dispersive media, the two-way range will not generally be equal to twice the one-way range.

The analysis of the effects of multipath on one-way range was presented previously by this author in Ref. 1 and by J. R. Smith in Ref. 2. Theoretical equations for one-way range errors were verified experimentally by use of a multipath device, MVM'73 Radio Frequency Subsystem, Block 3 receiver/exciter subsystem (RCV) and the Mu-1 ranging machine.

This report presents theoretical equations which can be used to analyze the effects of multipath on two-way range. In addition, some experimental data, which show good agreement with the theory, will be presented.

II. Theoretical Equations

A. Exact Formulas

The geometry for two-way range error analysis may be seen in Fig. 1. For this geometry the two-way range error is simply the algebraic sum of the one-way range error for the uplink signal and the one-way range error for the downlink signal.

The equation for two-way range can be expressed as

$$(t_g)_T = (t_{g1})_a + (t_{g1})_b + \epsilon_{ga} + \epsilon_{gb} \tag{1}$$

and the two-way range error as

$$(\epsilon_g)_T = \epsilon_{ga} + \epsilon_{gb} \tag{2}$$

where

$(t_{g1})_a$ = group delay of the uplink signal in the absence of multipath, s

$(t_{g1})_b$ = group delay of the downlink signal in the absence of multipath, s

ϵ_{ga} = error in the uplink delay due to multipath, s

ϵ_{gb} = error in the downlink delay due to multipath, s

For simplicity, assume that the primary and leakage paths are the same for the uplink and downlink signals (Fig. 1). Then from the equations derived in Ref. 1, and assuming a free-space media for both leakage and primary paths

$$\epsilon_{ga} = \frac{(\ell_2 - \ell_1)}{c} A \left(\frac{A + \cos\theta_a}{1 + 2A\cos\theta_a + A^2} \right) \tag{3}$$

$$\epsilon_{gb} = \frac{(\ell_2 - \ell_1)}{c} A \left(\frac{A + \cos\theta_b}{1 + 2A\cos\theta_b + A^2} \right) \tag{4}$$

where

$$\theta_a = \frac{-2\pi f_a}{c} (\ell_2 - \ell_1) + \psi_a \tag{5}$$

$$\theta_b = \frac{2\pi f_b}{c} (\ell_2 - \ell_1) + \psi_b \tag{6}$$

and

A = ratio of the magnitudes of the leakage and primary signals as measured at the input port to the transponder (Fig. 1)

ℓ_1, ℓ_2 = physical path lengths, respectively, of the primary and leakage paths going one-way, m

c = speed of light ($\cong 3 \times 10^8$ m/s)

f_a, f_b = uplink and downlink frequencies, respectively, in Hz

ψ_a, ψ_b = phase angles of reflection coefficients (if any) in the leakage path for uplink and downlink signals, respectively, in radians

The terms ψ_a and ψ_b in Eqs. (5) and (6) have been added for generality. It is assumed that the reflection coefficient phase angles do not change with frequency over the frequency interval of interest and, therefore, only affect the location of the upper and lower bounds of range error (see Appendix A).

It is also of interest to examine the effects of multipath on the AGC signal level as observed on the ground receiver. If the transponder is similar to that of the MVM'73 spacecraft where the downlink output signal of the transponder is kept constant even if the uplink signal is varying, then the AGC signal level error at the ground receiver will vary according to the relationship. (Ref. 1):

$$|F_b|_{dB} = 10 \log_{10} [1 + 2A\cos\theta_b + A^2] \tag{7}$$

If the transponder is a translator or a zero delay device, the AGC signal level error measured at the ground receiver will vary according to the relationship

$$|F_T|_{dB} = 10 \log_{10} [(1 + 2A\cos\theta_a + A^2)(1 + 2A\cos\theta_b + A^2)] \tag{8}$$

B. Approximate Formulas

The exact equations presented above are somewhat difficult to analyze because the uplink and downlink phases change at different rates. In the cases of small leakage one can make approximations which show a type of modulation effect produced by the uplink and downlink error functions adding together. If x represents the terms having factors of A in the denominators of Eqs. (3) and (4) one can use the small x approximation that $(1 + x)^{-1} \cong 1 - x$. Then, from substitutions into Eq. (2), omitting higher order terms of A after multiplication and the use of trigonometric identities, one obtains the approximate formula

$$\begin{aligned}(\epsilon_g)_T &\approx A \left(\frac{\ell_2 - \ell_1}{c} \right) \\ &\quad \times [\cos\theta_a + \cos\theta_b - A(\cos 2\theta_a + \cos 2\theta_b)] \\ &\approx 2A \left(\frac{\ell_2 - \ell_1}{c} \right) \left[\cos\frac{1}{2}(\theta_b - \theta_a) \cos\frac{1}{2}(\theta_b + \theta_a) \right. \\ &\quad \left. A\cos(\theta_b - \theta_a)\cos(\theta_b + \theta_a) \right]\end{aligned} \tag{9}$$

The accuracy of the above approximate formula is better than 3% if $A \leq 0.1$. If the difference between the uplink

and downlink signals is small, then the error curves will be similar to an amplitude-modulated signal where the envelope of the modulation is proportional to cos $[(1/2)(\theta_b - \theta_a)]$ and the carrier signal is given by cos $[(1/2)(\theta_b + \theta_a)]$.

Similarly, when the small leakage signal approximations are used in Eq. (8), the following approximate formula is obtained

$$|F_T|_{dB} \simeq 10 \log_{10}\left[1 + 4A \cos\frac{1}{2}(\theta_b - \theta_a) \cos\frac{1}{2}(\theta_b + \theta_a)\right] \tag{10}$$

C. Sample Cases

Figures 2 through 13 are sample case plots of Eqs. (2) and (8) for leakage signal levels of −30 dB, −20 dB, and −10 dB relative to the primary signal. Figures 2 through 7 are plots applicable for 2113-MHz uplink and 2295-MHz downlink cases, while Figs. 8 through 13 are applicable to 2113-MHz uplink and 8415-MHz downlink cases. For these sample cases, the leakage path is initially assumed to be 3048 cm (100 ft) longer than the primary path. Then the leakage path is increased and errors are plotted as a function of increasing differential path lengths. Error curves for other differential path lengths will be similar in shape, but the amplitudes will differ by the ratio of the differential path lengths. At some critical differential path length the errors become worst case, and the upper and lower bounds will be twice those for one-way range. (See Appendix A.)

In the sample case plots it is of interest to note the similarity of the periodicity and shapes of the range and signal level error curves. This fact can be used to advantage, as will be described in the following suggested experiment.

D. Application

Although the two-way theory is complex, the multipath effects can be separated out in practice. Picture an experimental setup where the zero delay device horn is moved along the direction of the primary path. Measurements of the signal level and range are simultaneously recorded as a function of the zero delay device horn position. To obtain at least two cycles of change, the S-band zero delay horn should be moved a minimum of 27.2 cm (10.7 in.) while at X-band, the ZDD horn should be moved at least 11.4 cm (4.5 in.). After the experimental data has been obtained, a curve fit can be made to the experimental AGC signal level data using Eq. (8). Then determining the position at which the signal level amplitude error is zero, it can be assumed that at the same position the two-way range error is also zero (Figs. 2 to 13). This procedure should produce an error of only a few nanoseconds if the peak-to-peak AGC signal level change is less than 2 dB. For larger AGC ripples (indicating severe multipath conditions) a curve fit of experimental data should be made to both theoretical range and signal level equations given by Eqs. (2) and (8).

III. Experimental Verification

Ranging tests were performed at the Telecommunications Development Laboratory (TDL) using the Block 3 RCV, MVM'73 Radio Frequency Subsystem, and the MU-1 ranging machine. The multipath device[1] described in Ref. 1 was inserted into a cable path that simultaneously carried both the uplink 2113 MHz and downlink 2295 MHz range-coded signals. A block diagram of the test setup at TDL may be seen in Fig. 14. For the two-way range tests, the initial test parameters of the Block 3 RCV and MU-1 ranging machine were the same as previously reported in Ref. 1.

A cable of the appropriate length was inserted into the leakage path of the multipath device to make the one-way leakage path delay become 22.8 ns longer than the delay through the primary path. The multipath device attenuator was adjusted so that the one-way leakage signal was −10.55 dB relative to the primary signal. The leakage path length was then varied by means of a phase shifter (line stretcher) in the leakage path. Two-way range changes and received signal level were measured as functions of the phase shifter setting.

Table 1 shows a comparison of experimental and theoretical values. The theoretical two-way range values were computed from Eq. (2). It can be seen that the agreement between theoretical and experimental range values were typically better than 2 ns. From Table 1 it can also be seen that the theoretical values of signal level changes agreed with experimental values to within 0.5 dB. Eq. (7) was used for the theoretical values for signal level changes because the MVM'73 radio-frequency subsystem transponder was used for these tests rather than a zero delay device. Although it is known that the group delay of the spacecraft receiver system changes as a function of received uplink signal level, no attempt was made to correct the experimental data for these changes.

[1]The isolators in the multipath device were replaced by short lengths of Uniform Tubes UT141 semi-rigid cables.

IV. Conclusion

Equations for two-way range error due to multipath have been presented. Although only a limited amount of experimental data was obtained, reasonably good agreement was found between theory and experiment.

For a future experiment with a dish-mounted zero-delay device, one could mount a zero-delay horn on rails and then record two-way signal level and range changes as a function of horn position. With this data a correlation analysis can be made between experimental data and the theoretical equations. This should enable determination of the true range which would be obtained in the absence of multipath. It should be pointed out that this experimental procedure would be valid only if the multipath phenomenon is caused by one dominant leakage signal. If there are multiple leakage signals, the present analysis would have to be made more general.

Table 1. Results of two-way range test with the multipath device (Uplink frequency = 2.113 GHz, downlink frequency = 2.295 GHz)

Phase shifter setting	$\ell_2 - \ell_1$, cm	Range change			Downlink signal level change		
		Measured[a], ns	Theoretical[b], ns	Difference, ns	Measured, dB	Theoretical, dB	Difference, dB
0	684.00	0.00	0.00	0.00	—	+1.11	—
10	684.83	− 5.27	− 5.13	−0.14	0.00	0.0	0.00
20	685.67	−10.44	−10.81	0.37	—	−0.85	—
30	686.50	−14.75	−14.70	−0.05	−1.54	−1.03	−0.51
40	687.33	−15.75	−15.66	−0.09	−1.09	−0.45	−0.64
50	688.17	−15.09	−14.59	−0.50	−0.02	0.59	−0.61
60	689.00	−12.23	−11.38	−0.85	+1.19	1.71	−0.52
70	689.83	− 8.22	− 6.36	−1.86	—	2.68	—
80	690.67	− 4.32	− 1.31	−3.01	2.97	3.44	−0.47
90	691.50	0.16	2.57	−2.41	3.48	3.95	−0.47
100	692.33	2.34	5.15	−2.81	3.77	4.22	−0.45
110	693.17	4.21	6.63	−2.42	3.83	4.23	−0.40
120	694.00	5.45	7.20	−1.75	3.65	4.01	−0.36
130	694.83	5.10	6.93	−1.83	3.24	3.53	−0.29
140	695.67	4.29	5.76	−1.47	—	2.81	—
150	696.50	2.14	3.48	−1.34	1.54	1.86	−0.32
160	697.33	− 1.79	− 0.14	−1.65	0.37	0.76	−0.39
170	698.17	− 6.48	− 4.96	−1.47	—	−0.31	—
180	699.00	−10.74	− 9.42	−1.32	—	−0.99	—

[a]Calculated standard error on the measured relative range was typically ±0.5 ns

[b]Based on $A = 0.297$ (−10.55 dB)

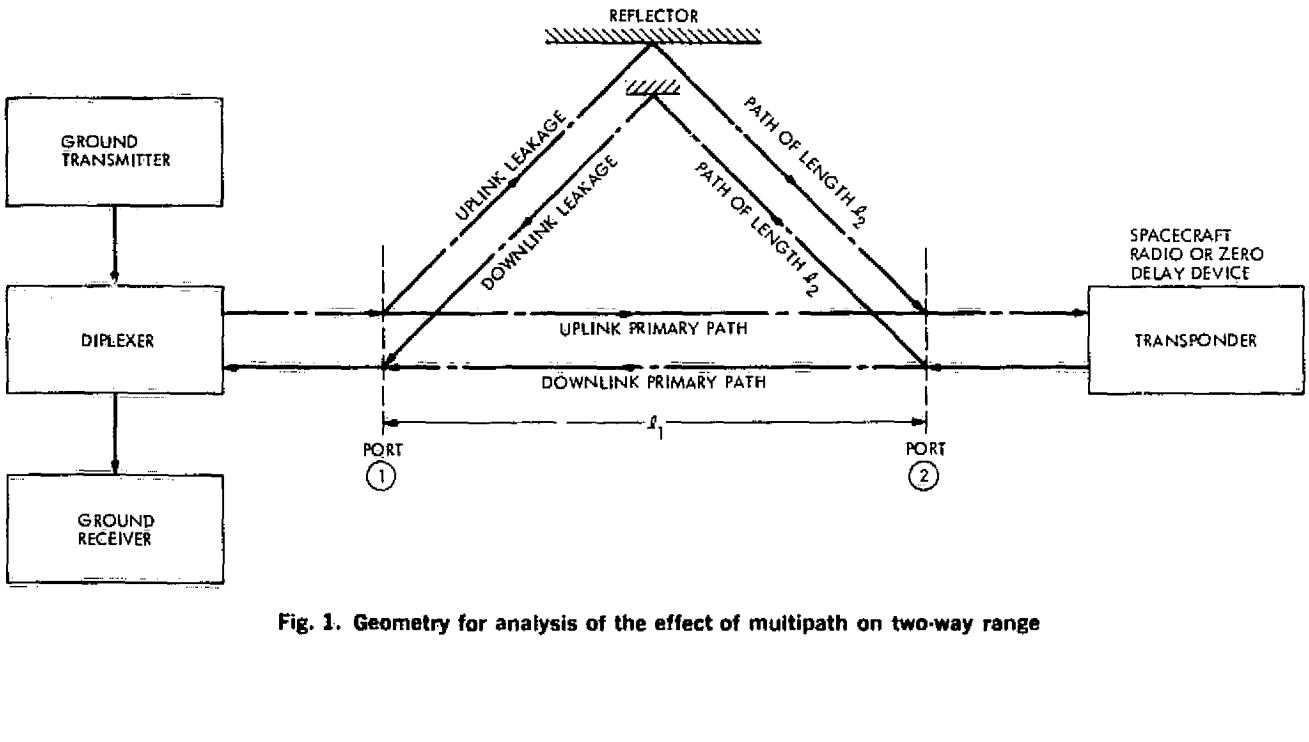

Fig. 1. Geometry for analysis of the effect of multipath on two-way range

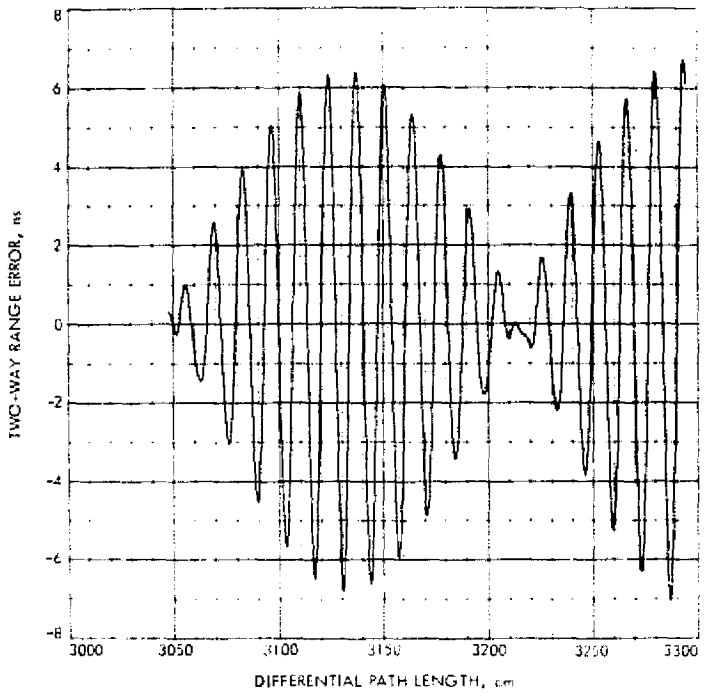

Fig. 2. Two-way *range* error sample case: $\ell_2 - \ell_1 = 3048$ cm (100 ft); one-way leakage signal is −30 dB relative to primary signal; uplink signal is 2113 MHz, and downlink signal is 2295 MHz; $\varphi_a = \varphi_b = 0$

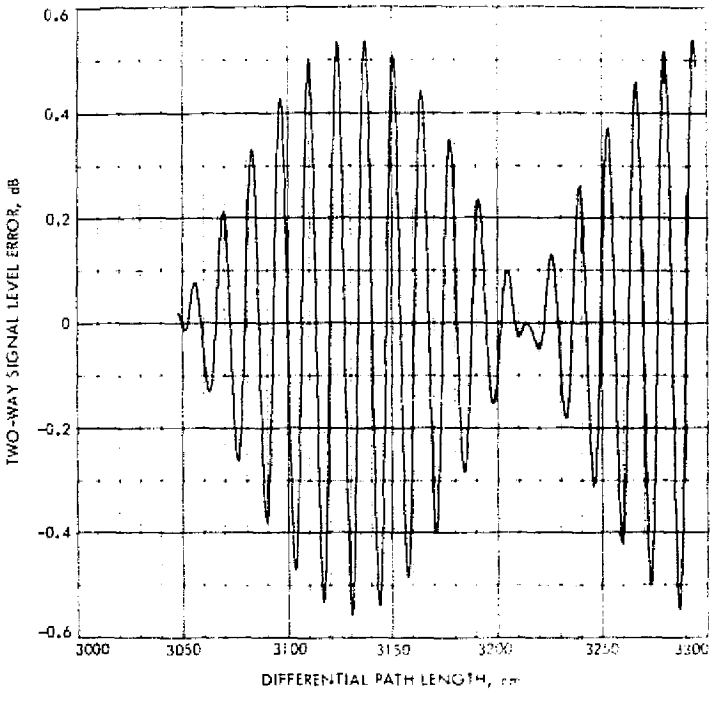

Fig. 3. Two-way *signal* level error sample case (same parameters as Fig. 2)

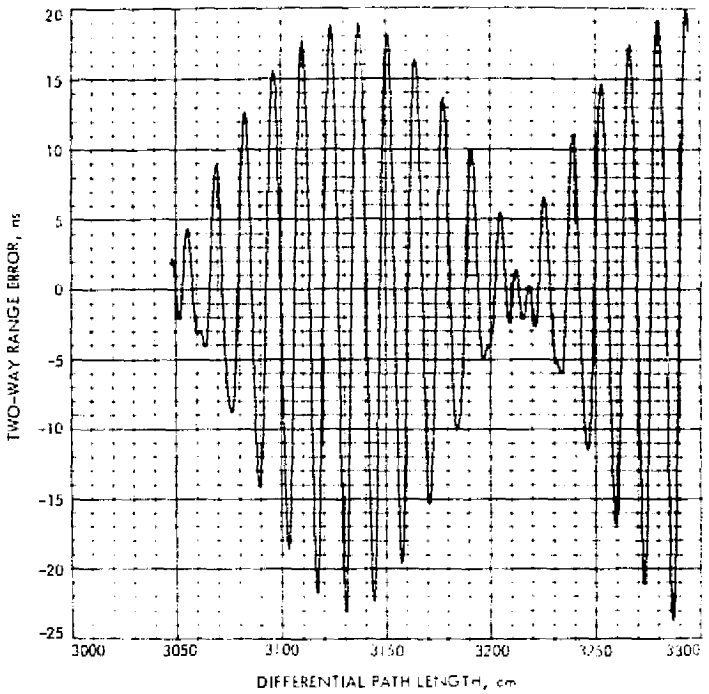

Fig. 4. Two-way *range* error sample case: same parameters as Fig. 2 except leakage signal is −20 dB relative to primary signal

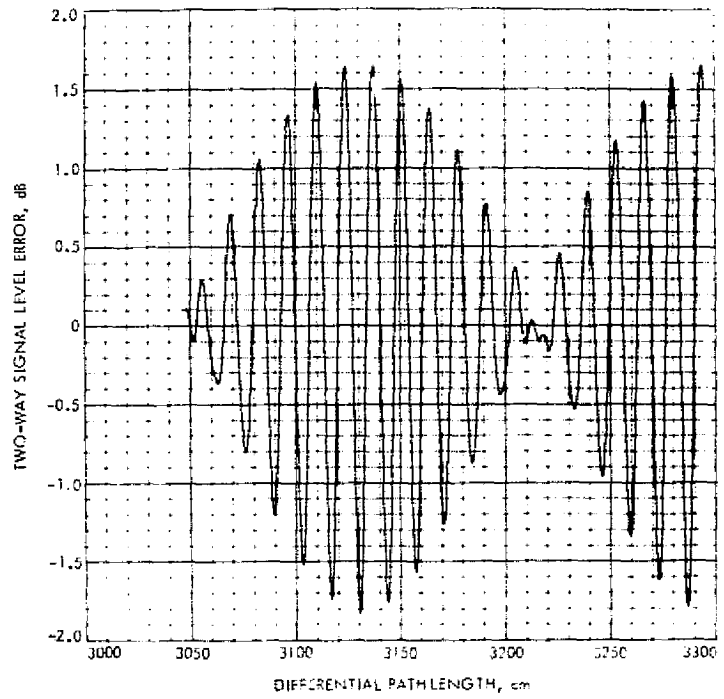

Fig. 5. Two-way *signal* level error sample case: same parameters as Fig. 2 except leakage signal is −20 dB relative to primary signal

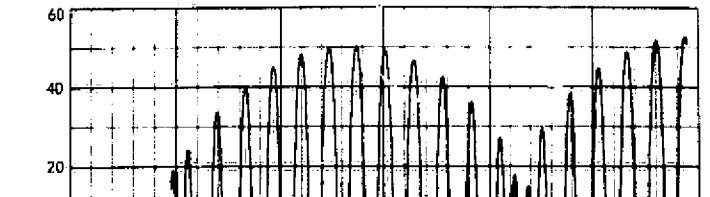

Fig. 6. Two-way *range* error sample case: same parameters as Fig. 2 except leakage signal is −10 dB relative to primary signal

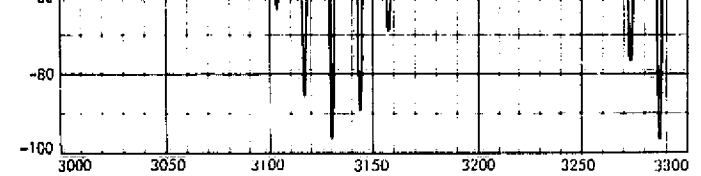

Fig. 7. Two-way *signal* level error sample case: same parameters as Fig. 2 except leakage signal is −10 dB relative to primary signal

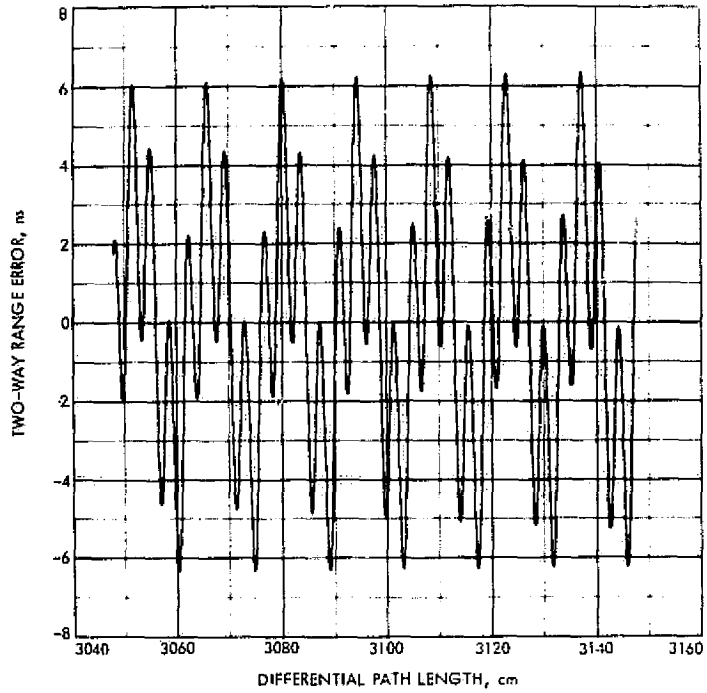

Fig. 8. Two-way *range* error sample case: $L_2 - L_1 = 3048$ cm (100 ft); one-way leakage signal is −30 dB relative to primary signal; uplink signal is 2113 MHz, and downlink signal is 8415 MHz; $\psi_u = \psi_b = 0$

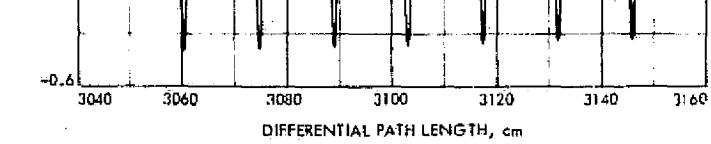

Fig. 9. Two-way *signal* level error sample case (same parameters as Fig. 8)

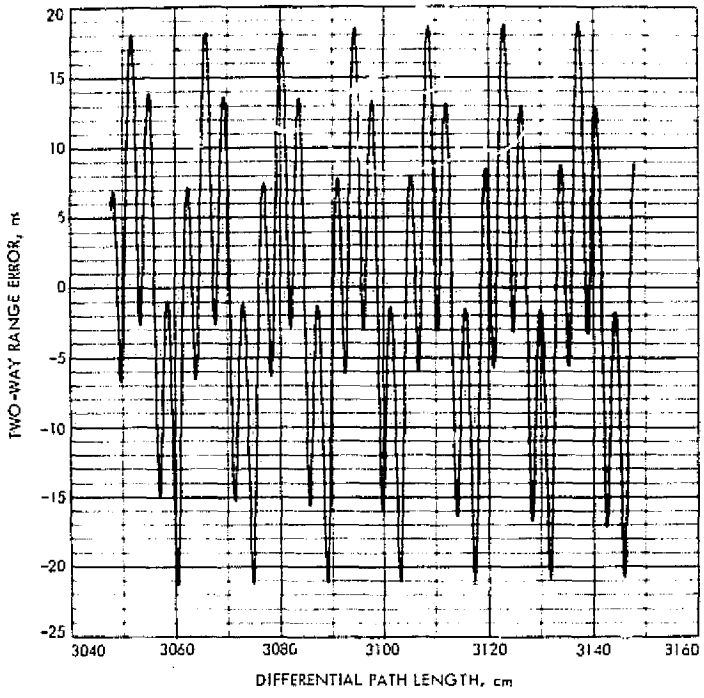

Fig. 10. Two-way *range* error sample case: same parameters as Fig. 8 except leakage signal is −20 dB relative to primary signal

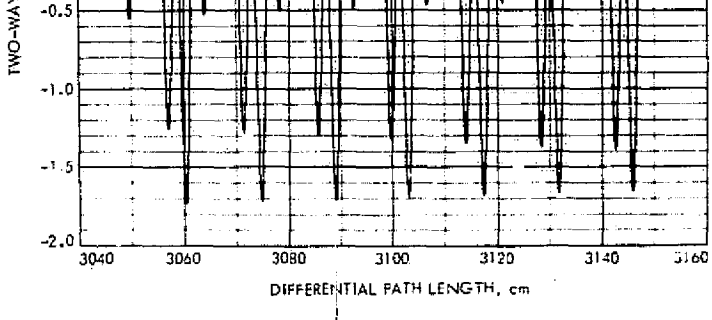

Fig. 11. Two-way *signal* level error sample case: same parameters as Fig. 8 except leakage signal is −20 dB relative to primary signal

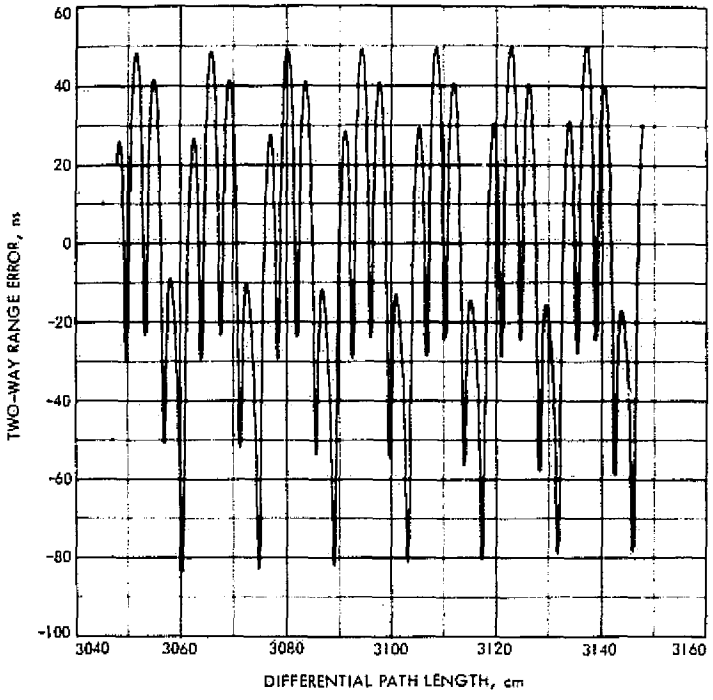

Fig. 12. Two-way *range* error sample case: same parameters as Fig. 8 except leakage signal is −10 dB relative to primary signal

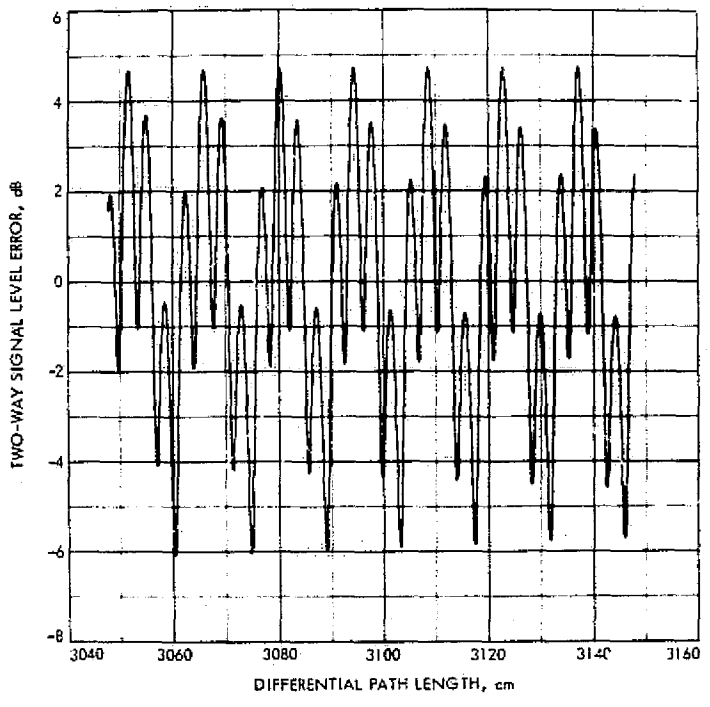

Fig. 13. Two-way *signal* level error sample case: same parameters as Fig. 8 except leakage signal is −10 dB relative to primary signal

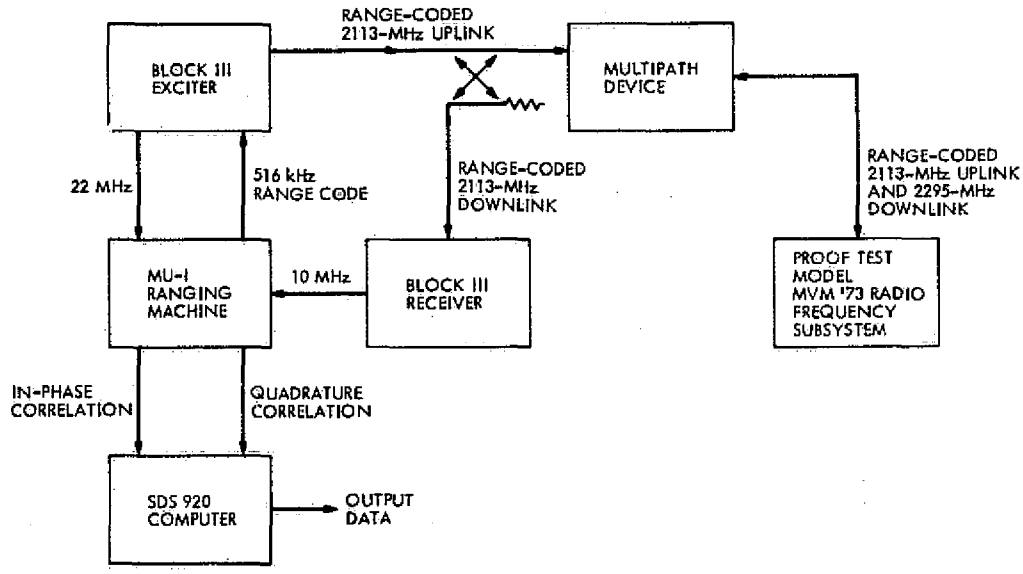

Fig. 14. Measurement setup for two-way range tests with the multipath device

Appendix A

Upper and Lower Bounds for Two-Way Range Error

As can be seen from the sample case plots (Figs. 2 to 13), the error for two-way range will be at a *local* upper or lower bound when the modulation envelope is at a maximum or minimum. At some critical differential path length, the two-way range error will be exactly two times the upper or lower bound of the one-way range error (Ref. 1). To find where this condition occurs, let θ_a and θ_b as given by Eqs. (5) and (6) be related as follows

$$\theta_b = \theta_a - 2\pi k \tag{A-1}$$

where k is a positive integer. Then the two-way range error given by Eq. (2) becomes

$$(\epsilon_g)_T = 2A\left(\frac{\ell_2 - \ell_1}{c}\right)\left(\frac{A + \cos\theta_a}{1 + 2A\cos\theta_a + A^2}\right) \tag{A-2}$$

Also note that the two-way signal level error as given by Eq. (8) becomes

$$|F_T|_{dB} = 20\log_{10}[1 + 2A\cos\theta_a + A^2] \tag{A-3}$$

From Eq. (A-3), it can be seen that the peak-to-peak change in signal level will be

$$\Delta_{dB} = 40\log_{10}\left[\frac{1 + A}{1 - A}\right] \tag{A-4}$$

which is exactly a factor of two greater than the dB signal level ripple for the one-way case (Ref. 1).

Upper Bound

Assuming that the conditions of Eq. (A-1) exist, then assume further that

$$\theta_a = -2\pi m \tag{A-5}$$

where m is a positive integer. Substitution of Eq. (A-5) into Eqs. (A-2) and (A-3) gives

$$(\epsilon_g)_T = \left(\frac{2A}{1 + A}\right)\left(\frac{\ell_2 - \ell_1}{c}\right) \tag{A-6}$$

$$|F_T|_{dB} = 40\log_{10}(1 + A) \tag{A-7}$$

These upper bounds of error for two-way range and signal level are exactly twice those of the corresponding one-way range case (Ref. 1). To find the critical differential path length which produces these conditions, first substitute Eq. (A-5) into (A-1) to obtain

$$\theta_b = -2\pi(m + k) \tag{A-8}$$

Then substitutions of Eqs. (5) and (6) into Eqs. (A-5) and (A-8), respectively, and solving for $\ell_2 - \ell_1$ results in

$$\ell_2 - \ell_1 = \left(\frac{c}{f_a}\right)\left[m + \frac{\psi_a}{2\pi}\right] \tag{A-9}$$

$$\ell_2 - \ell_1 = \left(\frac{c}{f_b}\right)\left[m + k + \frac{\psi_b}{2\pi}\right] \tag{A-10}$$

For simplicity assume that there is only one reflection coefficient in the leakage path and $\psi_a = \psi_b = \pi$. Then equating Eq. (A-9) to Eq. (A-10) and manipulation results in

$$f_b = f_a\left[\frac{2(m + k) + 1}{2m + 1}\right] \tag{A-11}$$

The condition of Eq. (A-11) must be fulfilled if two-way range error is exactly twice the one-way range value. To show a practical application of Eq. (A-11), one can find from trial and error that $m = 11$ and $k = 1$ are the minimum values of m and k which will give $f_b \simeq 2295$ MHz when $f_a = 2113$ MHz. From substitution of these values in Eqs. (A-11) and (A-9)

$$f_b = 2296.7 \text{ MHz}$$

$$\ell_2 - \ell_1 = 163.3 \text{ cm } (5.36 \text{ ft})$$

and from Eq. (A-6)

$$(\epsilon_g)_T = 10.89\left(\frac{A}{1 + A}\right)$$

where $(\epsilon_g)_T$ is given in nanoseconds.

Lower Bound

To find where the two-way lower bound is exactly twice the one-way lower bound, assume that the condition of Eq. (A-1) exists, and assume further that

$$\theta_a = -(2n-1)\pi \tag{A-12}$$

where n is a positive integer. Then Eqs. (A-2) and (A-3) become

$$(\epsilon_g)_T = -\left(\frac{2A}{1-A}\right)\left(\frac{\ell_2-\ell_1}{c}\right) \tag{A-13}$$

$$|F_T|_{dB} = 40\log_{10}[1-A] \tag{A-14}$$

To find the differential path length which produces these lower bounds, substitute Eq. (A-12) into Eq. (A-1) to obtain

$$\theta_b = -(2n-1)\pi - 2\pi k \tag{A-15}$$

Then substitutions of Eqs. (5) and (6) into Eqs. (A-12) and (A-15), respectively, and then solving for $\ell_2 - \ell_1$ results in

$$\ell_2 - \ell_1 = \frac{c}{f_a}\left[\left(\frac{2n-1}{2}\right) + \frac{\psi_a}{2\pi}\right] \tag{A-16}$$

$$\ell_2 - \ell_1 = \frac{c}{f_b}\left[\left(\frac{2n-1+2k}{2}\right) + \frac{\psi_b}{2\pi}\right] \tag{A-17}$$

Assuming that $\psi_a = \psi_b = \pi$ and then from equating Eq. (A-16) to Eq. (A-17), one obtains

$$f_b = f_a\left[\frac{n+k}{n}\right] \tag{A-18}$$

As an example of the use of Eq. (A-18) one can find from trial and error that values of $n = 23$ and $k = 2$ will give $f_b \simeq 2295$ MHz when $f_a = 2113$ MHz. From substitutions of these values into Eqs. (A-18) and (A-16), one obtains

$$f_b = 2296.7 \text{ MHz}$$

$$\ell_2 - \ell_1 = 326.5 \text{ cm } (10.71 \text{ ft})$$

and from Eq. (A-13):

$$(\epsilon_g)_T = -21.77\left(\frac{A}{1-A}\right)$$

where $(\epsilon_g)_T$ is given in nanoseconds.

Although in the examples given, the calculated downlink frequency of 2296.7 MHz is only approximately equal to 2295 MHz, one can expect to find local upper and lower bounds at differential path lengths close to 163.3 cm (5.36 ft) and 326.5 cm (10.71 ft). It is of interest to note that even for these small differential path length values, significant error in the S-band two-way range will occur if the multipath signal is strong. This type of strong multipath effect for small differential path lengths on the MVM'73 spacecraft was pointed out by J. R. Smith (Ref. 3).

Acknowledgments

The experimental work at the Telecommunications Development Laboratory was supported by D. L. Brunn of the Spacecraft Radio Section. The computer program for the sample case plots in this article was written by T. Cullen of the Communications Elements Research Section.

References

1. Otoshi, T. Y., "S/X Band Experiment: A Study of the Effects of Multipath on Group Delay," in *The Deep Space Network Progress Report 42-24*, pp. 40–50, Pasadena, Calif., Dec. 15, 1974.

2. Smith, J. R., "Viking Ranging Investigation Team," IOM 3382-74-076, July 30, 1974 (JPL internal document).

3. Smith, J. R., "Viking Ranging Investigation Team," IOM 3382-74-102, Oct. 15, 1974 (JPL internal document).

Maximum Likelihood vs Threshold Frame Synchronization

B. K. Levitt
Communications Systems Research Section

Mariner 10 (MVM'73) uses a threshold-type algorithm to acquire frame synchronization. In reviewing this scheme, the question arose as to why a threshold approach was selected over a maximum likelihood detection scheme. This paper answers that question in the context of an uncoded telemetry link over a binary symmetric channel. For a given communication link it is demonstrated that, at the expense of a variable acquisition time, a threshold scheme can simultaneously achieve a lower probability of false sync acquisition and a smaller expected acquisition time than its maximum likelihood counterpart.

I. The Problem

In a binary signaling scheme, frame synchronization is usually provided by prefixing each frame of transmitted data (M bits) with a fixed binary pattern or sync word (L bits). At the receiver, frame synchronization is acquired by locating the noisy replicas of the transmitted sync words periodically imbedded in the received data stream.

Suppose we are dealing with uncoded data received over a binary symmetric channel (crossover probability ϵ): the optimum frame sync decision is then based on the Hamming distance metric. In particular, we examine successive binary L-tuples $\rho_1, \rho_2, \cdots$ within the received bit stream (see Fig. 1): we know that one of the first M such L-tuples must be received sync word ρ_{m^*}. Statistically, m^* is uniformly distributed over $(1,M)$. To compare these received L-tuples with the sync word pattern s, we form the likelihood parameters $D_1, D_2, \cdots$, where D_m is the Hamming distance between ρ_m and s. Typically, D_{m^*} will be near 0, while the other $(M\text{-}1)$ parameters D_m within a frame of received data will be near $L/2$ (assume s is a Barker (Ref. 1) or Neuman-Hofman (Ref. 2) sequence, and the $(M\text{-}L)$ information bits in each frame of transmitted data are independent, equally likely 1's and 0's). We acquire frame synchronization by correctly identifying m^* over $(1,M)$: this is a detection problem with many solutions, some of which are discussed below.

II. Some Solutions

Suppose we are constrained to make a sync decision over a *single* frame of received data. Then the optimum maximum likelihood (ML) approach is to decide $m^* = \hat{m}$ if

$$D_{\hat{m}} = \min \{ D_m : m = 1,2, \cdots, M \} \qquad (1)$$

The advantage of such a scheme is that the sync acquisition time is deterministic: assuming a unique minimum exists, we are guaranteed a sync decision will be made

after observing one frame of received data. On the other hand, if $D_{\hat{m}}$ is not particularly close to zero, we are still forced to make a sync decision, even though our confidence in that decision is low. Thus, if the bit error probability ϵ is too large, the ML scheme may have an unacceptably large probability of false sync acquisition, $Pr[FS]$.

We can improve $Pr[FS]$ by making a joint ML sync decision over more than one frame of received data (say, N frames): thus we can decide $m^* = \hat{m}$ if

$$\sum_{k=0}^{N-1} D_{\hat{m}+kM} = \min \left\{ \sum_{k=0}^{N-1} D_{m+kM} : m = 1,2, \cdots, M \right\} \tag{2}$$

The averaging over several frames of received data implied by the summation in Eq. (2) provides a degree of noise immunity and results in a significant decrease in $Pr[FS]$. However, our sync acquisition time is now N frames of received data, and our storage requirements are increased proportionally.

An alternative approach is to delay making a sync decision until we are reasonably confident it is correct. To this end, we can successively compare D_1, D_2, etc., with some predetermined threshold T: we decide that $\rho_{\hat{m}}$ is a received sync word if $D_{\hat{m}}$ is the *first* metric to satisfy the threshold test

$$D_m \leq T \tag{3}$$

The selection of the threshold T involves a tradeoff between frame sync reliability and acquisition time. Clearly, $Pr[FS]$ decreases as T gets smaller. However, if T is too small, we may not recognize the first few received sync words due to excessive ($T + 1$ or more) bit errors within them: then the sync acquisition time (now a random variable) may be several frames of received data. Note that if the first received sync word ρ_{m^*} is the first received L-tuple to satisfy the threshold test, the corresponding acquisition time is m^*/M frames: consequently, the threshold synchronization scheme above has a *minimum* expected acquisition time of

$$\frac{\overline{m^*}}{M} = \frac{M+1}{2M} \text{ frames} \tag{4}$$

(assuming a correct sync decision is made). The design criterion for a given telemetry link (fixed M,L,ϵ) is to select a threshold T for which $Pr[FS]$ is acceptably small and the mean acquisition time is of the order of ½ frame.

As in the maximum likelihood approach, if storage capacity permits, a more reliable sync decision can be made by using a joint threshold test over N frames of received data: determine the first location $\hat{m}$ which satisfies the test

$$\sum_{k=0}^{N-1} D_{m+kM} \leq T \tag{5}$$

III. Comparison of *ML* and Threshold Synchronization

The maximum likelihood synchronization technique above is optimum, in the sense that it minimizes the probability of false sync acquisition, *only when the observable is a fixed amount of received data.* A threshold scheme can outperform its ML counterpart operating on the same N-fold Hamming distance metric,

$$\sum_{k=0}^{N-1} D_{m+kM}$$

provided the threshold T is properly chosen, at the expense of having a variable acquisition time.

The general hypothesis is that for any ϵ,M,L, and N, there exists a T such that the $Pr[FS]$ and the mean acquisition time will both be smaller than in the ML case. I am not prepared to prove this general statement; however, it is shown to hold below in the particular case $N = 1$, $M = 7056$, and $L = 31$. (This combination of M and L corresponds to the Mariner 10 high-rate video telemetry mode, which was of interest during my initial investigation of the frame sync problem.)

Using union bounding techniques, one can derive upper bounds for the probability of false sync acquisition for the ML scheme of Eq. (1) and the threshold approach of Eq. (3) (derivations are similar to the appendix of Ref. 3):

$$Pr[FS]\Big|_{ML} < (M-1)2^{-L}(1-\epsilon)^L \sum_{k=0}^{L} \binom{L}{k} \left(\frac{\epsilon}{1-\epsilon}\right)^k \sum_{\ell=0}^{k} \binom{L}{\ell} \tag{6}$$

$$Pr[FS]\Big|_{T} < (M-1)2^{-(L+1)} \sum_{k=0}^{T} \binom{L}{k} + \frac{\min(A,B)}{1-A} \tag{7}$$

where

$$A \equiv 1 - (1-\epsilon)^L \sum_{k=0}^{T} \binom{L}{k} \left(\frac{\epsilon}{1-\epsilon}\right)^k \tag{8}$$

$$B \equiv (M-1)\, 2^{-L} \sum_{k=0}^{T} \binom{L}{k} \tag{9}$$

For sufficiently small ϵ, these bounds should be fairly tight.

The acquisition time is fixed at 1 frame of received data in the ML scheme. In the threshold case, a simple Markov analysis (similar to Section II, Appendix, Ref. 3) yields the result

$$\text{mean acquisition time}\Big|_T = \left(\frac{M+1}{2M} + \frac{A}{1-A}\right) \text{frames} \tag{10}$$

provided $Pr[FS]\Big|_T << 1$.

The formulas in Eqs. 6–10 were used to generate Figs. 2 and 3. They show that for any value of ϵ, a value of T can be found to make the threshold scheme superior to the ML approach:

$$Pr[FS]\Big|_T \leq Pr[FS]\Big|_{ML} \tag{11}$$

$$\text{mean acquisition time}\Big|_T \leq 1 \text{ frame} \tag{12}$$

For small bit error rates ($\epsilon < 10^{-5}$), the probabilities of false sync acquisition for the ML and $T = 0$ threshold schemes are comparable (actually, $Pr[FS]\Big|_{T=0} \sim \frac{1}{2} Pr[FS]\Big|_{ML}$); however, there is a factor of 2 advantage for the threshold approach with regard to the mean acquisition time. As ϵ increases from 10^{-3} to 10^{-2}, the mean acquisition time for the $T = 0$ case rises toward 1 frame; simultaneously, $Pr[FS]\Big|_{T=0}$ increases much more slowly than $Pr[FS]\Big|_{ML}$, yielding more than an order-of-magnitude performance advantage at $\epsilon = 10^{-2}$. In the region $9.6 \times 10^{-3} < \epsilon < 1.3 \times 10^{-2}$, the $T = 0$ and $T = 1$ thresholds both satisfy Eqs. (11) and (12); over the range $1.3 \times 10^{-2} < \epsilon < 2.5 \times 10^{-2}$, these constraints uniquely require the threshold $T = 1$. The graphs indicate where T must be increased as ϵ increases further. Of course, the bounds on $Pr[FS]$ become progressively looser as ϵ becomes large.

References

1. Barker, R. H., "Group Synchronization of Binary Digital Systems," *Communication Theory*, edited by Jackson, Butterworth, London, pp. 273-287, 1953.

2. Neuman, F., and Hofman, L., "New Pulse Sequences With Desirable Correlation Properties," *Proc. Nat. Telemetry Conf.*, Washington, D.C., pp. 277–282, Apr. 1971.

3. Levitt, B. K., "Frame Synchronization Performance Analysis for MVM'73 Uncoded Telemetry Modes," in *The Deep Space Network*, Technical Report 32-1526, Vol. XIX, pp. 126–136. Jet Propulsion Laboratory, Pasadena, Calif., Feb. 15, 1974.

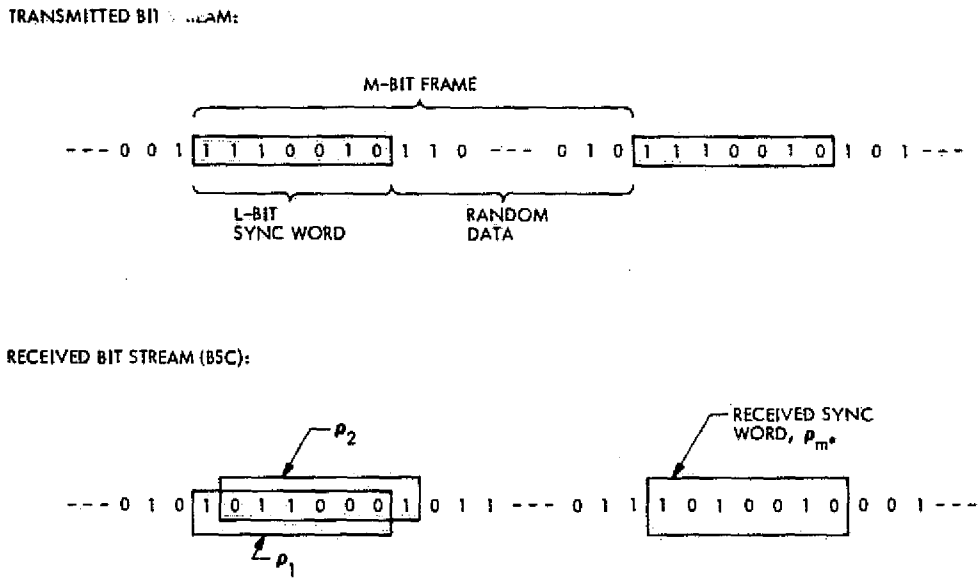

Fig. 1. Frame synchronization formats for uncoded transmission over a binary symmetric channel

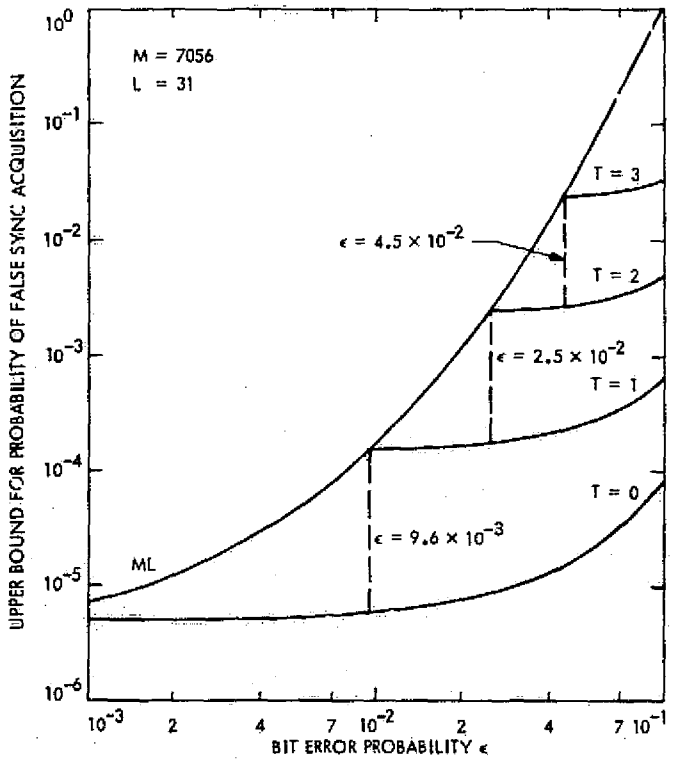

Fig. 2. Performance comparison of threshold and maximum likelihood frame synchronization techniques

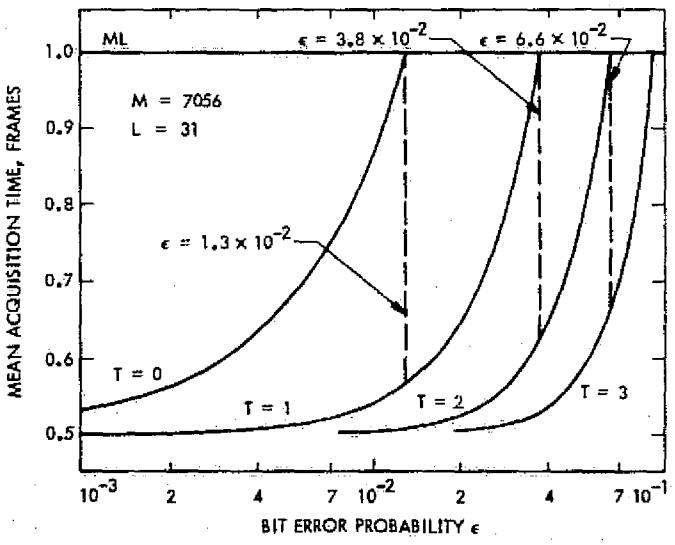

Fig. 3. Comparison of mean acquisition times for threshold and maximum likelihood frame synchronization techniques

Further Applications of the Atmospheric Fading Model to Sequential Decoding Performance

B. K. Levitt
Communications Systems Research Section

The Deep Space Network is interested in predicting whether it will be able to achieve a satisfactory performance level on Pioneer Venus 1978 (PV'78) telemetry over a fading channel. In an earlier article, a theoretical model for the combined effects of log-normal fading and a noisy carrier reference on sequentially decoded phase-shift keyed (PSK) telemetry was used to analyze the PV'78 large probe link at 256 bps. This model is now applied to the 16-bps small probe telemetry mode.

I. Introduction

An analytical model was recently developed for predicting the combined effects of log-normal fading and a noisy carrier reference on convolutionally encoded/sequentially decoded phase-shift-keyed (PSK) telemetry (Ref. 1). In a previous article (Ref. 2), this model was used to analyze the Pioneer Venus 1978 (PV'78) large probe telemetry link at 256 bps. As part of a continuing DSN support study, a similar examination of the 16-bps small probe telemetry mode is reported here.

II. Assumptions

As in the 256-bps case, the desired frame deletion rate was set at 10^{-2}. The received signal-to-noise ratio P_T/N_o required to achieve this level of performance was computed as a function of the severity of the channel fading, characterized by the variance σ_x^2 of the log-amplitude fluctuations. Using experimental data from the Russian Venera space probes, Woo (Ref. 3, Eqs. 12 and 13) has shown that

$$\sigma_x^2 = 0.0142\left(\frac{L}{55}\right)^{11/6} \tag{1}$$

where L is the atmospheric path length of the probe-to-Earth telemetry link, in km.

The fading/noisy reference model incorporates processing losses in the data and carrier tracking channels (Ref. 2, Eqs. 2 and 3); at 16 bps, these anticipated losses are

$$L_D = 2.32 \text{ dB} \tag{2}$$

$$L_C = 1.00 \text{ dB} \tag{3}$$

It was again assumed that a standard DSN sequential decoder could perform about 25,000 computations/second in real-time operations; this translates into a computational capacity $N = 1562.5$ computations/bit at 16 bps. A value of N an order of magnitude larger than this was also used to determine whether a significant improvement in performance could be achieved by resorting to non-real-time decoding.

As in the 256-bps analysis, we constrained the tracking loop to have a carrier reference phase jitter σ_ϕ^2 compatible with very long baseline interferometry (VLBI) requirements. This required that the received carrier signal-to-noise ratio in the (two-sided) threshold phase-locked loop bandwidth $2B_{Lo}$ satisfy the constraint (Ref. 2, Eq. 4)

$$\eta \equiv \frac{P_T \cos^2\theta}{N_0 2B_{Lo} L_C} \gtrsim (10 + 14.1\,\sigma_\chi^2)\ \text{dB} \qquad (4)$$

where θ is the modulation angle, and $2B_{Lo} = 12$ Hz.

Finally, despite previously expressed reservations (Ref. 1, "Commentary," p. 60; Ref. 2, "Results"), the analysis of the 16-bps link was performed using Layland's formula for the characteristic decoder memory time T_m (Ref. 4, Eq. 6) in the fading/noisy reference model. There are plans to determine this parameter empirically so as to maximize the agreement between our analytical model and experimental evidence.

III. Results

As a reference point for design control table purposes, in order to measure losses due to fading, noisy carrier reference, and receiver processing, an idealized 16-bps link with $\sigma_\chi^2 = 0$, $L_D = L_C = 0$, and a perfect carrier reference was analyzed. The results are contrasted in Table 1 with the 256-bps case (Ref. 2, Fig. 1) as a function of the decoding rate C. We find that the slower telemetry link requires a 0.50-dB smaller received bit energy-to-noise ratio ρ for real-time decoding, with a lesser savings in the non-real-time case.

Figure 1 still neglects the fading, but incorporates the noisy reference and processing losses into the analysis of the 16-bps link with real-time decoding. Strictly from a telemetry viewpoint, we see that our desired frame deletion rate of 10^{-2} could be achieved in this case with P_T/N_0 as low as 22.03 dB at a corresponding modulation angle $\theta = 46.8$ deg; however, the tracking loop parameter η would then be 6.96 dB, which would not satisfy the VLBI requirement, $\eta = 10$ dB in the absence of fading. The minimum received signal-to-noise ratio which simultaneously satisfies the data and carrier channel requirements is $P_T/N_0 = 23.19$ dB at $\theta = 31.7$ deg, an increase of 1.16 dB over the data requirement alone.

Using Fig. 1 and a similar set of curves for the non-real-time decoding case, the variation of P_T/N_0 with θ is shown in Fig. 2 for a deletion rate of 10^{-2} in the absence of fading. The solid curves indicate the regions where $\eta \geq 10$ dB.

The remaining graphs deal with the effects of atmospheric fading, which, we have already noted, is characterized by σ_χ^2. During its approximately 2-hour descent to the surface of Venus, σ_χ^2 will vary from an initial value of zero to a maximum value on the surface, when the atmospheric path length L in Eq. (1) is greatest. Referring to Fig. 3, suppose the probe-to-Earth transmission angle is ϕ relative to the radial direction; assuming Venus has a radius of 6050 km, and the atmosphere is homogeneous and ends abruptly 55 km above the surface of Venus (Ref. 5; Ref. 3, p. 8), a transmission from the surface has an atmospheric path length

$$L = \sqrt{(6105)^2 - (6050 \sin\phi)^2} - 6050 \cos\phi,\ \text{km} \qquad (5)$$

Equations (1) and (5) have been combined in Graph 3 to provide a curve of σ_χ^2 at the surface of Venus vs the transmission angle ϕ. Two values of ϕ have commonly been used as benchmarks for the PV'78 mission; the corresponding values of σ_χ^2 from Fig. 4 are

$$\sigma_\chi^2 = \begin{cases} 0.014; & \phi = 0^\circ \\ 0.049; & \phi = 60^\circ \end{cases} \qquad (6)$$

Figure 5 represents the degradation of the link in Fig. 1 due to log-normal fading, when $\sigma_\chi^2 = 0.049$. As before, the optimum operating point with regard to our telemetry performance requirement only ($P_T/N_0 = 24.48$ dB; $\theta = 50.9$ deg) does not satisfy the VLBI requirement ($\eta \geq 10.69$ dB). To simultaneously meet both needs, the minimum received $P_T/N_0 = 24.94$ dB (an increase of 0.46 dB, which is less than in the nonfading case of Fig. 1) at $\theta = 41.1^\circ$. In analyzing the 16-bps link over the probe lifetime, this represents the worst case requirement for $\phi = 60^\circ$.

Figure 6 is an extension of Fig. 5 and demonstrates how our link requirements vary with σ_χ^2 for real-time decoding; Fig. 7 does the same for the non-real-time

case. For the $\sigma_x^2 = 0.049$ case, Fig. 7 shows that increasing the computational capacity an order of magnitude lowers the required P_T/N_0 to 24.79 dB, which is a trivial savings of 0.15 dB over the real-time decoding requirement.

As an example, Table 1 and Figs. 2 and 6 were used to generate the design control table shown in Table 2 for the 16-bps link with $\sigma_x^2 = 0.049$ and real-time decoding. The entries for this table are derived in the manner described for the 256-bps link (Ref. 2). Unlike the 256-bps case, the carrier and data channel margins are equal at 16 bps. In the example of Table 2, the overall link margin (minimum of the carrier and data channel margins) is 5.78 dB; this can be compared with an overall margin of 2.45 dB for the equivalent 256-bps link. Note that the noisy reference and fading losses for these two links are virtually identical:

$$\text{noisy reference loss} = \begin{cases} 2.12 \text{ dB; 16 bps} \\ 2.10 \text{ dB; 256 bps} \end{cases} \quad (7)$$

$$\text{fading loss} = \begin{cases} 2.74 \text{ dB; 16 bps} \\ 2.75 \text{ dB; 256 bps} \end{cases} \quad (8)$$

References

1. Levitt, B. K., "Performance Degradation of Uncoded and Sequentially Decoded PSK Systems Due to Log-Normal Fading," in *The Deep Space Network Progress Report 42-23*, pp. 58–67, Jet Propulsion Laboratory, Pasadena, Calif., Oct. 15, 1974.
2. Levitt, B. K., "Pioneer Venus 1978: Telemetry Performance Predicts," in *The Deep Space Network Progress Report 42-24*, Jet Propulsion Laboratory, Pasadena, Calif., Dec. 15, 1974.
3. Woo, R., et al., *Effects of Turbulence in the Atmosphere of Venus on Pioneer Venus Radio — Phase 1*, Technical Memorandum 33-644, Jet Propulsion Laboratory, Pasadena, Calif., June 30, 1973.
4. Layland, J. W., "A Model for Sequential Decoding Overflow Due to a Noisy Carrier Reference," in the Proceedings of the International Telemetering Conference (ITC'74), held Oct. 15–17, 1974, Los Angeles, Calif.
5. Yakovlev, O. I., Efimov, A. I., and Timofeeva, T. S., "Venera-7 Space-Probe Data on Propagation of Radio Waves Through the Venusian Atmosphere and Through the Interplanetary Plasma," *Kosm. Issle*, Vol. 9, No. 5, pp. 748–753, September–October, 1971.

C – 2

Table 1. Required signal-to-noise ratios for ideal lossless telemetry links at 16 and 256 bps (reference case)

No fading ($\sigma_\chi^2 = 0$); perfect carrier reference; no system losses ($L_D = L_C = 0$); frame deletion rate = 10^{-2}

Parameter	Real-time processing		Non-real-time processing	
C, comp/s	2.5×10^4		2.5×10^5	
R_B, bps	16	256	16	256
$N = C/R$, comp/bit	1562.5	97.7	15,625	977
$\rho = E_B/N_0$, dB	2.08	2.58	1.77	2.14

Table 2. Telecommunications design control table

Telemetry mode: PV'78 small probe-to-earth telemetry link; Convolutional coding ($K = 32$, $r = \frac{1}{2}$) with sequential decoding; Real-time processing, $N = 1562.5$ comp/bit

Performance	No.	Parameter	Nominal value, dB	Comments
	1	Available P_T/N_0	30.72	Transmitter: 10 W Receiver: 26.1 °K, 30° elev
Carrier	2	Threshold snr, η	10.00	VLBI requirement
	3	Fading loss	0.69	$\sigma_\chi^2 = 0.049$
	4	System loss, L_C	1.00	
	5	$2B_{L0}$	10.79	12 Hz
	6	$\cos^2\theta$	−2.46	$\theta = 41.1°$
	7	Required P_T/N_0	24.94	Nos. (2+3+4+5−6)
	8	Margin	5.78	Nos. (1−7)
Telemetry	9	Ideal ρ (lossless)	2.08	Deletion rate = 10^{-2}
	10	Noisy reference loss	2.12	
	11	Fading loss	2.74	$\sigma_\chi^2 = 0.049$
	12	System loss, L_D	2.32	
	13	Rate, R_B	12.04	16 bps
	14	$\sin^2\theta$	−3.64	$\theta = 41.1°$
	15	Required P_T/N_0	24.94	Nos. (9+10+11+12+13−14)
	16	Margin	5.78	Nos. (1−15)

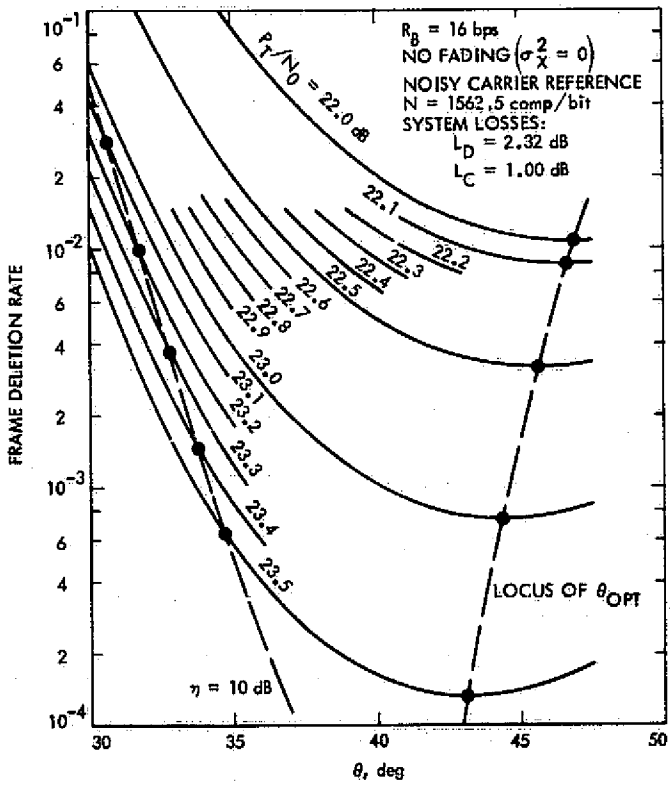

Fig. 1. Signal-to-noise requirements for 16-bps telemetry link in the absence of fading, with real-time decoding

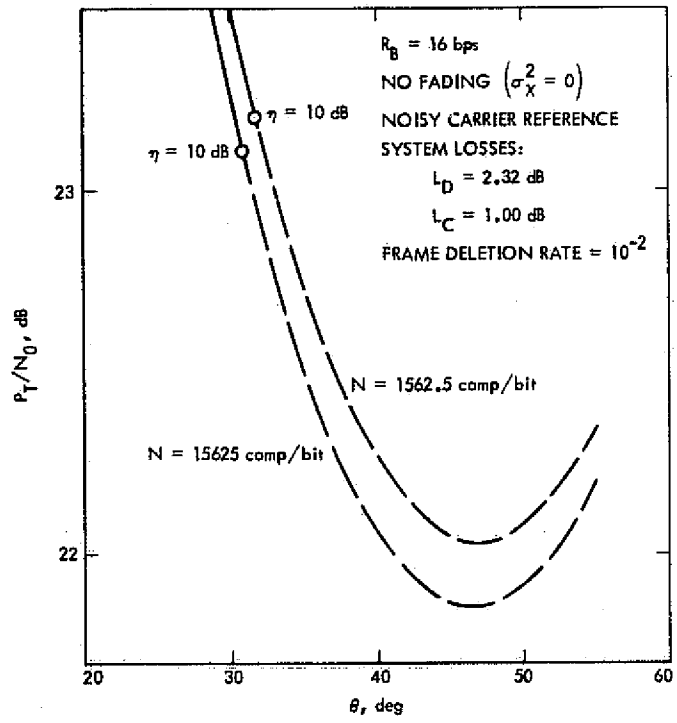

Fig. 2. Signal-to-noise ratios required to achieve a frame deletion rate of 10^{-2} in the absence of fading

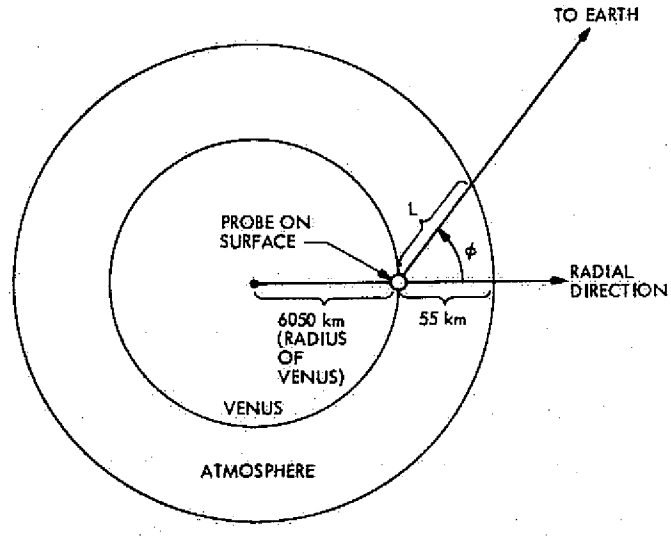

Fig. 3. Variation of atmospheric path length L with transmission angle ϕ from the surface of Venus

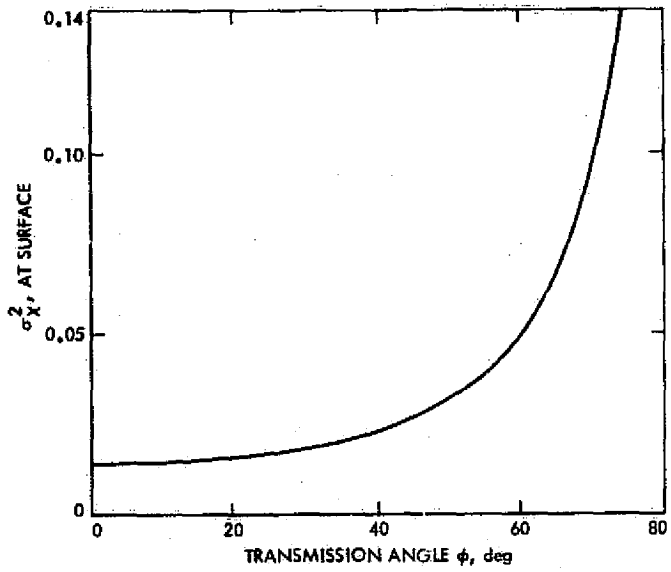

Fig. 4. Variation of log-normal fading parameter σ_x^2 at the surface of Venus with probe transmission angle

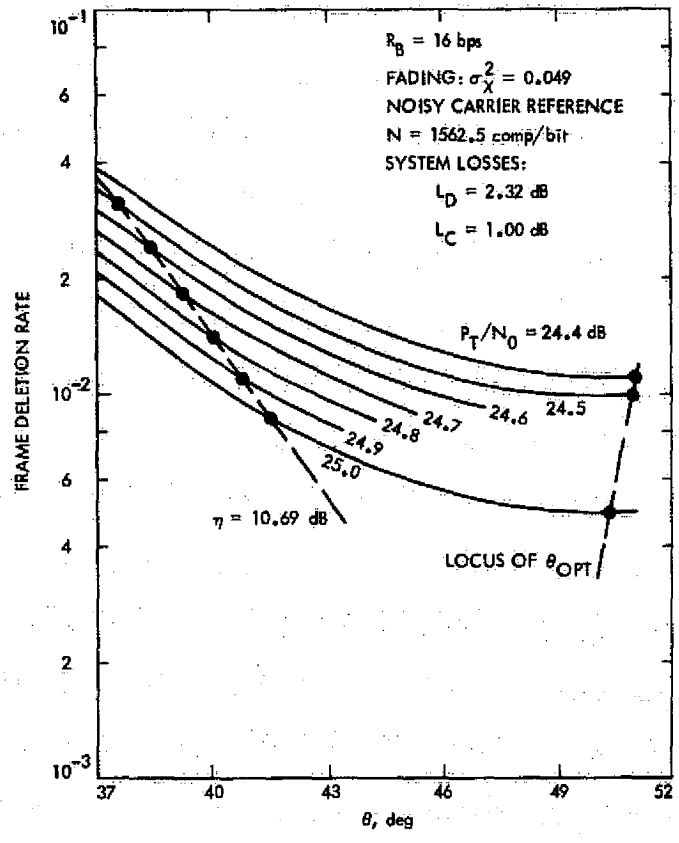

Fig. 5. Signal-to-noise requirements in the presence of fading (σ_x^2 = 0.049) with real-time decoding

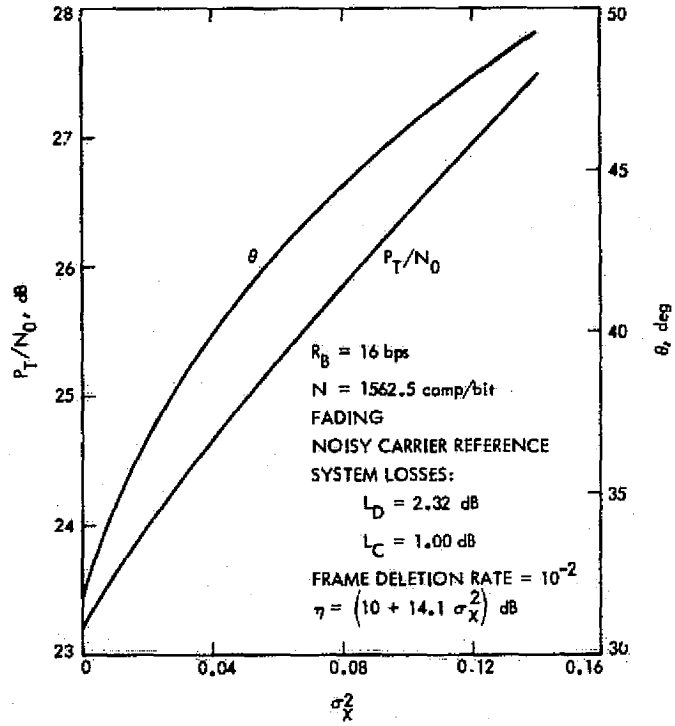

Fig. 6. Degradation of 16-bps telemetry link with real-time decoding as a function of atmospheric fading parameter σ_x^2

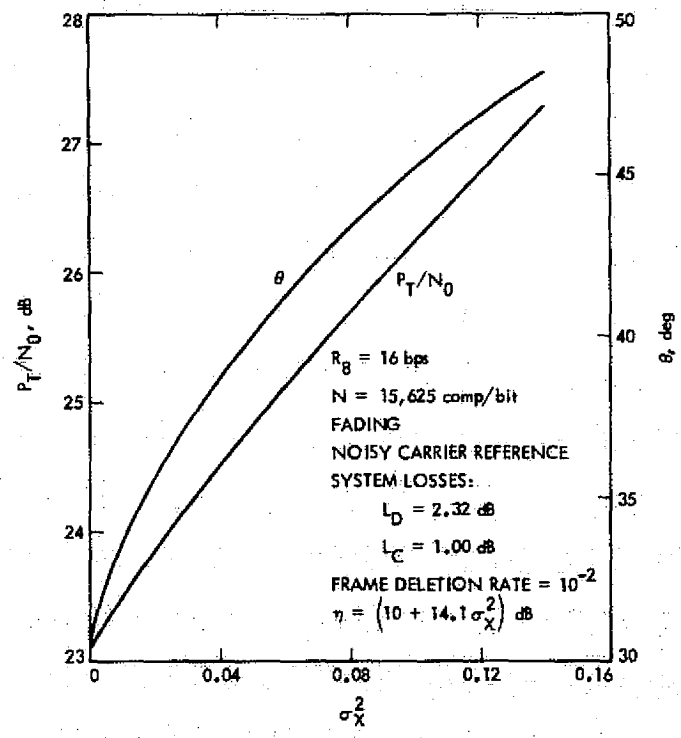

Fig. 7. Non-real-time decoding version of Fig. 5

A Multiple-Rate Command System

R. F. Emerson
Communications Systems Research Section

The impact of a multiple-rate command capability on the present end-to-end ground spacecraft command system has been studied. Limitations in the present command system include a maximum average command word (71 bits or less) transfer rate of 1 word per second and a mean time between failure of 13 hours for the ground portion of the system. Command rates are currently set by end-of-mission (EOM) requirements. Adding a multiple-rate command capability to the present spacecraft command subsystem would result in more reliable flight computer updates during mission phases which could support higher than EOM command rates. During non-catastrophic spacecraft anomalies, commanding could be made more reliable by decreasing the command data rate below EOM requirements. In addition, a flexibility of command rate could be used to optimally apportion command activity between the 26-m and 64-m antenna Deep Space Stations when multiple-spacecraft missions are in progress. The increase in hardware cost necessary to implement a multiple-rate command capability is estimated to be less than 1% of that of current command flight hardware.

I. Introduction

This report describes the results of an investigation into the overall ground/spacecraft command system. The investigation was directed to increasing the ability of the command system by incorporating a multiple-rate capability. The present command system with its capabilities and limitations is outlined. This is followed by a discussion of the impact and benefits which a multiple-rate requirement would have on the system. The impact is shown to be small, but the return in improved utilization would permit greater command traffic and complexity at less cost than the present system expanded to meet the same requirements of traffic and complexity.

II. The Commanding of Spacecraft

Experience over the last decade has shown that a spacecraft's mission is beset with unpredictability, targets of opportunity, and extensions to the prime mission which are most easily handled by remote control. The ground-based command system presented in this report imple-

ments this remote control and thus provides for optimum use of the spacecraft in flight. By combining the technical expertise, data processing power, and decision making capabilities of a ground support team with a reliable and efficient command link, both the operation of the spacecraft and the usefulness of data returned by the spacecraft are improved. An overall view of the present system is provided to furnish a base for the discussion of one improvement in the system, specifically, the capability of commanding a spacecraft at any of several predetermined bit rates consistent with performance requirements and mission phase.

Unmanned planetary missions in the past and through Mariner Jupiter/Saturn 1977 (MJS'77) have not had a major requirement for more than one command bit rate. This, however, is not the case starting with Mariner Jupiter/Uranus 1979 (MJU'79). The third section addresses some solutions to this requirement. The advantages of this improvement, called a Multiple-Rate Command System (MRCS), extend beyond the requirements of the MJU'79 mission. An MRCS would provide improvements in the overall reliability and operations costs on all missions.

III. The Present Command System

The present command system is a combination of special-purpose hardware, computing equipment, software, and organizations within the laboratory responsible for the design, maintenance, and use of the system.

A. Functional Description

Before attempting to delineate the parts of the system, an overview of the functional elements and requirements will serve as a basis upon which to build the description of the system. Figure 1 shows the functional elements and their relationships. General command requirements and sequences are created by a Mission Planning Team (Box 1). This information, combined with the present state of the spacecraft, is used to generate the command strategy, that is, the exact sequence of commands required to change the present state of the spacecraft into that required for the mission plan (Box 2). In real time, the hardware of the Multimission Command System is configured (Box 3) to support a specific mission. The configuration and subsequent performance are monitored (Box 7) to insure usability. Also in real time, the commands generated in Box 2, above, are translated into sequences of bits (digital patterns) (Box 4), which are used to modulate the ground station transmitter (Box 6). On board the spacecraft, received commands are checked for transmission errors, decoded, executed, and the new state of the spacecraft is telemetered back to the ground (Boxes 8 and 9). Telemetry data and ground system monitor information are used to insure that the commands have been transmitted and received correctly (Box 5). The telemetry is also used in non-real time as an input to the next command sequence generation (Boxes 1 and 2). Emergency, nonstandard, and rapid response to new conditions require complex checking, feedback, and feedthrough paths within the command system. These complex paths, however, do not change the fundamental functions presented above.

B. Organizational Structure

The organizational structure of the present system is presented in Tables 1 and 2. Table 1 expands upon the functional requirements showing the relationship between the users, designers, and operators of the equipment. The first column provides a reference to the functional diagram of Fig. 1. The second lists the organization that is the primary user of that functional element. The next two columns describe the special-purpose hardware required for the function and organization responsible for its design. Similarly, the general-purpose computing equipment, the software for it, and the design organization are listed in the next three columns. The last column lists the organization responsible for operating the equipment.

Table 2 uses the information of Table 1 rearranged in terms of the four major functional installations within the command system. These are presented in the center of the table and are:

(1) Mission planning, command generation, and command simulation.

(2) Mission computing and control.

(3) Deep Space Network and network control.

(4) Spacecraft command equipment.

Flanking this listing are the organizations responsible for the development and for the operations of each installation.

C. Present Implementation and Capabilities

The following discusses, in general terms, the equipment used by the present command system to meet the functional requirements. It is organized along the equipment boundaries rather than the previously described functional boundaries.

1. Ground communications. The communications of all command-related information between the control installation (Mission Control and Computing Center (MCCC))

and the Deep Space Station (DSS) is over the high-speed data line (HSDL). The data are sent serially in blocks of 1200 bits at a rate of 4800 bits/s. Block throughput rate for this duplex channel is 99.5% (Ref. 1). This HSDL bit rate, however, does not adequately describe the transfer rate of commands through the high-speed data line. When the block structure is examined in detail (Refs. 2 and 3), it is seen that the maximum command word rate, for commands of 71 bits or less, is about 1 per second. For present bit rates this is more than adequate. However, for command element radiation times approaching 1 command element per 2 seconds, serious difficulties may be encountered.

The overall channel is protected against errors within the block. The probability of accepting a bad block is less than 2×10^{-10}. This is provided by a 33-bit polynomial check word sent as part of each block. Line outages are defined as a minimum of 10 blocks in error (Ref. 4). These outages are protected against by a feedback path between the DSS and MCCC. The mean-time-to-failure of this type of outage has been measured at 4.76 hours. In addition, 87.5% of the outages have a duration of less than or equal to 1 minute (Ref. 4). Therefore, the probability of an interruption exceeding 1 minute is 6.25×10^{-4}.

2. Command Modulator Assembly. The Command Modulator Assembly (CMA) is a special peripheral for the Telemetry and Command Processor (TCP) (Ref. 5). The CMA provides the interface between the TCP and the exciter through which command bits are sent. In addition, the CMA sets and checks the operation of itself, reporting to the TCP both correct and incorrect operations. Because of the multimission requirements, the CMA has been designed to modulate the exciter with an FSK or PSK waveform (Ref. 6). Each of these options is controlled from the TCP. The selection is communicated from mission operations via the Network Operations Control Center (NOCC) over the HSDL.

Each command bit is verified both when received by the CMA and when sent to the exciter. If a descrepancy should occur at any time during radiation (bit value, frequency, modulation index, exciter/transmitter operation, etc.) the CMA or the TCP will cause commanding to abort. In the process, invalid commands are not allowed to reach the spacecraft decoder. The abort condition is also reported to the other elements of the command system so that corrective action may be taken. In addition to the automatic abort actions, a manual abort may be performed. This permits aborting valid but incorrect commands.

The CMA can operate at rates up to 1000 bits/s to a resolution of 1% or less (10 μs in period). The resolution in setting other frequencies associated with modulation is 0.1 Hz from 1000 Hz to 1 MHz.

The measured reliability and repairability figures taken from continuing performance studies are: mean time between failures (MTBF) = 196 hours, mean time to repair (MTTR) = 14.5 minutes. These figures include the reliability of both the TCP and CMA (Ref. 7). A further constraint associated with the CMA is that the bit rate does not exceed 1/20 of the subcarrier frequency. This constraint is imposed by the subcarrier frequency validation circuitry (Ref. 8).

3. Telemetry and Command Processor. The function of the Telemetry and Command Processor (TCP) for command is to accept command bit patterns through the HSDL, check and reject data corrupted by transmission errors, set and check the operation of the CMA, send command words to the CMA at the proper time, notify MCCC of the radiation or abort of each command element, and maintain, under control of MCCC, a stack of commands identical to those contained in the command queue at MCCC. If the HSDL should fail, commands can be entered into the TCP manually.

With the TCP processing command data only, bit rates as high as 32 bits/s have been successfully demonstrated. When processing telemetry, the maximum bit rate is limited to about 8 bits/s.

The reliability information given above for the CMA applies to the TCP as well. (MTBF = 196 hours; MTTR = 14.5 minutes.)

4. Command Detector Unit. The following describes a digital Command Detector Unit (CDU) of the Viking type (Ref. 9). This type of device has been accepted by the MJS'77 Project and will probably be accepted by the MJU'79 Project. The digital CDU acquires both subcarrier phase and bit synchronization by maximum likelihood detection of digital correlations performed on the input signal. The phase tracking of the signal is also accomplished digitally. As presently designed, the CDU demodulates a signal whose subcarrier is fixed at 512 Hz and whose bit rate is selectable at the time of CDU manufacture at 1 Hz or from 2 to 256 Hz in even increments.

A bit error rate of 1×10^{-5} is selected as a threshold value. At this threshold the probability of false acquisition is 1×10^{-4}, while the probability of false out-of-lock is 1×10^{-5}. For a single command of the Viking type, the

probability of incorrect execution is 10^{-6} and the probability of failure to respond is 10^{-3}. For a Viking block of 50 words the probabilities are 5×10^{-5} and 5×10^{-2}, respectively (Ref. 10).

5. Central Computer and Sequencer Subsystem. The spacecraft Central Computer and Sequencer Subsystem (CC&S) performs several activities in the command chain. The detected bits of a command message are received serially from the CDU, tested for start of message, and assembled into words. The words are decoded, checked for parity, and routed to the appropriate spacecraft subsystem. A delay of 10 bit times permits the aborting of a command after it has been received and decoded. The abort is indicated by a loss-of-lock in the CDU.

The speed of the present CC&S, with its flight software, permits a decoding bit rate of 50 Hz maximum (i.e., provided the CC&S does no other processing) and a typical decoding rate of 20 Hz. A change in the flight software philosophy could double this rate (Ref. 11).

6. Mission Control and Computing Center. The Multimission Real-Time Command System accepts the command data as a file and communicates these data to the appropriate DSS. Responses from the DSS are used to verify that commands are sent in a proper and timely way. Full control of the command operation is maintained by the command operator. The Mission Control and Computing Center (MCCC)–DSS software maintains a feedback control of the DSS command subsystem via the HSDL.

Mission Control and Computing Center facilities are designed to handle nine DSS/TCPs simultaneously. Each DSS is handled through a communicator having a capacity of 3000 queue elements (71 bits). The functions within the MCCC command system can be processed at rates greater than 1000 bits/s (Ref. 4).

The reliability and maintainability of the MCCC command system have been measured for a period greater than 1.5 years. These measurements show that the present MTBF is 23 hours and the MTTR is 9 minutes (Ref. 12).

7. Other elements. The Flight Data System (FDS), Network Operations and Control Center, and the ground telemetry processing do not have a direct impact upon the multiple-rate capabilities of the command system and will not be amplified upon in the present report. Table 3 presents a summary of the above information.

IV. Multiple-Rate Command System

Certain improvements in the performance of the command function can be obtained by permitting the bit rate of commands to be adjustable in flight. Such a system has been investigated for feasibility and applicability. The proposed Multiple-Rate Command System (MRCS) would permit the radiation and reception of commands at several rates to one spacecraft. The choice of rates would be predetermined, but the selection would be done in real time during the flight.

The CDU is the only component in the total command system that prevents the immediate testing and adoption of MRCS. Philosophically, the changes required to make the CDU compatible with MRCS are small. Likewise, the hardware required represents less than a 1% increase in the cost of the flight equipment. Before outlining the changes required in the CDU, a brief review is presented of the benefits that MRCS would provide.

A. Benefits Obtainable With MRCS

The benefits obtainable from MRCS accrue from three sources: (1) increased rates over those of end-of-mission (EOM) limitations, (2) decreased rates under those usable throughout the mission, and (3) the flexibility in selecting rates as a function of resources.

1. Benefits from increased rates (above normal EOM). Considering the overall performance of the command system, higher rates will increase the probability of completing a command sequence. This benefit arises from the moderate reliability of the ground command system. Measurements to date of ground system reliability show an MTBF of about 13 hours (Ref. 11). Using an exponential reliability function (Fig. 2), this represents a probability of completing an 8-hour command sequence of 54.0%, for 4 hours of 73.5%, and for 2 hours of 85.7%. Assuming for the moment that the 4 to 1 range in rates is compatible with the space link performance, that is that the signal-to-noise ratio (SNR) does not drop below the threshold, the probability that a command sequence could be completed in an 8-hour shift is 54% at the 8-hour rate, 92.9% at the 4-hour rate, and 99.96% at the 2-hour rate. The above figures assume an idealized system operation where repairs require negligible time. The figures, however, do serve to place an upper bound upon the improvement and to indicate the relative improvement resulting from shorter command sequence times. Furthermore, at 1 bit/s, 8 hours of command represents 28,800 bits. For on-board computers with 18-bit words, this would represent a 1600-word update. Such an update is typical for a Mariner class spacecraft.

MJS'77, a typical spacecraft of the next era, contains 3 computers with 4000 words of storage each (Ref 13). Limiting a worst case update to 80% of the available storage and excluding the loading of the back-up computers, the maximum command sequence time at 1 bit/s would be about 48 hours. Continuous operation for 48 hours has only a 2.5% probability of occurring. At a command rate of 4 bits/s, the time would be 12 hours and the corresponding probability of completing the command update without ground system failure would be 39.8%. Commanding at 8 bits/s would result in a 6-hour sequence, which could be repeated in a 12-hour pass, yielding an 86.3% probability of completion.

An alternate view of the use of the system would be to limit command sequences to those of a length such that the probability of completion exceeds some value. For the following discussion, 80% has been used as the minimum allowable probability of completion. At the MTBF of 13 hours, this yields sequences no greater than 2.90 hours. Table 4 gives update sizes versus bit rate for this time (80% of 12,000 words equals 9600 words). If such a sequence were sent twice, the reliability would be 96% and take 5.8 hours. For three transmissions, the reliability would be 99.2%, and the time would be 8.7 hours. This, again, neglects repair time, but for the present system 98% of the repairs would be completed in less than 1 hour, thus increasing the overall time required for the double transmission to less than 6.8 hours and the triple transmission to less than 10.7 hours. Both are well within a 12-hour pass.

The command acquisition time is fixed at 90 bit times. Thus for 1, 2, 4, 8, and 16 bits/s this results in 90, 45, 22.5, 11.25, and 5.625 seconds, respectively. The MJS'77 Project has specified a commanding sequence in which the CDU lock is broken after each block of about 1000 bits (Ref. 13). If such a strategy is adopted, it will increase the overall active command time required (i.e., the time that the system must be up). This results in a corresponding reduction in probability of completion. For any specific mission with values of ST_B/N_0 at the spacecraft and commands sent in blocks of N bits, a series of curves could be generated to provide an optimum strategy at each point in the mission. Aside from the above outline of such a process, the generation of such curves is outside the scope of this report.

By completing a command sequence with a high probability in less than 8 hours, a second shift would be obviated. The staffing for command costs about $160,000 per year for a shift of 8 hours, 7 days per week (Ref. 14). For long-term missions such as MJU'79 (11 years), this reduction in operations staffing can result in large savings.

The number of commands per unit time has increased as missions have become more complex. With continued increasing complexity, longer missions, and expanding options within a mission, this increase should continue. The increased traffic places a heavy load upon the DSN. By 1977, 16% of the tracking time will be required for command. This figure excludes extended missions and, as a result, is probably low. Furthermore, in these initial calculations, no attempt has been made to include the effects of view period. This also may result in a value too low for some periods. The ability to select a bit rate compatible with mission phase from a set with adequate range will aid in keeping the net loading within bounds.

2. Benefits from decreased rates (below normal EOM). The benefit achievable from decreased bit rates comes mostly from the increase in received SNR over the command channel. The most outstanding benefit of this type is in the event of a spacecraft emergency where commandability can be increased.

Such a condition has been encountered in the design of the Viking 1975 mission (Ref. 15). At superior conjunction with the 26-m, 10-kW subnet and the low-gain antenna 30 deg off axis (a condition possible through loss of attitude sensor lock), the required bit rate to maintain a bit error rate threshold of 1×10^{-5} is less than the fixed 4 bits/s.

MJS'77 will require the 64-m, 100-kW station at its 16-bit/s rate to command out of trouble at Saturn encounter and beyond (Ref. 14). With the present design of the MJU'79 mission, at Uranus encounter and during probe insertion, the spacecraft will be commanded to an attitude where further command must be at 1 bit/s to be reliably accepted. This condition occurs with the 64-m subnet at 100 kW.

With the exception of MJU'79, no provision has been made to avoid these difficulties. The lower bit rates of MRCS would improve the commandability in these cases. MJU'79, recognizing the extent of the problem, is requiring that at least 2 rates, 1 and 16, be available.

3. Benefits from the flexibility of bit rate. The flexibility in selecting bit rate delivers benefit in two areas: (1) it permits the optimization of the entire command link over the mission in terms of command reliability (a combination of link performance and ground system reliability),

and (2) it permits the allocation of command activity between the two subnets (26 and 64 m).

B. Changes Required to Support MRCS

In this section only those changes required to test and apply MCRS will be discussed. This set of changes may not result in the most efficient MRCS, but does result in an MRCS with a lower overall system impact. The final section will discuss briefly those areas which require further study and which may result in a more optimum system.

1. Changes required of the ground system. No hardware changes are required for the ground command system to be able to support MRCS up to a rate of 16 bits/s. However, procedures must be developed to permit the changing of rate during a pass, monitoring this activity, and verifying it. This requires the coordination of activities between Mission Operations System (MOS) and NOCC. The DSS is transparent to these activities.

2. Changes required of the flight system. The changes required of the flight system are of both the hardware and software type.

Two elements of the command subsystem hardware are affected. First, the CDU rate selection must be made flight programmable. Second, an interface from the CC&S to CDU must be developed to activate the rate change.

The change in flight software involves only a small expansion to handle the CDU interface. It does not represent a change in philosophy. This modified on-board command subsystem is shown schematically in Fig. 3. Command modulation delivered from the Radio Frequency Subsystem (RFS) is processed by the digital CDU. The demodulated command bits, with indicators showing CDU status, are sent to the CC&S where the commands are decoded. When a rate selection command is recognized, the pertinent information is sent back to the Rate Selection Storage Register through an appropriate interface. Data from the Rate Register are communicated in parallel with the CDU where it controls timing signals.

3. Use of MRCS. The spacecraft command operation can be broken into two subtypes: (1) discrete commanding, and (2) on-board computer updating. Discrete commanding is characterized by a low density of command words; therefore, no appreciable gain can be obtained by increasing the bit rate. However, computer updates are characterized by high command density and would benefit from higher bit rates.

A command sequence involving a computer update would probably consist of: (1) acquisition of command uplink at lowest rate, (2) transmit rate change command for higher rate as a discrete command, (3) break bit sync lock and reacquire higher bit rate, (4) transmit update at high rate, and (5) transmit rate change command for lowest rate. In addition, the CC&S would be required to monitor command activity. If no activity occurred within a given period of time, the CC&S would command the CDU to the lowest rate.

This sequence of operations would insure optimum commandability at all times excluding spacecraft emergency, and would provide for greatest commandability in the event of a spacecraft emergency.

C. Other Approaches to MRCS and Their Impact

The approach discussed so far has assumed that the CDU resides within a flight command system which includes the CC&S. While this simplifying assumption is valid for JPL spacecraft, it may not be so industry-wide.

Two approaches have been considered for a "stand-alone" CDU which would meet the MRCS requirements. The first includes, essentially, a limited decoder which would process a command message header and set its operation for the proper bit rate. The second approach would determine, without the aid of a special header, the bit rate being transmitted and lock to it.

Analysis of these two options is still in progress; thus a complete and fair comparison of the two approaches cannot be made at this time. Preliminary studies, however, indicate that the first of the two approaches (i.e., a CDU containing a limited decoder) would require changes in the MCCC, DSN, and NOCC hardware and/or software. This would be in addition to those procedural changes required of the base system described in Subsection IV-B. Neither of these changes would be required for the second type of "stand-alone" CDU.

V. Conclusions

Multiple-rate commanding is compatible with the major portion of the present command system. It would provide advantages in system reliability, network loading, and operations costs. Ground system effective reliability can be increased from 2.5 to 86.3% for a worst-case on-board computer load. By permitting optimum rate commanding through either the 26-m or 64-m subnets, the availability of the total network is increased. The shorter command

periods will, further, reduce operations costs, a significant effect for the long-term missions of the next era. These advantages can be obtained without extensive and costly changes to the present spacecraft/ground command system.

The work in process analyzing the above candidates for performance and total system impact will lead to an optimum on-board CDU. By considering the total system impact, such a CDU will be optimized in the global sense rather than in the narrow confines of its discipline.

References

1. McClure, J. P., *4800 bps High Speed Data Error Statistics*, IOM, Jan. 5, 1973 (JPL internal document).
2. *Deep Space Network Systems Requirements—Detailed Interface Design*, Section IV (Command), 820-13, Apr. 15, 1972 (JPL internal document).
3. Poulson, P. L., White, J. H., and Frasier, C. E., *Division Software Planning Document for the Redesign and Implementation of the MCCC Command Subsystem*, 1824-1, Rev. A, May 15, 1973 (JPL internal document).
4. McClure, J. P., *High Speed Data Outage and Block Burst Distribution*, IOM 3380-73-175, Nov. 8, 1973 (JPL internal document).
5. *Operations and Maintenance, Command Modulator Assembly*, TM 01105, Feb. 15, 1971 (JPL internal document).
6. *Telecommunications Systems Design Techniques Handbook*, Technical Memorandum 33-571, edited by R. E. Edelson, Jet Propulsion Laboratory, Pasadena, California, July 15, 1972.
7. Frampton, R., and Tucker, W., *Command System Monthly Report for May 1974*, IOM 421-PF-CMD021, Jan. 5, 1974 (JPL internal document).
8. Allen, W., *Command Standard*, IOM 3381-74-113, June 12, 1974 (JPL internal document).
9. Tegnelia, C., and Meahl, M., *Final Report, Digital Command Detector Development*, 900-547, Apr. 28, 1972 (JPL internal document).
10. Mathison, R. P., "MJS'77/VO'75 PSK Command System," presented at the PPDSWG Meeting, Jet Propulsion Laboratory, Pasadena, California, Apr. 22, 1974.
11. Emerson, R. F., *Comments on Reliability for Command*, IOM 331-74-92, July 24, 1974 (c.f. Emerson, R. F. IOM 331-74-92, *Extensions*, IOM 331-74-102, Aug. 7, 1974) (JPL internal documents).
12. Long, R., *Weekly MCCF Reliability Report*, June 30, 1974 (JPL internal document).
13. McKinney, J. C. "MJS Command System Project Requirements Overview," presented at the End-to-End Command Study Team, Jet Propulsion Laboratory, Pasadena, California, June 26, 1974.
14. Pierson, R., *Proposed MJS'77 Command Baseline Design Change*, IOM 3621-73-021 Feb. 5, 1973 (JPL internal document).
15. Byers, R., "Command System," presented at the PPDSWG Meeting, Jet Propulsion Laboratory, Pasadena, California, Apr. 22, 1974.

Table 1. Functional delegation to organizations

Function	User organization	Special hardware	Development organization	Computers	Software	Development organization	Operation organization
1. Mission planning	Project Office (200) Project Engineering Division (290)	None	—	360/75 nonreal time (Mission Computing Facility (MCF))	Sequence of events	Flight Applications Programming Section (915)	Mission Computing Section (918)
2. Generate command strategy	Project Office (200) Project Engineering Division (290)	None	—	1108 nonreal time (Scientific Computing Facility (SCF)) 360/75 real and nonreal time	Assembler for onboard computer command generation simulation Sequence generation Command generation and simulation	Data Systems Engineering Section (916), (292), (361), (363), (340) Flight Applications Programming Section (915)	Science and Engineering Computing Section (914) Mission Computing Section (918)
3. Configure ground system	DSN Systems Engineering (430) Space Flight Operations Section (295)	Network Control Systems—Computer Network (NOCC)	DSN Data Systems Development Section (338)	Modcomp Sigma 5 [real time] (Network Data Processing Area (NDPA))	NCS Command System NCS Support Program	DSN Data Systems Development Section (338)	DSN Facility Operations (422)
4. Translate commands	Project Office (200) Space Flight Operations Section (295)	None	—	360/75 real time (MCF)	Real-Time Multimission Command System—Command Translator	Data Systems Engineering Section (916) Flight Applications Programming Section (915)	Mission Computing Section (918)
5. Process telemetry (for command)	Project Office (200) Project Engineering Division (290) Space Flight Operations Section (295)	DSN-receiver Subcarrier demodulator Symbol synchronizer Data decoder Block decoder Ground communications equipment (HSDL)	R.F. Systems Development Section (335) DSN Data Systems Development Section (338)	Interdata 4 (Data Decoder Assembly (DDA)) SDS 920 (TCP) 360/75 real time (MCF)	Data Decoder Program TCP Program Real-Time Multimission Telemetry System	DSN Data Systems Development Section (338) DSN Data Systems Development Section (338) Flight Applications Programming Section (915)	DSN Facility Operations (422) Mission Computing Section (918)
6. Transmit commands	Space Flight Operations Section (295)	Transmitter and modulator Antenna Antenna Control Processor Command Modulator Assembly Ground communications equipment	R.F. Systems Development Section (335) DSN Engineering Section (332) DSN Data Systems Development Section (338)	SDS 910 (Antenna Pointing Subsystem (APS)) Telemetry and Command Processor (SDS920) (TCP) 360/75 Real-Time System (MCF)	Antenna Pointing Subsystem Program TCP Program Real-Time Multimission Command System	DSN Data Systems Development Section (338) Data Systems Engineering Section (916)	DSN Facility Operations (422) Mission Computing Section (918)

Table 1 (contd)

Function	User organization	Special hardware	Development organization	Computers	Software	Development organization	Operation organization
7. Monitor ground system (see No. 3 (NCS))						DSN Systems Engineering (430)	
8. Process commands	Project Office (200)	Spacecraft radio Command Detector Unit Modulation Detector Assembly (MDA)	Spacecraft Radio Section (336) Spacecraft Telecommunications Section (339)	On-board control computer (CC&S) On-board data computer Flight Data System (FDS) Guidance and control computer (APS)		Spacecraft Computer Section (361) Spacecraft Data Storage Section (363) Guidance and Control Division (340) System Design and Integration Section (292)	

Table 2. Installations versus organizations

Development organization	Functional installation	Operating organization
Data Systems Engineering (916) Flight Applications Programming (915) Systems Design and Integration (292) Spacecraft Computers (361) Spacecraft Data Storage (363) Guidance and Control (340)	Mission planning Command generation Command simulation	Mission Computing (918) Science and Engineering Computing (914)
Data Systems Engineering (916) Flight Applications Programming (915)	Mission computing and control	Mission Computing (918)
DSN Data Systems Development (338) R.F. Systems Development (335)	Deep Space Network and network control	DSN Facility Operations (422)
Spacecraft Radio (336) Spacecraft Telecommunications (339) Spacecraft Computers (361) Spacecraft Data Storage (363) Guidance and Control (340)	Spacecraft command equipment	Space Flight Operations (through command link) (295)

Table 3. Performance characteristics of system elements

Element	Throughput	Reliability			Flexibility	Error rate	Accuracy
		MTBF	MTTRS	Redundancy			
High-speed data line (HSDL)	4800 bits/s 4–1200 bit blocks/s 6 command words/block ≃ 1 command word/s (includes feedback checking) Block throughput rate 99.5%	4.76 h for outages of 10 blocks or more 38 h for outages of 1 min or more	14.8 m $\alpha = 0.9958$*	Partial or full	N/A	From 1×10^{-5} to 5×15^{4} bit error rate From 3×10^{-4} to 5×10^{-3} block error rate 1×2^{-35} undetected bit error rate	N/A
Command Modulator Assembly (CMA)	1000 bits/s	196 h (includes TCP)	14.5 m $\alpha = 0.9988$	Partial or full	Mode (1) Frequency shift keying (FSK) (2) Phase shift keying (PSK) (3) Direct carrier phase modulation (4) PSK-PN (sync) (5) PSK-Manchester II coded	Theoretical (predicted) bit error rate 1×10^{-6}	
					Subcarrier 100 Hz to 1 MHz		0.1-Hz resolution
					Sine or squarewave data rate 1 bit/s to 1 kbit/s		10-μs resolution in period above 1 bit/s
					Modulation voltage 50 to 800 mV peak		3.14-mV resolution
					FSK frequency 100 Hz to 1 MHz		0.1-Hz resolution accuracy is tied to station reference frequency
Telemetry and Command Processor (TCP)	32 bits/s no telemetry 8 bits/s telemetry	196 h (includes CMA)	14.5 m $\alpha = 0.9988$	Partial or full	Programmed for multimission application	N/A	N/A

Table 3 (contd)

Element	Throughput	Reliability			Flexibility	Error rate	Accuracy
		MTBF	MTTRS	Redundancy			
Command Detector	256 bits/s	—	—	Full	1 to 256 bits/s (even rates)	Bit error rate at threshold, SNR + 10.5 dB, 1×10^{-5}. Acquisition Failure 1×10^{-4}. False out-of-lock 1×10^{-5}. Single command. Incorrect execution 1×10^{-6}. Failure to respond 1×10^{-3}. 50-word block commands. Incorrect execution 5×10^{-5}. Failure to respond 5×10^{-2}.	N/A
Central Computer and Sequencer (CC&S)	50 bits/s command decoding only 20 bits/s shared tasks Doublable with a change in flight software	—	—	Full	Fully programmable	N/A	N/A
Mission Control and Computing Center (MCCC)	>1000 bits/s	24 h	9 min $\alpha = 0.9932$	Partial or full	Fully programmable	N/A	N/A
Flight Data System (FDS)		—	—	Full	Limited format selection	N/A	N/A
Network Operations and Control Center (NOCC)	Rate change confirmed within 5 min—manual (Block II–Block III)				N/A	N/A	N/A

*$\alpha = \dfrac{\text{MTBF}}{\text{MTBF} + \text{MTTR}}$ = uptime ratio

Table 4. Bit rate versus update size

Bit rate, bits/s	Approximate words in 2.90 h
1	580
2	1160
4	2320
8	4640
16	4280
32	18560
64	37120
128	74240

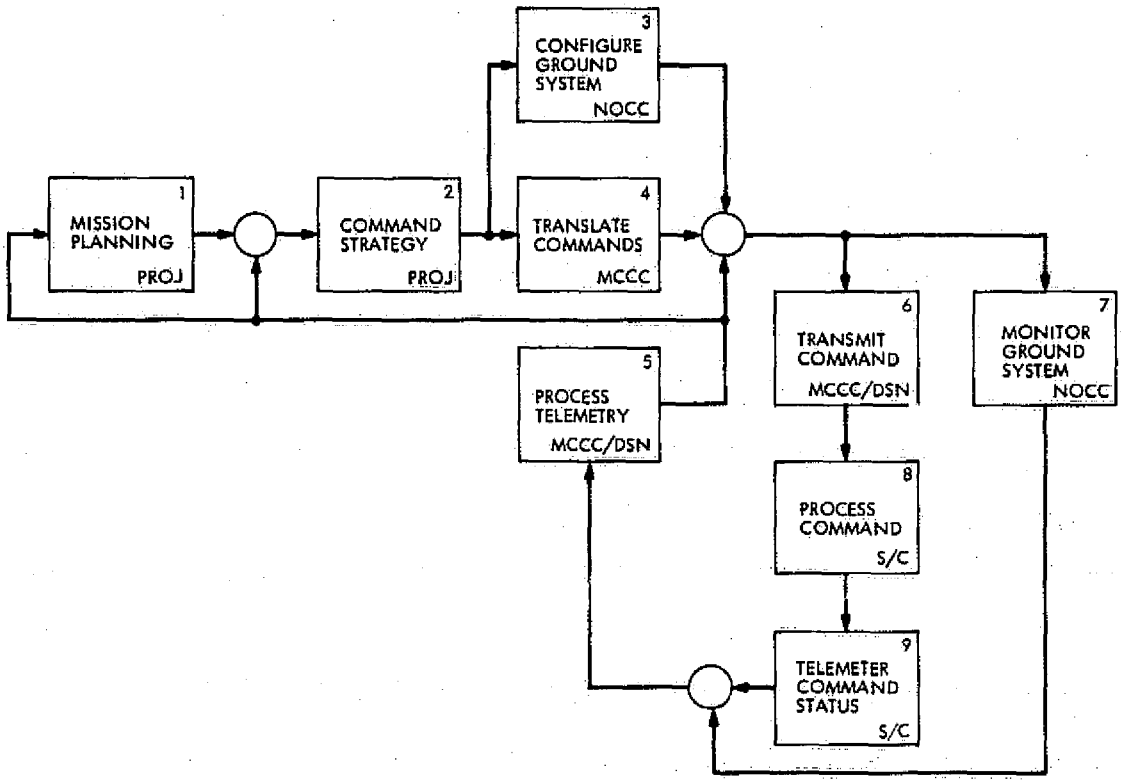

Fig. 1. Command System functional block diagram

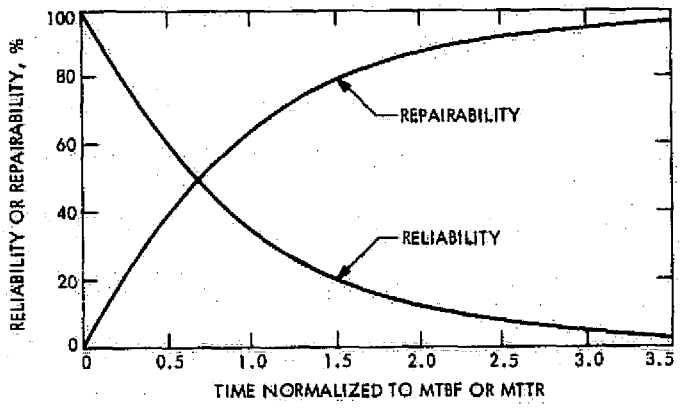

Fig. 2. Reliability and repairability vs normalized MTBF and MTTR

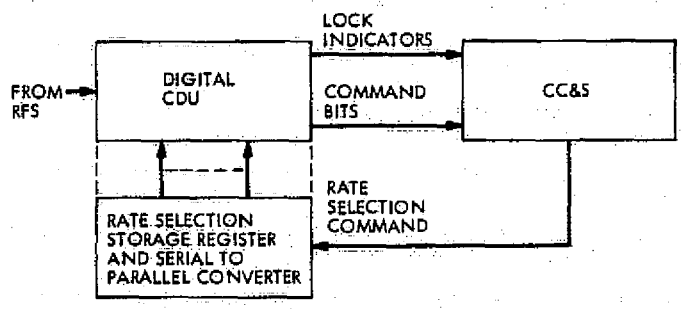

Fig. 3. Block diagram of MRCS on-board command subsystem

Golay–Viterbi Decoding: Results of the MVM'73 X-Band Telemetry Experiment

L. D. Baumert and R. J. McEliece
Communications Systems Research Section

The X-band convolutionally coded telemetry data from the Mariner 10 X-band telemetry experiment have been used to evaluate the performance of the Golay–Viterbi concatenated coding system proposed for Mariner Jupiter/Saturn 1977 (MJS'77).

On January 15, 1974, nearly 70 minutes of simulated X-band convolutionally coded telemetry was recorded at the Goldstone 64-m antenna station. One object of this experiment was the quantitative evaluation of the $K = 7$, rate ½ convolutionally coded, Viterbily decoded telemetry system which is scheduled for use on all Mariner-class spacecraft after 1976. The relevant experimental parameters were:

Data rate:	2.9 kb/s
Nominal E_b/N_0:	3.0 dB
Data sequence:	···10101010···
Code sequence:	···11010111010111010···
Subcarrier frequency:	177.1 kHz
Symbol Synchronizer Assembly (SSA) matched filter quantization:	Sign plus 5 bits magnitude

The bit error probability was calculated over intervals of 1-min duration; the results are shown in the upper curve of Fig. 1. Notice that the bit error probability exceeded the nominal threshold of 5×10^{-3} during the latter half of the experiment. For further details of this part of the experiment, consult the memo by Springett and Kollar (Ref. 1).

After the telemetry was Viterbily decoded, an *error* tape, containing about 10^7 bits, 1 denoting an error, 0 no error, was produced. This tape was then "decoded" by a Golay decoder identical to that proposed for use in the MJS'77 concatenated coding scheme for nonvideo telemetry (Ref. 2). That is, the Viterbi error sequence was assumed to be a sequence of noisy 24-fold interleaved 24-bit Golay codewords, and each such codeword was decoded according to the decoding algorithm $B1$ of Ref. 2. Again the bit error probability was calculated over 1-min intervals; the results are shown in the lower curve of Fig. 1. Notice that the Golay decoder made no bit errors until the Viterbi bit error P_v probability exceeded the 5×10^{-3} threshold. However, during the periods when $P_v > 5 \times 10^{-3}$, the Golay performance also exceeded its threshold 5×10^{-5}.

References

1. Springett, J. C., and Kollar, F. J., "Results of the MVM'73 X-Band Telemetry Experiment," private communication, May 1974.

2. Baumert, L. D., and McEliece, R. J., "A Golay–Viterbi Concatenated Coding Scheme for MJS'77," in *The Deep Space Network*, Technical Report 32-1526, Vol. XVIII, pp. 76–84, Jet Propulsion Laboratory, Pasadena, Calif., Dec. 15, 1973.

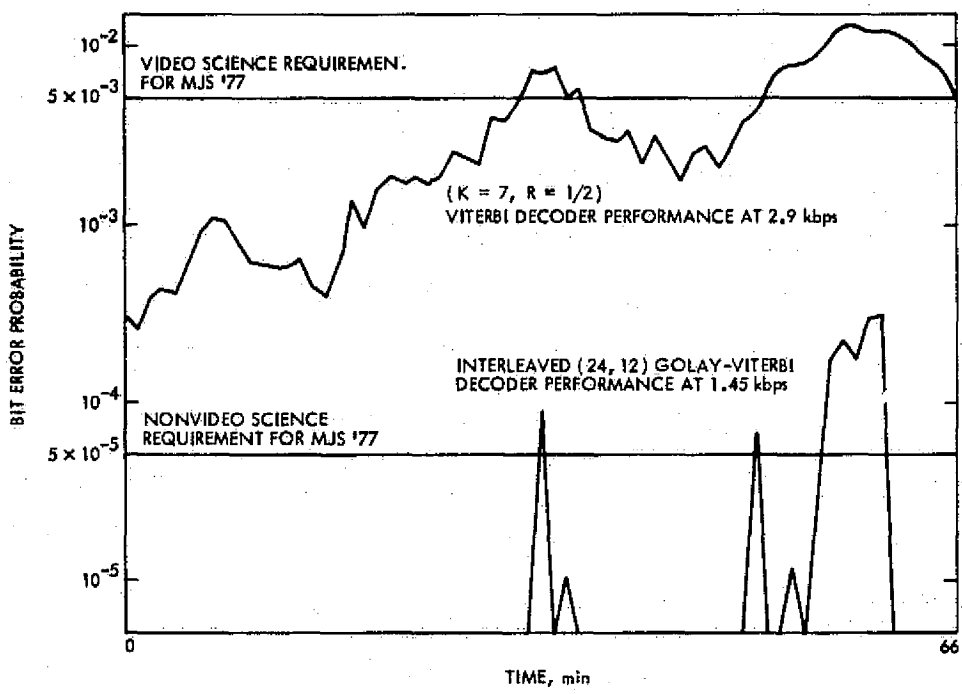

Fig. 1. X-band telemetry experiment coded data results

A Signal Combiner for Antenna Arraying

H. Wilck
Communications Systems Research Section

The signal combiner performs the phasing and summing of a high data rate spacecraft telemetry signal received simultaneously at three DSN stations. The signals are combined at the subcarrier level after they have been microwaved to a common site. Before summing the signals the combiner delays them by the amount necessary to compensate for differences in phase due to unequal station-to-spacecraft distances and microwave delays. A tracking loop continuously adjusts for changes in signal delay so that correct phasing is automatically maintained throughout the spacecraft pass.

The signal combiner was successfully used in an experiment designed to improve the quality of real-time video data of the Mariner 10 spacecraft at its second Mercury encounter. Two 26-m antenna stations were arrayed with one 64-m antenna station at the Goldstone Deep Space Communications Complex. This combination produced an improvement in signal-to-noise ratio of 0.8 dB when compared to the 64-m antenna station by itself.

I. Introduction

A spacecraft signal received simultaneously at several tracking stations is affected by an independent noise contribution at each station. An improvement in signal-to-noise ratio (SNR) can therefore be obtained by combining the outputs from various receiving locations in an appropriate manner. This technique is sometimes referred to as "station arraying." Due to differences in spacecraft-to-station distances, the signal arrives with a different delay at each station. These delays vary with spacecraft position. Further delays, which are fixed but generally unequal, are incurred in relaying the signals to a common site. Compensation must be made for all of these delays if a meaningful combination of the signals is to be achieved.

Signal combination at the radio frequency (RF) or intermediate frequency (IF) level would be most desirable, but the technology for synchronizing the signals to the degree required is not yet available. Combining the signals at the subcarrier level, where synchronization requirements are less severe, is an attractive alternative. In fact, if the distance between stations is small and the data rate and subcarrier frequency are low, such that the delay difference amounts to only a small fraction of the

bit time, the signals can be combined without delay compensation. This has been demonstrated by J. M. Urech (Ref. 1). At higher data rates and subcarrier frequencies a variable delay device is needed to phase the signals correctly. The design of the signal combiner was motivated by the problem of phasing the Mariner 10 117.6 kbits/s telemetry signal from three stations to an accuracy of 85 ns (1% of the bit time), with signal delays varying over a range of more than 50 μs during an 8-hr period. The signal combiner provides delay compensation that automatically tracks the changing signal delays and keeps the signals correctly phased throughout the spacecraft pass. The combiner also performs the summation of the properly phased signals.

II. Mariner 10 117.6-kbits/s TV Enhancement Experiment

Two 26-m antenna stations, DSSs 12 and 13, and one 64-m antenna station, DSS 14, were arrayed for the reception of the Mariner 10 high-rate TV data during the second Mercury encounter. The purpose of this experiment was to improve the quality of real-time video data and to demonstrate the arraying technology. Figure 1 describes the experiment configuration in general terms. The receiver baseband outputs from DSSs 12 and 13 are microwaved to DSS 14 via GCF 10, the Communications Switching Center located at DSS 12. The baseband outputs consist of a 177.1-kHz squarewave subcarrier modulated by 117.6-kbits/s telemetry data. The DSS 14 receiver baseband output is microwaved to GCF 10 and back to realize a fixed signal delay of 110 μs. This is necessary to assure that the signal from DSS 14 arrives later at the combiner input than the other two signals, at all times. At DSS 14 the three microwaved baseband signals are fed to the input of the signal combiner, which delays the signals from DSSs 12 and 13 by the amount required to synchronize them with the signal from DSS 14. Once properly phased, the signals are affected by a weighting factor according to their individual SNRs and combined in a summing amplifier. The weighting factors are chosen to optimize the SNR of the sum. The combined signal proceeds from the output of the signal combiner to the baseband input of the Subcarrier Demodulator Assembly (SDA). From there on, the signal is processed in the normal manner by the rest of the telemetry chain.

The three participating stations were in the "listen-only" mode for the experiment. The baseband signal SNRs of the 26-m antenna stations were about 10 dB below that of the 64-m station. Assuming signal addition with optimum weighting (discussed in a later paragraph on "mixing ratio") and perfect phasing, the SNR of the sum is

$$SNR_s = SNR_1 + SNR_2 + SNR_3$$

where

SNR_s = SNR of the combined signal

SNR_1 = SNR of the signal from DSS 14

SNR_2 = SNR of the signal from DSS 13

SNR_3 = SNR of the signal from DSS 12

The improvement in SNR of the combined signal over that of the 64-m antenna station by itself is

$$\frac{SNR_s}{SNR_1} = \frac{SNR_1}{SNR_1} + \frac{SNR_2}{SNR_1} + \frac{SNR_3}{SNR_1}$$
$$= 1 + 0.1 + 0.1 = 1.2 = 0.8 \text{ dB}$$

The following definitions are useful for discussing the delay relationships:

DV_2 = the variable spacecraft signal delay seen at DSS 13 with respect to DSS 14 ($DV_2 = 20$ μs, means that the signal arrives at DSS 13 20 μs later than at DSS 14)

DV_3 = the variable signal delay seen at DSS 12 with respect to DSS 14

DF_2 = the fixed delay incurred in microwaving the signal from DSS 13 to DSS 14

DF_3 = the fixed delay incurred in microwaving the signal from DSS 12 to DSS 14

DF_1 = the fixed delay in microwaving the signal from DSS 14 to GCF 10 and back to DSS 14

DC_2 = the variable delay the signal combiner must impart to the DSS 13 signal in order to phase it with the DSS 14 signal

DC_3 = the variable delay the signal combiner must impart to the DSS 12 signal to phase it with the DSS 14 signal.

The signal combiner does not delay the signal from DSS 14.

If the three signals are to arrive at the summing point in phase, the total delay incurred by each must be the same. Therefore $DF_1 = DV_2 + DF_2 + DC_2 = DV_3 + DF_3 + DC_3$ so that

$$DC_2 = DF_1 - DF_2 - DV_2$$

$$DC_3 = DF_1 - DF_3 - DV_3$$

where

$$DF_1 = 110\ \mu s$$

$$DF_2 = 82\ \mu s$$

$$DF_3 = 55\ \mu s$$

$$\left.\begin{aligned} DV_2 &= -57 \text{ to } +6\ \mu s \\ DV_3 &= -43 \text{ to } +9\ \mu s \end{aligned}\right\} \text{for Mercury II encounter}$$

From the above it can be computed that the signal combiner had to provide delays ranging from 22 to 85 μs for the DSS 13 signal and 46 to 98 μs for the DSS 12 signal.

The rate of change of the variable delays was less than 10 μs/h at all times, i.e., $dDV_2/dt < 10\ \mu s/h$ and $dDV_3/dt < 10\ \mu s/h$.

III. Brief Functional Description of the Signal Combiner

Figure 2 shows a block diagram of the signal combiner. Signals 1, 2, and 3 are the baseband signals from the three receiving stations to be combined. Signal 1, which arrives more delayed than the other two, is fed directly to the summing amplifier. Two identical but independently variable delay channels (Channel A and Channel B on the diagram) bring Signal 2 and Signal 3 into phase agreement with Signal 1 before they reach the summing amplifier, where the three signals are added to produce the combined output.

Briefly, each delay channel functions as follows: The signal to be delayed is sampled at a rate of 2.5 MHz. The samples are then converted from analog to digital form and stored in a first in/first out (FIFO) buffer for a controllable length of time (delay). The control for the buffer delay is derived from the correlation of the buffer output with Signal 1. After leaving the FIFO buffer the delayed samples are reconverted to analog and fed to the summing amplifier.

IV. Detailed Discussion of the Signal Combiner

The three combiner input signals are conditioned by three essentially identical input amplifiers provided with front panel adjustable attenuators and rms voltmeters to monitor the amplifier outputs. The signal + noise voltages out of all three amplifiers are set to the same level. This makes it easier to obtain known mixing ratios. The input amplifiers limit the signal bandwidths to 1 MHz to prevent aliasing in the sampling process that follows.

From the input amplifier, Signal 1 proceeds directly to the summing amplifier; however, at the same time a quantized version of the signal is produced by a sample-and-hold (S/H) followed by a 1-bit analog-to-digital (A-D) converter. The sampling rate is 2.5 MHz. This digitized version of Signal 1 is used only for the purpose of correlation with Signals 2 and 3.

After passing through its input amplifier, Signal 2 is sampled at a rate of 2.5 MHz and then quantized by an 8-bit A-D converter. The 2.5-MHz sampling rate was chosen so as not to degrade the 177.1-kHz squarewave subcarrier appreciably. The use of an 8-bit A-D converter makes the quantization error negligibly small.

The 8-bit samples then pass through a serial FIFO buffer. The buffer output rate is determined by a fixed 2.5-MHz clock, while the buffer input rate is governed by a separate variable clock of approximately 2.5 MHz but asynchronous with respect to the output clock. Making the input clock slightly faster than the output clock will cause the number of samples stored in the buffer (buffer fill) to increase, since more samples are put into the buffer than are withdrawn. Conversely, an input clock lower in frequency than the output clock will cause the buffer fill to decrease. The length of time a sample remains in the buffer (delay) is a function of buffer fill and the phase difference between input and output clock. Therefore, the buffer delay can be continuously adjusted by controlling the input clock frequency. The approximate buffer delay can be calculated using the formula

$$\text{BUFFER DELAY} = \text{BUFFER FILL} \times \text{CLOCK PERIOD}$$

The maximum delay that can be achieved obviously depends on the length or capacity of the buffer. The buffers used in the signal combiner are 8 bits wide × 512 words long. With a clock period of 0.4 μs the delay would be 512 × 0.4 μs = 204.8 μs for a completely full buffer and zero for an empty one. In practice, however, due to internal propagation time limitations the buffer

cannot be run completely full or completely empty at 2.5 MHz, so that the actual maximum delay is about 180 μs and the minimum is 20 μs.

Parallel and series connected Fairchild 3341 FIFO memories (Ref. 2) were used to implement the delay buffers. A digital front panel display of the buffer fill is provided as an acquisition aid. At the output of the FIFO delay Signal 2 is correlated with Signal 1. This correlation, which is maximum when the signals agree in phase, is digitally displayed on the front panel. Furthermore the difference of the correlation of Signal 1 with Signal 2 advanced 90 deg of subcarrier phase and that of Signal 1 with Signal 2 retarded 90 deg is also developed. This difference, designated "quadrature" correlation, crosses zero when Signal 2 agrees in phase with Signal 1 and is, therefore, suitable as a control function for the delay tracking loop. Values for both the correlation and the quadrature correlation are generated once a second.

The quadrature correlation passes through a front panel controlled digital attenuator, which provides a means to manually adjust the loop gain.

A 16-bit digital-to-analog (D-A) converter translates the digital quadrature correlation values into an analog voltage, which is applied to the input of a voltage-controlled oscillator (VCO). The D-A converter output is also displayed by a front panel voltmeter.

The VCO consists of a John Fluke 644A frequency synthesizer adjusted so that the input voltage controls its frequency over a range of 20 Hz around a center frequency of 2.5 MHz. The VCO can also be switched to manual control, which is required during acquisition. The output frequency of the VCO determines the FIFO buffer input clock rate, thus closing the loop.

The control loop functions as follows: It is assumed that Signal 2 is initially in phase with Signal 1. If Signal 2 now advances (in phase) with respect to Signal 1 the quadrature correlation increases. This causes the VCO input voltage and, therefore, its output frequency to rise, making the FIFO buffer input clock rate higher. As a consequence there is an increase in buffer fill and delay, retarding Signal 2. The action of the loop tends to bring Signal 2 back into phase with Signal 1. The phasing error is less than 50 ns.

At the output of the FIFO buffer, Signal 2, which is now correctly phased with Signal 1, is reconverted to analog by an 8-bit D-A converter and then applied to the input of the summing amplifier.

As can be seen in Fig. 2, Signal 3 is processed by Channel B in the same manner as Signal 2 is by Channel A.

Signal 2 and Signal 3 are weighted by gains α_2 and α_3, respectively, before they are summed with Signal 1. These gains are chosen to optimize the SNR of the combined signal. The selection of α_2 and α_3 is discussed in a later paragraph. The summing amplifier itself consists of an operational amplifier followed by a 50-Ω cable driver and a front panel adjustable attenuator. An rms voltmeter is provided to monitor the combined output. Figure 3 is a photograph of the signal combiner.

V. Control Loop Acquisition Procedure

The delay tracking loop acquisition must be performed manually. The loop is opened by switching the VCO control to manual. Monitoring the FIFO buffer fill and varying the VCO frequency by hand, the operator must adjust the delay to within $\pm$ 2.8 μs of the value for correct phasing. The loop can then be closed by switching VCO control back to automatic. If the delay is more than 2.8 μs away from the right value when the loop is closed, false lock will result. This is due to the periodicity of the subcarrier correlation which allows the loop to lock at intervals of 360 deg of the 177.1-kHz subcarrier. Only one of these points, namely where both the subcarrier and the data correlate, is correct. It is possible to find this point by slowly varying the buffer delay and searching for the highest correlation peak with the aid of the correlation display. However, since this procedure can be somewhat time consuming, a Fortran program was written to predict the FIFO buffer fill as a function of time to an accuracy of $\pm$ 2 counts, which corresponds to a delay of $\pm$ 0.8 μs and is better than required. The program computes the variable delays from the station coordinates and antenna pointing angle predicts. It then combines variable and fixed delays to determine the FIFO buffer fill as a function of time and prints it at user selectable intervals. Armed with the program output, an operator can accomplish the task of acquisition in a few seconds.

VI. Best Mixing Ratio

The three inputs to the summing amplifier of Fig. 4 are three versions of the same signal affected by independent noise contributions.

S = signal power

N = noise power

SNR = signal-to-noise ratio

Inputs 2 and 3 are weighted by gains α_2 and α_3, respectively. The weighting should be such that SNR_s is maximum. Since the signals correlate and the noise does not

$$SNR_s = \frac{(\sqrt{S_1} + \alpha_2\sqrt{S_2} + \alpha_3\sqrt{S_3})^2}{N_1 + \alpha_2^2 N_2 + \alpha_3^2 N_3} \quad (1)$$

SNR is maximum if

$$\frac{\partial SNR_s}{\partial \alpha_2} = \frac{\partial SNR_s}{\partial \alpha_3} = 0$$

and

$$\left(\frac{\partial^2 SNR_s}{\partial \alpha_2^2} \cdot \frac{\partial^2 SNR_s}{\partial \alpha_3^2}\right) - \left(\frac{\partial^2 SNR_s}{\partial \alpha_2 \partial \alpha_3}\right)^2 > 0 \text{ and } \frac{\partial^2 SNR_s}{\partial \alpha_n^2} < 0$$

The above conditions result in the system of equations:

$$\alpha_2 = \frac{\sqrt{S_2}(N_1 + \alpha_3^2 N_3)}{N_2(\sqrt{S_1} + \alpha_3\sqrt{S_3})}$$

$$\alpha_3 = \frac{\sqrt{S_3}(N_1 + \alpha_2^2 N_2)}{N_3(\sqrt{S_1} + \alpha_2\sqrt{S_2})}$$

which is solved by

$$\alpha_2 = \frac{N_1\sqrt{S_2}}{\sqrt{S_1}N_2} \qquad \alpha_3 = \frac{N_1\sqrt{S_3}}{\sqrt{S_1}N_3}$$

These are the values of α_2 and α_3 that maximize SNR_s and substituting them into Eq. (1) yields

$$SNR_{s(\max)} = SNR_1 + SNR_2 + SNR_3$$

It can be shown that similar results hold for n inputs with

$$\alpha_n = \frac{N_1\sqrt{S_n}}{\sqrt{S_1}N_n}$$

and

$$SNR_{s(\max)} = SNR_1 + SNR_2 + \cdots + SNR_n$$

For the Mariner 10 television (TV) enhancement experiment a value of 0.3 was used for α_2 and α_3 with the signal combiner input attenuator set such that

$$S_1 + N_1 = S_2 + N_2 = S_3 + N_3$$

The sensitivity of SNR_s to α_2 and α_3 is low, so that their accuracy is not very critical.

VII. Conclusion

The signal combiner performed as predicted during the preencounter tests and the Mercury II encounter. The combined signal showed an improvement in ST_b/N_0 of 0.8 ± 0.1 dB over the DSS 14 signal by itself. No significant operational difficulties were encountered. The Mariner 10 TV enhancement experiment has clearly demonstrated that antenna arraying is practical and can be used to improve telemetry performance. A combination of two 64-m antennas, if they were available within the same complex, could produce a 3-dB improvement in signal-to-noise ratio.

References

1. Urech, J. M., "Telemetry Improvement Proposal for the 85-ft Antenna Network," *Space Programs Summary*, No. 37-63, Vol. II, pp. 116–120, Jet Propulsion Laboratory, Pasadena, Calif.,

2. "The 3341 First In/First Out Serial Memory," *Optimos Manual*, pp. 74–79, Fairchild Semiconductor, Mountain View, Calif., September 1972.

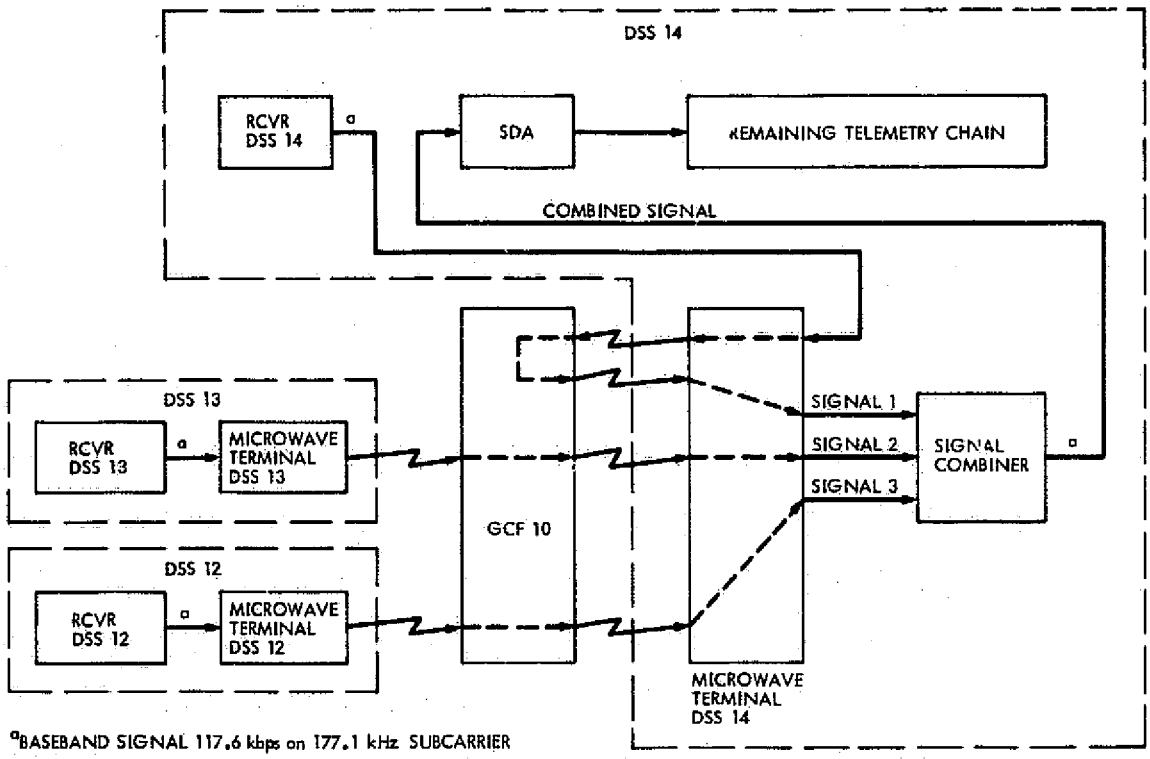

Fig. 1. MVM TV enhancement experiment configuration

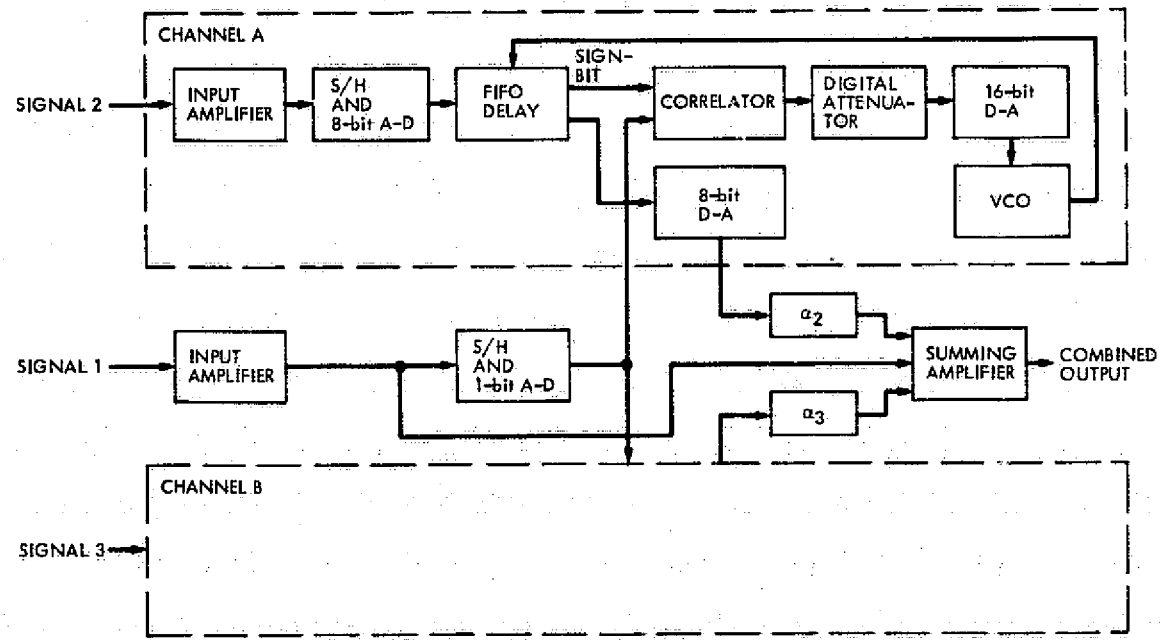

Fig. 2. Signal combiner block diagram

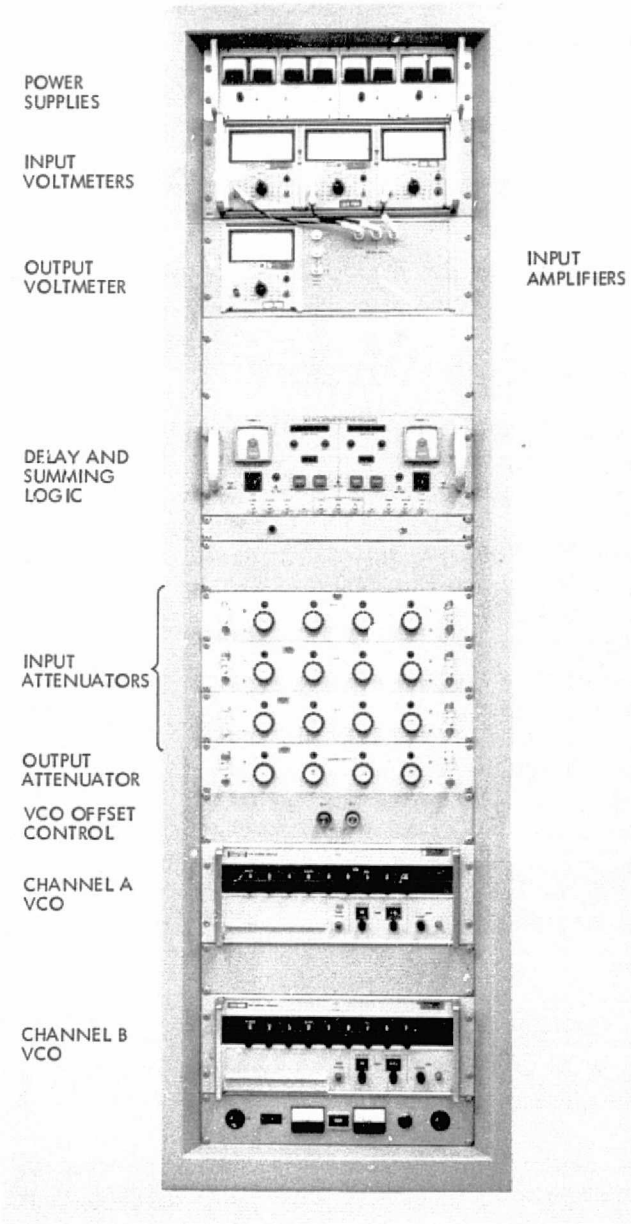

Fig. 3. Signal combiner

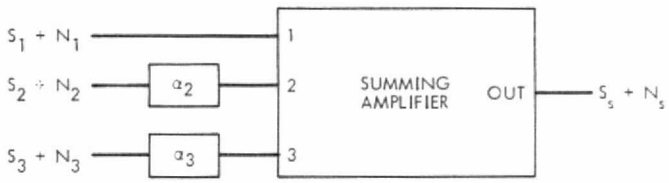

Fig. 4. Mixing ratio

DSN Research and Technology Support

E. B. Jackson and A. L. Price
R. F. Systems Development Section

The activities of the Development Support Group in operating and maintaining the Venus Station (DSS 13) and the Microwave Test Facility (MTF) are discussed and summarized and progress noted. Major activities include preparation for a planned "automated station demonstration" and equipment modification and testing required therefor, flux density measurements of the radiation from the Planet Jupiter and various radio sources, commencement of active collection of solar energy data at DSS 13, on-antenna testing and successful implementation of the 400-kW X-band planetary radar system into DSS 14, completion of the on-site system testing and shipment of the DSS 43 100-kW transmitter system, continued transmission of clock synchronization timing signals to the overseas 64-m antenna stations, expanded activity in support of the Pioneer 10 and 11 science program as Pioneer 11 passed by Jupiter, and continued support of various radio science activities planned in the FY 75 JPL Radio Science Plan.

During the two-month period ending December 15, 1974, the Development Support Group, in its operation of the Venus Station (DSS 13) and the Microwave Test Facility (MTF), made progress on various projects as discussed herein.

I. In Support of Section 331

Station Automation (Pulsars)

As part of the overall DSN Station Automation Project (RTOP 68 "Station Monitor and Control"), a demonstration is planned using the Venus Station to perform a pulsar track under remote control from JPL in Pasadena.

In addition to the modifications to the computer and 26-m antenna servo system previously discussed (Ref. 1), the waveguide switching system has also been interfaced with the SDS-930 computer. The SDS-930 computer now has *control* of the input termination for the maser, i.e., either the antenna feedhorn or the ambient temperature waveguide load can be selected as the input termination for the maser. The SDS-930 computer can *monitor* which termination is in use, and also monitor the polarization which has been selected by the operator. As a result of

previous testing, the servo system has been further modified to connect the SDS-910B antenna pointing input error signals directly to the rate amplifier, rather than coming in through the integrator. The computer now performs the integration with software. This connection is *only* effective when the computer is being used as part of this demonstration.

Testing of the system being automated consumed 121 hours, while actual observation of pulsars, at 2388 MHz, left-circular polarization (LCP), with the 26-m antenna, was performed for 70-1/4 hours. The pulsars observed are tabulated in Table 1.

II. In Support of Section 333

A. Radio Star Calibration

With the receiver tuned to 2278.5 MHz, and the 26-m antenna adjusted to receive right-circular polarization (RCP), received flux density measurements were made of radio sources Cassiopeia A, Cygnus A, and Virgo A during 44-1/4 hours of observation. These measurements are made in a semi-automated fashion using the noise adding radiometer (NAR) with programmer to control antenna movement and data taking cycles through the medium of an interface with the SDS-910B antenna pointing computer.

B. Sky Survey

With the 26-m antenna fixed in azimuth and progressively positioned in elevation, 503 hours of data were automatically collected during the night and weekend hours when the station is not manned. Completing one cycle of elevation positions at 88.8 deg, a new cycle was started at 80.0 deg, and by the end of the period observations had been taken through 80.6 deg elevation. Additionally, 24 hours of observation of the pole star, Polaris, were performed. All observations are made at 2295 MHz, with the 26-m antenna adjusted to receive RCP and the NAR collecting and storing the data on magnetic tape.

C. Faraday Rotation

With the two systems under evaluation performing well, the residue of the earlier installation (two rotating antenna systems, receivers, and test oscillators) was collected and returned to the Stanford Research Institute. Some difficulty was experienced with the data recording system being triggered by noise, but a modification performed by Bruce Parham of Section 333 solved that problem, and, at the end of the period, the system is working well.

D. Solar Energy Instrumentation

In support of the project to gather precision data on solar energy impinging on the Goldstone area, the Solar Energy Instrumentation Data Acquisition System has been transferred from DSS 14 to DSS 13 along with the associated sensors. This system consists of a multiplexer, analog-to-digital converter, programmer, various readouts, clock, and digital magnetic tape recorder with a small printer providing a record for operator use. Additionally, for off-line use, there is a digital tape player and a line printer. As currently configured, the system has eight analog and four digital channels, with a capability of approximately 300 total analog and digital channels for which cards are available. Three sensors (outdoor air temperature, dew point hygrometer, and pyranometer) are currently collecting data. The system is installed in building G-60 with the pyranometer installed on the roof.

Additionally, two mirror test tables have been set up in the desert northeast of the Microwave Test Facility (MTF). One table will be periodically cleaned while the other will be left untouched; the mirrors on both tables will have reflectivity measurements made periodically.

III. In Support of Section 335

A. X-Band Planetary Radar

Radio frequency (RF) testing at the 300-kW RF power level was successfully accomplished with the feedcone on the DSS 14 antenna. Full transmit system testing, under closed-loop phase control, was then performed for a 5-hour period, during which careful radiation survey measurements were made. Later, radiation intensity survey measurements were also taken with the antenna in "worst case" Saturn tracking positions. In neither case were dangerous levels found at any ground position. The survey is described in more detail elsewhere in this issue.

During the first operational radar tracks starting December 10, 1974, the transmitting system performed well, although some trouble was experienced with the receiver and correlator. Later, a malfunctioning traveling-wave tube was removed and replaced in the buffer amplifier.

Although DSS 14 personnel have been provided with "red-lined" documentation suitable for operation and troubleshooting, work is continuing on preparation of documentation suitable for transfer, along with cleanup of the remaining items of Engineering Change Order (ECO) implementation required.

B. DSS 43/63 100-kW Transmitter Testing

The Philco Ford Corporation (PFC) installation team has left for Spain to aid in the installation of the DSS 63 100-kW transmitter system, and all equipment has been shipped to them.

For both systems, modifications have been made to the dual ignitron deck assemblies, and successful checkout accomplished. Also, spare filter reactors and all logic cards have been tested while the focusing magnet assemblies have been modified and tested.

Using the "test bed," four rebuilt and modified X-3060 klystrons have been tested. One failed the acceptance test and was returned to the manufacturer (Varian Associates). The other three required on-site retuning by a manufacturer's engineer prior to acceptance. Using one of the retuned klystrons, a 12-hour "stability" test at the 100-kW power level was performed on the RF cabinet destined for DSS 43. After successful completion of this test, the system was dismantled, the transformer rectifier assembly was weighed (14,526 kg (32,025 lb)), and shipment to Australia was accomplished. Only minor items remain to be shipped.

C. Microwave Power Transmission

In preparation for the forthcoming prototype panel testing (March 1975), the power distribution transformer in the collimation tower building was relocated, and ground fault interrupters were put into the circuits to protect all power outlets. In preparation for installation of the final array, all existing microwave dishes were removed from the tower to minimize wind loading.

D. Block IV Receiver/Exciter (DSS 14)

Support of work on the Block IV Receiver/Exciter Subsystem has continued. This work included the modification of the temporary receiver and exciter manual control panels, fabrication of temporary cabling, and general subsystem troubleshooting and maintenance.

Subsystem performance testing and test procedure verification have been started and will continue. In preparation for doppler frequency error tests, the long-run hardline coaxial cables used in the Block IV Receiver/Exciter at DSS 14 are being tested using conventional procedures, insertion loss, time domain reflectometry and spectrum analysis. Past experience has shown that these tests may locate only the more severe cabling faults. It is therefore planned to use the special Digital Instrumentation Subsystem (DIS) monitor program for final evaluation. If possible, a comparison with similar tests on the present Block III Receiver/Exciter cabling will be made.

Preliminary work has been started to provide the capability for rework and testing of Block IV Receiver/Exciter electronic modules at DSS 13 utilizing contractor personnel. This would facilitate the completion of the subsystem.

A total of 97 manhours of support has been provided at DSS 14 by Development Support Group JPL personnel during the last two months.

IV. In Support of Section 391

Differential VLBI

As part of the overall DSN effort to develop the capability to navigate a spacecraft using distant radio sources as references, we provided tracking support to fast-switching VLBI measurements between the Pioneer spacecraft and various reference radio sources. A total of 21 hours of station support, of which 13 hours were actual tracking, was provided.

V. In Support of Section 422

Clock Synchronization Transmissions

The punched paper tapes, which are used as input data by the station computers with which to accomplish clock synchronization transmissions, have shown gradually increasing error rates due to improper sprocket hole punching and spacing. During the last two months several reschedulings were required and some transmissions were canceled for this reason. When the December tapes arrived, the error rate was so high that complete replacement was necessary. The replacement tapes, which were punched on a different machine at JPL, are usable. During this period six transmissions for a total time of 6-3/4 hours have been made as scheduled by the DSN.

VI. In Support of Section 825

A. Pioneer 10, 11 Science Support

DSS 13 continued to provide an average of 14.5 hours per week of observation. Measurements of the radiation level from Jupiter and the radio source calibrators tabulated in Table 2 were made at 2295 MHz, with the 26-m antenna adjusted to receive RCP. Observations were

made for a total of 130-3/4 hours, with the data being semi-automatically collected by the NAR.

B. Interstellar Molecular Recombination Line Search

Continuing with the attempt (Ref. 2) to detect recombination lines of carbon, 51 hours of support were given to this project. During the 36-3/4 hours of actual tracking, observations were made of the region around W51 and S140, using a frequency of 2273.9 MHz with the antenna adjusted to receive RCP.

Similar observations are also made on the DSS 14 64-m antenna and are part of the JPL Radio Science Plan for FY 75 described as "Interstellar Microwave Spectroscopy," OSS-188.

References

1. Jackson, E. B., and Price, A. L., "DSN Research and Technology Support," in *The Deep Space Network Progress Report 42-24*, p. 78, Jet Propulsion Laboratory, Pasadena, Calif., Dec. 15, 1974.
2. Jackson, E. B., "DSN Research and Technology Support," in *The Deep Space Network Progress Report 42-22*, p. 111, Jet Propulsion Laboratory, Pasadena, Calif., Aug. 15, 1974.

Table 1. Pulsars selected for test observation at DSS 13 (10/16–12/15)

0031−07	1237+25	1929+10
0329+54	1604−00	1933+16
0355+54	1642−03	2021+51
0525+21	1706−16	2045−16
0823+26	1749−28	2111+46
0833−45	1818−04	2218+47
1133+16	1911−04	

Table 2. Radio source calibrators used for Pioneer science support (10/16–12/15)

3C17	3C147	3C353
3C48	3C309.1	PKS 0237-23
3C123	3C348	

Hybrid Integrated Circuit Development

C. F. Foster
R. F. Systems Development Section

This report describes the development of a single hybrid circuit to replace the control portion of a 15-line computer interface consisting of 25 discrete integrated circuits. The primary requirements of this hybrid development are the standardization of a logical design to implement the requirements of the Deep Space Network standard interface requirement and the reduction of system downtime due to complex troubleshooting.

I. Introduction

The control portion (handshaker) of the standard DSN 15-line interface (Ref. 1) performs all the information transfer protocol and generally relates necessary communication between computer and device before data can be successfully transferred. A handshaker circuit that satisfies these computer and device interface requirements has been designed (Fig. 1) and will function between any desired combination computer and peripheral device. This circuit is both device and computer independent and operates in the half duplex mode using a fully interlocked request and acknowledge control transfer (Ref. 2).

The handshaker circuit contains 25 transistor-transistor logic (TTL) integrated circuit (IC) packages and 25 wirewrap IC sockets (Fig. 2) all mounted on a 120 mm × 115 mm circuit board. This method requires 750 connections, 50 of which are for B+ and ground. Because this circuit is designed such that it feeds signals from one stage to another, dependent on conditions within its feedback and/or external inputs, it is extremely difficult to troubleshoot (i.e., even if every IC was replaced with fully tested units, it would take a minimum of 15 min, and the fault could still be in the sockets or in one of the 750 connections).

A requirement to reduce Deep Space Station downtime resulted in the investigation of hybrid circuits as a means to replace multiple discrete integrated circuits with a single package and to provide a standardization of the logic design.

II. Implementation

The initial hybrid development utilizes the same TTL circuit design as the discrete design. The TTL circuit chips are bonded to a package that is 36 mm × 36 mm, with 24 pins. The TTL interconnect circuitry within the hybrid is similar to a standard printed circuit (PC) board in that the circuit traces are etched. Due to its small size, circuit crossovers can be made with short gold wire jumpers bonded to the traces. This method, because it

eliminates the need for multilayer boards to solve circuit crossovers, greatly reduces design time and cost over the conventional PC board. The completed hybrid circuit package is shown in Fig. 3, and a single chip has been enlarged in Fig. 4 to show the wire bonding.

III. Conclusion

The hybrid handshaker circuit has been successfully evaluated with the coherent reference generator and the PDP-11 minicomputer using the 15-line interface. The hybrid circuit has reduced the system parts inventory by 10 to 1, based on stocking one each of every type of IC. The system assembly has been reduced from 750 connections to 48, thereby improving both reliability and enhancing quality control. By reducing parts by 24 and interconnections by over 700, the system testability has been improved as well as downtime due to testing and repair. Because the TTL chips can be removed with heat, the hybrid can be returned to the factory for repair at a fraction of replacement cost. The completed prototype hybrid handshaker will undergo further testing outside of the development group.

The results of these tests will be used to evaluate this approach and determine if further design effort is required.

References

1. Fry, W. C., *Deep Space Network Standard Interface*, Spec. ES50834A, June 4, 1973 (JPL internal document).
2. Foster, C. F., *Complete Logical Operation and Test Procedure of Handshaker Circuit*, Spec. TP510942A, in preparation (JPL internal document).

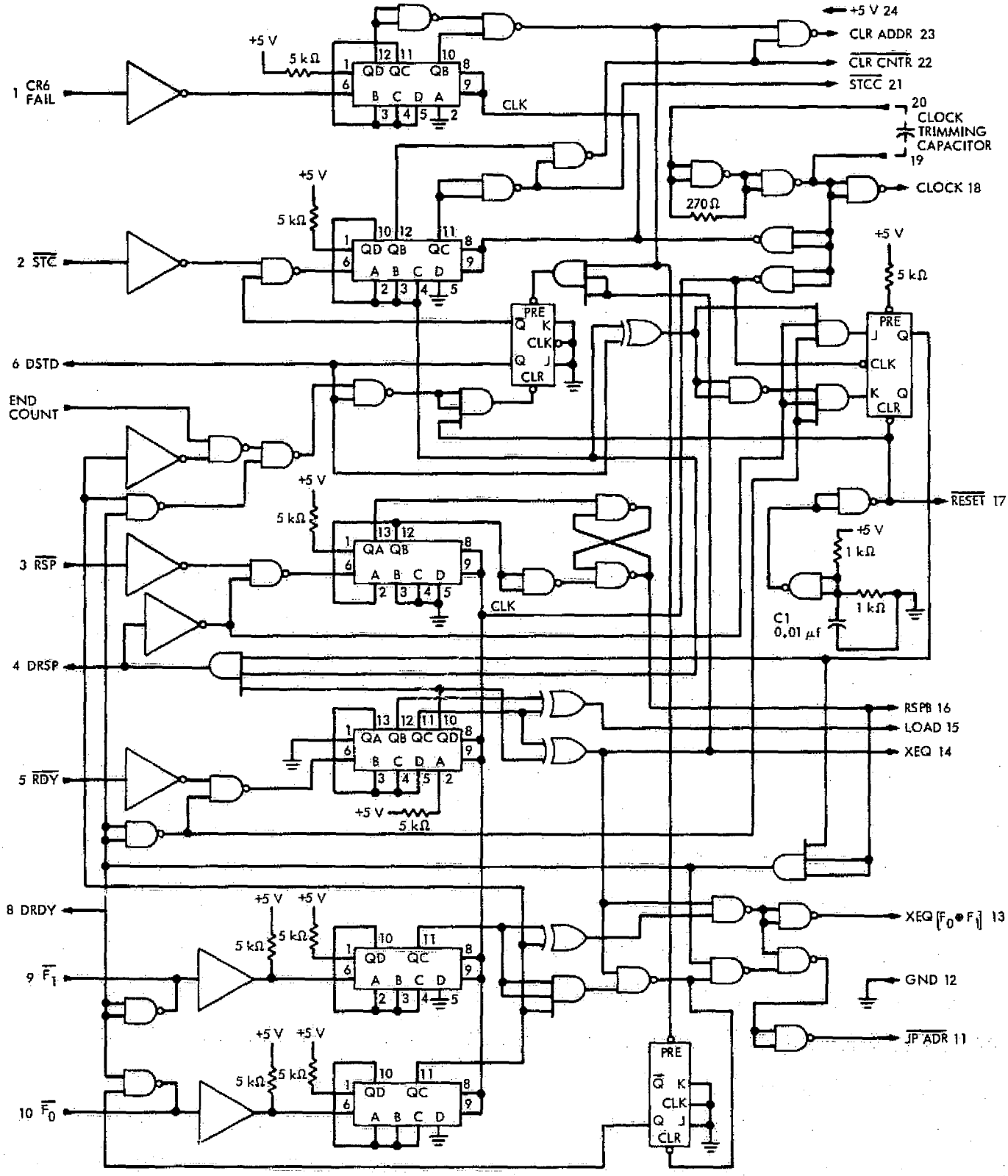

Fig. 1. CRG computer interface handshaker logic diagram

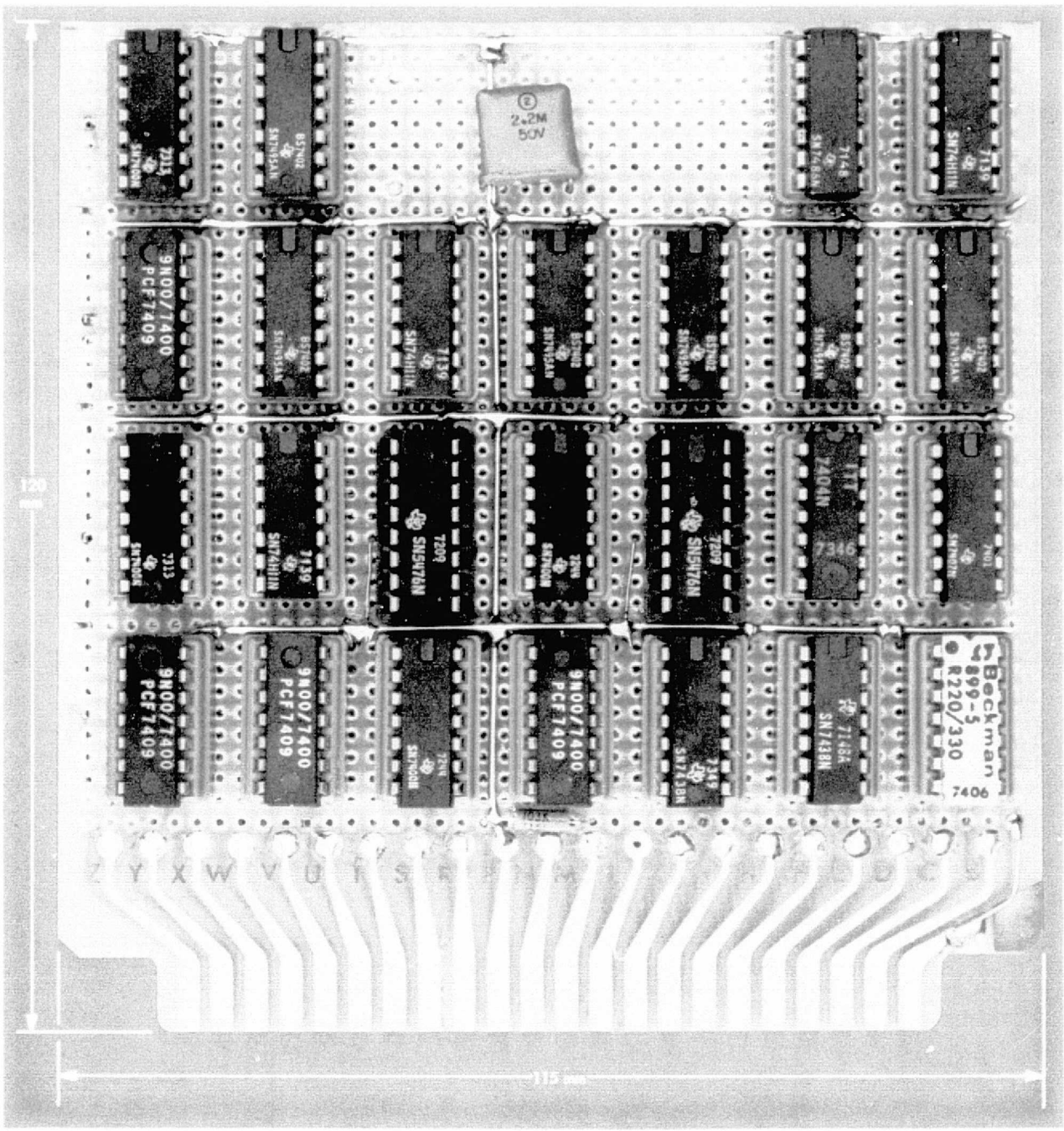

Fig. 2. Computer interface handshaker logic (discrete)

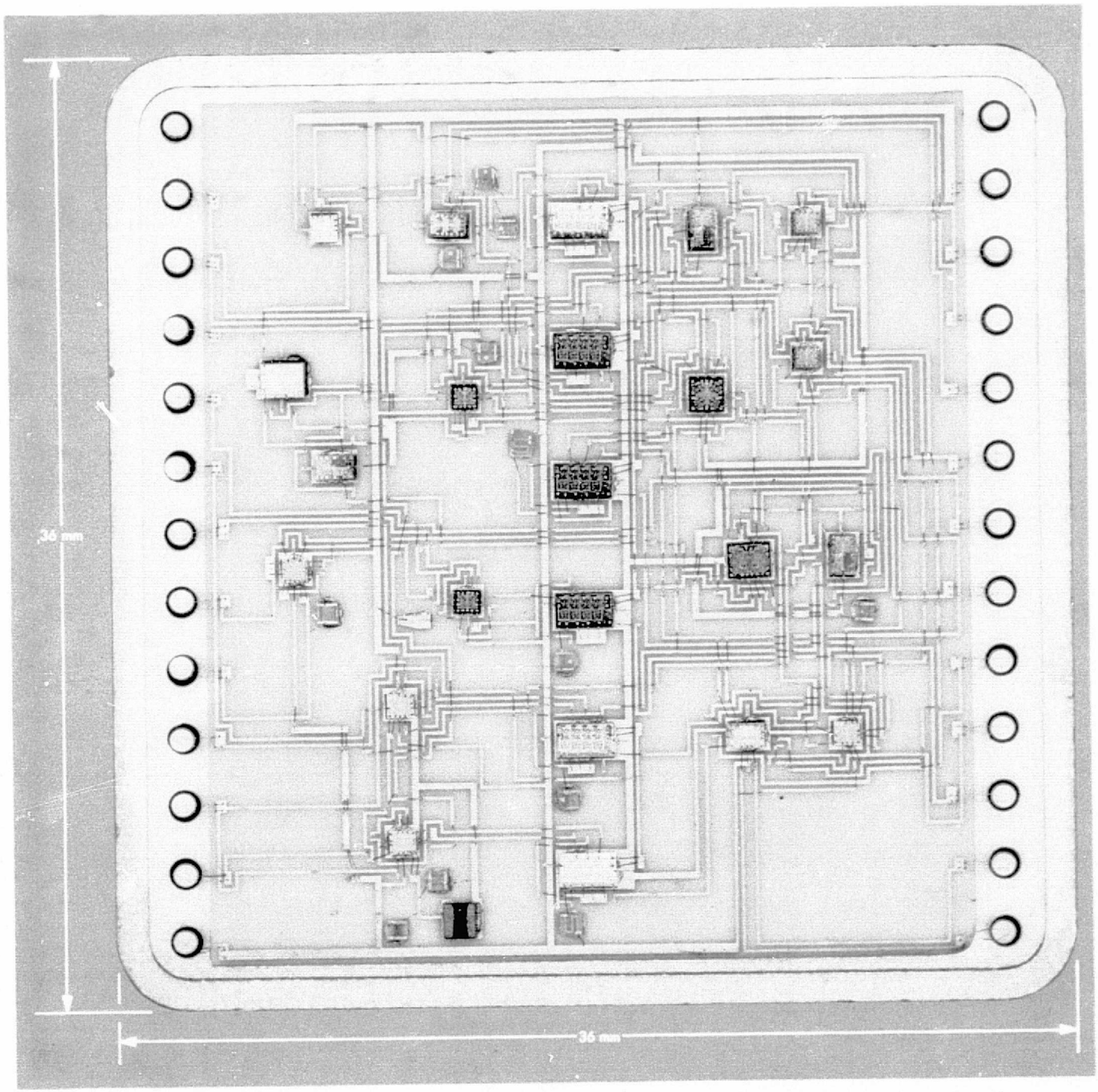

Fig. 3. CRG computer interface handshaker logic (hybrid)

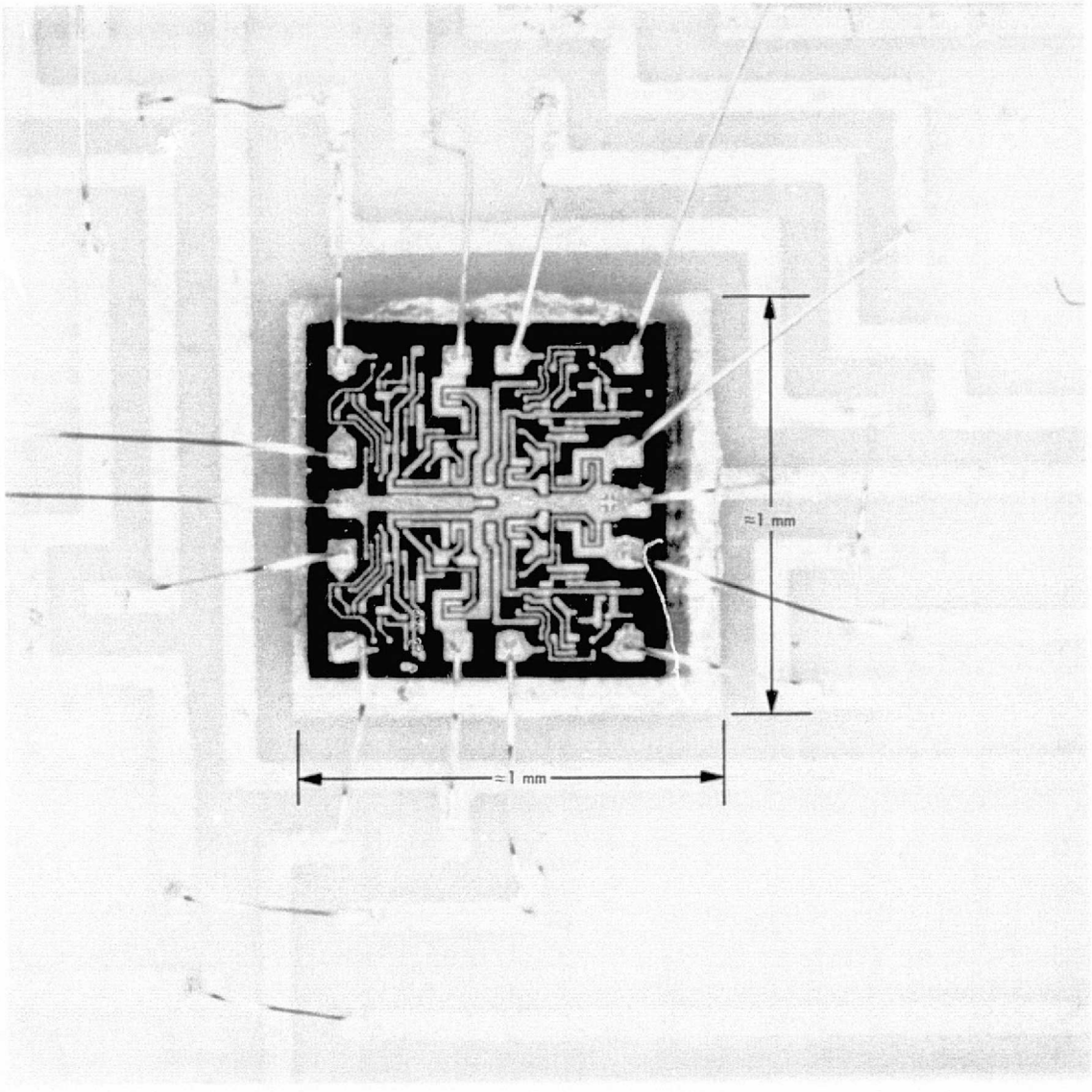

Fig. 4. Hybrid circuit chip mount

Automated Pulsar Data Collector

S. S. Brokl
Communications Systems Research Section

The pulsar data collector is a self-contained automated subsystem for the DSS 13 Automation Demonstration. It relieves the 900-series computer from much of the software previously used for data collection. The pulsar data collector is a high speed, periodic signal sampler and integrator which has demonstrated faster operation and higher resolution than existing devices.

I. Introduction

The automated pulsar receiver (Ref. 1) in conjunction with the pulsar data collector are fully programmable subsystems for the Pulsar Automation System at DSS 13. The pulsar receiver is a self-contained, 30 MHz-to-baseband receiver with three selectable predetection bandwidths, a diode power detector, an attenuator, and a variable postdetection filter.

The pulsar data collector is a self-contained, periodic signal sampler and integrator, interfaced with an XDS 900-series computer. The data collector uses a high speed (4 μs conversion time) 12-bit analog-to-digital (A-D) converter. Once the pulsar parameters are programmed into the receiver and the data collector, the computer is free to carry on other tasks as the data collector takes the data and stores them in its own memory. Upon completion, the data collector signals the computer that the observation has ended.

II. The Problem

Limits of the present pulsar timer (Ref. 2) and its implementation as a data collector are its low speed and resolution, its heavy reliance on software and its need for large amounts of computer memory space. With DSS 13 automation, large observation programs and memory allocated to data storage exhaust present memory space in existing 900-series computers. Also, with the current pulsar observing system, it is not possible to increase the resolution of the observations while maintaining phase.

The new pulsar data collector is self-contained with its own memory, high speed transistor-transistor logic (TTL), and Schottky logic control elements. It can maintain phase when parameters are changed to expand the resolution of the observation. It has no operator controls and can be programmed by any 900-series computer.

III. Hardware Implementation

Figure 1 is a block diagram of the new pulsar data collector presently installed at DSS 13 and controlled by the XDS 930 computer. The data collector may be used with any 900-series computer without any hardware modifications. The station 1-s tick (1 pulse/s) and a frequency synthesizer are used to establish the precise timing for the data collector.

There are two single-instruction Energize Output M (EOM) codes used to program the pulsar data collector from the 930 computer. Both EOM codes are manually set with dual-in-line switches within the data collector. This allows changing of the instruction codes easily and makes the data collector compatible with any 900-series computer.

One EOM is used for control. When it is followed by the proper Parallel Output (POT) word from the computer, it sets up the register pointer or starts the data collector in one of three modes: initial-start, start-on-next-major-cycle-clearing-memory, and start-on-next-major-cycle-not-clearing-memory. Initial-start starts the data collector on the next 1–s tick (1 pulse/s).

The second EOM is used for data transfer. The following POT or Parallel Input (PIN) word causes the transfer of a 24-bit word from the computer to the register pointed to in the data collector, or from the data collector register to the computer, respectively.

The register pointer operates in four modes and sets up the condition for transfer of data between the computer and the registers. The memory address counter (A) and the memory (M) are considered registers. In the first mode, the register pointer will point only to the register designated in the POT word following the control EOM and will not change until commanded by a new control EOM POT sequence. In the second mode, the register pointer will increment to the next register in sequence after a data transfer POT has occurred. It will not increment beyond the M position. In the M position, the increment after POT or PIN will refer to the memory address counter (A). The third mode is the same as the second except the increment will occur after a data transfer PIN. In the fourth mode, the increment will occur after a data transfer POT or PIN and is used for memory testing.

There are eight binary registers in the data collector. The maximum number of bits for each register is as follows:

X	16
Y	24
Δ	24
L	24
N	16
D	16
A	13
M	24

The data stored in the X and Y buffer-hold registers must be the 2's complement of the actual number used as the divisor for determining minor and major cycle pulses from the frequency synthesizer input. The Δ register stores the delay of the number of minor cycle pulses to wait after a major cycle pulse before starting data collection. The L register holds the number of minor cycle pulses delayed plus the number of minor cycle pulses to be used as data points. The N register holds the number of major cycles to be observed. The D hold register cannot be programmed directly but is cleared by every initial start command. The D register holds the number of major cycle pulses that have occurred between the end of one observation and the start of the next observation.

The X and Y counters are used as modulo n dividers where n max for X = 2^{16} and n max for Y = 2^{24}. The X counter sets the number of frequency synthesizer pulses for each minor cycle pulse; the Y counter sets the number of minor cycle pulses for each major cycle pulse.

The major cycle length is generally set to the period or repetition rate of the observed pulsar. The minor cycle pulses are then the number of samples during this period. The X and Y counters are not stopped between observations, and their reference values are changed only at the very beginning of a major cycle. New values from the computer are kept in buffer registers. As long as the product of X and Y is kept the same, phase will be maintained between observations.

A 16-bit up/down counter is used as the N counter with the major cycle pulses being counted. During observation, the N counter counts down from the number loaded into the N hold register. When the count reaches zero, a computer interrupt is fired to signal completion of the observation and the counter starts counting up. At the beginning of the next observation, the number counted up to in the N counter is transferred to the D hold register. With each new start command the N counter is reset to a down counter with the value of the N hold register in it.

The Δ and L counter is cleared by the major cycle pulse and counts up with each minor cycle pulse; the maximum count is 2^{24}. This counter, in conjunction with two 24-bit comparators and the Δ and the L hold registers, controls the start and end of data collection and the storage of the data in memory. The value of Δ determines at which minor cycle pulse (relative to the beginning of the major cycle) data are first taken and stored in the first memory location. It can be 0 to 2^{24}. The value of L should be the value of Δ plus the number of samples to be stored in memory. Data are taken at each minor cycle pulse between Δ and L. The value of the number of samples may be from 1 to 8000, which is the minimum and maximum size of the memory.

Pulsars only emit significant radiation during about 1/10 of the period. By using new values in the X, Y, Δ and L hold registers determined from full-period observations, one can take all the observations during a limited fraction of the period, thus increasing the resolution without destroying the phase of the observed data.

The memory address counter is controlled by the start and end pulses from Δ and L comparators while data are being collected. When the memory is being controlled by the computer, the address counter is set to an effective memory location when the register pointer is pointing to the A register. The address counter automatically increments at the end of a POT or PIN when the register pointer is pointing to the M register. During data collection, the address counter always starts at zero and stops at L. The memory automatically cycles through starting at zero with each new major cycle pulse.

The 8K × 24-bit memory is comprised of two Standard Memories, Inc. 8K × 18-bit stand alone memory modules. Every third bit in each module is not used, giving 48,000 spare bits in each module. The output of the memory (M_o) is in 2's complement.

During the first scan of data after an initial–start or start-on-the-next-major-cycle-with-clear-memory, the First-N-Inhibit prevents the old data within the memory from being added to the new data. This effectively clears the memory by storing only the new data in each memory location. During subsequent scans, the contents of the effective memory location are called up, added to the new data point, stored in the adder-hold-register and written back in the effective memory location for each minor cycle pulse.

The A-D converter is a Datel ADC-N-12C 12–bit, 2's complement bipolar converter, with a sample and hold module ahead of it. The maximum conversion rate is 4 μs. The data collector is independent of the converter and may be used with new higher speed devices as they become available.

The PIN data multiplexer (MUX) allows data from any of the registers or memory to be selectively read into the 930 computer. The register being read is dependent on the register pointer position after a control EOM, as described earlier.

IV. Software

Table 1 shows the EOM codes and POT bit positions for control of the Automated Pulsar Receiver. Also included is a skip-if-signal-not-set (SKS) test for automatic mode. When the receiver is in the local mode the computer has no control of the functions.

Table 2 shows the EOM codes and POT bit positions for control and data transfer of the pulsar data collector. An interrupt to the 930 computer is also supplied to signal completion of an observation.

V. Conclusion

The automated pulsar receiver and data collector are subsystems for the DSS 13 automation demonstration. These subsystems have been installed, tested, and are now operational.

The first test results for PSR 0329-54 and PSR 0833-45 shown in Fig. 2 give an example of the high resolution available with the pulsar data collector. The horizontal axis is time and is 5,000 samples long. The vertical axis is the power density of the pulsar proportional to the integration number and average received power. Pulsar 0329 has an average rate with a period of 700 ms. Plot 1 shows the results of two, full-period integrations. Plot 2 shows the results of taking the same number of observations during the first half of the period only.

Pulsar 0833 has a fast rate with a period of 83 ms. Plot 3 shows a full period observation after an initial start. Plot 4 is an example of applying the expansion technique, showing greater detail of the pulsar emission. Data points were taken every 8.3 μs.

References

1. Foster, C. F., "Automated Pulsar Receiver," in *The Deep Space Network Progress Report 42-20*, pp. 135-138, Jet Propulsion Laboratory, Pasadena, Calif., Apr. 15, 1974.

2. Slekys, A., "A New Pulsar Timer," in *The Deep Space Network Progress Report*, Technical Report 32-1526, Vol. XIII, pp. 133-138, Jet Propulsion Laboratory, Pasadena, Calif., Feb. 15, 1973.

Table 1. Automated pulsar receiver control codes

Instruction	Code	Followed by instruction	Function
SKS	31015	—	Skip if receiver in remote
EOM	30515	—	Reset and disable remote outputs
EOM	31115	—	Set and enable remote outputs
EOM	30115	POT	Attenuator set
EOM	30215	POT	Predetection bandwidth set
EOM	30415	POT	Postdetection bandwidth set

POT Word Format	
Attenuator	Six bits, right justified. Minimum attenuation = 01 octal, maximum attenuation = 77 octal, 0.5 dB steps from 0 to 31.5 dB.
Predetection Bandwidth	Two bits, right justified. Octal: 0 = 10 MHz bandwidth; 1 = Wide bandwidth; 2 = 1 MHz bandwidth
Postdetection Bandwidth	Fifteen bits, right justified. Minimum time constant = 00001 octal, maximum time constant = 77777 octal, 1μs steps from 0 to 31 ms.

Table 2. Automated pulsar data collector control codes

Instruction	Code[a]	Followed by instruction	Function
EOM	30016	POT	Control, sets up register point and command instructions.
EOM	30116	POT	Data transfer, from computer to data collector register indicated in control word.
EOM	30116	PIN	Data transfer, from data collector register indicated in control word to the computer.

Control POT Word Format

Octal number	Function
01	X register point
02	Y register point
03	A register point
04	L register point
05	N register point
06	D register point
07	A register point
00	M register point
10[b]	Increment after POT
20[b]	Increment after PIN
040	Initial start
100	Start on next major cycle pulse clearing memory
300	Start on next major cycle pulse not clearing memory

Data Transfer Word Format

Register	Maximum word length
X	16 bits, right justified
Y	24 bits
A	24 bits
L	24 bits
N	16 bits, right justified
D	16 bits, right justified
A	13 bits, right justified
M	24 bits

[a]May be changed by dual-in-line switches in data collector.
[b]May be mixed with preceding control words.

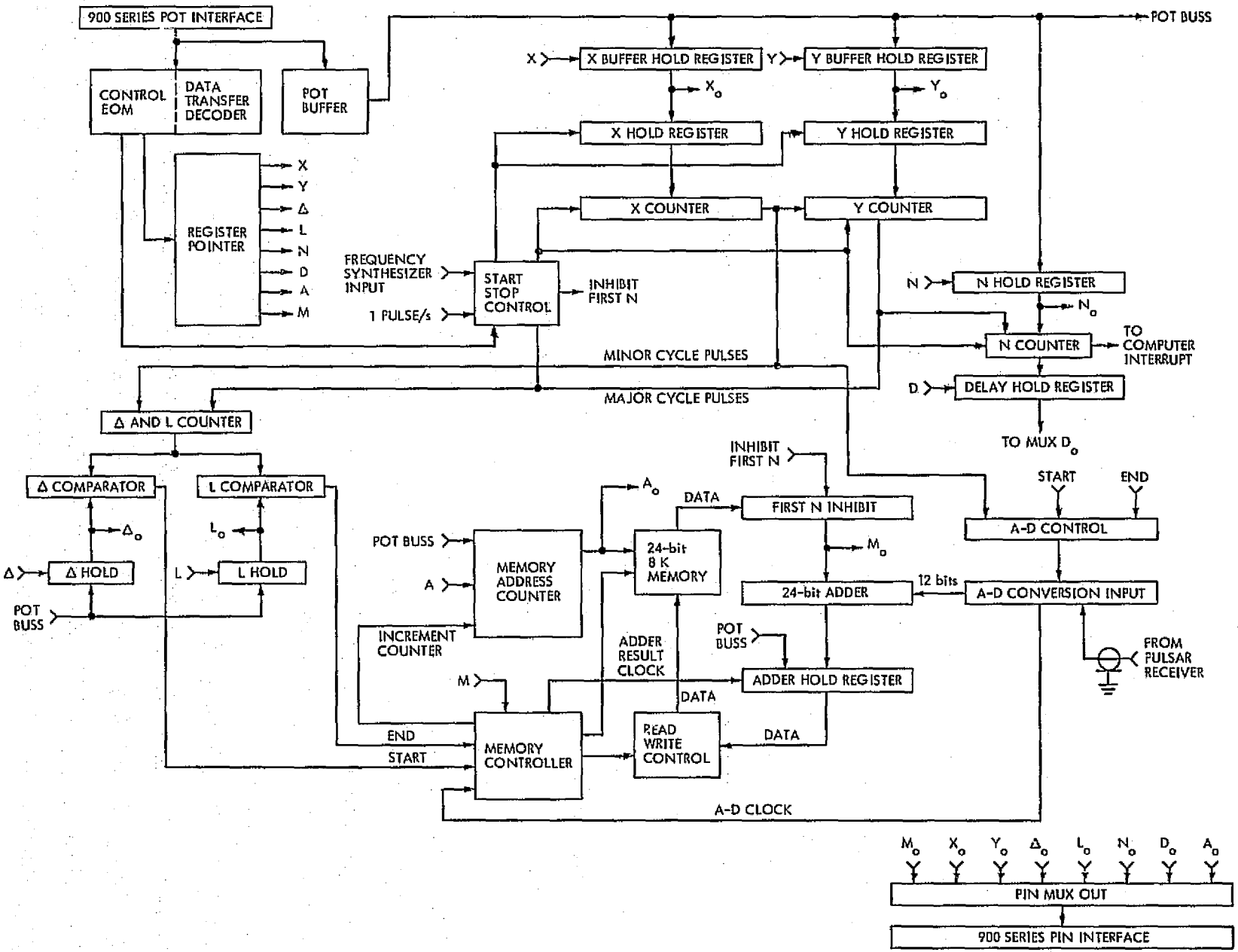

Fig. 1. Pulsar data collector block diagram

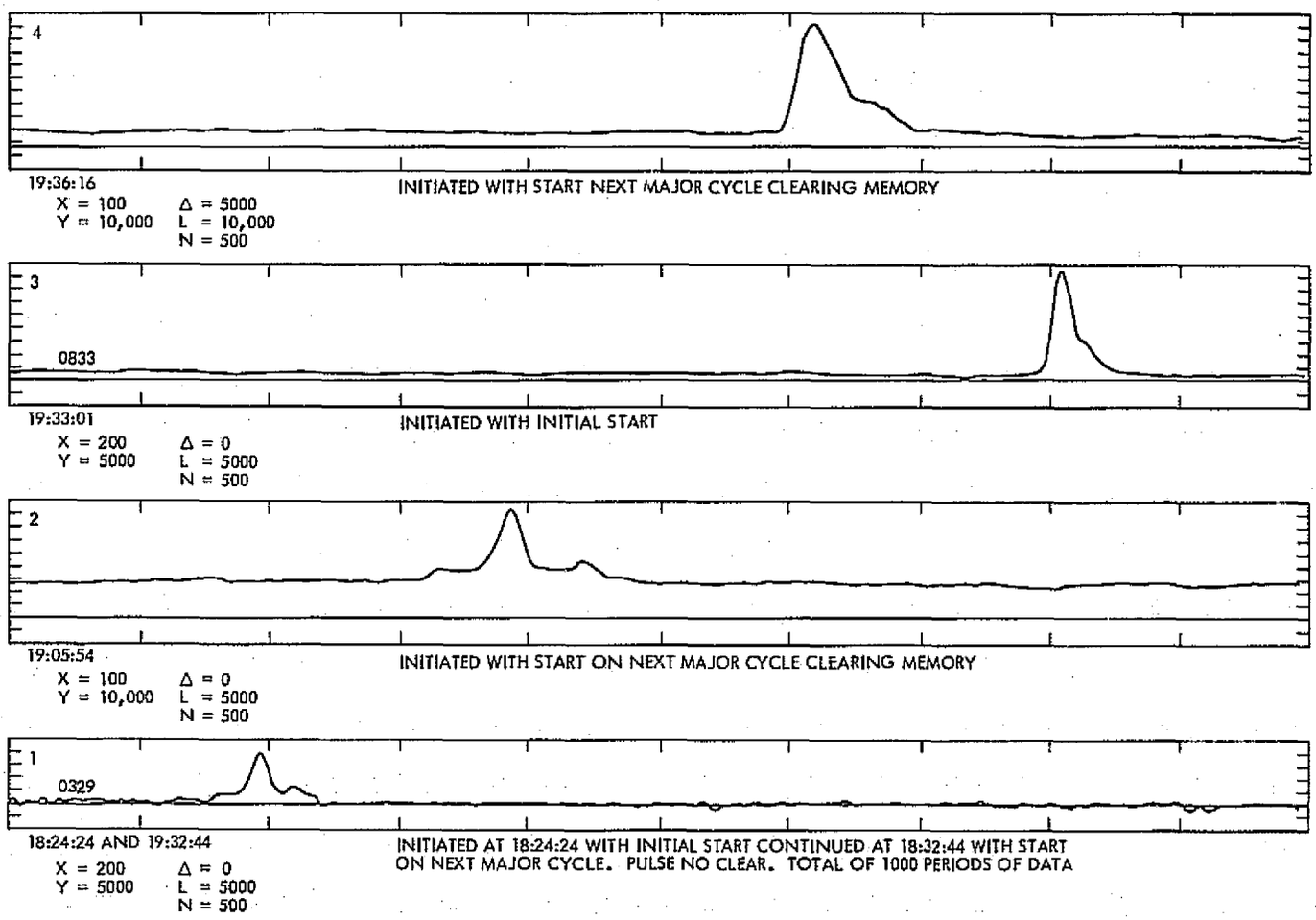

Fig. 2. Pulsar data plots, July 26, 1974

Automatic Total Recall Program for Replay of DSN 7-Track DODRs

F. M. Hlavaty
DSN Data Systems Development Section

The requirement exists for the capability to obtain as complete and accurate a record as possible of all high-speed data communication between the mission control center and the DSN ground stations in support of deep space mission operations. The Automatic Total Recall System was designed and developed for that express purpose. This article describes the functional aspects of the software operating in that system.

I. Introduction

The Deep Space Station (DSS) Telemetry and Command Subsystem (TCD) supports deep space mission operations by providing a data detection and processing capability, which in operation with the Ground Communications Facility (GCF) provides a communications link between the spacecraft and the mission control center. The TCD is responsible for transmitting commands to the spacecraft and for recovering incoming telemetry from the spacecraft. In performing mission support functions, the TCD generates a real-time log of all telemetry and command data transmitted over the high-speed data communication link between the DSS and the mission control center. The recording is on a 7-track magnetic tape directly connected to the Telemetry and Command Processor (TCP). The digital tape serves as the Telemetry and Command Digital Original Data Record (DODR) for the TCD.

II. Purpose

The purpose of the Automatic Total Recall System (ATRS) program is to provide automatic or manual capability for replaying to the mission control center the Digital Original Data Record (DODR) located at the DSS. The objective of the ATRS program is to create a complete master data record of spacecraft data, as free from error as possible.

The need for replaying the DODR arises from the possible presence of data outages occurring in high-speed data transmission between the DSS and the mission control center. The data outages may be the result of existing noise on the high-speed data lines or the complete loss of high-speed data communication due to a hardware malfunction. By providing the capability to replay the original data record, ATRS allows the mission control center to reconstruct a complete record of data transmission.

III. Program Structure

The ATRS program was developed and implemented on the TCP, an XDS 920 computer with 16K words of core memory. Associated with the TCP are two XDS 7-track high-density recorder tape transports capable of reading and writing information at 200 and 556 bpi. The program was implemented in assembly language and modularly structured to accommodate future expansion and facilitate maintenance operations. The program resides on magnetic tape and is loaded into the TCP by means of a paper tape bootstrap loader.

IV. Modes of Operation

The primary source of program input and control identifies the mode of operation. When the ATRS program is initially loaded and configured, the local DSS operator specifies the mode of operation as automatic or manual. In automatic operation, program input requests and control directives are issued by the mission control center by means of high-speed data transmission lines. The DSS remains in a passive state, observing and monitoring the remote inputs and the program status and summary reports generated during the data replay operation.

In the manual mode of operation, program control is retained at the DSS. Initialization and input request parameters are specified by the mission control center and are transmitted to the DSS by voice communication lines. The directives are then entered by the operator at the console keyboard device.

In either mode of operation, the destination and type of program output remains invariant. Output to the mission control center consists of recalled telemetry, command or monitor data transmitted along with accompanying status blocks by means of high-speed data lines. Output at the DSS is directed to the console typewriter and consists of the acknowledgment of remote inputs and the display of status and summary reports generated by replay processing.

V. Replay Process

ATRS expects to receive three types of program input: replay initialization, replay request and replay control directives. The content of program input is the same for both modes of program operation with only the input format varying. For automatic operation, replay parameters are formatted into 50-word high-speed data block images; for manual operation, the replay parameters are entered as uniquely defined text messages.

The initialization directives establish the overall time limits for a particular replay sequence and designate the type of data to be recalled. The data to be recalled are selected by specifying one or more user or data-dependent type codes.

The replay request directives establish the start and stop day specification and the begin and end time limits associated with a particular set of data outages. From one to 19 data gaps may be specified in each replay request directive.

The replay control parameters enable the user to interrogate and to exercise direct control over the program. Control directives permit the user to initiate, temporarily suspend, resume or terminate program operation, and to request the status associated with the last completed replay request or to request the program's current execution state.

When ATRS processing is initiated, the program proceeds to search the 7-track DODR mounted on the tape unit. Upon encountering a data record on the tape in which the time is equal to or later than the replay start time specified in the initialization directive, the DODR is considered to be properly positioned and a status block is transmitted to the mission control center indicating this condition. At this point the ATRS program is ready to process replay request directives. Upon receiving such a directive, the program sequentially examines each data gap specification and proceeds to read DODR records searching for the data associated with a particular data gap. The DODR records contain the exact images of five data blocks which were originally transmitted in real-time by the TCD Subsystem over high-speed data lines. Each block within the DODR record is examined to determine if the current block falls within the replay window identified by the data gap specification; if not, the block is bypassed and the next block in the record is tested. When the data block falls within the replay window, the program proceeds to test the block against the requested data type specification. If the data type criteria are satisfied, the block is transmitted over high-speed data lines to the mission control center.

When a replay request gap has been satisfied (i.e., when the last data block in the replay window has been located), a status block is sent to the mission control center. The status block contains the number of tape read errors encountered and the total number of DODR block transmissions initiated while processing the latest replay request gap. At the same time a message containing

similar status information is displayed on the DSS console typewriter.

The ATRS program has the capability to accept and process replay request gap specifications in which the start time is earlier than the time in the current DODR record. Such regressive time requests cause the DODR tape to backspace until the record time is compatible with the request time.

The Automatic Total Recall System program is capable of supporting the Pioneer, Helios and Viking missions. The program has the capacity to replay any DODR whose record and data block formats conform with the DSN System Requirements Detailed Interface Design.

Figures 1 through 3 provide information relating to program functions, data flow, and DODR record format, respectively.

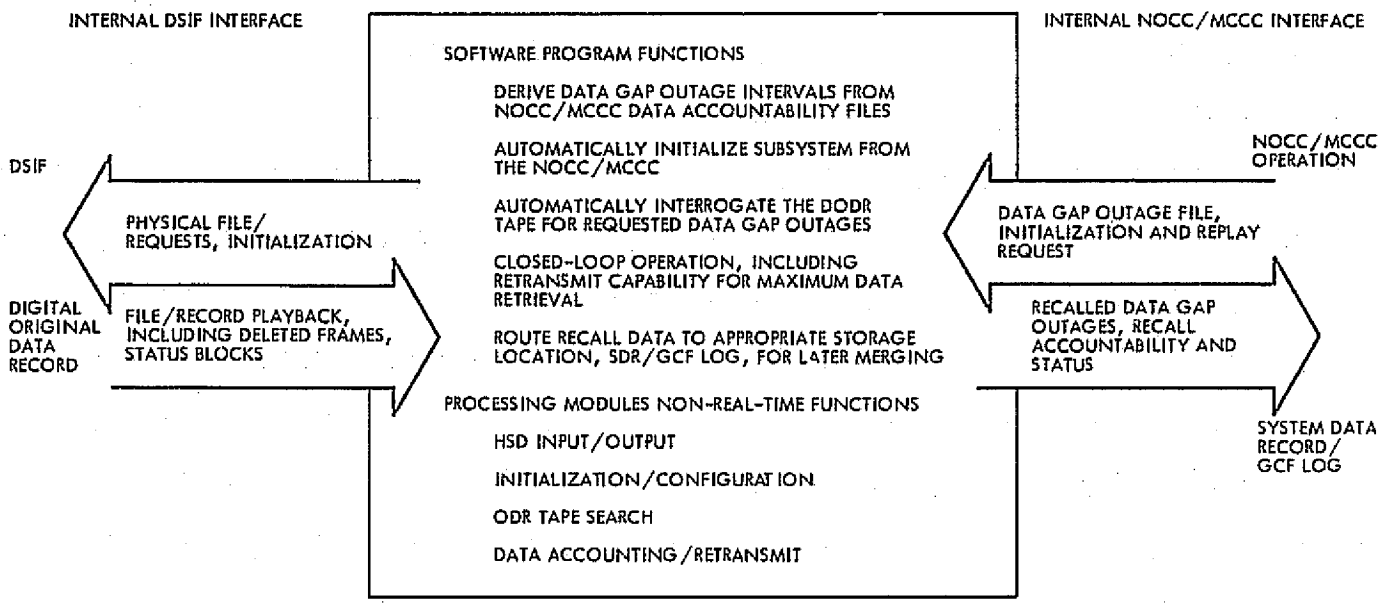

Fig. 1. Automatic total recall system functions

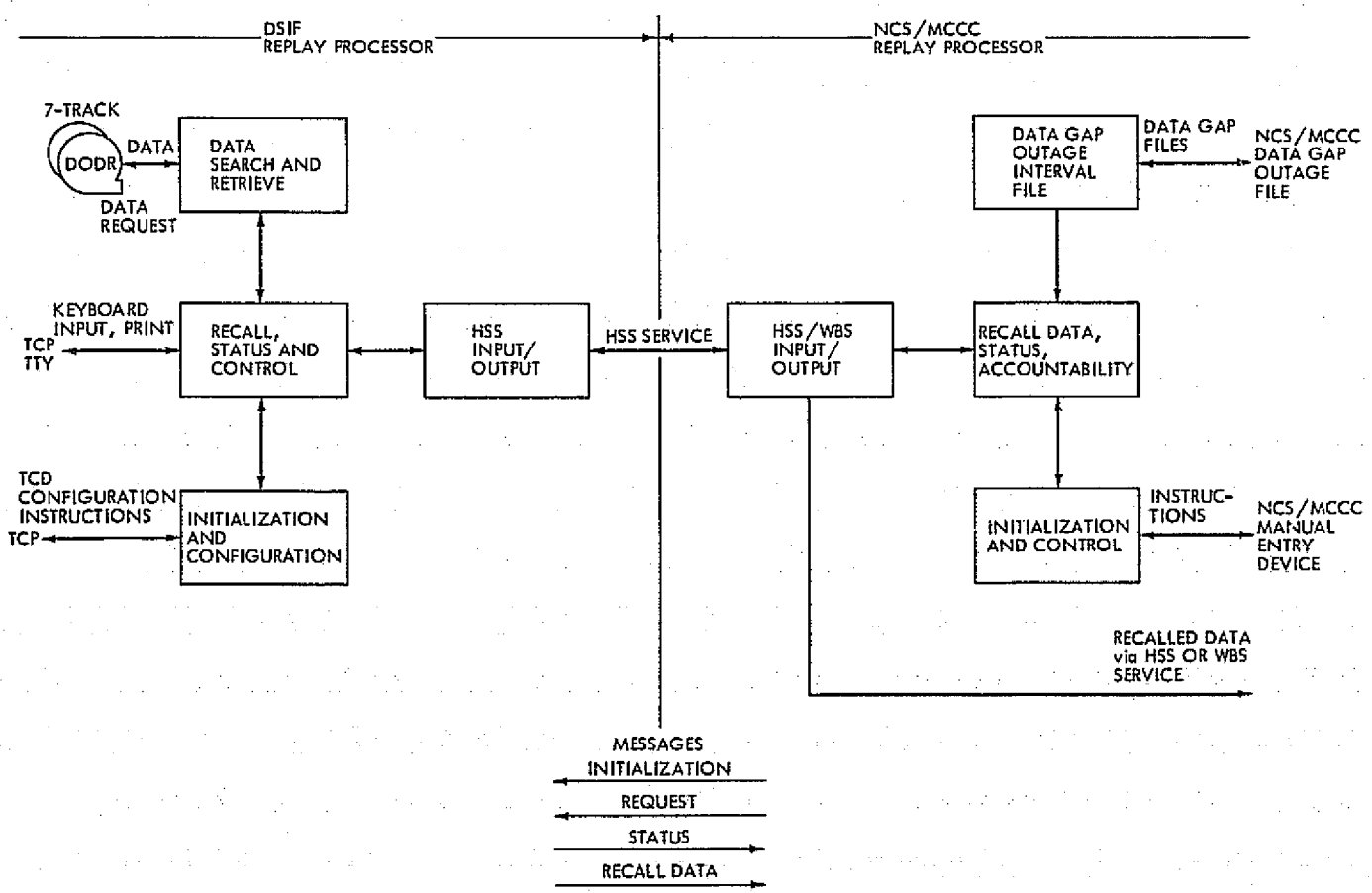

Fig. 2. Automatic total recall system data flow chart

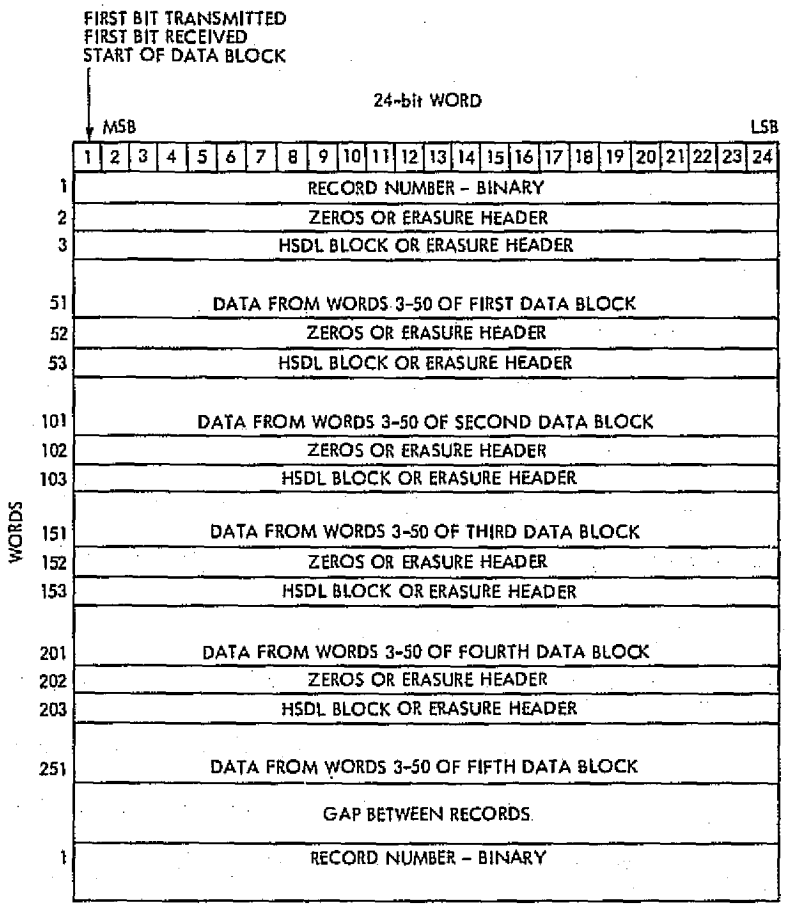

Fig. 3. TCP DODR record format, 1200-bit GCF blocks, 7-track, 200 or 556 bpi

A New Radio Frequency Angular Tropospheric Refraction Model

A. L. Berman and S. T. Rockwell
Network Operations Section

In the previous Deep Space Network Progress Report a new angular tropospheric refraction model that very accurately reflected precise optical refraction data was presented. In this report, the above optical refraction model is transformed to a refraction model applicable at radio (S- and X-Band) frequencies. The accuracies of this new model are:

$$\begin{aligned} 1\sigma \text{ uncertainty} &\approx 0.002\ deg \qquad EL \geq 5\ deg \\ &\approx 0.005\ deg \qquad 5 > EL \geq 0\ deg \\ &\approx 0.015\ deg \qquad 0 > EL \geq -3\ deg \end{aligned}$$

I. Introduction

In a previous article (Ref. 1) the authors presented a new angular tropospheric refraction model which very accurately modeled existing optical angular refraction data, as follows:

$$R = F_p F_t \left(\exp \left\{ \frac{\sum_{j=0}^{8} K_{j+3} [U(Z)]^j}{1 + \Delta_3(Z)} \right\} - K_{12} \right)$$

$$F_p = \left(\frac{P}{P_0} \left\{ 1 - \frac{\Delta_1(P,Z)}{1 + \Delta_3(Z)} \right\} \right)$$

$$F_t = \left(\frac{T_0}{T} \left\{ 1 - \frac{\Delta_2(T,Z)}{1 + \Delta_3(Z)} \right\} \right)$$

$$\Delta_1(P,Z) = (P - P_0)\{\exp [A_1(Z - A_2)]\}$$

$$\Delta_2(T,Z) = (T - T_0)\{\exp [B_1(Z - B_2)]\}$$

$$\Delta_3(Z) = (Z - C_0)\{\exp [C_1(Z - C_2)]\}$$

where

R = refraction, sec

Z = actual zenith angle, deg

EL = elevation angle

$EL = 90 \text{ deg} - Z$

$$U(Z) = \left\{\frac{Z - K_1}{K_2}\right\}$$

$K_1 = 46.625$

$K_2 = 45.375$

$K_3 = 4.1572$

$K_4 = 1.4468$

$K_5 = 0.25391$

$K_6 = 2.2716$

$K_7 = 1.3465$

$K_8 = -4.3877$

$K_9 = 3.1484$

$K_{10} = 4.5201$

$K_{11} = -1.8982$

$K_{12} = 0.89000$

P = pressure, mm Hg

$P_0 = 760.00$ mm Hg

$A_1 = 0.40816$

$A_2 = 112.30$

T = temperature, kelvins

$T_0 = 273.00$ K

$B_1 = 0.12820$

$B_2 = 142.88$

$C_0 = 91.870$

$C_1 = 0.80000$

$C_2 = 99.344$

More pertinent for use at JPL, however, would be an angular refraction model which would possess very high accuracy at S- and X-band (radio) frequencies. At the time, it was hoped that a reasonably accurate method could be found to transform the optical refraction model to a radio-frequency refraction model. Past attempts to accomplish this will be dealt with first, and then a new method to accomplish the transformation will be proposed.

II. Past Attempts to Transform Angular Refraction Models From Optical to Radio Frequencies

To facilitate a discussion of past attempts to generate angular tropospheric refraction models for use at radio frequencies, let the following notation be introduced:

$R_{OP} = R(P,T,Z)$ = optical refraction model from above

$R_{RF} = R_{RF}(P,T,Z,RH)$ = radio frequency refraction model

P = pressure

T = temperature

Z = zenith angle

RH = relative humidity

$N(h) = ND(h) + NW(h)$

$N(h)$ = total refractivity at radio frequencies

$ND(h)$ = dry, or optical component, of refractivity

$NW(h)$ = wet component of refractivity

h = height

h_0 = station height

s = parameter surface value

$ND(h_0) = ND_s$

$NW(h_0) = NW_s$

$N(h_0) = N_s$

In general, attempts to construct a radio frequency refraction model consisted of appropriating an empirical model from optical refraction work which would give the functional dependence on Z (say $R_Z(Z)$), and then scaling this expression by the total radio frequency surface refractivity, i.e.,

$$\text{refraction} \approx \left(\frac{N_s}{N_R}\right) R_Z(Z)$$

where N_R = reference optical refractivity.

At this point, one must ask, what are the implications of this procedure? Since any signal (that is of interest here) must traverse the entire troposphere, and is of course, continually being refracted, one might think that instead of being proportional to surface refractivity, angu-

lar refraction is really more nearly proportional to total (integrated) tropospheric refractivity, i.e.,

$$\text{Refraction} \propto \int N(h)\,dh$$

However, refraction could also be proportional to surface refractivity if it could be assumed that there exists some $f(h)$ such that:

$$N(h) \approx N_s f(h)$$

so that

$$\text{refraction} \propto \int N_s f(h)\,dh = N_s \int f(h)\,dh$$

Making the assumption that

$$ND(h) \sim ND_s f_1(h)$$

$$NW(h) \sim NW_s f_2(h)$$

one would have for the optical case:

$$\begin{aligned} R_Z \propto \int ND(h)\,dh &= \int ND_s f_1(h)\,dh \\ &= ND_s \int f_1(h)\,dh \end{aligned}$$

For the radio frequency case:

$$\begin{aligned} R_{RF} \propto \int N(h)\,dh &= \int \{ND(h) + NW(h)\}\,dh \\ &= \int \{ND_s f_1(h) + NW_s f_2(h)\}\,dh \\ &= ND_s \int f_1(h)\,dh + NW_s \int f_2(h)\,dh \end{aligned}$$

Without precise knowledge of the form of $f_1(h)$ and $f_2(h)$, the only way that the surface refractivities could be used to transform from the optical case to the radio case would be if

$$f_1(h) \approx f_2(h)$$

Then

$$R_{RF} \propto (ND_s + NW_s) \int f_1(h)\,dh$$

and indeed

$$R_{RF} \propto (ND_s + NW_s)\left[\frac{R_2(Z)}{ND_s}\right]$$

However, it is well known that wet refractivity "decays" much more rapidly than dry refractivity (for instance, Ref. 4), so that $f_1(h)$ and $f_2(h)$ are quite dissimilar; thus, the procedure of scaling an optical angular refraction model by the total surface radio refractivity to achieve a radio angular refraction model would appear to be seriously flawed.

III. Method Used to Transform From an Optical to a Radio Frequency Refraction Model

From the previous section it was seen that

$$R_{RF} \propto N_s = ND_s + NW_s$$

is a poor choice. A more logical choice would be

$$\begin{aligned} R_{RF} \propto \int N(h)\,dh &= \int \{ND(h) + NW(h)\}\,dh \\ &= \int ND(h)\,dh + \int NW(h)\,dh \\ &= \int ND(h)\,dh \left\{1 + \frac{\int NW(h)\,dh}{\int ND(h)\,dh}\right\} \end{aligned}$$

Similarly, for the optical case (using the model previously presented):

$$R_{OP} \propto \int ND(h)\,dh$$

Combining the above, one arrives at the equation that will be used for the radio frequency angular refraction model:

$$R_{RF}(P,T,Z,RH) \approx R_{OP}(P,T,Z)\left\{1 + \frac{\int NW(h)\,dh}{\int ND(h)\,dh}\right\}$$

IV. Determination of Ratio of Integrated Wet Refractivity to Integrated Dry Refractivity

In attempting to determine an analytical parametric representation for the expression:

$$\frac{\int NW(h)dh}{\int ND(h)\,dh}$$

The most difficult problem by far lies with the integrated wet refractivity. Berman first showed in 1970 (Ref. 2) that

$$\int ND(h)\,dh = AP_s\left[\frac{R}{g}\right]$$

where

$A = 77.6$

P_s = surface pressure, mbar

R = perfect gas constant

g = gravitational acceleration

$g/R = 34.1°\text{C/km}$

and also gave an expression to approximate the integrated wet refractivity:

$$\int NW(h)\,dh =$$

$$\left[\frac{C_1 C_2 (RH)_s}{\gamma}\right]\left\{\frac{\left(1-\frac{C}{T_0}\right)^2}{B-AC}\right\}\exp\left(\frac{AT_0-B}{T_0-C}\right)$$

where

$C_1 = 77.6$

$C_2 = 29341.0$

RH = relative humidity

γ = temperature lapse rate

$C = 38.45$

T_0 = extrapolated surface temperature

$A = 7.4475 \ln(10)$

$B = 2034.28 \ln(10)$

Chao (Ref. 5) later improved upon the integrated wet refractivity with the expression:

$$\int NW(h)\,dh = 1.63\times 10^2\left\{\frac{e_0^{1.23}}{T_0^2}\right\} + 2.05\times 10^2\,\alpha\left\{\frac{e_0^{1.46}}{T_0^4}\right\}$$

where

e_0 = surface vapor pressure, N/m^2

T_0 = surface temperature, K

α = temperature lapse rate, K/km

However, both of these expressions depend upon one or more parameters not measurable at the surface (i.e., temperature lapse rate, etc.), and neither is particularly accurate. Going back to the previous section, if the altitude-dependent refractivities could really be represented as

$$ND(h) \sim ND_s f_1(h)$$

$$NW(h) \sim NW_s f_2(h)$$

and if the above refractivities could be integrated, i.e., if A below could be evaluated as

$$A = \frac{\int f_2(h)\,dh}{\int f_1(h)\,dh}$$

then one might simply expect that

$$\frac{\int NW(h)\,dh}{\int ND(h)\,dh} \approx A\left\{\frac{NW_s}{ND_s}\right\}$$

To test this hypothesis, the authors had ten cases used in Ref. 2. Although a very small number, the cases were alternate day and night profiles selected throughout the year (December, February, April, August, September). A least-squares linear curve fit to the above data was performed as follows:

$$\frac{\int NW(h)\,dh}{\int ND(h)\,dh}; \qquad A\left\{\frac{NW_s}{ND_s}\right\}$$

The fit yielded the following:

$A = 0.3224$

$\sigma(\%) = 00.93\%$

$$\times\left[\sigma(\%) = 100\times\sigma\left(\frac{\int NW(h)\,dh}{\int ND(h)\,dh} - A\left\{\frac{NW_s}{ND_s}\right\}\right)\right]$$

Translated to centimeters of integrated refractivity, one would have

$$\sigma(\text{cm}) = 2.0\,\text{cm}$$

Table 1 and Fig. 1 present the detailed analysis of the ten cases described.

As a totally independent check of this observed relationship, use can be made of work done by Chao (Ref. 4) on wet and dry refractivity profiles. Combining Eqs. (9), (10), (13), (14), (15), and (16) from Ref. 4, one has:

$$ND(h) = ND_s\left(1-\frac{h}{42.7}\right)^4 \qquad h \le 12.2\,\text{km}$$

$$= \frac{70}{269}ND_s\left\{\exp\left(-\frac{(h-12.2)}{6.4}\right)\right\} \qquad h \ge 12.2\,\text{km}$$

$$NW(h) = NW_s\left(1-\frac{h}{13}\right)^4 \qquad h \le 13\,\text{km}$$

$$= 0 \qquad h \ge 13\,\text{km}$$

Performing the dry refractivity integration, one has

$$\int_0^\infty ND(h)\,dh = \int_0^{12.2} ND_s\left(1-\frac{h}{42.7}\right)^4 dh + \int_{12.2}^\infty \frac{70}{269} ND_s\left\{\exp\left(-\frac{(h-12.2)}{6.4}\right)\right\} dh$$

$$= ND_s\int_0^{12.2}\left(1-\frac{h}{42.7}\right)^4 dh + \frac{70}{269} ND_s\int_{12.2}^\infty \exp\left[-\frac{(h-12.2)}{6.4}\right] dh$$

transforming the first integral by

$$\left(1-\frac{h}{42.7}\right) = x$$

$$dh = -42.7\,dx$$

so that

$$\int\left(1-\frac{h}{42.7}\right)^4 dh = -42.7\int x^4\,dx = -42.7\frac{x^5}{5} = -\frac{42.7}{5}\left[\left(1-\frac{h}{42.7}\right)^5\right]_0^{12.2} = 6.952$$

Transforming the second integral by

$$-\frac{(h-12.2)}{6.4} = x$$

$$dh = -6.4\,dx$$

so that

$$\int \exp\left[-\frac{(h-12.2)}{6.4}\right] dh = -6.4\int \exp(x)\,dx = -6.4\exp(x) = -6.4\left[\exp\left(-\frac{(h-12.2)}{6.4}\right)\right]_{12.2}^\infty = 6.4$$

Or, finally

$$\int_0^\infty ND(h)\,dh = ND_s(6.952) + \frac{70}{269} ND_s(6.4) = 8.6174(ND_s)$$

Performing the wet refractivity integration, one has

$$\int_0^\infty NW(h)\,dh = \int_0^{13} NW_s\left(1-\frac{h}{13}\right)^4 dh = NW_s\int_0^{13}\left(1-\frac{h}{13}\right)^4 dh$$

Transforming the integral by

$$\left(1-\frac{h}{13}\right) = x$$

$$dh = -13\,dx$$

$$\int\left(1-\frac{h}{13}\right)^4 dh = -13\int x^4\,dx = -13\frac{x^5}{5} = \frac{13}{5}\left[\left(1-\frac{h}{13}\right)^5\right]_0^{13} = 2.6$$

so that

$$\int_0^\infty NW(h)\,dh = 2.6(NW_s)$$

Combining the integrated wet refractivity and the integrated dry refractivity yields

$$\frac{\int_0^\infty NW(h)\,dh}{\int_0^\infty ND(h)\,dh} = \frac{2.6(NW_s)}{8.6174(ND_s)} = 0.30172\left(\frac{NW_s}{ND_s}\right)$$

This is to be compared to the previously determined relationship from actual data of:

$$\frac{\int_0^\infty NW(h)\,dh}{\int_0^\infty ND(h)\,dh} \approx 0.3224\left(\frac{NW_s}{ND_s}\right)$$

Since the value of the 1σ standard deviation

$$1\sigma = 00.93\%\ (\sim 2\ \text{cm})$$

found from actual data compares favorably with the most recent modeling published by Chao in Ref. 5 ($\sim$3 cm for combined night and day profiles), and since the basic relationship seems verifiable by average profiles presented by Chao; the determined expression will be adopted for use with the optical refraction model. The surface refractivity (Ref. 2) is defined as:

$$NW_s = \frac{(RH)_s C_1 C_2}{T_s^2}\exp\left(\frac{AT_s - B}{T_s - C}\right)$$

$$ND_s = C_1\frac{P_s}{T_s}$$

so that one would obtain

$$\left\{1 + \frac{\int_0^\infty NW(h)\,dh}{\int_0^\infty ND(h)\,dh}\right\} \cong 1 + (0.3224)\frac{(RH)_s C_2}{T_s P_s}\exp\left(\frac{AT_s - B}{T_s - C}\right)$$

To integrate this expression into the optical model, the pressure term must be converted from mbar to mm:

$$P_s(\text{mbar}) = P_s(\text{mm}) \times \frac{1013}{760}$$

so that one would finally have

$$\left\{1 + \frac{\int NW(h)\,dh}{\int ND(h)\,dh}\right\} \cong 1 + \frac{(7.1 \times 10^3)\,(RH)_s}{T_s P_s}\exp\left(\frac{AT_s - B}{T_s - C}\right)$$

where

$(RH)_s$ = surface relative humidity (100% = 1.0)

T_s = surface temperature, K

P_s = surface pressure, mm of Hg

$A = 17.149$

$B = 4684.1$

$C = 38.450$

V. Final Angular Tropospheric Radio Frequency Refraction Model

The following gives the complete radio frequency angular tropospheric refraction model:

$$R = F_p F_t F_w\left(\exp\left\{\frac{\sum_{j=0}^{8} K_{j+3}[U(Z)]^j}{1 + \Delta_3(Z)}\right\} - K_{12}\right)$$

$$F_p = \left(\frac{P}{P_0}\left\{1 - \frac{\Delta_1(P,Z)}{1 + \Delta_3(Z)}\right\}\right)$$

$$F_t = \left(\frac{T_0}{T}\left\{1 - \frac{\Delta_2(T,Z)}{1 + \Delta_3(Z)}\right\}\right)$$

$$F_w = \left(1 + \frac{W_0 RH}{TP}\left\{\exp\left[\frac{W_1 T - W_2}{T - W_3}\right]\right\}\right)$$

$$\Delta_1(P,Z) = (P - P_0)\,\{\exp\,[A_1(Z - A_2)]\}$$

$$\Delta_2(T,Z) = (T - T_0)\,\{\exp\,[B_1(Z - B_2)]\}$$

$$\Delta_3(Z) = (Z - C_0)\,\{\exp\,[C_1(Z - C_2)]\}$$

where

R = refraction, sec

Z = actual zenith angle, deg

EL = elevation angle

$EL = 90\ \text{deg} - Z$

$$U(Z) = \left\{\frac{Z - K_1}{K_2}\right\}$$

$K_1 = 46.625$

$K_2 = 45.375$

$K_3 = 4.1572$

$K_4 = 1.4468$

$K_5 = 0.25391$

$K_6 = 2.2716$

$K_7 = 1.3465$

$K_8 = -4.3877$

$K_9 = 3.1484$

$K_{10} = 4.5201$

$K_{11} = -1.8982$

$K_{12} = 0.89000$

P = pressure, mm Hg

$P_0 = 760.00$ mm Hg

$A_1 = 0.40816$

$A_2 = 112.30$

T = temperature, kelvins

$T_0 = 273.00$ K

$B_1 = 0.12820$

$B_2 = 142.88$

$C_0 = 91.870$

$C_1 = 0.80000$

$C_2 = 99.344$

RH = Relative humidity (100% = 1.0)

$W_0 = 7.1 \times 10^3$

$W_1 = 17.149$

$W_2 = 4684.1$

$W_3 = 38.450$

VI. Model Accuracies

The inaccuracies introduced by the wet refractivity term predominate over the inaccuracies presented in Ref. 1. Considering

$$1\sigma = 1.00\%$$

the maximum 1σ angular errors would be

Z, deg	ΔR, sec	ΔR, deg
0–85	6	0.002
85–90	18	0.005
90–93	50	0.015

VII. Fortran Subroutines

Reference 1 presented two Fortran subroutines, corresponding to the full optical refraction model and an abbreviated version. These two routines have been transformed to the radio frequency version of the refraction model, and are presented in Appendixes A and B. The Fortran subroutine SBEND (Appendix A) represents the full model, while XBEND (Appendix B) gives the abbreviated version. Inputs required are:

PRESS = pressure, mm of Hg

TEMP = temperature, K

HUMID = % of relative humidity (100% = 1.0)

ZNITH = actual zenith angle, deg

and the subroutines return with

R = refraction correction, sec

References

1. Berman, A. L., and Rockwell, S. T., "A New Angular Tropospheric Refraction Model" in *The Deep Space Network Progress Report 42-24*, Jet Propulsion Laboratory, Pasadena, Calif., Dec. 15, 1974.

2. Berman, A. L., "A New Tropospheric Range Refraction Model" in *Space Programs Summary*, No. 37-65, Vol. II, pp. 140–153, Jet Propulsion Laboratory, Pasadena, Calif., Sept. 30, 1970.

3. Ondrasik, V. J., and Thuleen, K. L., "Variations in the Zenith Tropospheric Range Effect Computed From Radiosonde Balloon Data" in *Space Programs Summary*, No. 37-65, Vol. II, pp. 25–35, Jet Propulsion Laboratory, Pasadena, Calif., Sept. 30, 1970.

4. Chao, C. C, "New Tropospheric Range Corrections With Seasonal Adjustment" in *The Deep Space Network Progress Report*, No. 32-1526, Vol. VI pp. 67–73, Jet Propulsion Laboratory, Pasadena, Calif., Dec. 15, 1971.

5. Chao, C. C., "A New Method To Predict Wet Zenith Range Correction From Surface Measurements" in *The Deep Space Network Progress Report*, No. 32-1526, Vol. XIV, pp. 33–41, Jet Propulsion Laboratory, Pasadena, California, April 15, 1973.

Table 1. Surface refractivity vs integrated refractivity

$A = 0.3224$ $\sigma = 0.93\%$

Case	$100 \times \frac{NW_s}{ND_s}$ (%)	$A \times \left\{100 \times \frac{NW_s}{ND_s}\right\}$ (%)	$100 \times \frac{\int NW(h)\,dh}{\int ND(h)\,dh}$ (%)	Δ (%)	Δ, cm
1	4.86	1.57	2.27	+0.70	+1.48
2	3.76	1.21	2.17	+0.96	+2.03
3	5.74	1.85	1.80	-0.05	−0.11
4	5.34	1.72	1.37	−0.35	−0.74
5	4.74	1.53	1.75	+0.22	+0.47
6	7.14	2.30	2.17	−0.13	−0.28
7	24.11	7.77	8.55	+0.78	+1.65
8	31.72	10.23	9.12	−1.11	−2.35
9	7.29	2.35	4.58	+2.23	+4.72
10	9.89	3.19	2.69	−0.50	−1.06

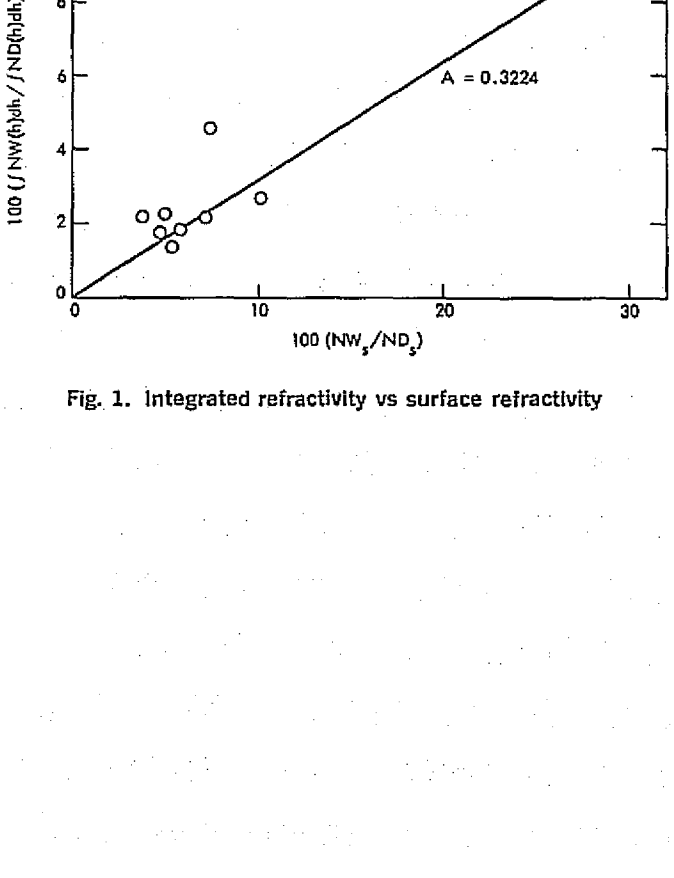

Fig. 1. Integrated refractivity vs surface refractivity

Appendix A

Subroutine SBEND

```
00101     1*          SUBROUTINE SBEND(PRESS,TEMP,HUMID,ZNITH,R)
00103     2*          DIMENSION A(2),B(2),C(2),E(12),P(2),T(2),Z(2)
00104     3*          P(1) = 760.00
00105     4*          T(1) = 273.00
00106     5*          Z(1) = 91.870
00107     6*          P(2) = PRESS
00110     7*          T(2) = TEMP
00111     8*          Z(2) = ZNITH
00112     9*          A(1) = .40816
00113    10*          A(2) = 112.30
00114    11*          B(1) = .12820
00115    12*          B(2) = 142.88
00116    13*          C(1) = .80000
00117    14*          C(2) = 99.344
00120    15*          E(1) = 46.625
00121    16*          E(2) = 45.375
00122    17*          E(3) = 4.1572
00123    18*          E(4) = 1.4468
00124    19*          E(5) = .25391
00125    20*          E(6) = 2.2716
00126    21*          E(7) =-1.3465
00127    22*          E(8) =-4.3877
00130    23*          E(9) = 3.1484
00131    24*          E(10)= 4.5201
00132    25*          E(11)=-1.8982
00133    26*          E(12)= .89000
00134    27*          W0   = 7100.0
00135    28*          W1   = 17.149
00136    29*          W2   = 4684.1
00137    30*          W3   = 38.450
00140    31*          D3=1.+DELTA(Z,C,Z(2))
00141    32*          FP=(P(2)/P(1))*(1.-DELTA(P,A,Z(2))/D3)
00142    33*          FT=(T(1)/T(2))*(1.-DELTA(T,B,Z(2))/D3)
00143    34*          FW=1+(W0*HUMID*EXP((W1*T(2)-W2)/(T(2)-W3))/(T(2)*P(2)))
00144    35*          U=(Z(2)-E(1))/E(2)
00145    36*          X=E(11)
00146    37*          DO 1 I=1,8
00151    38*        1 X=E(11-I)+U*X
00153    39*          R=FT*FP*FW*(EXP(X/D3)-E(12))
00154    40*          RETURN
00155    41*          END


00101     1*          FUNCTION DELTA(A,B,Z)
00103     2*          DIMENSION A(2),B(2)
00104     3*          DELTA=(A(2)-A(1))*EXP(B(1)*(Z-B(2)))
00105     4*          RETURN
00106     5*          END
```

Appendix B

Subroutine XBEND

```
00101     1*          SUBROUTINE XBEND(PRESS,TEMP,HUMID,ZNITH,R)
00103     2*          DIMENSION E(12)
00104     3*          P     = 760.00
00105     4*          T     = 273.00
00106     5*          E(1)  = 46.625
00107     6*          E(2)  = 45.375
00110     7*          E(3)  = 4.1572
00111     8*          E(4)  = 1.4468
00112     9*          E(5)  = .25391
00113    10*          E(6)  = 2.2716
00114    11*          E(7)  =-1.3465
00115    12*          E(8)  =-4.3877
00116    13*          E(9)  = 3.1484
00117    14*          E(10)= 4.5201
00120    15*          E(11)=-1.8982
00121    16*          E(12)= .89000
00122    17*          W0    = 7100.0
00123    18*          W1    = 17.149
00124    19*          W2    = 4684.1
00125    20*          W3    = 38.450
00126    21*          FP=PRESS/P
00127    22*          FT=T/TEMP
00130    23*          FW=1+W0*HUMID*EXP((W1*TEMP-W2)/(TEMP-W3))/(TEMP*PRESS)
00131    24*          U=(ZNITH-E(1))/E(2)
00132    25*          X=E(11)
00133    26*          DO 1 I=1,8
00136    27*        1 X=E(11-I)+U*X
00140    28*          R=FT*FP*FW*(EXP(X)-E(12))
00141    29*          RETURN
00142    30*          END
```

A New Approach to the Evaluation and Prediction of Wet Tropospheric Zenith Range Refraction

A. L. Berman
Network Operations Section

The best current model for predicting wet tropospheric zenith range refraction exhibits an uncertainty of approximately 3.0 cm (1σ). This report presents an approach that has the potentiality of reducing the uncertainty to the range of approximately 1.5 to 2.0 cm (1σ). Furthermore, the current model requires both surface parameters as well as tropospheric parameters, while the approach dealt with in this report requires only surface parameters.

I. Introduction

The last five years have seen a substantial effort at the Jet Propulsion Laboratory to evaluate and, hence, be able to predict zenith range refraction. Determination of the dry component of range refraction is quite straightforward; therefore, most activity has been expended in attempting to develop accurate methods to evaluate the wet component of range refraction. In 1970 this author proposed a model based on the assumption of constant relative humidity as follows (Ref. 3):

$$\Delta R_W = 10^{-6} \int_0^\infty NW(h)\, dh$$

$$= \left[\frac{C_1 C_2 (RH)_s}{\gamma}\right] \left\{\frac{(1 - \frac{C}{T_0})^2}{B - AC}\right\} \exp\left(\frac{AT_0 - B}{T_0 - C}\right)$$

where

ΔR_W	=	wet zenith range refraction (cm)
$NW(h)$	=	wet component of refractivity
h	=	height above observer (km)
C_1	=	77.6
C_2	=	29341.0
RH	=	relative humidity (100% = 1.0)
γ	=	temperature lapse rate (K/km)
C	=	38.45
T_0	=	extrapolated surface temperature, K
A	=	7.4475 (ln 10)
B	=	2034.28 (ln 10)
s	=	surface parameter value

This model exhibited a standard deviation of approximately:

$$1\sigma \approx 4.0 \text{ cm}$$

In 1973, Chao (Ref. 6), assuming an adiabatic atmosphere model, improved upon the evaluation of wet zenith range refraction with the following expression:

$$10^{-6}\int_0^\infty NW(h)\,dh = 1.63 \times 10^2 \left\{\frac{e_0^{1.25}}{T_0^2}\right\} + 2.05 \times 10^2\,\alpha \left\{\frac{e_0^{1.40}}{T_0^3}\right\}$$

where

e_0 = surface vapor pressure, N/m²

T_0 = surface temperature, K

α = temperature lapse rate, K/km

This model produced a standard deviation for combined day and night cases of

$$1\sigma \approx 3.0 \text{ cm}$$

The uncertainty in even the Chao model is large, however, when compared to an average wet zenith range refraction of approximately 10 cm; thus efforts to improve upon this model would not be entirely academic.

II. New Approach to Evaluation of Wet Zenith Range Refraction

In the course of developing a new radio frequency angular tropospheric refraction model (Ref. 1), it was found necessary to evaluate the ratio of wet zenith range refraction to dry zenith range refraction. Letting

$N(h)$ = $ND(h) + NW(h)$, the total refractivity at radio frequencies

$ND(h)$ = dry or optical component of refractivity

$NW(h)$ = wet component of refractivity

h = height

h_0 = observer height

s = parameter surface value

$ND(h_0) = ND_s$

$NW(h_0) = NW$

$N(h_0) = N_s$

and defining

$$\Delta R_W = 10^{-6}\int_0^\infty NW(h)\,dh$$

$$\Delta R_D = 10^{-6}\int_0^\infty ND(h)\,dh$$

It was necessary to determine some f such that:

$$f = \frac{\Delta R_W}{\Delta R_D} = \frac{\int_0^\infty NW(h)\,dh}{\int_0^\infty ND(h)\,dh}$$

It was empirically found that there existed strong correlation between the ratios of wet and dry zenith range refraction and of wet and dry surface refractivity, i.e. that

$$f = \frac{\Delta R_W}{\Delta R_D} \approx K\left[\frac{NW_s}{ND_s}\right]$$

with $K \approx 0.32$.

There is an immediate implication that, if indeed there existed strong correlation, then this (assumed) relationship might be useful in predicting wet zenith range refraction.

If

$$\frac{\Delta R_W}{\Delta R_D} \approx K\left[\frac{NW_s}{ND_s}\right]$$

then

$$\Delta R_W \approx K\left[\frac{\Delta R_D}{ND_s}\right](NW_s)$$

Defining

C_1 = 77.6

C_2 = 29341.0

RH = relative humidity

R = perfect gas constant

g = gravitational acceleration

g/R = 34.1 °C/km

P = pressure

T = temperature

s = surface parameter value

A = 7.4475 ln(10)

B = 2034.28 ln(10)

C = 38.45

one would have from Ref. 3:

$$\Delta R_D(\text{cm}) = (10^{-1})\, C_1 P_s \left[\frac{R}{g}\right]$$

$$ND_s = C_1 \left[\frac{P_s}{T_s}\right]$$

$$NW_s = \frac{C_1 C_2 (RH)_s}{T_s^2} \exp\left(\frac{AT_s - B}{T_s - C}\right)$$

so that

$$\Delta R_W \approx K \left\{\frac{(10^{-1})\, C_1 P_s \left[\frac{R}{g}\right]}{C_1 \frac{P_s}{T_s}}\right\} \times \frac{C_1 C_2 (RH)_s}{T_s^2} \exp\left(\frac{AT_s - B}{T_s - C}\right)$$

$$\approx K \left\{\frac{R\, T_s}{g(10)}\right\} \frac{C_1 C_2 (RH)_s}{T_s^2} \exp\left(\frac{AT_s - B}{T_s - C}\right)$$

$$\approx K \left\{\frac{R}{g}\right\} \frac{C_1 C_2 (RH)_s}{(10)\, T_s} \exp\left(\frac{AT_s - B}{T_s - C}\right)$$

now

$$\left\{\frac{R}{g}\right\} \frac{C_1 C_2}{(10)} = \frac{(77.6)(29341.)}{34.1} = 6677.0$$

so that finally

$$\Delta R_W \approx K (RH)_s \left[\frac{6677.0}{T_s}\right] \exp\left(\frac{AT_s - B}{T_s - C}\right)$$

The above expression is simpler than those referred to previously, and more significantly, it is only dependent upon surface parameters, unlike previous expressions that depended upon one or more tropospheric parameters not directly measurable from the ground. In 1970, J. V. Ondrasik considered a very similar approach, that is, correlating zenith wet range refraction with surface wet refractivity (Ref. 4, P. 34), i.e.,

$$\Delta R_W \approx K_0 \{NW_s\} + K_1$$

but (apparently) dropped the idea as unpromising.

Table 1 presents a detailed listing of 10 selected atmospheric cases previously described in Refs. 1 and 3. The standard deviations described in the table are as follows:

$$\sigma(\text{cm}) = \sigma\left(\Delta R_W - K\left[\frac{\Delta R_D}{ND_s}\right] NW_s\right), \text{cm}$$

$$\sigma(\%) = 100 \times \sigma\left(\frac{\Delta R_W}{\Delta R_D} - K\left[\frac{NW_s}{ND_s}\right]\right), \%$$

The results of a least-squares curve fit of these 10 cases to:

$$\Delta R_W; K\left[\frac{\Delta R_D}{ND_s}\right] NW_s$$

yielded

$$K = 0.3224$$

$$\sigma(\text{cm}) \sim 2.0 \text{ cm}$$

This data can also be seen in Fig. 1.

As a check to the basic procedure, use was made of data presented by Ondrasik in 1970 (Ref. 4, p. 34, Fig. 11). Although this data consists of

$$\Delta R_W \text{ vs } NW_s$$

the process of predicting

$$\Delta R_W \approx K\, NW_s$$

should yield a substantially similar uncertainty. Using the average integrated wet refractivity relationship derived in Ref. 1 (and based on work done by Chao, Ref. 5), i.e.,

$$10^{-6} \int_0^\infty NW(h)\, dh \approx 0.26\, NW_s, \text{ cm}$$

yielded the following standard deviation:

$$1\sigma = 1\sigma(\Delta R_W - 0.26\, NW_s)$$

$$= 2.3 \text{ cm}$$

which is at least a similar number to that uncertainty obtained from the proposed procedure.

III. Consideration of the Differences in Day and Night Wet Refractivity Profiles

It has been suggested here that there exists a strong (empirical) relationship between integrated wet refractivity and surface wet refractivity:

$$\Delta R_W \approx K\left[\frac{\Delta R_D}{ND_s}\right] NW_s$$

Since there is little dynamic variation in the term $(\Delta R_D/ND_s)$, the above relationship implies an "average" wet profile, say $f_{AVE}(h)$, such that

$$\Delta R_W = 10^{-6} \int_0^\infty NW(h)\, dh$$

$$\approx 10^{-6} \int_0^\infty NW_s\, f_{AVE}(h)\, dh$$

$$\approx \left[10^{-6} \int_0^\infty f_{AVE}(h)\, dh\right] NW_s$$

$$\approx \left[K\left\{\frac{\Delta R_D}{ND_s}\right\}\right] NW_s$$

The main considerations which detract from an "average" wet refractivity profile are fluctuations in relative humidity:

$$RH(h) \neq (RH)_s$$

and near surface variations in temperature. Whereas the fluctuations in relative humidity appear very random, the variations in surface temperature are much more systematic and can be characterized as either day or night type profiles. A typical appearance of night and day temperature profiles is shown in Fig. 2.

If one assumes an "average" wet refractivity profile, then obviously using a "night" NW_s will give too small a total wet zenith range refraction; conversely, using a "day" NW_s will lead to too large a total wet zenith range refraction. This can be seen in Fig. 3.

The conclusion one expects is that the K (= 0.3224) previously determined would be larger for night only profiles and smaller for day only profiles. This in fact turns out to be the case. The data previously analyzed was separated into day only and night only profiles, and yielded the following results:

Day profiles

K = 0.2896

σ(cm) = 1.1 cm

Night profiles

K = 0.3773

σ(cm) = 1.9 cm

This data appears in Table 2 and Fig. 4.

IV. Adjustment of Surface Temperature to Reflect Differences in Day and Night Profiles

In the previous section it was pointed out that systematic diurnal surface temperature variations cause systematic distortions in attempting to fit total wet zenith range refraction to surface wet refractivity. As a final attempt to explore ways to account for this effect the following was tried:

Let

T_{MIN} = lowest previous 24-h temperature

T_{MAX} = highest previous 24-h temperature

Then, to moderate the night and day profile distortions define:

$$T(\text{night profiles}) = \frac{3T_{MIN} + T_{MAX}}{4}$$

$$T(\text{day profiles}) = \frac{3T_{MAX} + T_{MIN}}{4}$$

Entering these temperatures into the previously described cases yielded

K = 0.3281

σ(cm) = 1.3 cm

The results can be seen in Table 3 and Fig. 5.

V. Conclusions

From the (admittedly) small data set at hand, there appears to be a strong correlation between total wet zenith range refraction and wet surface refractivity, in the form of

$$R_W = K\left[\frac{\Delta R_D}{ND_s}\right] NW_s$$

$$= K(RH)_s\left[\frac{6677.0}{T_s}\right]\exp\left(\frac{AT_s - B}{T_s - C}\right)$$

Depending on how the equation is used, it appears to potentially yield an uncertainty in total wet zenith range refraction of

$$\sigma(\text{cm}) \approx 1.5 \text{ to } 2.0 \text{ cm}$$

Also, it possesses the advantage of being dependent on surface parameters only, in contrast to previous methods. Table 4 presents a comparison of previous results contrasted to results from the proposed procedure. Obviously, however, a much larger data set would have to be analyzed before the results presented in this report could be verified and accepted.

References

1. Berman, A. L., and Rockwell, S. T., "A Proposal for a New Radio Frequency Angular Tropospheric Refraction Model For Use Within The DSN," IOM 421C-74-321, Dec. 5, 1974 (JPL internal document).

2. Berman, A. L., and Rockwell, S. T., "A New Angular Tropospheric Refraction Model," in *The Deep Space Network Progress Report 42-24*, Jet Propulsion Laboratory, Pasadena, Calif., Dec. 15, 1974.

3. Berman, A. L., "A New Tropospheric Range Refraction Model," in *Space Programs Summary*, No. 37-65, Vol. II, pp. 140–153, Jet Propulsion Laboratory, Pasadena, Calif., Sept. 30, 1970.

4. Ondrasik, V. J., and Thuleen, K. L., "Variations in the Zenith Tropospheric Range Effect Computed From Radiosonde Balloon Data," in *Space Programs Summary*, No. 37-65, Vol. II, pp. 25–35, Jet Propulsion Laboratory, Pasadena, Calif., Sept. 30, 1970.

5. Chao, C. C., "New Tropospheric Range Corrections With Seasonal Adjustment," in *Deep Space Network Progress Report*, No. 32-1526,Vol. VI, pp. 67–73, Jet Propulsion Laboratory, Pasadena, Calif., Dec. 15, 1971.

6. Chao, C. C., "A New Method to Predict Wet Zenith Range Correction From Surface Measurements," in *The Deep Space Network Progress Report*, No. 32-1526, Vol. XIV, pp. 33–41, Jet Propulsion Laboratory, Pasadena, Calif., April 15, 1973.

Table 1. Surface refractivity vs integrated refractivity ($A = 0.3224$, $\sigma = 0.93\%$)

Case	$100 \times \frac{NW_s}{ND_s}$, %	$A \times \left\{100 \times \frac{NW_s}{ND_s}\right\}$, (%)	$100 \times \frac{\int NW\,(h)\,dh}{\int ND\,(h)\,dh}$, (%)	Δ (%)	Δ (cm)
1	4.86	1.57	2.27	+0.70	+1.48
2	3.76	1.21	2.17	+0.96	+2.03
3	5.74	1.85	1.80	−0.05	−0.11
4	5.34	1.72	1.37	−0.35	−0.74
5	4.74	1.53	1.75	+0.22	+0.47
6	7.14	2.30	2.17	−0.13	−0.28
7	24.11	7.77	8.55	+0.78	+1.65
8	31.72	10.23	9.12	−1.11	−2.35
9	7.29	2.35	4.58	+2.23	+4.72
10	9.89	3.19	2.69	−0.50	−1.06

Table 2. Surface refractivity vs integrated refractivity

Case	$100 \times \frac{NW_s}{ND_s}$	$A \times \left\{100 \times \frac{NW_s}{ND_s}\right\}$	$100 \times \frac{\int NW(h)\,dh}{\int ND(h)\,dh}$	Δ (%)	Δ (cm)
		Day profiles (even) $A = 0.2896$ $\sigma = 0.50\%$			
2	3.76	1.09	2.17	+1.08	+2.29
4	5.34	1.55	1.37	−0.18	−0.38
6	7.14	2.07	2.17	+0.10	+0.21
8	31.72	9.19	9.12	−0.07	−0.15
10	9.89	2.86	2.69	−0.17	−0.36
		Night profiles (odd) $A = 0.3773$ $\sigma = 0.89\%$			
1	4.86	1.83	2.27	+0.44	+0.93
3	5.74	2.17	1.80	−0.37	−0.78
5	4.74	1.79	1.75	−0.04	−0.09
7	24.11	9.10	8.55	−0.55	−1.16
9	7.29	2.75	4.58	+1.83	+3.87

Table 3. Surface refractivity vs integrated refractivity
$A = 0.3281 \quad \sigma = 0.63\%$

Case	$100 \times \frac{NW_s{}^a}{ND_s}$	$A \times 100 \times \frac{NW_s{}^a}{ND_s}$	$100 \times \frac{\int NW(h)\,dh}{\int ND(h)\,dh}$	Δ (%)	Δ (cm)
1	6.43	2.11	2.27	+0.16	+0.34
2	2.92	0.96	2.17	+1.21	+2.55
3	7.18	2.36	1.80	−0.56	−1.18
4	4.45	1.46	1.37	−0.09	−0.19
5	6.19	2.03	1.75	−0.28	−0.59
6	5.61	1.84	2.17	−0.33	+0.70
7	26.43	8.67	8.55	−0.12	−0.25
8	29.02	9.52	9.12	−0.40	−0.84
9	9.83	3.23	4.58	+1.35	+2.85
10	7.70	2.52	2.69	+0.17	+0.36

[a]"Modified" surface temperature in calculation of NW_s

Table 4. 1σ Uncertainties in wet zenith range refraction

Data source	Ref. 3	Ref. 6		Proposed Approach		
Model	Berman 1970	Berman 1970	Chao 1973	$K = 0.3224$	$K_D = 0.2896$ $K_N = 0.3773$	Modified surface temperature
Day profiles	1.5 cm	3.5 cm	2.0 cm	—	1.1 cm	—
Night profiles	5.5 cm	4.9 cm	4.1 cm	—	1.9 cm	—
Composite	3.5 cm	4.2 cm	3.0 cm	2.0 cm	1.5 cm	1.3 cm

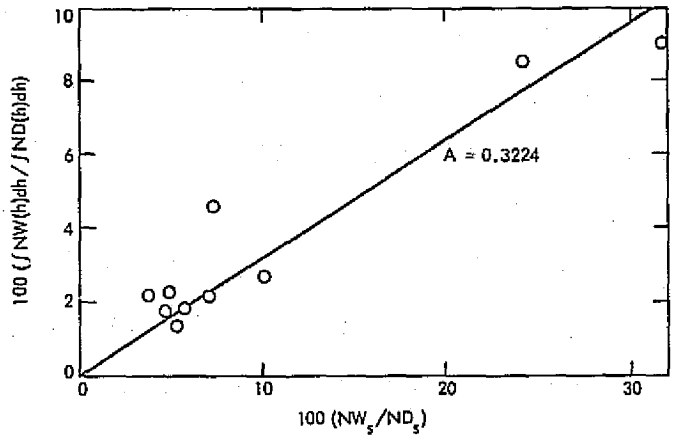

Fig. 1. Integrated refractivity vs surface refractivity, $A = 0.3224$

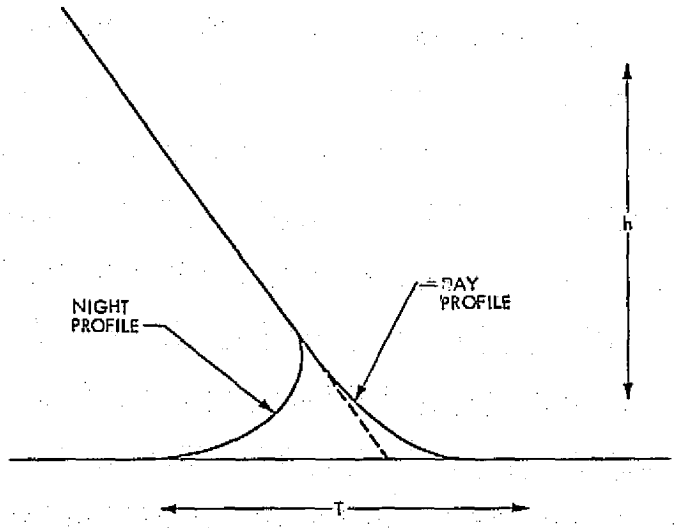

Fig. 2. Typical night and day temperature profiles

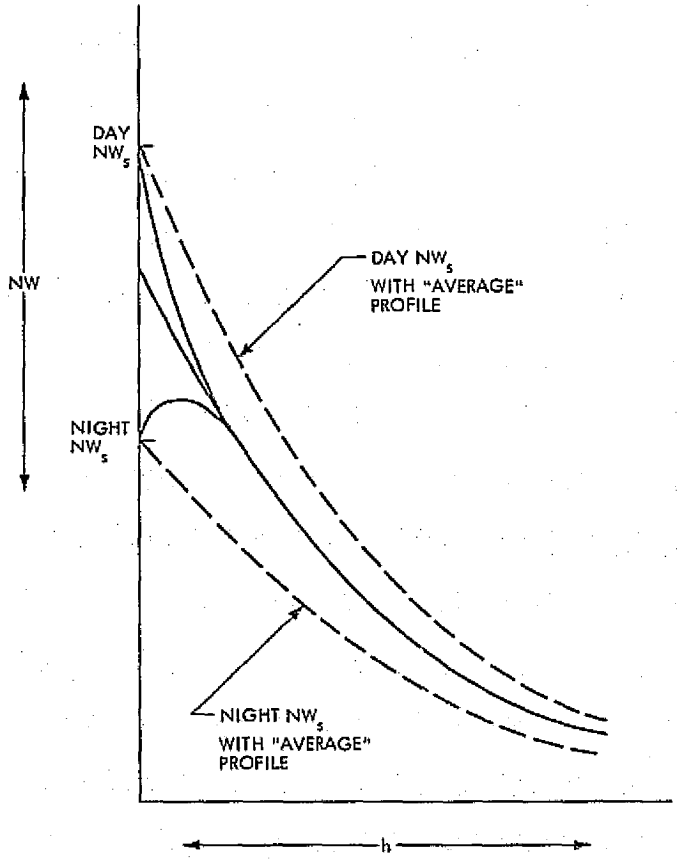

Fig. 3. Typical night and day refractivity profiles

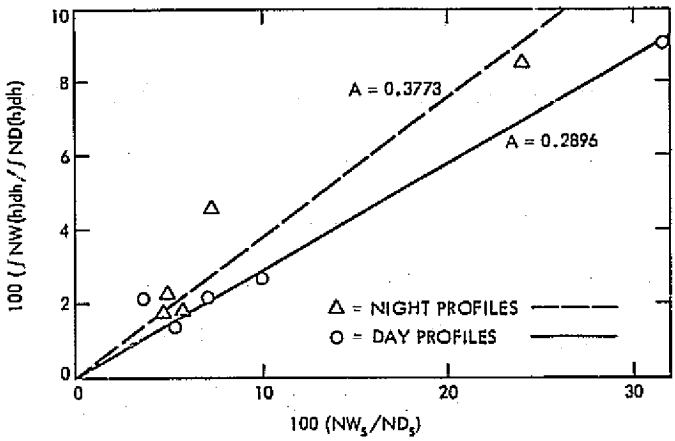

Fig. 4. Integrated refractivity vs surface refractivity, $A = 0.3773$ and $A = 0.2896$

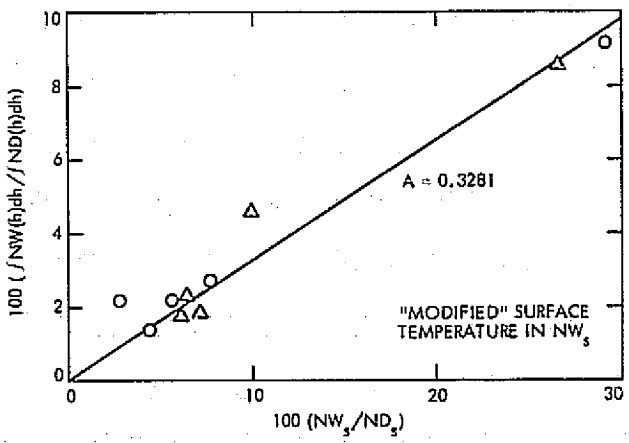

Fig. 5. Integrated refractivity vs surface refractivity, $A = 0.3281$

Doppler Phase-Noise Measurement Using Mean-Sweep Techniques

R. C. Bunce
Network Operations

This paper describes an investigation leading to techniques to reduce the error present in the DSN station measurement of doppler phase-noise variance and standard deviation. The error source of concern is the doppler counter resolver, which sorts continuous phase data into finite group intervals. The intervals are 3.5 deg (1 MHz bias) or 18 deg (5 MHz bias) wide.

Counter operation is covered to define parameters, and then appropriately limited model functions for the variance, its estimate, and the error are stated. The model introduces linear and sinusoidal mean-sweep functions to investigate their effect on the error.

Machine-programming of the model yields results which indicate that mean-sweep significantly reduces the measurement error when phase-noise standard deviation is low (less than 2 deg at 1 MHz bias, or 10 deg at 5 MHz bias). Linear sweep is the most accurate technique, but sinusoidal sweep is recommended as the more feasible; errors with the latter do not exceed 0.15 deg rms (1.0 MHz bias) in the region of interest.

Finally, the recommended parameters and the expected residual error are stated for use in test program configuration and data reduction; the error is asymptotic to a universal constant variance offset which can be appropriately subtracted to compensate for the group interval width at all noise levels.

I. Introduction

Present doppler phase-noise measurement techniques yield reasonably accurate estimates when the noise standard deviation (sigma) exceeds 2 deg rms (1.0 MHz bias) or 10 deg (5.0 MHz bias). However, when sigma is smaller than these values, the estimate obtained is increasingly variable with certain initial conditions, becoming practically meaningless below 1.0 deg (1.0 MHz bias) or 5.0 deg (5.0 MHz bias). Sigma levels within these regions are encountered in strong-signal coherent S-band test modes and X-band operations and test procedures.

An initial condition of interest in this region arises from the finite time-resolution of the doppler counter resolver. The resolver estimates the time-position of waveform zero-crossings, which form a continuously distributed set when random noise is present. The mean value of this set is, however, stationary with respect to adjacent resolver pulses when these pulses are time-coherent with the bias period, the usual test case. The time difference between the mean-value zero-crossing and the adjacent (earlier) resolver pulse, its estimate, is an error variable with initial conditions and cannot normally be predicted.

As this initial offset varies, the final estimate of sigma varies. When sigma is small, this variation is too large to yield meaningful measures with confidence. However, if this initial offset is intentionally varied by a known "mean-sweep" function during data collection, the error will tend to average, and the total possible variation will presumably decrease. The following discussion investigates this possibility in detail by modeling the resolver behavior during application of various sweep forms.

II. Doppler Counter Operation and Measurement Model

Doppler phase-noise measurement in the DSN stations is done by processing a set of doppler counter samples. Reduction of this data set yields an estimate of random phase-noise variance σ_ϕ^2 and/or standard deviation σ_ϕ. The latter is simply the rms value of the noise.

The variance and standard deviation depend on signal strength, mode of operation, system temperature, system noise, and many other factors. Doppler noise standard deviation is as low as 1 or 2 deg or less under strong-signal coherent conditions, when system noise is minimized.

The actual noise data extracted from the counter samples is a residual on the order of 1×10^{-8} of the phase accumulation between samples. The total differential phase between each sample is primarily the counter bias phase-accumulation over the sample period τ. The accumulation is normally between 10^5 cycles and 10^8 cycles, depending on the period τ and the bias frequency B. At the end of each sample period, the accumulated total cycle count (since reset) is read out as an integer. The readout is not the differential phase; the counter acts as a continuous digital integrator, summing these differentials. In addition, the counter is mechanized to obtain meaningful residual data by means of a resolver that measures (each sample period) the time position of the final waveform (positive-going) zero crossing of the period, within a resolution of 10 ns ($\Delta\tau$). The resolver tabulates the number of 10-ns intervals, an integer K. This integer is also read out and understood as an estimate ($K\Delta\tau$) of the true resolver period ΔT between the timing pulse that ended the sample period (t_p) and the time of the final positive-going zero crossing (t_z). The period $K\Delta\tau$ is not precisely equal to ΔT, and thus is not correct, for the tabulation is stopped at t_z, which normally occurs at some point between discrete resolver increments $K\Delta\tau$ and $(K + 1)\,\Delta\tau$.

Expressed quantitatively,

$$\begin{aligned} t_z &= t_p + \Delta T \\ &= t_p + K\Delta\tau + \delta T \\ &\qquad 0 \le \delta T \le \Delta\tau \end{aligned} \tag{1}$$

where

ΔT = true time increment from t_p to the zero crossing t_z

$\Delta\tau$ = fixed resolver time increment, 10 ns

δT = error of $K\Delta\tau$ in measuring ΔT

K = resolver increment index or count

The quantity of interest is the residual phase ϕ_R, which is the (accumulated) difference between the true phase and the nominal phase due to bias alone. This can be expressed as a frequency integral yielding the integrated integer I described above:

$$\begin{aligned} I &= \int_{t_0}^{t_p + \Delta T} [B - \dot{\phi}_R(t)]\, dt \\ &= B[(t_p - t_0) + \Delta T] - \int_{t_0}^{t_p + \Delta T} \dot{\phi}_R(t)\, dt \\ &= B[(t_p - t_0) + \Delta T] - \phi_R \end{aligned}$$

where t_0 = time of first zero crossing after reset.

The nominal, due to bias alone, is

$$I_0 = \int_{t_0}^{t_p + \Delta T_0} B\, dt = B[(t_p - t_0) + \Delta T_0]$$

where t_0 is repeated; the start time is theoretically irrelevant. Or

$$(I - I_0) = \Delta I = B[\Delta T - \Delta T_0] - \phi_R$$

$$\phi_R \equiv \int_{t_0}^{t_z} \dot{\phi}_R(t)\, dt$$

Although actual mechanization restricts ΔT to a range of values, with small differences of ΔI completing the relationship, it simplifies the model, without loss of generality, to assume I and I_0 equal, with ΔT having complete freedom. This lead to

$$\begin{aligned}\phi_R &= B[\Delta T - \Delta T_0] \\ &= B[K\Delta\tau - K_0\Delta\tau] + B[\delta T - \delta T_0] \end{aligned} \quad (2)$$

By similar development, the estimate of ϕ_R, $\hat{\phi}_R$ can be shown to be

$$\begin{aligned}\hat{\phi}_R &= B[(K - K_0)\,\Delta\tau] \\ &= \phi_R - (\delta\phi - \delta\phi_0) + \int_{t_p + K\Delta\tau}^{t_p + K\Delta\tau + \delta T} \dot{\phi}_R(t)\, dt \end{aligned} \quad (3)$$

The integral is considered negligible; residual frequency components are too small to build up any appreciable value over the short time span. This yields (in parallel with ϕ_R)

$$\begin{aligned}\hat{\phi}_R &= B[K - K_0]\,\Delta\tau = \phi_R - B(\delta T - \delta T_0) \\ &= \phi_R - (\delta\phi - \delta\phi_0)\end{aligned}$$

These stable forms allow a convenient scaling; it is to set $K_0 = 0$ (shift the index origin to K_0) and simultaneously define the phase of the set of resolver levels ϕ_K by the notation

$$\phi_K = K\Delta\phi - \delta\phi_0 \quad (4)$$

where

$$\Delta\phi = B\Delta\tau = 3.6 \text{ deg (1 MHz) or } 18 \text{ deg (5 MHz)}$$

and

$$\delta\phi = B\delta T_0 = \text{the offset of mean } \phi_R \text{ from the nearest lower resolver level}$$

These combine to

$$\begin{aligned}\phi_R &= \phi_K + \delta\phi \\ \hat{\phi}_R &= \phi_K + \delta\phi_0 = K\Delta\phi \end{aligned} \quad (5)$$

where

$$K = \cdots, -2, -1, 0, 1, 2, \cdots$$

$$-\infty < \phi_R < +\infty$$

The residual phase argument ϕ_R consists of all deviations from nominal bias phase. To further limit the discussion, consideration will be given to only two contributions; all others will be assumed negligible. The two are:

(1) Intentional, known, and deterministic deviations of the true mean from the nominal (bias) mean.

(2) Random phase noise, assumed stationary, gaussian, and normally distributed, with variance σ_ϕ^2.

With these, ϕ_R becomes

$$\phi_R = \bar{\phi} + \phi$$

where

$\bar{\phi}$ = intentional mean displacement of the entire ϕ distribution from nominal

ϕ = phase-noise displacement from $\bar{\phi}$ at any instant of measure

The phase quantities above and their time equivalents are diagrammed in Fig. 1, with a superimposed typical phase-noise probability density function. Note the actual measure ϕ at time t_z occurs between resolver levels ϕ_4 and ϕ_5. The (index-shifted) resolver readout would be the "K" index of ϕ_4, equivalent to $K\Delta\phi$ of $\hat{\phi}_R$, or "4," and any zero-crossing in the shaded area A_4 would yield this readout. The area A_4 thus represents the probability of the reading $4\Delta\phi$; other area probabilities would occur similarly.

After observation of Fig. 1, it becomes apparent that the various probability areas, such as A_4 shown, vary for given ϕ_K if the mean dimension $\bar{\phi}$ is varied, and that this will certainly not degrade the data if the mean variation is known.

The effect of sweeping is actually to vary the location of all $P(\phi)$ with respect to the $\{\phi_K\}$. Various initial $\delta\phi_0$ will thus obviously alter the result, since the ϕ_K are a function of $\delta\phi_0$. In fact, the purpose of mean-sweep is to eliminate or reduce the error due to arbitrary initial unknown $\delta\phi_0$ with a compensating, known, and averaging $\bar{\phi}$ function.

At the extreme, without sweep, if the entire $P(\phi)$ (of small variance) were (essentially) confined within one resolver level, then only a single reading would occur with high probability. The variance estimate would then be (nearly) zero. However, moving the mean would shift the distribution into various levels, and at least some data would seemingly be meaningful after mean-shift subtraction and other processing.

The effects of mean-shift by various deterministic functions is difficult to determine analytically because the $P(\phi)$ integral is transcendental. However, these effects can be readily modeled for machine computation, and this approach prevails in the remainder of the discussion.

III. Resolver Error Model Function and Mean-Sweep

Variance is estimated from data as the mean-square value of the data set, all data as deviations from the average value. During data collection, probabilities are not normally tabulated; they simply "occur" as variations in the number of data samples in the various class intervals. For finite data, the number of class intervals obtained is directly proportional to the resolution of the data samples with respect to the standard deviation.

Phase samples from the DSN doppler counter occur in class intervals $\Delta\phi$ wide, all samples in the class interval yielding the same value, $K\Delta\phi$, where K is the index of the interval.

For example, in Fig. 1, without differencing, the relative contribution of the shaded area (A_4) to the variance estimate would be (assuming an infinite sample population with $\bar{\phi} = 0$, and neglecting mean offset of the area)

$$\sigma_\phi^2(A_4) = (4\Delta\phi)^2 \int_{\phi_4}^{\phi_5} P(\phi)\, d\phi$$

$$4\Delta\phi = \phi_4 + \delta\phi_0 = \hat{\phi}_R \tag{6}$$

while the true contribution is

$$\sigma_\phi^2(A_4) = \int_{\phi_4}^{\phi_5} \phi^2\, P(\phi)\, d\phi \tag{7}$$

Equations (6) and (7) show the essential error source; errors occur because, with sample data, a single value is used to represent the mean-square data of an entire region, the group interval. The true variance is defined such that the data are continuous and samples are "inside" the integral, squared for integration with the corresponding probability density coordinate. There is obviously some value of phase that could be subtracted from $4\Delta\phi$ of (6) (holding A_4 constant) for equivalence with (7); such values, however, would not be static, but would rather depend on ϕ_K. The "correction" is thus nonstatic and must be determined as a function of the areas, or, finally, of the variance estimate.

It is intuitive that the variance error will increase when the probability integral is large with respect to variance. When the limits are infinite, this integral is unity, and the entire estimate is a single measure, which is meaningless.

On the other hand, when the interval is (relatively) small with respect to variance, the estimate and true values asymtotically approach, for the relative change in argument across each interval is small.

If mean-sweep is introduced, the class interval associated with a given estimate, such as $4\Delta\phi$, shifts in location, while the actual estimated angle $(\hat{\phi}_R - \bar{\phi})$ takes on a variety of values. A "weighted average" contribution to variance thus occurs for each $\phi_K = K\Delta\phi - \delta\phi$. The model for this estimate and its true counterpart can be expressed in some detail by (including a nonzero initial mean)

$$\sigma_\phi^2 = \left\{ \int_{-\infty}^{+\infty} \int_{-\infty}^{+\infty} [\bar{\phi} - \phi(t)]^2\, P[\bar{\phi} - \phi(t)]\, d\phi\, dt \right\} - (MN)^2 \tag{8}$$

$$= \left\{ \int_{-\infty}^{+\infty} \left[\sum_{K=-\infty}^{\infty} \int_{\phi_K - \bar{\phi}(t) - \Delta\phi}^{\phi_K - \bar{\phi}(t)} \phi^2\, P(\phi)\, d\phi \right] dt \right\} - (MN)^2 \tag{9}$$

$$\hat{\sigma}_\phi^2 = \left\{ \frac{\tau}{T} \sum_{M=1}^{\frac{T}{\tau}} \sum_{K=-K_L}^{K_L} [K\Delta\phi - \bar{\phi}(M\tau)]^2 \int_{\phi_K - \bar{\phi}(M\tau) - \Delta\phi}^{\phi_K - \bar{\phi}(M\tau)} P(\phi)\, d\phi \right\} - (MN)^2 \tag{10}$$

σ_ϕ = phase noise variance

$\hat{\sigma}_\phi$ = estimate of σ_ϕ during typical measurement

ϕ = phase noise deviation from mean (continuous variable)

$P(\phi)$ = probability density function of argument; commonly "normal" or "gaussian"

K = index of resolver phase levels, modulo B_τ

ϕ_K = expression of resolver levels as incremental phase deviations, $\Delta\phi$ wide, from ϕ_m, the phase level nearest the nominal mean

$\Delta\phi$ = ϕ_K increment, 3.6 deg (1.0 MHz) or 18 deg (5.0 MHz)

MN = $P(\phi)$ mean value, exclusive of $\overline{\phi}$

τ = sample interval, usually 1.0 or 0.1 s

T = total measurement period, 10 s to several minutes

$-K_L, K_L$ = lower and upper index limits for class intervals of obtained data

$\overline{\phi}(t), \overline{\phi}(M\tau)$ = deviations of mean value of ϕ distribution, at time t, from nominal value. At times $M\tau$, the nominal (null) value is the modulo B_τ bias waveform phase within the resolver; $\phi_m + \delta\phi_m = 0$; $\overline{\phi}(t)$, $\overline{\phi}(M\tau)$ are presumed intentional and known

Note that (9) differs from (10) in that (10) is not only discrete in the mean-sweep function, but also the phase measures $\{K\Delta\phi - \overline{\phi}(M\tau)\}$ are again outside of the probability integral. Each set of measures therefore represents, as before, a class interval of probability given by the class interval integral. Conversely, (9) is exact, since ϕ^2 is within the integral.

Note that, in (10), many more class intervals are obtained because the mean-sweep function is not constant, but steps to various values. These intervals are *not* distinct but overlap; the error is not "removed," but rather "pseudo-averaged" to some difference value by sweeping.

Various undesirable effects mentioned earlier, but not evident in (10), lead to actual data reduction as a differencing of the sequential $\{K\Delta\phi\}$ obtained. Upon differencing, the defining expressions become somewhat intricate multiple sums and integrals:

$$\sigma_\phi^2 = \frac{1}{2}\left\{\int_{-\infty}^{+\infty}\int_{-\infty}^{+\infty}\int_{-\infty}^{+\infty}[\phi_2 - \phi_1 - \Delta M(t)]^2 \times P[\phi_2 - \overline{\phi}(t+\tau)]\,P[\phi_1 - \overline{\phi}(t)]\,d\phi_1 d\phi_2\,dt\right\} - \frac{(MN)^2}{2} \tag{11}$$

$$\hat{\sigma}_\phi^2 = \frac{1}{2}\left\{\frac{\tau}{T}\sum_{M=1}^{\frac{T}{\tau}}\sum_{K=-K_L}^{K_L}\sum_{N=-K_L}^{K_L}[N\Delta\phi - \Delta M(M\tau)]^2 \times\int_{\phi_K - \overline{\phi}(M\tau)+\Delta\phi}^{\phi_K - \overline{\phi}(M\tau)+\Delta\phi} P(\phi_2)\,d\phi_2 \times\int_{\phi_K - \overline{\phi}(M\tau-\tau)}^{\phi_K - \overline{\phi}(M\tau-\tau)+\Delta\phi} P(\phi_1)\,d\phi_1\right\} - \frac{(MN)^2}{2} \tag{12}$$

where

ΔM = intentional change in mean phase during sample period

ϕ_1, ϕ_2 = two arbitrary sequential phase measures, taken τ seconds apart

Note that the bias mean offset from ϕ_m, $\delta\phi_m$, contained in all ϕ_K, is *not* normally known, so any mean-sweep function will necessarily have an arbitrary zero reference, whose effect may or may not be finally significant. Also, if $P(\phi)$ is a stationary function about the mean, MN will be zero upon differencing, and may be dropped.

The factor "½" in each expression results because the differenced distribution variance is automatically twice as large as the variance of the primary distribution. This is well established and will not be covered here.

For actual machine programming, $P(\phi)$ was considered gaussian and therefore stationary. The error-function subroutine, adjusted for gaussian form, was used to evaluate the integrals. Also, (11) could feasibly be expressed as a single integral since the difference between variates in a gaussian distribution is itself a gaussian distribution with doubled variance. Sweep is obviously irrelevant since it would simply "subtract out" as an additive contribution. However, to avoid undue complication, (12) is easier to handle in the double-integral form, since mean-differences cause probability changes between samples. The single-integral form was modeled, but it was more complicated than (11), so it was dropped in favor of the expression as stated.

Data on available DSN hardware indicated that sinusoidal modulation index could be set within a tolerance of $\pm 5\%$. With this in mind, a simulation program for (12) was automated. The program routine to calculate estimated sigma was:

$$\hat{\sigma}_\phi^2 = \left\{ \frac{\tau}{8T} \sum_{M=1}^{T/\tau} \sum_{K=-K_L}^{K_L} \sum_{N=-K_L}^{K_L} (N\Delta\phi)^2 [\operatorname{erf}(\theta_2) - \operatorname{erf}(\theta_1)] \right.$$
$$\left. \times [\operatorname{erf}(\theta_4) - \operatorname{erf}(\theta_3)] - \frac{\tau}{2T} \sum_{M=1}^{T/\tau} [\hat{\Delta}M(M\tau)]^2 \right\}^{1/2}$$

$$\theta_1 = \frac{[K\Delta\phi - \bar{\phi}(M\tau - \tau) - \delta\phi_0]}{\sqrt{2}\,\sigma_\phi}$$

$$\theta_2 = \theta_1 + \Delta\phi/\sqrt{2}\,\sigma_\phi$$

$$\theta_3 = \frac{[(K+N)\Delta\phi - \bar{\phi}(M\tau) - \delta\phi]}{\sqrt{2}\,\sigma_\phi}$$

$$\theta_4 = \theta_3 + \Delta\phi/\sqrt{2}\,\sigma_\phi$$

$$K_L = \text{int}\,[6\sigma_\phi/\Delta\phi] + 1$$

$$\bar{\phi}(M\tau) = \begin{cases} 0 \text{ (no sweep)} \\ (M\tau/T)\,\Delta\phi \text{ (linear sweep)} \\ \phi_M \sin[2\pi M\tau/T] \text{ (sinusoidal sweep)} \end{cases}$$

$$\hat{\Delta}M(M\tau) = \begin{cases} 0 \text{ (no sweep)} \\ (\tau/T)\,\Delta\phi \text{ (linear sweep; no appreciable error)} \\ \hat{\phi}_M \{\sin[2\pi M\tau/T] - \sin[2\pi(M\tau - \tau)/T]\} \end{cases}$$

$\hat{\phi}_M$ = estimated modulation index, deg

ϕ_M = true modulation index, deg

$\delta\phi_0$ = initial offset, $0 < \delta\phi_0 < \Delta\phi$ (13)

Note that ϕ_M, the true (but unknown) modulation index, appears in the error function integral, while $\hat{\phi}_M$, the data reduction value, appears only in the rms correction due to sinusoidal sweep.[1] Since the resolver mean offset $\delta\phi_0$ is modulo $\Delta\phi$, it is evident that limiting $\delta\phi_0$ to a spread of $\Delta\phi$ will cover all variation. An initial investigation with machine programming of (13) alone indicated that the error variation with modulation index ϕ_M tended to increase when ϕ_M was greater than $\Delta\phi$ or less than about $\Delta\phi/3$. Therefore, detailed investigation was limited to this range.

An error measure was also in the program along with a mean error (offset) calculation. These measures were

$$\theta_0(\hat{\sigma}_\phi) = \frac{1}{m+n} \sum_{a=1}^{m} \sum_{b=1}^{n} \hat{\sigma}_\phi(\phi_{M_a}, \delta\phi_{0_b})$$

$$\epsilon_{\text{rms}}^0(\hat{\sigma}_\phi) = \left[\frac{1}{m+n} \sum_{a=1}^{m} \sum_{b=1}^{n} [\hat{\sigma}_\phi(\phi_{M_a}, \delta\phi_{0_b}) - \theta_0(\hat{\sigma}_\phi)]^2 \right]^{1/2} \quad (14)$$

[1]In (13), this correction has been separated from the main argument for independent evaluation. This is possible upon differencing; the cross-correlation is zero.

Results used had the tolerance spread

$$m = 3 \text{ for } \phi_M = \hat{\phi}_M, \hat{\phi}_M + 5\%, \hat{\phi}_M - 5\%$$
$$n = 4 \text{ for } \delta\phi_0 = 0, 0.9, 1.8, 2.7° \quad (15)$$

where

$\theta_0(\hat{\sigma}_\phi)$ = the mean error, or average offset, between given sigma and its estimates

$\epsilon_{\text{rms}}^0(\hat{\sigma}_\phi)$ = the rms value of the variation in $\hat{\sigma}_\phi$ for given σ_ϕ due to (uncontrollable) tolerances in ϕ_M and initial values of $\delta\phi_0$.

The error statistic ϵ_{rms}^0 is not a random variate but is bounded by the tolerance excursions and their combined effects.

Equations (14) and (15) complete the quantitative description of the model program. The program inputs were sigma (σ_ϕ), sample interval (τ), sweep repetition period (T), and estimated modulation index ($\hat{\phi}_M$). The fundamental sweep frequency was obviously τ/T Hz. To avoid the region where autocorrelation effects would possibly occur in practice, τ was chosen as 1.0 s. The period T was then set arbitrarily at 10.0 s. This yields the lowest practical sinusoidal sweep frequency (0.1 Hz) available at the DSN sites. A lower frequency would yield a higher sweep resolution, obviously desirable, but not presently feasible.

Sigma values from 0.4 to 3.0 deg were processed as the modulation index was varied over the stated range. Also, highly resolved linear sweep ($\tau/T = 0.01$) as well as no-sweep conditions were cycled, and the various data were collected for analysis.

IV. Mean-Sweep Effects and Error Analysis

The error statistic ϵ_{rms}^0 represents a medium value of the variation in the estimate of the error, as to be expected when measuring doppler phase-noise sigma while sweeping. With the highly resolved linear sweep, this error was all but undetectable. Such sweep would be preferable to all other forms, except that it is difficult to mechanize during coherent testing.

At the other extreme, the error with "no-sweep" was larger than σ_ϕ itself at the lower values (below 0.5 or 2.5 deg) and rendered the measure questionable until σ_ϕ was greater than 2.0 deg (or 10 deg). For sigma greater

than these levels, sweep made little difference; the error was negligible.

With sinusoidal sweep, the error in the region of interest was less than one-fourth the no-sweep level for all modulation indices programmed. Within this bound, however, the relative error was very sensitive to the actual $\hat{\phi}_M$. The $\hat{\phi}_M$ between 1 and 3 deg was tried, and the optimum value appears to be about 1.5 deg. The error distribution with various $\hat{\phi}_M$ was very erratic within these small limits, but finally insignificant because of their low absolute level. Within the measurable range, the rms error never exceeded 0.15 deg (1.0 MHz) while sweeping ($\sigma_\phi = 0.4$ deg), and this model level, in practice, will undoubtedly be masked by other system contributions.

In order to facilitate easy mechanization, a modulation index of 2.0 deg was selected for test use, as compatible with the DSN Command Modulator Assembly (CMA) equipment.

A typical sinusoidal-sweep error distribution of $\hat{\sigma}_\phi$, yielding ϵ^0_{rms} and θ_0, is shown in Fig. 2 as a function of $\delta_{\phi 0}$ and $\hat{\phi}_M$. The figure, for a σ_ϕ of 0.6 deg, clearly shows the pseudo-sinusoidal nature of the error; peak error is less than 1.5 times the rms value.

Composite error results described above are shown in Fig. 3. Note the large error reduction in the small-sigma range by sinusoidal sweeping as opposed to the existing no-sweep condition. Also note the convergence of all data at about 2 deg (or 10 deg); sweeping to improve statistics above these levels is, as noted, superfluous.

The statistic θ_0 in (14) is very interesting. For $\hat{\phi}_M$ of 2 deg, the selected value θ_0 varies from an asymptote of about 1.040 deg (1.0 MHz) at the higher levels of σ_ϕ down to 1.023 deg at the minimum measurable level, an insignificant change of only 0.017 deg across the entire field. It obviously differs little from a constant rms offset, apparently related to the resolver increment $\Delta\phi$.

With a little manipulation, the limiting value of this offset can be shown to have a well-known quantization error value (omitting intermediate steps):

$$\lim_{\sigma \to \infty} (\theta_0)^2 = \left[\lim_{\sigma \to \infty} \sum_{k=-\infty}^{\infty} \frac{1}{\Delta\phi} \int_{(k-\frac{1}{2})\Delta\phi}^{(k+\frac{1}{2})\Delta\phi} \phi^2 P(\phi,\sigma)\, d\phi - \sigma_\phi^2 \right] = \frac{\Delta\phi^2}{12} \tag{16}$$

For $\Delta\phi = 3.6$ deg (1.0 MHz), this is 1.039 deg, in excellent agreement with the data. Since the variation in θ_0 with σ_ϕ is so small, the easiest correction to data is to simply subtract the θ_0 limit as an rms level:

$$\hat{\sigma}_{\phi\,\text{corrected}} = \hat{\sigma}_c = \left[\hat{\sigma}^2 - \frac{\Delta\phi^2}{12} \right]^{1/2} \tag{17}$$

This is the expression recommended for DSN doppler noise correction (with or without sweep) to account for the finite resolver group interval error, as desired.

The final distribution of $\hat{\sigma}_c$ with (17) and sinusoidal sweep with $\phi_M = 2$ deg applied (one-sigma error limits) for no sweep is shown in Fig. 4; $\hat{\sigma}_\phi$ (corrected) is the expected range of values during DSN data reduction when the specified sweep is used.

V. Conclusions

The primary purpose of doppler phase-noise measurement is to estimate the noise content of the doppler data obtained operationally and to assure that this noise is within specified bounds. This discussion has concentrated on the low-noise cases.

Operational data occurs with natural mean-sweep, often nearly linear, as a result of relative ground–spacecraft motion. Testing without sweep thus cannot accurately predict the operational noise in the strong-signal region; the estimate (as analyzed here) will normally be too variable.

In the S-band region (1.0-MHz bias) the no-sweep error is small except for somewhat unusual conditions, normally without operational application. Low-noise occurs, for example, when testing under fully coherent conditions, resulting in cancellation of exciter noise within the doppler extractor. However, when such conditions are encountered, as during trouble-shooting, mean-sweep will improve the residual measure (of the receiver) by reducing adverse resolver effects. Such effects have been encountered in practice.

In the X-band region (5.0-MHz bias), system noise is comparable to or less than resolver error without sweep. Measure of system noise, as it occurs operationally, appears to require a correction such as that of the sweep technique. It will remove a significant variability present during test, but normally absent during active tracking.

Sweep with the stated parameters reduces the rms of the test error by as much as 4-to-1 in the applicable region.

Independent of sweep effects, there exists a resolver quantization offset error, unavoidable because of the incremental pulse spacing. This will be present on all data, operational and test, and is about 1 deg at S-band (1.0 MHz) or 5 deg at X-band (5.0 MHz). If system noise or operational data outside of counter effects are to be measured, this offset must be removed. However, if an operational noise estimate is to be made, this may or may not be included as appropriate. For testing without this effect, it is recommended that the offset be extracted from the calculated estimate of counter input noise.

To summarize, when the bias is fixed and coherent, a sinusoidal sweep (by exciter phase modulation), with amplitude 2 deg and frequency 0.1 Hz, will adequately simulate natural operational sweep. This will reduce counter error sufficiently that meaningful results at sigma levels below 2 deg (1 MHz) and 10 deg (5 MHz) can be obtained. An additional fixed resolver quantization error of 1.039 deg (S-band) or 5.19 deg (X-band) may be subtracted (variance subtraction) as desired; it is a "built in" error on all doppler counter measures.

Definition of Symbols
(all time notation in seconds; all phase notation in cycles or degrees)

A_K Kth area of probability density function between resolver levels

a index (subscript) for modulation index

B bias frequency, 1.0 to 5.0 MHz

b index (subscript) for initial mean offset angle $\delta\phi_0$

ϵ^0_{rms} root-mean-square error of given sigma measure

K resolver level index, resolver level phase subscript

K_0 nominal K nearest (below) bias-mean zero-crossing

K_L summation limit for K (absolute)

M discrete measurement index and subscript

m summation limit, modulation index

N differential K on successive measures

n summation limit, initial offset phase

$P(\phi)$ probability density function notation

t time, general notation, s

t_p time of measurement pulse

t_z time of first positive-going zero-crossing after t_p

T total measurement period; period of periodic sweep

ΔT actual time from t_p to t_z in resolver

ΔT_0 mean value of ΔT, due to bias alone

Δ_T resolver time increment, 10 ns

$\Delta\phi$ resolver phase increment $B\Delta_T = 3.6$ deg (1.0 MHz), 18 deg (5.0 MHz)

ΔM change in $\bar{\phi}$ between successive measures

δT resolver time error in measurement of ΔT

δT_0 mean value of δT, due to bias alone

$\delta\phi$ resolver phase error in measurement of ϕ_R

$\delta\phi_0$ mean value of $\delta\phi$, due to bias alone

ϕ phase-noise displacement, general

ϕ_K resolver level phase notation set

ϕ_R total residual phase displacement from bias mean

$\hat{\phi}_R$ $K\Delta\phi$, the resolver estimate of ϕ_R

ϕ_M phase modulation index during sinusoidal sweep

$\hat{\phi}_M$ operational estimate of ϕ_M

$\bar{\phi}$ intentional mean displacement of $P(\phi)$ from bias mean; sweep function value

θ_0 mean value of rms error between σ_ϕ and $\hat{\sigma}_\phi$, given σ_ϕ

τ sampling interval, nominally 1 s

σ_ϕ sigma (standard deviation) of ϕ

$\hat{\sigma}_\phi$ estimate of σ_ϕ using counter data

$\hat{\sigma}_c$ corrected value of $\hat{\sigma}_\phi$, based on θ_0

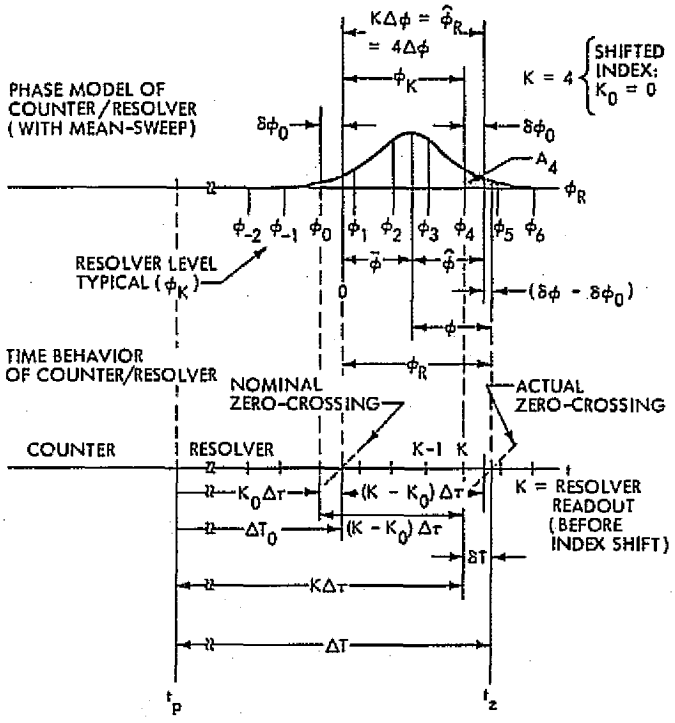

Fig. 1. Doppler counter resolver time/phase relationships

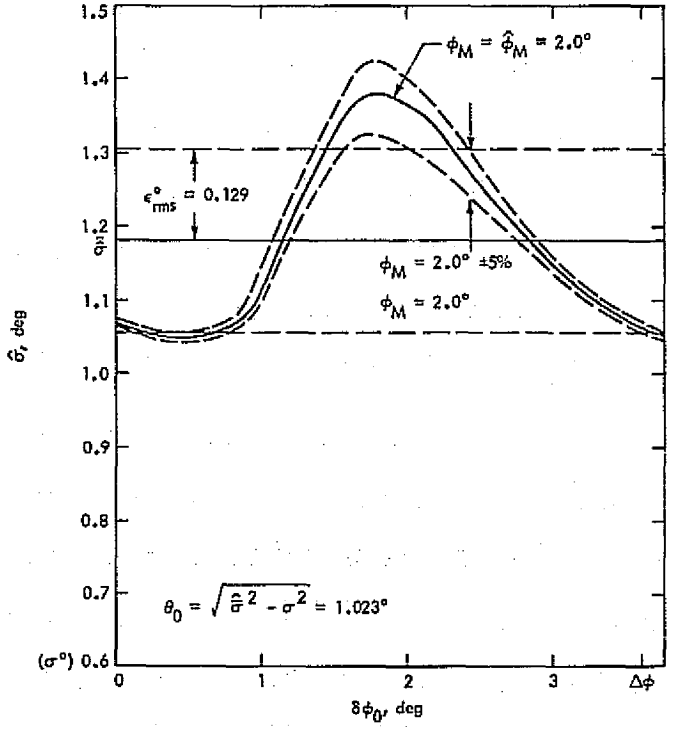

Fig. 2. Typical variation in noise sigma estimate $\hat{\sigma}°$ as a function of resolver mean offset ϕ_0 and modulation index tolerance $\phi_M \pm 5\%$; $\sigma = 0.6$ deg

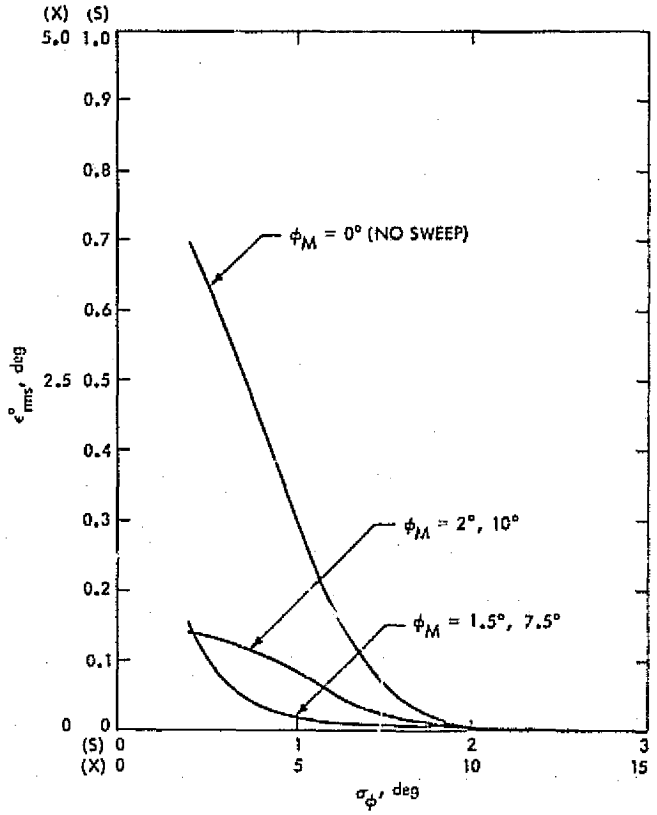

Fig. 3. Phase-noise measurement error as a function of sinusoidal mean-sweep for various modulation indices

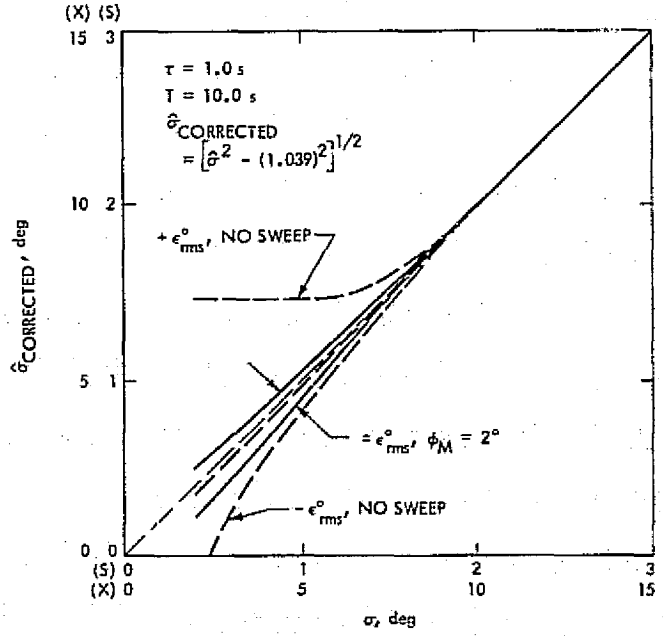

Fig. 4. Corrected sigma estimate vs sigma: no-sweep and sinusoidal sweep (mod index = 2°)

Bibliography

Anderson, J. D., Null, G. W., and Thornton, C. T., *The Evaluation of Certain Astronomical Constants from the Radio Tracking of Mariner II*, Technical Report 32-476, Jet Propulsion Laboratory, Pasadena, Calif., reprinted from *Progr. Astronaut. Aeronaut.*, Vol. 14, 1964.

Anderson, J. D., *Determination of the Masses of the Moon and Venus and the Astronomical Unit from Radio Tracking Data of the Mariner II Spacecraft*, Technical Report 32-816, Jet Propulsion Laboratory, Pasadena, Calif., July 1, 1967.

Anderson, J. D., et al., "The Radius of Venus as Determined by Planetary Radar and Mariner V Radio Tracking Data," *J. Atmos. Sci.*, pp. 1171–1174, Sept. 25, 1968.

Anderson, J. D., and Hilt, D. E., "Improvement of Astronomical Constants and Ephemerides from Pioneer Radio Tracking Data," *AIAA J.*, Vol. 7, No. 6, pp. 1048–1054, June 1969.

Anderson, J. D., "Determination of Astrodynamic Constants and a Test of the General Relativistic Time Delay With S-Band Range and Doppler Data From Mariners 6 and 7," *Space Research*, Vol. XI, pp. 105–112, Akademie-Verlag, Berlin, 1971.

Barnum, P. W., et al., *Tracking and Data System Support for the Mariner Mars 1971 Mission: Orbit Insertion Through End of Primary Mission*, Technical Memorandum 33-523, Vol. III, Jet Propulsion Laboratory, Pasadena, Calif., May 15, 1973.

Barnum, P. W., and Renzetti, N. A., *Tracking and Data System Support for the Mariner Mars 1971 Mission: Extended Mission Operations*, Technical Memorandum 33-523, Vol. IV, Jet Propulsion Laboratory, Pasadena, Calif., Dec. 15, 1973.

Bathker, D. A., *Radio-Frequency Performance of an 85-ft Ground Antenna: X-Band*, Technical Report 32-1300, Jet Propulsion Laboratory, Pasadena, Calif., July 1, 1968.

Bathker, D. A., *Radio Frequency Performance of a 210-ft Ground Antenna: X-Band*, Technical Report 32-1417, Jet Propulsion Laboratory, Pasadena, Calif., Dec. 15, 1969.

Bathker, D. A., *Predicted and Measured Power Density Description of a Large Ground Microwave System*, Technical Memorandum 33-433, Jet Propulsion Laboratory, Pasadena, Calif., Apr. 15, 1971.

Baumert, L., et al., *Coding Theory and Its Applications to Communications Systems*, Technical Report 32-67, Jet Propulsion Laboratory, Pasadena, Calif., Mar. 31, 1961.

Baumgartner, W. S., *High-Power CW Radar Transmitter*, Technical Report 32-656, Jet Propulsion Laboratory, Pasadena, Calif., Sept. 1, 1964.

Berman, A. L., *Tracking System Data Analysis Report, Ranger VII Final Report*, Technical Report 32-719, Jet Propulsion Laboratory, Pasadena, Calif., June 1, 1965.

Biber, K. W., and Whittlesey, A. C., *Description and Analysis of 890-MHz Noise-Measuring Equipment*, Technical Report 32-898, Jet Propulsion Laboratory, Pasadena, Calif., Mar. 31, 1966.

Brockman, M. H., and Posner, E. C., *Power Requirements for Deep-Space Telecommunication Links*, Technical Report 32-1395, Jet Propulsion Laboratory, Pasadena, Calif., reprinted from *IEEE Spectrum*, Vol. 6, No. 3, pp. 95–99, Mar. 1969.

Bunce, R. C., *Unified S-Band Receiver-Exciter Subsystem*, Technical Report 32-809, Jet Propulsion Laboratory, Pasadena, Calif., Sept. 15, 1968.

Butman, S., "A General Formulation of Linear Feedback Communication Systems with Solutions," *IEEE Trans. Inform. Theor.*, Vol. IT-15, No. 3, pp. 392–400, May 1969.

Butman, S., "Rate Distortion Over Band-Limited Feedback Channels," *IEEE Trans. Inform. Theor.*, Vol. IT-17, No. 1, pp. 110–112, Jan. 1971.

Butman, S., and Timor, U., "Interplex—An Efficient Multichannel PSK/PM Telemetry System", *IEEE Trans. Commun.*, Vol. COM-20, No. 3, pp. 415–419, June 1972.

Cain, D. L., and Hamilton, T. W., *Determination of Tracking Station Locations by Doppler and Range Measurements to an Earth Satellite*, Technical Report 32-534, Jet Propulsion Laboratory, Pasadena, Calif., Feb. 1, 1964.

Carey, C. N., and Sjogren, W. L., *Gravitational Inconsistency in the Lunar Theory: Confirmation by Radio Tracking*, Technical Report 32-1290, Pt. II, Jet Propulsion Laboratory, Pasadena, Calif., reprinted from *Science*, Vol. 160, No. 3830, pp. 875–876, May 24, 1968.

Carpenter, R. L., *Study of Venus by CW Radar—1964 Results*, Technical Report 32-963, Jet Propulsion Laboratory, Pasadena, Calif., reprinted from *Astron. J.*, Vol. 71, No. 2, pp. 142–152, Mar. 1966.

Chadwick, H. D., and Springett, J. C., "The Design of a Low Data Rate MSFK Communication System," *IEEE Trans. Commun. Technol.*, Vol. COM-18, No. 6, pp. 740–750, Dec. 1970.

Chaney, W. D., *Final Mariner II Tracking System Data Analysis Report*, Technical Report 32-727, Jet Propulsion Laboratory, Pasadena, Calif., Sept. 1, 1965.

Charles, F. J., and Lindsey, W. C., *Some Analytical and Experimental Phase-Locked Loop Results for Low Signal-to-Noise Ratios*, Technical Report 32-1027, Jet Propulsion Laboratory, Pasadena, Calif., reprinted from *Proc. IEEE*, Vol. 54, No. 9, pp. 1152–1166, Sept. 1966.

Clark, B. G., et al., "High Resolution Observations of Compact Radio Sources at 13 cm," *Astrophys. J.*, Vol. 161, pp. 803–809, Sept. 1970.

Clauss, R. C., et al., *Total System Noise Temperature: 15°K*, Technical Report 32-691, Jet Propulsion Laboratory, Pasadena, Calif., Nov. 1964.

Clauss, R. C., *A 2388-Mc Two-Cavity Maser for Planetary Radar*, Technical Report 32-583, Jet Propulsion Laboratory, Pasadena, Calif., reprinted from *Microwave J.*, Vol. 8, pp. 74–77, May 1965.

Clauss, R. C., *A Traveling Wave Maser for Deep Space Communication at 2295 and 2388 MHz*, Technical Report 32-1072, Jet Propulsion Laboratory, Pasadena, Calif., Feb. 15, 1967.

Cohen, M. H., et al., "Compact Radio Source in the Nucleus of M87," *Astrophys. J.*, Vol. 158, No. 2, Pt. 2, pp. L83–L85, Nov. 1969.

Coyner, J. V., Jr., *Radial Rib Antenna Surface Deviation Analysis Program*, Technical Memorandum 33-518, Jet Propulsion Laboratory, Pasadena, Calif., Dec. 15, 1971.

Curkendall, D. W., and McReynolds, S. R., "A Simplified Approach for Determining the Information Content of Radio Tracking Data," *J. Spacecraft Rockets*, Vol. 6, No. 5, pp. 520–525, May 1969.

Curkendall, D. W., and Stephenson, R. R., "Earthbased Tracking and Orbit Determination—Backbone of the Planetary Navigation System," *Astronaut. Aeronaut.*, Vol. 7, No. 5, pp. 30–36, May 1970.

Curkendall, D. W., "Planetary Navigation: The New Challenges," *Astronaut. Aeronaut.*, Vol. 7, No. 5, pp. 26–29, May 1970.

"The Deep Space Network—An Instrument for Radio Navigation for the Mariner Mission to Mars—1969," *Proceedings of the Second International Conference of STM and AERA*, Reidel Publishing Company, Holland, May 1969.

Description of the Deep Space Network Operational Capabilities as of January 1, 1966, Technical Memorandum 33-255, Jet Propulsion Laboratory, Pasadena, Calif., July 1, 1966.

Didday, R. L., and Lindsey, W. C., *Subcarrier Tracking Methods and Communication System Design*, Technical Report 32-1317, Jet Propulsion Laboratory, Pasadena, Calif., reprinted from *IEEE Trans. Commun. Technol.*, Vol. COM-16, No. 4, pp. 541–550, Aug. 1968.

Downs, G. S., a[illegible]chley, P. E., "Observations of Interstellar Scintillations of Pulsar Signals at [illegible]8 MHz," *Astrophys. J.*, Vol. 163, No. 1, Pt. 2, pp. L11–L16, Jan. 1971.

Downs, G. S., et al., "Mars Radar Observation, A Preliminary Report," *Science*, Vol. 174, No. 4016, pp. 1324–1327, Dec. 24, 1971.

Easterling, M., *A Long-Range Precision Ranging System*, Technical Report 32-80, Jet Propulsion Laboratory, Pasadena, Calif., July 10. 1961.

Easterling, M., *Methods for Obtaining Velocity and Range Information from CW Radars*, Technical Report 32-657, Jet Propulsion Laboratory, Pasadena, Calif., Sept. 1, 1964.

Easterling, M., and Goldstein, R., *The Effect of the Interplanetary Medium on S-Band Telecommunications*, Technical Report 32-825, Jet Propulsion Laboratory, Pasadena, Calif., Sept. 1, 1965.

Efron, L., and Solloway, C. B., *Proceedings of the Conference on Scientific Applications of Radio and Radar Tracking in the Space Program*, Technical Report 32-1475, Jet Propulsion Laboratory, Pasadena, Calif., July 1, 1970.

Esposito, P. B., and Wong, S. K., "Geocentric Gravitational Constant Determined from Mariner 9 Radio Tracking Data," paper presented at the International Symposium on Earth Gravity Models (American Geophysical Union, NASA), St. Louis, Aug. 1972.

Fearey, J. P., and Renzetti, N. A., "Navigation Results on the Mariner Mars Mission to Mars 1969," International Navigation Conference, Hamburg, Oct. 1969.

Fjeldbo, G., Kliore, A. J., and Seidel, B. L., "Bistatic Radar Measurements of the Surface of Mars with Mariner 1969," *Icarus*, Vol. 16, No. 3, pp. 502–508, June 1972.

Fjeldbo, G., and Eshleman, V. R., "Radio Occultation Measurements and Interpretations," in *The Atmospheres of Venus and Mars*, p. 225, Gordon and Breach, Science Publishers, Inc., New York, N.Y., 1968.

Flanagan, F. M., et al., *Deep Space Network Support of the Manned Space Flight Network for Apollo: 1962–1968*, Technical Memorandum 33-452, Vol. I, Jet Propulsion Laboratory, Pasadena, Calif., July 1970.

Flanagan, F. M., et al., *Deep Space Network Support of the Manned Space Flight Network for Apollo: 1969–1970*, Technical Memorandum 33-452, Vol. II, Jet Propulsion Laboratory, Pasadena, Calif., May 1, 1971.

Fredricksen, H., *Error Correction for Deep Space Network Teletype Circuits*, Technical Report 32-1275, Jet Propulsion Laboratory, Pasadena, Calif., June 1, 1968.

Georgevic, R. M., *Mathematical Model of the Solar Radiation Force and Torques Acting on the Components of a Spacecraft*, Technical Memorandum 33-494, Jet Propulsion Laboratory, Pasadena, Calif., Oct. 1, 1971.

Goldstein, R., Stevens, R., and Victor, W. K., *Radar Exploration of Venus: Goldstone Observatory Report for October–December 1962*, Technical Report 32-396, Jet Propulsion Laboratory, Pasadena, Calif., Mar. 1, 1965.

Goldstein, R. M., *The Analysis of Uncooperative Radar Targets*, Technical Report 32-658, Jet Propulsion Laboratory, Pasadena, Calif., Sept. 1, 1964.

Goldstein, R. M., et al., *The Superior Conjunction of Mariner V*, Technical Report 32-1092, Jet Propulsion Laboratory, Pasadena, Calif., Apr. 1, 1967.

Goldstein, R. M., "Radar Time-of-Flight Measurements to Venus," *Astron. J.*, Vol. 73, No. 9, Aug. 1968.

Goldstein, R. M., et al., "Preliminary Radar Results of Mars," *Radio Sci.*, Vol. 5, No. 2, pp. 475–478, Feb. 1970.

Goldstein, R. M., and Rumsey, H., "A Radar Snapshot of Venus," *Science*, Vol. 169, Sept. 1970.

Goldstein, R. M., "Radar Observations of Mercury," *Astron. J.*, Vol. 76, No. 10, pp. 1152–1154, Dec. 1971.

Golomb, S. W., "New Problems of Space Communications: Part I. Beware of the Tigers," *Astronautics*, Vol. 7, No. 6, p. 19, June 1962.

Golomb, S. W., "New Problems in Space Communications: Part 3," *Astronautics*, Vol. 7, No. 8, p. 26, Aug. 1962.

Golomb, S. W., "Ferreting Signals Out of Noise," *Int. Sci. Technol.*, No. 22, pp. 72–82 and 120, Oct. 1963.

Gordon, H. J., et al., *The Mariner 6 and 7 Flight Paths and Their Determination From Tracking Data*, Technical Memorandum 33-469, Jet Propulsion Laboratory, Pasadena, Calif., Dec. 1, 1970.

Gottlieb, P., et al., "Lunar Gravity over Large Craters from Apollo 12 Tracking Data," *Science*, Vol. 168, No. 3930, pp. 477–479, Apr. 1970.

Gray, R. M., and Tausworthe, R. C., "Frequency-Counted Measurements, and Phase Locking to Noise Oscillators," *IEEE Trans. Commun. Technol.*, Vol. COM-19, No. 1, pp. 21–30, Feb. 1971.

Gubbay, J., et al., "Variations of Small Quasar Components at 2,300 MHz," *Nature*, Vol. 224, No. 5224, pp. 1094–1095, Dec. 1969.

Gulkis, S., and Gary, B., "Circular Polarization and Total-Flux Measurements of Jupiter at 13.1 cm Wavelength," *Astron. J.*, Vol. 76, No. 1, pp. 12–16, Feb. 1971.

Hall, J. R., *Tracking and Data System Support for Lunar Orbiter*, Technical Memorandum 33-450, Jet Propulsion Laboratory, Pasadena, Calif., Apr. 1970.

Hamilton, T. W., et al., *The Ranger IV Flight Path and Its Determination From Tracking Data*, Technical Report 32-345, Jet Propulsion Laboratory, Pasadena, Calif., Sept. 15, 1962.

Hartop, R. W., *Power Loss Between Arbitrarily Polarized Antennas*, Technical Report 32-457, Jet Propulsion Laboratory, Pasadena, Calif., Sept. 1, 1964.

Havens, W. F., et al., *Scan Pointing Calibration for the Mariner Mars 1971 Spacecraft*, Technical Memorandum 33-556, Jet Propulsion Laboratory, Pasadena, Calif., Aug. 1, 1972.

Heftman, K., and Renzetti, N. A., "Data Return Capabilities of the Deep Space Network in the 1970's," AIAA Paper 67-648, *Proceedings of the AIAA Space Program Issues of the 70's Meeting*, Aug. 1967.

Higa, W. H., *Low-Level Microwave Mixing in Ruby*, Technical Report 32-1016, Jet Propulsion Laboratory, Pasadena, Calif., reprinted from *Proc. IEEE*, Vol. 54, No. 10, p. 1453, Oct. 1966.

Higa, W. H., "Time Synchronization via Lunar Radar," *Proc. IEEE*, Vol. 60, No. 5, pp. 552–557, May 1972.

Holmes, J. K., "On a Solution to the Second-Order Phase-Locked Loop," *IEEE Trans. Commun. Technol.*, Vol. COM-18, No. 2, pp. 119–126, Apr. 1970.

Holmes, J. K., "First Slip Times Versus Static Phase Error Offset for the First and Passive Second-Order Phase-Locked Loop," *IEEE Trans. Commun. Technol.*, Vol. COM-19, No. 2, pp. 234–235, Apr. 1971.

Holmes, J. K., and Tegnelia, C. R., *Digital Command System Second-Order Subcarrier Tracking Performance*, Technical Report 32-1540, Jet Propulsion Laboratory, Pasadena, Calif., Oct. 1, 1971.

Holmes, J. K., "Performance of a First Order Transition Sampling Digital Phase-Locked Loop Using Random-Walk Models," *IEEE Trans. Commun.*, Vol. COM-20, No. 2, pp. 119–131, Apr. 1972.

Hurd, W. J., and Anderson, T. O., *Digital Transition Tracking Symbol Synchronizer for Low SNR Coded Systems*, Technical Report 32-1488, Jet Propulsion Laboratory, Pasadena, Calif., reprinted from *IEEE Trans. Commun. Technol.*, Vol. COM-18, No. 2, pp. 141–147, Apr. 1970.

Jaffe, R., and Rechtin, E., *Design and Performance of Phase-Lock Loops Capable of Near-Optimum Performance over a Wide Range of Input Signal and Noise Levels*, Progress Report 20-243, Jet Propulsion Laboratory, Pasadena, Calif., Dec.

1, 1954; also available in *IRE Trans. Inform. Theory*, No. 1, pp. 66–67, Mar. 1955.

Jordan, J. F., "Orbit Determination for Powered Flight Space Vehicles on Deep Space Missions," *J. Spacecraft Rockets*, Vol. 6, No. 5, pp. 545–550, May 1969.

Kellerman, K. I., et al., "High Resolution Observations of Compact Radio Sources at 13 Centimeters," *Astrophys. J.*, Vol. 161, No. 3, pp. 803–809, Sept. 1970.

Kelly, A. J., *Microwave Probe for Plasma Plumes*, Technical Report 32-625, Jet Propulsion Laboratory, Pasadena, Calif., Feb. 1965.

Kliore, A., Cain, D. L., and Hamilton, T. W., *Determination of Some Physical Properties of the Atmosphere of Mars from Changes in the Doppler Signal of a Spacecraft on an Earth-Occultation Trajectory*, Technical Report 32-674, Jet Propulsion Laboratory, Pasadena, Calif., Oct. 15, 1964.

Kliore, A., and Tito, D. A., *Radio Occultation Investigations of the Atmosphere of Mars*, Technical Report 32-1157, Jet Propulsion Laboratory, Pasadena, Calif., reprinted from *J. Spacecraft Rockets*, Vol. 4, No. 5, pp. 578–582, May 1967.

Kliore, A., "Radio Occultation Measurements of the Atmospheres of Mars and Venus," in *The Atmospheres of Venus and Mars*, edited by J. C. Brandt and M. B. McElrow, p. 205, Gordon and Breach Science Publishers, Inc., New York, N.Y., 1968.

Kliore, A. J., et al., "Summary of Mariner 6 and 7 Radio Occultation Results on the Atmosphere of Mars," *Space Research*, Vol. XI, pp. 165–175, Akademie-Verlag, Berlin, 1971.

Kliore, A. J., et al., "Mariner 9 S-Band Martian Occultation Experiment: Initial Results on the Atmosphere and Topography of Mars," *Science*, Vol. 175, No. 4019, pp. 313–317, Jan. 1972.

Labrum, R. G., et al., *The Surveyor V, VI, and VII Flight Paths and Their Determination from Tracking Data*, Technical Report 32-1302, Jet Propulsion Laboratory, Pasadena, Calif., Dec. 1, 1968.

Laeser, R. P., et al., *Tracking and Data System Support for the Mariner Mars 1971 Mission: Prelaunch Phase Through First Trajectory Correction Maneuver*, Technical Memorandum 33-523, Vol. I, Jet Propulsion Laboratory, Pasadena, Calif., Mar. 15, 1972.

Layland, J. W., "On Optimal Signals for Phase-Locked Loops," *IEEE Trans. Commun. Technol.*, Vol. COM-17, No. 5, pp. 526–531, Oct. 1969.

Layland, J. W., and Lushbaugh, W. A., "A Flexible High-Speed Sequential Decoder for Deep Space Channels," *IEEE Trans. Commun. Technol.*, Vol. COM-19 No. 5, pp. 813–820, Oct. 1971.

Leavitt, R. K., *The Least-Squares Process of MEDIA for Computing DRVID Calibration Polynomials*, Technical Memorandum 33-542, Jet Propulsion Laboratory, Pasadena, Calif., May 15, 1972.

Levy, G. S., Otoshi, T. Y., and Seidel, B. L., *Ground Instrumentation for Mariner IV Occultation Experiment*, Technical Report 32-984, Jet Propulsion Laboratory, Pasadena, Calif., Sept. 15, 1966.

Levy, G. S., et al., *Lunar Range Radiation Patterns of a 210-Foot Antenna at S-Band*, Technical Report 32-1079, Jet Propulsion Laboratory, Pasadena, Calif.,

reprinted from *IEEE Trans. Antennas Propagation*, Vol. AP-15, No. 2, pp. 311–313, Mar. 1967.

Levy, G. S., et al., *The Ultra Cone: An Ultra-Low-Noise Space Communication Ground Radio-Frequency System*, Technical Report 32-1340, Jet Propulsion Laboratory, Pasadena, Calif., reprinted from *IEEE Trans. Microwave Theor. Tech.*, Vol. MTT-16, No. 9, pp. 596–602, Sept. 1968.

Levy, G. S., et al., "Pioneer 6: Measurement of Transient Faraday Rotation Phenomena Observed During Solar Occultation," *Science*, Vol. 166, No. 3905, pp. 596–598, Oct. 1969.

Lieske, J. H., and Null, G. W., "Icarus and the Determination of Astronomical Constants," *Astron. J.*, Vol. 74, No. 2, Mar. 1969.

Lieske, J. H., et al., "Simultaneous Solution for the Masses of the Principal Planets from Analysis of Optical Radar and Radio Tracking Data," *Celest. Mech.*, Vol. 4, No. 2, pp. 233–245, Oct. 1971.

Lindsey, W. C., *Optimum and Suboptimum Frequency Demodulation*, Technical Report 32-637, Jet Propulsion Laboratory, Pasadena, Calif., June 15, 1964.

Lindsey, W. C., *Improvements to be Realized Through the Use of Block-Coded Communication Systems*, Technical Report 32-947, Jet Propulsion Laboratory, Pasadena, Calif., reprinted from *IEEE Trans. Aerosp. Electron. Syst.*, Vol. AES-2, No. 3, pp. 364–366, May 1966.

Lindsey, W. C., *Phase-Shift-Keyed Signal Detection with Noisy Reference Signals*, Technical Report 32-968, Jet Propulsion Laboratory, Pasadena, Calif., reprinted from *IEEE Trans. Aerosp. Electron. Syst.*, Vol. AES-2, No. 4, pp. 393–401, July 1966.

Lindsey, W. C., *A Theory for the Design of One-Way and Two-Way Phase-Coherent Communication Systems: Phase-Coherent Tracking Systems*, Technical Report 32-986, Jet Propulsion Laboratory, Pasadena, Calif., July 15, 1969.

Lindsey, W. C., *Optimal Design of One-Way and Two-Way Coherent Communication Links*, Technical Report 32-988, Jet Propulsion Laboratory, Pasadena, Calif., reprinted from *IEEE Trans. Commun. Technol.*, Vol. COM-14, No. 4, pp. 418–431, Aug. 1966.

Lindsey, W. C., and Charles, F. J., *A Model Distribution for the Phase Error in Second-Order Phase-Locked Loops*, Technical Report 32-1017, Jet Propulsion Laboratory, Pasadena, Calif., reprinted from *IEEE Trans. Commun. Technol.*, Vol. COM-14, No. 10, pp. 662–664, Oct. 1966.

Lindsey, W. C., *Performance of Phase-Coherent Receivers Preceded by Bandpass Limiters*, Technical Report 32-1162, Jet Propulsion Laboratory, Pasadena, Calif., Sept. 15, 1967.

Lindsey, W. C., "Block Coding for Space Communications," *IEEE Trans. Commun. Technol.*, Vol. COM-17, No. 2, pp. 217–225, Apr. 1969.

Lindsey, W. C., *Block-Coded Communications*, Technical Report 32-1380, Jet Propulsion Laboratory, Pasadena, Calif., Aug. 15, 1969.

Lindsey, W. C., *Nonlinear Analysis of Generalized Tracking Systems*, Technical Report 32-1453, Jet Propulsion Laboratory, Pasadena, Calif., reprinted from *Proc. IEEE*, Vol. 57, No. 10, pp. 1705–1722, Oct. 1969.

Lindsey, W. C., and Simon, M. K., "The Effect of Loop Stress on the Performance of Phase-Coherent Communication Systems", *IEEE Trans. Commun. Technol.*, Vol. COM-18, No. 5, pp. 569–588, Oct. 1970.

Lindsey, W. C., and Simon, M. K., "Carrier Synchronization and Detection of Polyphase Signals," *IEEE Trans. Commun.*, Vol. COM-20, No. 3, pp. 441–454, June 1972.

Lindsey, W. C., *Synchronization Systems in Communication and Control*, Prentice-Hall, Inc., Englewood Cliffs, N. J., 1972.

Lindsey, W. C., and Simon, M. K., *Telecommunication Systems Engineering*, Prentice-Hall, Inc., Englewood Cliffs, N. J., 1973.

Lorell, J., Anderson, J. D., and Sjogren, W. L., *Characteristics and Format of the Tracking Data to Be Obtained by the NASA Deep Space Instrumentation Facility for Lunar Orbiter*, Technical Memorandum 33-230, Jet Propulsion Laboratory, Pasadena, Calif., June 15, 1965.

Lorell, J., Sjogren, W. L., and Boggs, D., *Compressed Tracking Data Used for First Iteration in Selenodesy Experiment, Lunar Orbiters I and II*, Technical Memorandum 33-343, Jet Propulsion Laboratory, Pasadena, Calif., May 1, 1967.

Lorell, J., and Sjogren, W. L., *Lunar Orbiter Data Analysis*, Technical Report 32-1220, Jet Propulsion Laboratory, Pasadena, Calif., Nov. 15, 1967.

Lorell, J., *Lunar Orbiter Gravity Analysis*, Technical Report 32-1387, Jet Propulsion Laboratory, Pasadena, Calif., June 15, 1969.

Lorell, J., et al., "Icarus: Celestial Mechanics Experiment for Mariner," *Int. J. Sol. Sys.*, Vol. 12, Jan. 1970.

Lorell, J., and Laing, P. A., *Compilation of Lunar Orbiter Tracking Data Used for Long-Term Selenodesy*, Technical Memorandum 33-419, Jet Propulsion Laboratory, Pasadena, Calif., Feb. 1, 1970.

Ludwig, A. C., et al., *Gain Calibration of a Horn Antenna Using Pattern Integration*, Technical Report 32-1572, Jet Propulsion Laboratory, Pasadena, Calif., Oct. 1, 1972.

Madrid, G. A., et al., *Tracking System Analytic Calibration Activities for the Mariner Mars 1971 Mission*, Technical Report 32-1587, Jet Propulsion Laboratory, Pasadena, Calif., Mar. 1, 1974.

Martin, D. P., *A Combined Radar–Radiometer With Variable Polarization*, Technical Memorandum 33-570, Jet Propulsion Laboratory, Pasadena, Calif., Oct. 15, 1972.

McEliece, R. J., *Optimal Communications Nets*, Technical Report 32-697, Jet Propulsion Laboratory, Pasadena, Calif., Apr. 15, 1965.

McNeal, C. E., *Ranger V Tracking Systems Data Analysis Final Report*, Technical Report 32-702, Jet Propulsion Laboratory, Pasadena, Calif., Apr. 15, 1965.

Melbourne, W. G., et al., *Constants and Related Information for Astrodynamical Calculations*, Technical Report 32-1306, Jet Propulsion Laboratory, Pasadena, Calif., July 15, 1968.

Melbourne, W. G., "Planetary Ephemerides," *Astronaut. Aeronaut.*, Vol. 7, No. 5, pp. 38–43, May 1970.

Merrick, W. D., et al., *Deep Space Communications*, Technical Release 34-10, Jet Propulsion Laboratory, Pasadena, Calif., Jan. 29, 1960; also available in *IRE Trans. Mil. Electron.*, Vol. MIL-4, No. 2-3, pp. 158–163, April–June 1960.

Miller, L., et al., *The Atlas-Centaur VI Flight Path and Its Determination from Tracking Data*, Technical Report 32-911, Jet Propulsion Laboratory, Pasadena, Calif., Apr. 15, 1966.

Moyer, T. D., *Mathematical Formulation of the Double-Precision Orbit Determination Program (DPODP)*, Technical Report 32-1527, Jet Propulsion Laboratory, Pasadena, Calif., May 17, 1971.

Muhleman, D. O., *Relationship Between the System of Astronomical Constants and the Radar Determinations of the Astronomical Unit*, Technical Report 32-477, Jet Propulsion Laboratory, Pasadena, Calif., Jan. 15, 1964.

Muhleman, D. O., Goldstein, R., and Carpenter, R., *A Review of Radar Astronomy—Parts I, II*, Technical Report 32-824, Jet Propulsion Laboratory, Pasadena, Calif., Jan. 30, 1966, reprinted from *IEEE Spectrum*, Oct. and Nov. 1965.

Muhleman, D. O., et al., *JPL Radar Range and Doppler Observations of Venus, 1961–1966*, Technical Report 32-1123, Jet Propulsion Laboratory, Pasadena, Calif., July 1, 1968.

Mulhall, B. D., et al., *Tracking System Analytic Calibration Activities for the Mariner Mars 1969 Mission*, Technical Report 32-1499, Jet Propulsion Laboratory, Pasadena, Calif., Nov. 15, 1970.

Mulholland, J. D., and Sjogren, W. L., *Lunar Orbiter Ranging Data*, Technical Report 32-1087, Jet Propulsion Laboratory, Pasadena, Calif., reprinted from *Science*, Vol. 155, No. 3758, pp. 74–76, Jan. 6, 1967.

Mulholland, J. D., *Proceedings of the Symposium on Observation, Analysis and Space Research Applications of the Lunar Motion*, Technical Report 32-1386, Jet Propulsion Laboratory, Pasadena, Calif., Apr. 1969.

Muller, P. M., and Sjogren, W. L., *Consistency of Lunar Orbiter Residuals With Trajectory and Local Gravity Effects*, Technical Report 32-1307, Jet Propulsion Laboratory, Pasadena, Calif., Sept. 1, 1968.

Muller, P. M., and Sjogren, W. L., *Mascons: Lunar Mass Concentrations*, Technical Report 32-1339, Jet Propulsion Laboratory, Pasadena, Calif., reprinted from *Science*, Vol. 161, No. 3842, pp. 680–684, Aug. 16, 1968.

Newburn, R. L., Jr., et al., *Earth-Based Research on the Outer Planets During the Period 1970–1985*, Technical Report 32-1456, Jet Propulsion Laboratory, Pasadena, Calif., Mar. 15, 1970.

Null, G. W., et al., *Mariner IV Flight Path and Its Determination From Tracking Data*, Technical Report 32-1108, Jet Propulsion Laboratory, Pasadena, Calif., Aug. 1, 1967.

O'Neil, W. J., et al., *The Surveyor III and Surveyor IV Flight Paths and Their Determination From Tracking Data*, Technical Report 32-1292, Jet Propulsion Laboratory, Pasadena, Calif., Aug. 15, 1968.

O'Neil, W. J., et al., *Mariner 9 Navigation*, Technical Report 32-1586, Jet Propulsion Laboratory, Pasadena, Calif., Nov. 13, 1973.

Otoshi, T. Y., *The Effect of Mismatched Components on Microwave Noise-Temperature Calibrations*, Technical Report 32-1345, Jet Propulsion Laboratory, Pasadena, Calif., reprinted from *IEEE Trans. Microwave Theor. Tech.*, Vol. MTT-16, No. 9, pp. 675–686, Sept. 1968.

Otoshi, T. Y., Stelzried, C. T., and Yates, B. C., "Comparisons of Waveguide Losses Calibrated by the DC Potentiometer, AC Ratio Transformer, and Reflectometer Techniques," *IEEE Trans. Microwave Theor. Tech.*, Vol. MTT-18, No. 7, pp. 406–409, July 1970.

Otoshi, T. Y., and Stelzried, C. T., "A Precision Compact Rotary Vane Attenuator," *IEEE Trans. Micro. Theor. Technique*, Vol. MTT-19, No. 11, pp. 843–854, Nov. 1971.

Pease, G. E., et al., *The Mariner V Flight Path and Its Determination From Tracking Data*, Technical Report 32-1363, Jet Propulsion Laboratory, Pasadena, Calif., July 1, 1969.

Posner, E. C., *Properties of Error-Correcting Codes at Low Signal-to-Noise Ratios*, Technical Report 32-602, Jet Propulsion Laboratory, Pasadena, Calif., June 15, 1964.

Potter, P. D., *The Design of a Very High Power, Very Low Noise Cassegrain Feed System for a Planetary Radar*, Technical Report 32-653, Jet Propulsion Laboratory, Pasadena, Calif., Aug. 24, 1964.

Potter, P. D., Merrick, W. D., and Ludwig, A. C., *Large Antenna Apertures and Arrays for Deep Space Communications*, Technical Report 32-848, Jet Propulsion Laboratory, Pasadena, Calif., Nov. 1, 1965.

Potter, P. D., *A Computer Program for Machine Design of Cassegrain Feed Systems*, Technical Report 32-1202, Jet Propulsion Laboratory, Pasadena, Calif., Dec. 15, 1967.

Potter, P. D., et al., *A Study of Weather-Dependent Data Links for Deep Space Applications*, Technical Report 32-1392, Jet Propulsion Laboratory, Pasadena, Calif., Oct. 15, 1969.

Rechtin, E., "Communication Techniques for Space Exploration," *IRE Trans. Space Electron. Telem.*, Vol. SET-5, No. 3, pp. 95–98, Sept. 1959.

Rechtin, E., Stevens, R., and Victor, W. K., *Data Transmission and Communications*, Technical Release 34-55, Jet Propulsion Laboratory, Pasadena, Calif., Apr. 30, 1960.

Rechtin, E., *Space Communications*, Technical Release 34-68, Jet Propulsion Laboratory, Pasadena, Calif., May 1, 1960.

Rechtin, E., Rule, B., and Stevens, R., *Large Ground Antennas*, Technical Report 32-213, Jet Propulsion Laboratory, Pasadena, Calif., Mar. 20, 1962.

Rechtin, E., *Lunar Communications*, Technical Memorandum 33-133, Jet Propulsion Laboratory, Pasadena, Calif., June 28, 1963.

Rechtin, E., "Surprises on Venus," *Int. Sci. Technol.*, No. 20, pp. 13–14, Aug. 1963.

Renzetti, N. A., et al., "Radio Tracking Techniques and Performance of the U.S. Deep Space Instrumentation Facility," *Space Research II, Proceedings of the Second International Space Science Symposium*, Florence, Italy, April 1961, North Holland Publishing Company, Amsterdam.

Renzetti, N. A., and Ostermier, B. J., *Communications with Lunar Probes*, Technical Report 32-148, Jet Propulsion Laboratory, Pasadena, Calif., Aug. 23, 1961.

Renzetti, N. A., *Tracking and Data Acquisition for Ranger Missions I–V*, Technical Memorandum 33-174, Jet Propulsion Laboratory, Pasadena, Calif., July 1, 1964.

Renzetti, N. A., *Tracking and Data Acquisition for Ranger Missions VI–IX*, Technical Memorandum 33-275, Jet Propulsion Laboratory, Pasadena, Calif., Sept. 15, 1966.

Renzetti, N. A., *Tracking and Data Acquisition Support for the Mariner Venus 1962 Mission*, Technical Memorandum 33-212, Jet Propulsion Laboratory, Pasadena, Calif., July 1, 1965.

Renzetti, N. A., *Tracking and Data Acquisition Report, Mariner Mars 1964 Mission: Near-Earth Trajectory Phase*, Technical Memorandum 33-239, Vol. I, Jet Propulsion Laboratory, Pasadena, Calif., Jan. 1, 1965.

Renzetti, N. A., *Tracking and Data Acquisition Report, Mariner Mars 1964 Mission: Cruise to Post-Encounter Phase*, Technical Memorandum 33-239, Vol. II, Jet Propulsion Laboratory, Pasadena, Calif., Oct. 1, 1967.

Renzetti, N. A., *Deep Space Network Support, Atlas/Centaur Missions 1–9*, Technical Memorandum 33-347, Jet Propulsion Laboratory, Pasadena, Calif., Sept. 15, 1967.

Renzetti, N. A., "Tracking and Data Acquisition System for Mariner Missions," *Proceedings of the Seventh International Symposium on Space Technology and Science*, Tokyo, 1967.

Renzetti, N. A., *Tracking and Data Acquisition Report, Mariner Mars 1964 Mission: Extended Mission*, Technical Memorandum 33-239, Vol. III, Jet Propulsion Laboratory, Pasadena, Calif., Dec. 1, 1968.

Renzetti, N. A., and Fearey, J. P., "The Deep Space Network: An Instrument for the Radio Navigation for the Mariner Mission to Mars 1969," IInd International Conference on Space Engineering, Venice, Italy, D. Reidel Publishing Co., Dordrecht, Holland, May 1969.

Renzetti, N. A., *Tracking and Data System Support for Surveyor: Missions I and II*, Technical Memorandum 33-301, Vol. I, Jet Propulsion Laboratory, Pasadena, Calif., July 15, 1969.

Renzetti, N. A., *Tracking and Data System Support for Surveyor: Missions III and IV*, Technical Memorandum 33-301, Vol. II, Jet Propulsion Laboratory, Pasadena, Calif., Sept. 1, 1969.

Renzetti, N. A., *Tracking and Data System Support for Surveyor: Mission V*, Technical Memorandum 33-301, Vol. III, Jet Propulsion Laboratory, Pasadena, Calif., Dec. 1, 1969.

Renzetti, N. A., *Tracking and Data System Support for Surveyor: Mission VI*, Technical Memorandum 33-301, Vol. IV, Jet Propulsion Laboratory, Pasadena, Calif., Dec. 1, 1969.

Renzetti, N. A., *Tracking and Data System Support for Surveyor: Mission VII*, Technical Memorandum 33-301, Vol. V, Jet Propulsion Laboratory, Pasadena, Calif., Dec. 1, 1969.

Renzetti, N. A., *Tracking and Data System Support for the Mariner Venus 67 Mission: Planning Phase Through Midcourse Maneuver*, Technical Memorandum 33-385, Vol. I, Jet Propulsion Laboratory, Pasadena, Calif., Sept. 1, 1969.

Renzetti, N. A., *Tracking and Data System Support for the Mariner Venus 67 Mission: Midcourse Maneuver Through End of Mission*, Technical Memorandum 33-385, Vol. II, Jet Propulsion Laboratory, Pasadena, Calif., Sept. 1, 1969.

Renzetti, N. A., *Tracking and Data System Support for the Pioneer Project: Pioneer VI. Prelaunch to End of Nominal Mission*, Technical Memorandum 33-426, Vol. I, Jet Propulsion Laboratory, Pasadena, Calif., Feb. 1, 1970.

Renzetti, N. A., *Tracking and Data System Support for the Pioneer Project: Pioneer VII. Prelaunch to End of Nominal Mission*, Technical Memorandum 33-426, Vol. II, Jet Propulsion Laboratory, Pasadena, Calif., Apr. 15, 1970.

Renzetti, N. A., *Tracking and Data System Support for the Pioneer Project: Pioneer VIII. Prelaunch Through May 1968*, Technical Memorandum 33-426, Vol. III, Jet Propulsion Laboratory, Pasadena, Calif., July 15, 1970.

Renzetti, N. A., *Tracking and Data System Support for the Pioneer Project: Pioneer IX. Prelaunch Through June 1969*, Technical Memorandum 33-426, Vol. IV, Jet Propulsion Laboratory, Pasadena, Calif., Nov. 15, 1970.

Renzetti, N. A., *Tracking and Data System Support for the Pioneer Project: Pioneer VI. Extended Mission: July 1, 1966–July 1, 1969*, Technical Memorandum 33-426, Vol. V, Jet Propulsion Laboratory, Pasadena, Calif., Feb. 1, 1971.

Renzetti, N. A., *Tracking and Data System Support for the Pioneer Project: Pioneer VII. Extended Mission: February 24, 1967–July 1, 1968*, Technical Memorandum 33-426, Vol. VI, Jet Propulsion Laboratory, Pasadena, Calif., Apr. 15, 1971.

Renzetti, N. A., *Tracking and Data System Support for the Pioneer Project: Pioneer VII. Extended Mission: July 1, 1968–July 1, 1969*, Technical Memorandum 33-426, Vol. VII, Jet Propulsion Laboratory, Pasadena, Calif., Apr. 15, 1971.

Renzetti, N. A., *Tracking and Data System Support for the Pioneer Project: Pioneer VIII. Extended Mission: June 1, 1968–July 1, 1969*, Technical Memorandum 33-426, Vol. VIII, Jet Propulsion Laboratory, Pasadena, Calif., May 1, 1971.

Renzetti, N. A., *Tracking and Data System Support for the Pioneer Project: Pioneers VI–IX. Extended Missions: July 1, 1969–July 1, 1970*, Technical Memorandum 33-426, Vol. IX, Jet Propulsion Laboratory, Pasadena, Calif., Aug. 15, 1971.

Renzetti, N. A., and Siegmeth, A. J., *Tracking and Data System Support for the Pioneer Project: Pioneers 6–9. Extended Missions: July 1, 1971–July 1, 1972*, Technical Memorandum 33-426, Vol. XI, Jet Propulsion Laboratory, Pasadena, Calif., May 1, 1973.

Renzetti, N. A., et al., *Tracking and Data System Support for the Mariner Mars 1969 Mission: Planning Phase Through Midcourse Maneuver*, Technical Memorandum 33-474, Vol. I, Jet Propulsion Laboratory, Pasadena, Calif., May 15, 1971.

Renzetti, N. A., et al., *Tracking and Data System Support for the Mariner Mars 1969 Mission: Midcourse Maneuver Through End of Nominal Mission*, Technical Memorandum 33-474, Vol. II, Jet Propulsion Laboratory, Pasadena, Calif., Sept. 1, 1971.

Renzetti, N. A., Linnes, K. W., and Taylor, T. M., *Tracking and Data System Support for the Mariner Mars 1969 Mission: Extended Operations Mission*, Technical Memorandum 33-474, Vol. III, Jet Propulsion Laboratory, Pasadena, Calif., Sept. 15, 1971.

Renzetti, N. A., *A History of the Deep Space Network: From Inception to January 1, 1969*, Technical Report 32-1533, Vol. I, Jet Propulsion Laboratory, Pasadena, Calif., Sept. 1, 1971.

Renzetti, N. A., "Radio Communications at Planetary Distances," paper presented at the International Convention on Radio Communication, Rome and Bologna, Italy, Mar. 1974.

Richter, H. L., Rechtin, E., and Walter, W. K., *National Ground-Based Surveillance Complex (U)*, Publication 146, Jet Propulsion Laboratory, Pasadena, Calif., Feb. 16, 1959 (Confidential).

Rusch, W. V. T., *Phase Error and Associated Cross-Polarization Effects in Cassegrainian-Fed Microwave Antennas*, Technical Report 32-610, Jet Propulsion Laboratory, Pasadena, Calif., May 30, 1965.

Rusch, W. V. T., and Stelzried, C. T., *Observations of the Lunar Eclipse of December 19, 1964, at a Wavelength of 3.3 MM*, Technical Report 32-1097, Jet Propulsion Laboratory, Pasadena, Calif., reprinted from *Astrophys. J.*, Vol. 148, No. 1, pp. 255–259, Apr. 1967.

Rusch, W. V. T., *Applications of Two-Dimensional Integral-Equation Theory to Reflector-Antenna Analysis*, Technical Memorandum 33-478, Jet Propulsion Laboratory, Pasadena, Calif., May 1, 1971.

Sanger, D. K., *Digital Demodulation with Data Subcarrier Tracking*, Technical Report 32-1314, Jet Propulsion Laboratory, Pasadena, Calif., Aug. 1, 1968.

Siegmeth, A. J., Purdue, R. E., and Ryan, R. E., *Tracking and Data System Support for the Pioneer Project: Pioneers 6–9. Extended Missions: July 1, 1970–July 1, 1971*, Technical Memorandum 33-426, Vol. X, Jet Propulsion Laboratory, Pasadena, Calif., Aug. 15, 1972.

Siegmeth, A. J., et al., *Tracking and Data System Support for the Pioneer Project: Pioneer 10–Prelaunch Planning Through Second Trajectory Correction December 4, 1969 to April 1, 1972*, Technical Memorandum 33-584, Vol. I, Jet Propulsion Laboratory, Pasadena, Calif., Apr. 1, 1973.

Simon, M. K., "Nonlinear Analysis of an Absolute Value Type of an Early-Late Gate Bit Synchronizer," *IEEE Trans. Commun. Technol.*, Vol. COM-18, No. 5, pp. 589–596, Oct. 1970.

Simon, M. K., "Optimization of the Performance of a Digital-Data-Transition Tracking Loop," *IEEE Trans. Commun. Technol.*, Vol. COM-18, No. 5, pp. 686–689, Oct. 1970.

Simon, M. K., and Lindsey, W. C., "Data-Aided Carrier Tracking Loops," *IEEE Trans. Commun. Technol.*, Vol. COM-19, No. 2, pp. 157–168, Apr. 1971.

Simon, M. K., "On the Selection of an Optimum Design Point for Phase-Coherent Receivers Employing Bandpass Limiters," *IEEE Trans. Commun.*, Vol. COM-20, No. 2, pp. 210–214, Apr. 1972.

Simon, M. K., "On the Selection of a Sampling Filter Bandwidth for a Digital Data Detector," *IEEE Trans. Commun.*, Vol. COM-20, No. 3, pp. 438–441, June 1972.

Sjogren, W. L., et al., *The Ranger V Flight Path and Its Determination From Tracking Data*, Technical Report 32-562, Jet Propulsion Laboratory, Pasadena, Calif., Dec. 6, 1963.

Sjogren, W. L., et al., *The Ranger VI Flight Path and Its Determination From Tracking Data*, Technical Report 32-605, Jet Propulsion Laboratory, Pasadena, Calif., Dec. 15, 1964.

Sjogren, W. L., *The Ranger III Flight Path and Its Determination From Tracking Data*, Technical Report 32-563, Jet Propulsion Laboratory, Pasadena, Calif., Sept. 15, 1965.

Sjogren, W. L., et al., *Physical Constants as Determined From Radio Tracking of the Ranger Lunar Probes*, Technical Report 32-1057, Jet Propulsion Laboratory, Pasadena, Calif., Dec. 30, 1966.

Sjogren, W. L., *Proceedings of the JPL Seminar on Uncertainties in the Lunar Ephemeris*, Technical Report 32-1247, Jet Propulsion Laboratory, Pasadena, Calif., May 1, 1968.

Sjogren, W. L., "Lunar Gravity Estimate: Independent Confirmation," *J. Geophys. Res.*, Vol. 76, No. 29, Oct. 10, 1971.

Sjogren, W. L., et al., "Lunar Gravity via Apollo 14 Doppler Radio Tracking," *Science*, Vol. 175, No. 4018, pp. 165–168, Jan. 14, 1972.

Slobin, S. D., "Beam Switching Cassegrain Feed System and Its Applications to Microwave and Millimeterwave Radioastronomical Observations," *Rev. Sci. Instr.*, Vol. 41, No. 3, pp. 439–443, Mar. 1970.

Spier, G. W., *Design and Implementation of Models for the Double Precision Trajectory Program (DPTRAJ)*, Technical Memorandum 33-451, Jet Propulsion Laboratory, Pasadena, Calif., Apr. 15, 1971.

Springett, J. C., and Simon, M. K., "An Analysis of the Phase Coherent-Incoherent Output of the Bandpass Limiter," *IEEE Trans. Commun. Technol.*, Vol. COM-19, No. 1, pp. 42–49, Feb. 1971.

Stelzried, C. T., *Post-Amplifier Noise Temperature Contribution in a Low-Noise Receiving System*, Technical Report 32-446, Jet Propulsion Laboratory, Pasadena, Calif., Jan. 1964.

Stelzried, C. T., Reid, M. S., and Petty, S. M., *A Precision DC-Potentiometer Microwave Insertion-Loss Test Set*, Technical Report 32-887, Jet Propulsion Laboratory, Pasadena, Calif., Mar. 15, 1966.

Stelzried, C. T., Reid, M. S., and Nixon, D., *Precision Power Measurements of Spacecraft CW Signal With Microwave Noise Standards*, Technical Report 32-1066, Jet Propulsion Laboratory, Pasadena, Calif., Feb. 15, 1968.

Stelzried, C. T., and Reid, M. S., *Precision Power Measurements of Spacecraft CW Signal Level With Microwave Noise Standards*, Technical Report 32-1070, Jet Propulsion Laboratory, Pasadena, Calif., reprinted from *IEEE Trans. Instrum. Measurement*, Vol. IM-15, No. 4, pp. 318–324, Dec. 1966.

Stelzried, C. T., and Rusch, W. V. T., *Improved Determination of Atmospheric Opacity From Radio Astronomy Measurements*, Technical Report 32-1115, Jet Propulsion Laboratory, Pasadena, Calif., reprinted from *J. Geophys. Res.*, Vol. 72, No. 9, pp. 2445–2447, May 1, 1967.

Stelzried, C. T., and Otoshi, T. Y., "Radiometric Evaluation of Antenna-Feed Component Losses," *IEEE Trans. Instrumen. Measurement*, Vol. IM-18, No. 3, pp. 172–183, Sept. 1969.

Stelzried, C. T., "Precision Microwave Waveguide Loss Calibrations," *IEEE Trans. Instrum. Measurement*, Vol. IM-19, No. 1, pp. 23–25, Feb. 1970.

Stelzried, C. T., *A Faraday Rotation Measurement of a 13-cm Signal in the Solar Corona*, Technical Report 32-1401, Jet Propulsion Laboratory, Pasadena, Calif., July 15, 1970.

Stelzried, C. T., et al., "The Quasi-Stationary Coronal Magnetic Field and Electron Density as Determined From a Faraday Rotation Experiment," *Sol. Phys.*, Vol. 14, No. 2, pp. 440–456, Oct. 1970.

Stelzried, C. T., "Operating Noise-Temperature Calibrations of Low-Noise Receiving Systems," *Microwave J.*, Vol. 14, No. 6, pp. 41–46, 48, June 1971.

Stelzried, C. T., et al., "Transformation of Received Signal Polarization Angle to the Plane of the Ecliptic," *J. Space. Rock.*, Vol. 9, No. 2, pp. 69–70, Feb. 1972.

System Capabilities and Development Schedule of the Deep Space Instrumentation Facility 1963–1967, Technical Memorandum 33-83, Jet Propulsion Laboratory, Pasadena, Calif., Mar. 2, 1962.

Tardani, P. A., *Madrid Site Selection Report*, Technical Memorandum 33-149, Jet Propulsion Laboratory, Pasadena, Calif., July 17, 1963.

Tausworthe, R. C., *A Precision Planetary Range-Tracking Radar*, Technical Report 32-779, Jet Propulsion Laboratory, Pasadena, Calif., reprinted from *IEEE Trans. Space Electron. Telem.*, Vol. SET-11, No. 2, pp. 78–85, June 1965.

Tausworthe, R. C., *Theory and Practical Design of Phase-Locked Receivers*, Technical Report 32-819, Vol. I, Jet Propulsion Laboratory, Pasadena, Calif., Feb. 15, 1966.

Tausworthe, R., *Cycle Slipping in Phase-Locked Loops*, Technical Report 32-1127, Jet Propulsion Laboratory, Pasadena, Calif., reprinted from *IEEE Trans. Commun. Technol.*, Vol. COM-15, No. 3, pp. 417–421, June 1967.

Tausworthe, R. C., Easterling, M. F., and Spear, A. J., *A High-Rate Telemetry System for the Mariner Mars 1969 Mission*, Technical Report 32-1354, Jet Propulsion Laboratory, Pasadena, Calif., Apr. 1, 1969.

Tausworthe, R. C., *DSS Subsystem Implementation by Time-Shared Computer*, Technical Memorandum 33-420, Jet Propulsion Laboratory, Pasadena, Calif., Oct. 1, 1969.

Tausworthe, R. C., "Convergence of Oscillator Spectral Estimators for Counted-Frequency Measurements," *IEEE Trans. Commun.*, Vol. COM-20, No. 2, pp. 213–217, Apr. 1972.

Tausworthe, R. C., "Simplified Formula for Mean-Slip Time of Phase-Locked Loops With Steady-State Phase Error," *IEEE Trans. Commun.*, Vol. COM-20, No. 3, pp. 331–337, June 1972.

Telecommunications Systems Design Techniques Handbook, Technical Memorandum 33-571, edited by R. E. Edelson, Jet Propulsion Laboratory, Pasadena, Calif., July 15, 1972.

Textor, G. P., Kelly, L. B., and Kelly, M., *Tracking and Data System Support for the Mariner Mars 1971 Mission: First Trajectory Correction Maneuver Through Orbit Insertion*, Technical Memorandum 33-523, Vol. II, Jet Propulsion Laboratory, Pasadena, Calif., June 15, 1972.

Thornton, J. H., Jr., *The Surveyor I and Surveyor II Flight Paths and Their Determination From Tracking Data*, Technical Report 32-1285, Jet Propulsion Laboratory, Pasadena, Calif., Aug. 1, 1968.

Timor, U., "Equivalence of Time-Multiplexed and Frequency-Multiplexed Signals in Digital Communications," *IEEE Trans. Commun.*, Vol. COM-20, No. 3, pp. 435–438, June 1972.

Titsworth, R. C., and Welch, L. R., *Power Spectra of Signals Modulated by Random and Pseudorandom Sequences*, Technical Report 32-140, Jet Propulsion Laboratory, Pasadena, Calif., Oct. 10, 1961.

Titsworth, R. C., *The Algebra of Periodic Sequences*, Technical Report 32-381, Jet Propulsion Laboratory, Pasadena, Calif., Jan. 7, 1963.

Titsworth, R. C., *Correlation Properties of Cyclic Sequences*, Technical Report 32-388, Jet Propulsion Laboratory, Pasadena, Calif., July 1, 1963.

Titsworth, R. C., *Optimal Ranging Codes*, Technical Report 32-411, Jet Propulsion Laboratory, Pasadena, Calif., Apr. 15, 1963.

Titsworth, R. C., *Equivalence Classes of Periodic Sequences*, Technical Report 32-568, Jet Propulsion Laboratory, Pasadena, Calif., June 15, 1964, reprinted from *Ill. J. Math.*, Vol. 8, No. 2, June 1964.

Titsworth, R. C., *The Role of Pseudorandom Codes in Communications*, Technical Memorandum 33-185, Jet Propulsion Laboratory, Pasadena, Calif., Aug. 3, 1964.

"Tracking and Data Acquisition System for Mariner Missions," *Proceedings of the Seventh International Symposium on Space Technology and Science*, Tokyo, May 1967.

Vegos, C. J., et al., *The Ranger IX Flight Path and Its Determination From Tracking Data*, Technical Report 32-767, Jet Propulsion Laboratory, Pasadena, Calif., Nov. 1, 1968.

Victor, W. K., Stevens, R., and Golomb, S. W., *Radar Exploration of Venus: Goldstone Observatory Report for March-May 1961*, Technical Report 32-132, Jet Propulsion Laboratory, Pasadena, Calif., Aug. 1, 1961.

Victor, W. K., Titsworth, R. C., and Rechtin, E., *Telecommunication Aspects of a Manned Mars Mission*, Technical Report 32-501, Jet Propulsion Laboratory, Pasadena, Calif., Aug. 20, 1963.

Viterbi, A. J., *Acquisition Range and Tracking Behavior of Phase-Locked Loops*, External Publication 673, Jet Propulsion Laboratory, Pasadena, Calif., July 14, 1959.

Viterbi, A. J., *On Coded Phase-Coherent Communications*, Technical Report 32-25, Jet Propulsion Laboratory, Pasadena, Calif., Aug. 15, 1960.

C - 3

Viterbi, A. J., *Classification and Evaluation of Coherent Synchronous Sampled-Data Telemetry Systems*, Technical Report 32-123, Jet Propulsion Laboratory, Pasadena, Calif., June 15, 1961.

Viterbi, A. J., *Phase-Locked Loop Dynamics in the Presence of Noise by Fokker-Planck Techniques*, Technical Report 32-427, Jet Propulsion Laboratory, Pasadena, Calif., Mar. 29, 1963; also reprinted in *IEEE Proc.*, Vol. 51, No. 12, pp. 1737–1753, Dec. 1963.

Viterbi, A. J., *Orthogonal Tree Codes for Communication in the Presence of White Gaussian Noise*, Technical Report 32-1120, Jet Propulsion Laboratory, Pasadena, Calif., reprinted from *IEEE Trans. Commun. Technol.*, Vol. COM-15, No. 2, pp. 238–242, Apr. 1967.

Winn, F. B., "Selenographic Location of Surveyor VI," in *Surveyor VI Mission Report: Part II. Science Results*, Technical Report 32-1262, Jet Propulsion Laboratory, Pasadena, Calif., Jan. 10, 1968.

Winn, F. B., "Post Landing Tracking Data Analysis," in *Surveyor VII Mission Report: Part II. Science Results*, Technical Report 32-1264, Jet Propulsion Laboratory, Pasadena, Calif., Mar. 15, 1968.

Winn, F. B., "Surveyor Post-Touchdown Analysis of Tracking Data," in *Surveyor Project Final Report: Part II. Science Results*, Technical Report 32-1265, Jet Propulsion Laboratory, Pasadena, Calif., June 15, 1968.

Winn, F. B., *Surveyor Posttouchdown Analyses of Tracking Data*, NASA SP-184, National Aeronautics and Space Administration, Washington, D.C., p. 369.

Wollenhaupt, W. R., *Tracking System Data Analysis Report, Ranger 4 Final Report*, Technical Report 32-523, Jet Propulsion Laboratory, Pasadena, Calif., Mar. 1, 1964.

Wollenhaupt, W. R., et al., *The Ranger VII Flight Path and Its Determination From Tracking Data*, Technical Report 32-694, Jet Propulsion Laboratory, Pasadena, Calif., Dec. 15, 1964.

NASA — JPL — Coml., L.A., Calif.